Electron Microscopy Study of Radiation Damage in Tungsten and Alloys

Xiaoou Yi B.E. MSc.

Wolfson College

University of Oxford



A thesis submitted for the degree of

Doctor of Philosophy

Michaelmas Term 2013

Electron Microscopy Study of Radiation Damage in Tungsten and Alloys

Xiaoou Yi, Wolfson College

Thesis abstract submitted for the degree of Doctor of Philosophy
Michaelmas Term 2013

The displacement damage induced by primary recoils of fusion neutrons in tungsten and alloys has been studied with self-ion irradiations, followed by damage characterization with electron microscopy.

Tungsten and alloys (≤ 5 wt.% Re, Ta, V) were implanted with 2 MeV W^+ ions over a dose range of 3.3×10^{17} - 2.5×10^{19} W^+m^{-2} at temperatures ranging from 300 to 750°C. Dislocation loops of **b** = ½<111> (> 60%) and **b** = <100> were identified, and that ½<111> loops were found more thermally stable. Among loops that were large enough for nature determination, at least 50% were found to be of interstitial type, with larger fractions in high-temperature and high-dose conditions. The diameter of loops did not exceed 20 nm, with the majority being ≤ 5 nm. The loop number density varied between 10^{22} and 10^{23} m^{-3}. The effects of ion dose, irradiation temperature, composition and grain orientation on damage microstructure were investigated.

In-situ irradiations (150 keV W^+ ions) were carried out as a complement to the bulk implantations. Qualitative trends in loop size, geometry and nature with irradiation dose and temperature were similar to bulk irradiated specimens. Also, the dynamics of defects and their effects on the damage evolution were explored. In-situ annealing of irradiated thin foils was performed to investigate the thermal stability of radiation damage in tungsten. The majority of microstructure transformations were completed within 15 min of annealing. However, extended durations did favour the increase of loop size and the fraction of ½<111> loops.

Preface

The work on the electron microscopy study of radiation damage in tungsten and alloys has generated a number of publications with collaborators from Argonne National Laboratory, USA (Dr. M. A. Kirk and Mr. P. Baldo) and Karlsruhe Institute of Technology, Germany (Prof. M. Rieth and Dr. J. Reiser). Additionally, the results have been presented at several workshops and conferences. Details are summarized as follows:

List of publications

1. 'Tungsten foil laminate for structural divertor applications – Analyses and characterization of tungsten foil', J. Reiser, M. Rieth, B. Dafferner, A. Hoffmann, **X. Yi**, D. E. J. Armstrong. Journal of Nuclear Materials 424 (2012) 197-203.

2. 'Hardening of Self-Ion Implanted Tungsten and Tungsten 5-wt% Rhenium', D. E. J. Armstrong, **X. Yi**, E. A. Marquis, S. G. Roberts. Journal of Nuclear Materials 432 (2013) 428-436.

3. 'In-situ irradiation study of self ion damaged W and W-5Re at 500°C', **X. Yi**, M. L. Jenkins, M. Briceno, S. G. Roberts, Z. Zhou, M. A. Kirk, Philosophical Magazine Vol. 93, No.14 (2013) 1715-1738.

4. 'Tungsten foil laminate for structural divertor applications – Tensile test properties of tungsten foil', J. Reiser, M. Rieth, A. Möslang, B. Dafferner, A. Hoffmann, **X. Yi**, D. E. J. Armstrong. Journal of Nuclear Materials 434 (2013) 357-366.

5. 'Spatial ordering of nano-dislocation loops in ion-irradiated materials', S. L. Dudarev, K. Arakawa, **X. Yi**, Z. Yao, M. L. Jenkins, M. R. Gilbert, P. M. Derlet, accepted by Journal of Nuclear Materials (2014).

6. 'Elastic trapping of dislocation loops in cascades in ion-irradiated tungsten foils', D. R. Mason, **X. Yi**, M. A. Kirk, S. L. Dudarev, submitted to Journal of New Physics (2014), arXiv:1402.0689.

7. 'Electron microscopy studies of radiation damage in 2 MeV W^+ implanted W and W-alloys', **X. Yi**, M. L. Jenkins, S. G. Roberts. (*Manuscript*)

8. 'In-situ irradiation studies of 150 keV W^+ implanted W and W-alloys: damage microstructure and thermal stability', **X. Yi**, M. L. Jenkins, S. G. Roberts. (*Manuscript*)

Presentations at conferences and workshops

- 2013/11: Invited talk on "In-situ transmission electron microscope observations of radiation damage effects in tungsten and iron" at the "Electron Microscopy and Multiscale Modelling" conference, Kyoto, Japan.

- 2013/09: Keynote presentation on "TEM of radiation damage in tungsten" at the Workshop on Tungsten for Nuclear Applications, University of Oxford.

- 2012/07: Quantitative Interpretation of TEM Imaging and Diffraction Data, University of Oxford.
  Poster: In-situ electron microscopy study of the temperature dependence of cascade collapse in self-ion irradiated tungsten.

- 2012/06: MAT-HHFM Monitor Meeting of EFDA (European Fusion Development Agreement).
  Talk: In-situ TEM observation of variable-temperature self-ion irradiation effects in W/W-alloys.

- 2011/05: 13th International Workshop on Plasma-Facing Materials and Components for Fusion Applications/1st International Conference on Fusion Energy Materials Science, Rosenheim, Germany.
  Poster: TEM characterization of self-ion damaged polycrystalline W and W alloy.

Acknowledgements

First of all, I'd like to give my most sincere thanks to Dr. M. L. Jenkins and Prof. S. G. Roberts for supervising this project. Their research expertise, persistent patience and encouragement have guided me through the four "tough" years of DPhil study. A substantial portion of this thesis involved external collaborations and access to user facilities. Thank you so much for making all this happen.

Second, it is my greatest pleasure and honour to work with the following people, Dr. D. E. J. Armstrong, Dr. M. Briceno, Mr. S. Xu, Mr. C. Hardie, Mr. C. Beck, Mr. A. Xu, Mr. J. Gibson and Dr. P. Edmondson (University of Oxford); Prof. S. L. Dudarev, Dr. D. Mason, Dr. M. Gilbert, Dr. Duc Nguyen-Manh (Culham Center for Fusion Energy); Prof. Z. Zhou (Shanghai University) and Prof. K. Arakawa (Shimane University) for enlightening discussions; Dr. M. A. Kirk and Mr. P. Baldo (Argonne National Laboratory), Dr. N. Peng (National Ion Beam Center, University of Surrey) and Dr. K. Hattar (Sandia National laboratory) for access to irradiation facilities; and finally Prof. M. Rieth and Dr. J. Reiser (Karlsruhe Institute of Technology) for the supply of test materials.

Third, I'd like to acknowledge Mr. S. Lett, Mr. I. Lloyd, Dr. N. Young, Mrs. G. Chapman, Mr. L. Walton, Mr. A. Norton and two previous members of the department Dr. S. Xu and Prof. Z. Yao for generous help with sample preparation and equipment training.

Fourth, I wish to thank heartily Miss S. He, Dr. M. Jiang, Miss M. Wu, Mr. Q. Chen, Dr. J. Jiang, Mr. Zhenhua Liu, Dr. Y. Zhu, Mr. Y. Zhong, Dr. H. Che, Mr. E. Brooks, Miss L. Wang, Mr. K. Yang, Miss. H. Wu, Miss. L. Qiao and many others, for sharing the happy moments with me and being there for me in the days of blue.

Fifth, I'd like to thank my parents Danqing Yi and Huifang Xie. Without their endless love and support, this long march pursuit of becoming a scientist since childhood would not have been possible.

Finally, many thanks to the China Scholarship Council and the China Oxford Scholarship Fund for financing my DPhil study, and EPSRC for the support of this research.

Xiaoou Yi

Wolfson College, University of Oxford.

To my dear parents, Danqing and Huifang.

Contents

Chapter 1 Literature review 1
1.1. Introduction 1
1.1.1. Fundamentals of nuclear fusion 1
1.1.2. Application of tungsten and challenges 2
1.2 Radiation damage mechanism 4
1.2.1. Displacement damage 5
1.2.2. Transmutation effects 10
1.2.3. Configurations of radiation damages 12
1.3. Overview of radiation damage studies on tungsten 14
1.3.1 Sources of irradiation 14
1.3.2. Fission neutron radiation of tungsten 16
1.3.3. Heavy/self-ion irradiation of tungsten 21
1.4. Research goals of this thesis 25

Chapter 2 Materials and methods 26
2.1. Introduction 26
2.2. Tungsten and alloy specimens 26
2.3. Irradiation facilities and conditions 29
2.4. Post-irradiation in-situ annealing experiments 35
2.5. Sample preparation 35
2.5.1. General pre-irradiation treatments 35
2.5.2. TEM samples for bulk irradiations 39
2.5.3. TEM samples for in-situ irradiation/annealing 39
2.6. Transmission electron microscopy techniques 41
2.6.1. Image rotation calibration 41
2.6.2. Foil thickness measurement 43
2.6.3. Dislocation loop characterization 47

2.6.4. Void characterization 56
2.7. Technical notes of data processing with Image J 58
2.7.1. The counting of loops 58
2.7.2. Loop size distribution 59
2.7.3. Loop Burgers vectors analysis 62

Chapter 3 Bulk Irradiated Tungsten and alloys 63
3.1. Introduction 63
3.2. Radiation damage microstructures 63
3.2.1. (300, 500, 750°C) / (0.5, 1.5, 4.5, 37.5 dpa) irradiated UHP-W 64
3.2.2. (300, 500°C) / (0.5, 1.5, 4.5 dpa) irradiated CG-W 70
3.2.3. (300, 500°C) / (0.5, 1.5, 4.5 dpa) irradiated W-5Re 75
3.2.4. (300, 500°C) / (0.5, 1.5, 4.5 dpa) irradiated W-(1, 5)Ta 80
3.2.5. (500°C / 1.5 dpa) irradiated W-5V 89
3.2.6. Damage microstructures in non z = [001] grains 91
3.3. Quantitative characterizations 94
3.3.1. Dislocation loop number densities 94
3.3.2. Dislocation loop Burgers vector characterization 99
3.3.3. Dislocation loop nature analysis 103

Chapter 4 In-situ Irradiated Tungsten and Alloys 114
4.1. Introduction 114
4.2. Early stage radiation damage in tungsten (0.01 dpa) 115
4.2.1. Defect yield and size distribution 118
4.2.2. Loop Burgers vector and nature determination 123
4.2.3. Cascade collapse efficiency 126
4.2.4. The fate of vacancies in the cascade 127
4.3. Microstructure evolution in tungsten (from 0.01 dpa to 1.0 dpa) 128
4.3.1. Microstructure evolution as a function of dose and temperature 128

4.3.2. Microstructure evolution as a function of alloying elements (Re, Ta, V) 131
4.3.3. Microstructure evolution as a function of grain orientation 134
4.4. Dynamic behaviour of observable point-defect clusters in tungsten and alloys 137
4.4.1. The motion of individual loops 137
4.4.2. Loop-loop elastic interactions and reactions 140
4.4.3. Loop-string and string-string elastic interactions and reactions 148
4.5. Post-irradiation characterizations 153
4.5.1. Radiation damage microstructures 153
4.5.2 Quantitative characterization and analyses 180

Chapter 5 In-situ Annealing of Radiation Damage in Tungsten 187
5.1. Introduction 187
5.2. Damage characterization during annealing 188
5.2.1. Evolution of the microstructure 189
5.2.2. Analysis of dislocation loop geometry and nature 190
5.2.3. Case studies of loop dynamic behaviour 199

Chapter 6 Discussions 207
6.1. Introduction 207
6.2. Low-dose radiation damage in tungsten (in-situ) 208
6.2.1. Defect nucleation mechanism 208
6.2.2. The role of irradiation temperature 211
6.2.3. Comparative studies with iron and molybdenum 212
6.3. Evolution of radiation damage in tungsten (in-situ; bulk) 215
6.3.1. The dynamic behaviour of dislocation loops 215
6.3.2. The role of irradiation temperature 224
6.3.3. The role of irradiation dose 225
6.3.4. The role of impurity atoms: C/O (interstitial) and Re/Ta/V (substitutional) 226
6.3.5. The role of crystallographic orientation 228

6.4. Thermal stability of radiation damage in tungsten (in-situ) 229

6.5. Effects of surface image forces and the validity of extracting bulk damage properties from 2 MeV W^+ implantations 229

6.6. Extensive comparison of bulk irradiations with thin-foil ion irradiations in tungsten 231

6.6.1. Depth distribution of radiation defects 231

6.6.2. Dislocation loop number density 232

6.6.3. The fraction of ½<111> loops against <100> loops 233

6.6.4. Statistics of loop nature (interstitial/vacancy) 233

6.7. A brief note on the observation of large vacancy loops in this thesis 234

Chapter 7 Conclusions 237

7.1. Summary of key results 237

7.2. Outlooks on the understanding of radiation damage in tungsten 239

References 242

Appendix 249

Chapter 1

Literature review

1.1. Introduction

1.1.1. Fundamentals of nuclear fusion

Fusion power has been widely acknowledged as a potential means to meet global energy needs in the future. The key process is essentially numerous deuterium-tritium (D-T) and deuterium-deuterium (D-D) reactions as illustrated in Fig 1.1. The particles fuse by overcoming a high energy Coulomb barrier (≥ 10 keV) and to achieve this, the D/T fuels are heated up to plasma state (≥ 100 million °C) within a ring-shaped magnetic vacuum chamber (so called tokamak) [1]. On one hand, the fast neutrons produced will be stopped by dense materials in the chamber walls and the heat generated will then be converted to electricity power. On the other, the He ash will be diverted towards the bottom of the chamber by the magnetic field and readily removed to avoid contamination of the plasma. The entire process is environmentally sustainable. No atmospheric pollution is involved or long-lived radioactive waste. Moreover, there are unlimited supplies of fuel. Deuterium naturally exists in (sea) water and can be extracted through electrolytic processes [2]. Tritium can be bred from the nuclear reactions between Li and neutrons [3]. The potential energy output of fusion reactions is remarkable. In principle, the lithium in a laptop battery along with half a bath of water could generate electricity equivalent to 40 tons of coal (200,000 kWh) [1].

1.1.2. Application of tungsten and challenges

Although controlled fusion reactions have been accomplished in small tokamaks, the demonstration of the commercialization of this technology requires scaling up in reactor size. To do this, the International Thermonuclear Experimental Reactor (ITER) is under construction in Caderache, France [4]. Table 1.1 summarizes its choice of machine parameters and the operating conditions with respect to plasma-facing components (PFC: first wall and divertor) [4, 5]. It can be inferred that these components, though not in direct contact with the hot plasma, must withstand high temperatures and high thermo-mechanical loads, together with high levels of radiation damage caused by fast neutrons. As a consequence, the PFC candidate material is expected to have a high melting temperature, outstanding thermal properties (high thermal conductivity and low thermal expansion coefficient), low activation and a high threshold for sputtering. The optimal candidates sought so far have been W, Be and carbon fibre composites (CFCs). However, light elements, especially C bring about severe issues on high erosion rates subject to plasma exposure, which contaminates the plasma, shorten the lifetime of tiles and trap the fusion fuels by co-deposition [6]. The latest wall design of ITER adopts a combination of W and Be tiles [7]: Be as first wall material, reduces the oxygen impurity levels in the plasma; while W as divertor material, the superb thermal properties of which helps to sustain the integrity of the component under high temperature and high heat flux conditions. Fig 1.2 illustrates the installation of an ITER-like wall in Europe's JET torus. Fuel retention in the chamber has reduced by a factor of 20 [8]. In the long run, a full tungsten wall chamber is desired.

Despite the promising outlook of applying tungsten to chamber walls and divertors (PFC and structural components), one needs to pay attention to the intrinsic brittleness of the material and the material property degradation effects due to fusion neutron irradiation.

Swelling, embrittlement (shown as the increase of the ductile-to-brittle transition temperature, DBTT), along with reduction of thermal conductivity [6, 9] further narrows the operating temperature window of tungsten to merely 800-1300°C [10]. In the next section, mechanisms of fusion neutron damage in tungsten will be summarized from two perspectives, i.e. the displacement damage and transmutation, in order to account for the degradation phenomena.

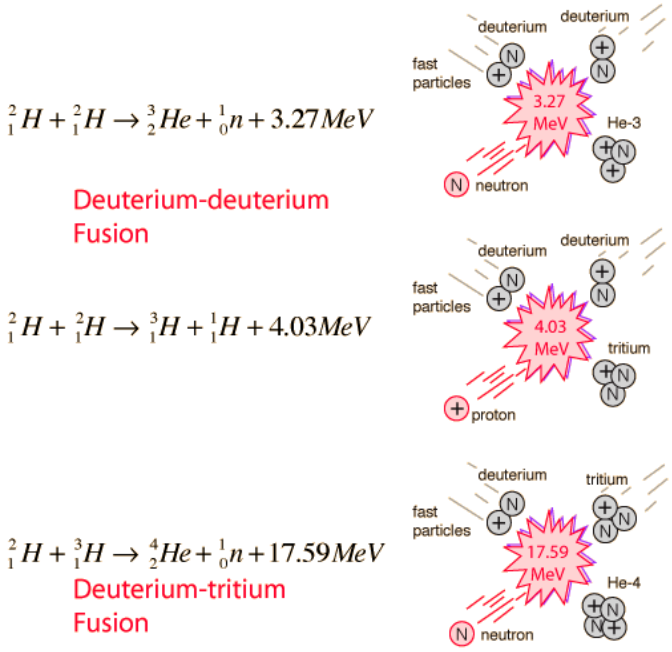


Fig 1.1 Fusion reactions of deuterium-tritium and deuterium-deuterium [11].

Table 1.1 The machine parameters and operating conditions of ITER [4, 5].

	ITER	
Fusion power	Input: 500 MW Output: 50 MW	
Plasma volume	836 m^3	
Heat flux	First wall Divertor	0.1-0.3 $MW \cdot m^{-2}$ ~10 $MW \cdot m^{-2}$
Neutron power flux	First wall	0.78 $MW \cdot m^{-2}$
Operating temperature	Plasma First wall Divertor	150 million °C ~500 °C 1200-3200°C

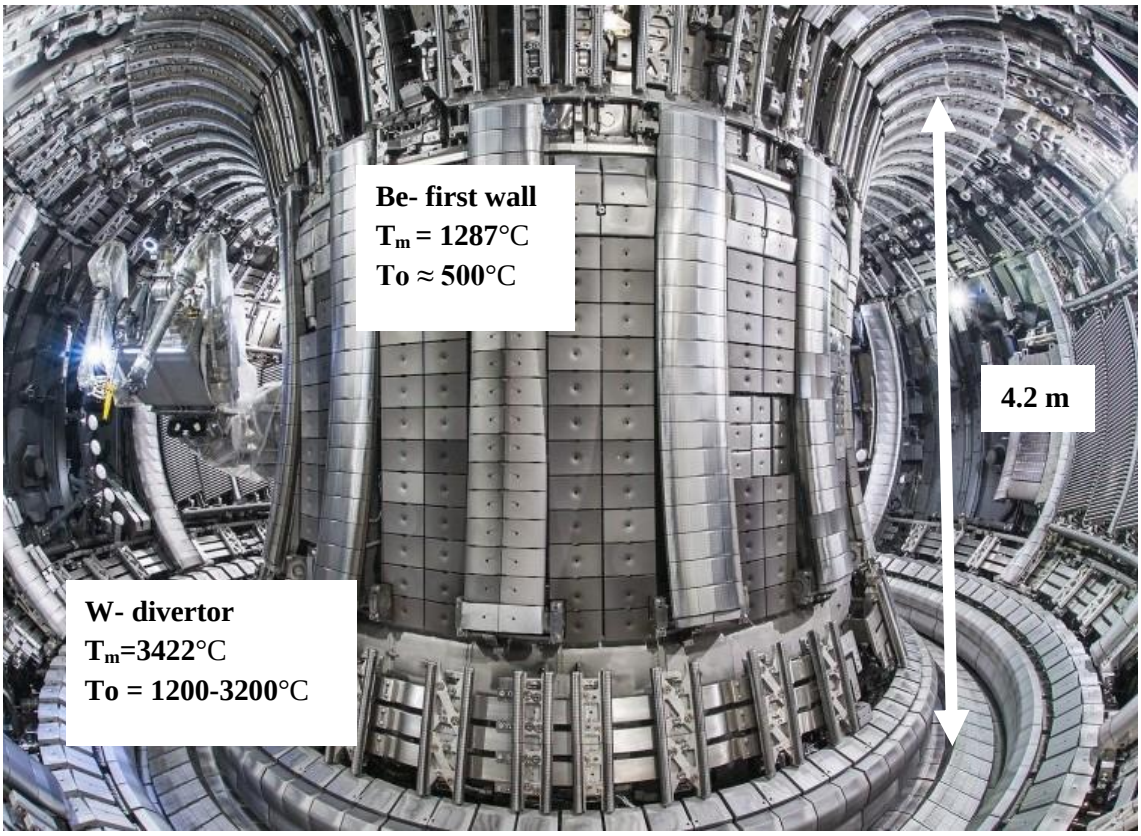


Fig 1.2 The interior view of the JET torus with the ITER-like Wall installed. The first wall is protected with Be tiles and tungsten tiles are used in the divertor [1]. T_m and T_o represent melting temperature and operating temperature respectively. Data were quoted from [7, 12, 13].

1.2 Radiation damage mechanism

Neutrons are uncharged particles, and mainly interact with materials through either scattering or absorption. The probability of the particular interaction route (also called the neutron cross section) depends on their energy [14]. According to Fig 1.3, the neutron energies in a fusion reactor fall into a wide spectrum [15]. Neutrons with energies $1 \leq E_n \leq 20$ MeV are termed fast neutrons [16], and their scattering with the lattice atoms have been found a major contribution to the displacement damage in materials (§ 1.2.1). Meanwhile, neutrons with energies of $1 \leq E_n \leq 10$ eV and 0.025 eV are specifically termed as slow neutrons and thermal neutrons respectively. Both of these play an important role in the absorption process, which favours the transmutation of atoms in the interacting material (§ 1.2.2).

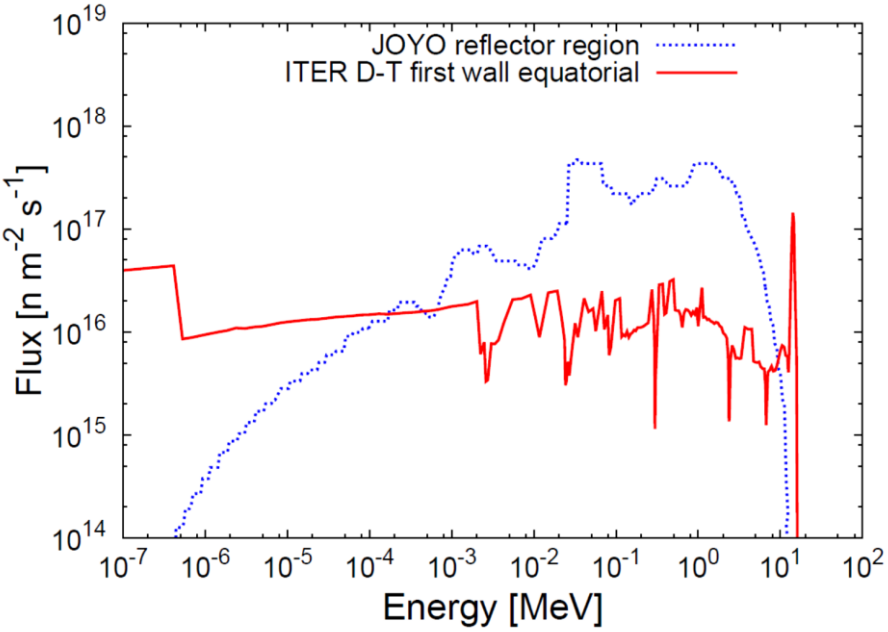


Fig 1.3 Simulated neutron flux spectrum for the ITER D-T first wall [15].

1.2.1. Displacement damage

Displacement damage initiates in a crystal once the bombarding neutron (E_n) strikes a stationary atom off its original lattice site. This atom, referred to as a primary knock-on (PKA), gains a given amount of kinetic energy (E_{PKA}) that dissipates in a sequence of collisions with other atoms (recoils). During each atomic displacement, a minimum kinetic energy must be transferred to the atom before it can be displaced from its lattice site. This minimum energy is called the displacement threshold energy E_d, and is dependent of the crystallographic orientation. Take tungsten for example, the displacement threshold energy for directions [001], [111] and [011] are 42 eV, 44 eV and 70 eV respectively [17].

The bombarding neutron encounters continuous kinetic energy loss as it overcomes E_d, and creates a spectrum of PKAs [18]. These PKAs of various energies may go on displacing other atoms in the lattice, leaving vacancies behind. When these displaced atoms finally come to rest, they are often regarded as self-interstitial atoms[1] (SIAs). Eventually, a

[1] In alloys, the displaced atom must be the primary component in order to be regarded as SIA.

cascade of displaced atoms (collisional phase: < 1 ps) is formed, consisting of hundreds of Frenkel pairs (interstitial and vacancy pair) [19]. The cascade continues to evolve, from the collisional phase to the thermal spike phase (~ 1 ps). Due to the large difference in the migration energy of self-interstitial atoms (SIAs) and vacancies (e.g. 0.088-0.102 eV versus 1.78 eV for tungsten [20, 21]), the spatial distribution of these irradiation-induced point defects features a high density core shell of vacancies surrounded by SIAs (Brinkman, Fig 1.4 [22]). Taken into account the crystallinity of the material, recent molecular dynamic (MD) simulations show that SIAs do not distribute evenly on the periphery of the vacancy core (depleted zone). Rather, they tend to reside locally and cluster [23].

In literature, the lifetime of a cascade often refers to the sum of durations of the first two stages just described, i.e. the collisional phase and the thermal spike phase. However, the cascade region continues to evolve at time scales beyond, including a quenching phase (~ 10 ps) when point defects and clusters form, and terminates at an annealing phase (> ns), during which further rearrangement, interaction of defects may occur, along with their diffusion out of the cascade [24].

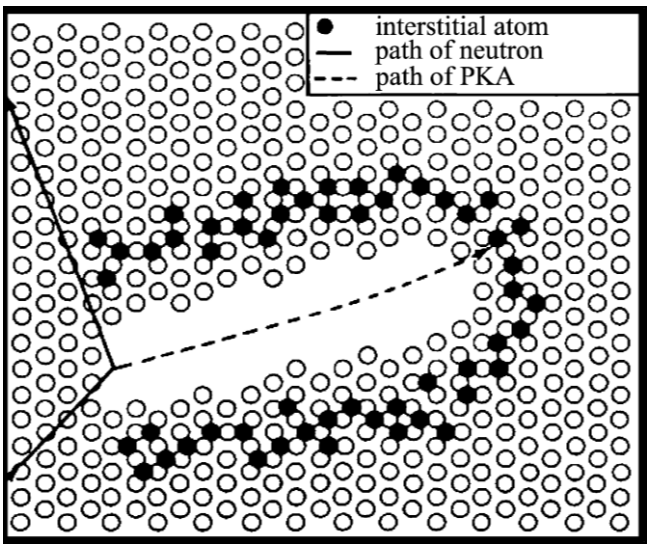


Fig 1.4 Image of the displacement spike, proposed by Brinkman [22].

The four phases of a collision cascade describe the atomic displacements in crystals qualitatively. In order to quantify the level of which, Kinchin and Pease (K-P) have proposed a simplified model to estimate the total number of displaced atoms in the cascade as a function of E_{PKA}, by assuming hard-sphere binary collision for all displacement events [25]. Moreover, it assumed an energy cut-off for E_{PKA}, above which any additional amount would be dissipated entirely in electronic excitation and ionization. The full result of the Kinchin-Pease approximation is summarized in Eq 1.1, and the relationship between E_{PKA} and the total number of displaced atoms (ν) is plotted in Fig 1.5. E_d and E_c represent the displacement threshold energy and the cut-off energy [24].

$$\nu(E_{PKA}) = \begin{cases} 0, & E_{PKA} < E_d \\ 1, & E_d < E_{PKA} < 2E_d \\ \dfrac{E_{PKA}}{2E_d}, & 2E_d < E_{PKA} < E_c \\ \dfrac{E_C}{2E_d}, & E_{PKA} \geq E_c \end{cases} \qquad Eq\ 1.1$$

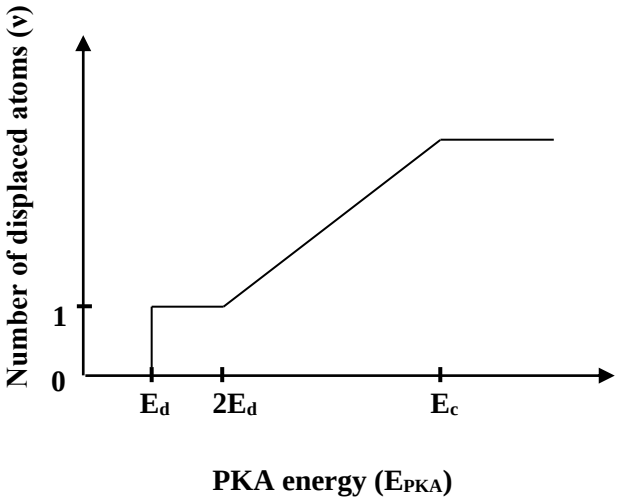


Fig 1.5 The number of displaced atoms in the cascade as a function of the PKA energy based on the Kinchin-Pease approximation [24].

The K-P model was the most widely cited of its kind, on the computation of the total number of atoms displaced by a given PKA. However, its treatment of the electronic stopping was inappropriate. A detailed theory on the partitioning of E_{PKA} by Lindhard et al [26] quantified the amount of which dissipated in elastic collisions and electronic losses. Norgett, Robinson and Torrens (NRT) modified the K-P model, taking into account Lindhard's energy partition rule. Eqs 1.2 - 1.7 summarize the NRT model [27]. To begin with, the damage energy T_d needs to be computed, which represent the amount of energy available to generate atomic displacements by elastic collisions. k is the displacement efficiency; $g(\epsilon)$ is a universal function which measures the inelastic energy loss; a_0 is the Bohr radius (tungsten: 139 pm [28]); e is the electronic charge; Z_1 and Z_2 are the atomic numbers of the projectile and target; and A_1 and A_2 are the mass numbers of the two atoms. For self-ion irradiations, $Z_1 = Z_2$ and $A_1 = A_2$ apply and the expressions may be further simplified. Next, the total number of displaced atoms (ν) is plotted as a function of the damage energy T_d, as illustrated in Fig 1.6.

$$T_d = \frac{E_{PKA}}{1 + kg(\epsilon)} \qquad Eq\ 1.2$$

$$g(\epsilon) = 3.4008\epsilon^{\frac{1}{6}} + 0.40244\epsilon^{\frac{3}{4}} + \epsilon \qquad Eq\ 1.3$$

$$k = 0.1337\ Z_1^{\frac{1}{6}}(Z_1/A_1)^{\frac{1}{2}} \qquad Eq\ 1.4$$

$$\epsilon = \left[\frac{A_2 E_{PKA}}{A_1 + A_2}\right][a/Z_1 Z_2 e^2] \qquad Eq\ 1.5$$

$$a = (9\pi^2/128)^{\frac{1}{3}}\, a_0\, [Z_1^{\frac{2}{3}} + Z_2^{\frac{2}{3}}]^{-\frac{1}{2}} \qquad Eq\ 1.6$$

$$\nu(T_d) = \begin{cases} 0, & T_d < E_d \\ 1, & E_d < T_d < \dfrac{2E_d}{0.8} \\ \dfrac{0.8T_d}{2E_d}, & \dfrac{2E_d}{0.8} < T_d < \infty \end{cases} \qquad Eq\ 1.7$$

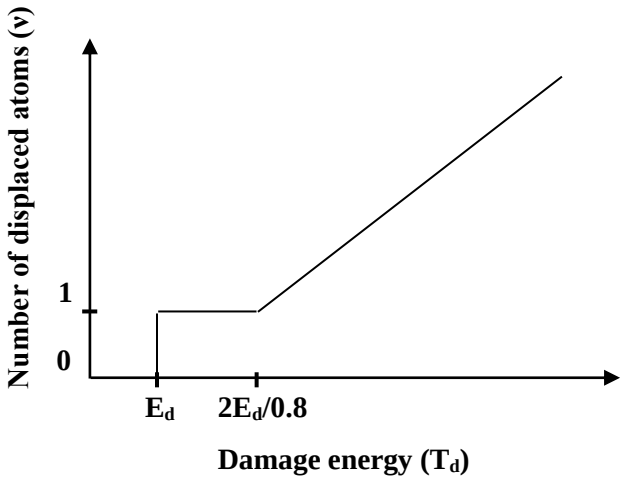


Fig 1.6 The number of displaced atoms in the cascade computed using the NRT model [27].

In the nuclear industry, the NRT model has been adopted as a standard for computing atomic displacements [27] and forms the basis of the SRIM code [29], which is the most commonly used package for simulations of irradiation damage profiles. The damage profiles calculated for irradiations in this thesis were all obtained from the SRIM 2008 package. Conventionally, the level of damage is not presented in the total number of displaced atoms (ν), but in units of dpa, short for displacements per atom. By definition, 'dpa' is the ratio between the number of displaced atoms in volume from the NRT equation and the number of atoms of the material in the same volume. There are a number of advantages with using dpa units. It serves as an atom-based measure of the radiation exposure [30] and it is independent of the irradiation environment (irradiation sources, energy spectra). Correlations between different irradiations could be thus established conveniently [31]. Despite of its convenience, the application of 'dpa' units requires careful handling. In the NRT model, scenarios of defect recombination, migration and clustering are not taken into account. Some corrected versions of the NRT model have been proposed accordingly based on results from MD simulations, e.g. athermal recombination-corrected and athermal mixing-corrected dpa. Further details of which can be found in [32]. In this thesis, all damage levels are presented in NRT-dpa values.

1.2.2. Transmutation effects

As previously stated, neutrons can be absorbed by an interacting nucleus. Electromagnetic (photons), charged (protons, α particles) or neutral particles (neutrons) are released subsequently, leading to the change of atomic number and/or mass number of the original nuclide. This process, known as transmutation or burn-up, changes the chemical composition and often also the microstructure of materials [30]. As a rule of thumb, the probability of neutron capture (cross section) by the nucleus of the absorbing material is inversely proportional to the square root of the neutron energy, as illustrated in Fig 1.7 [33]. Hence, it can be inferred that the major contribution of transmutation products originates from slow and thermal neutrons.

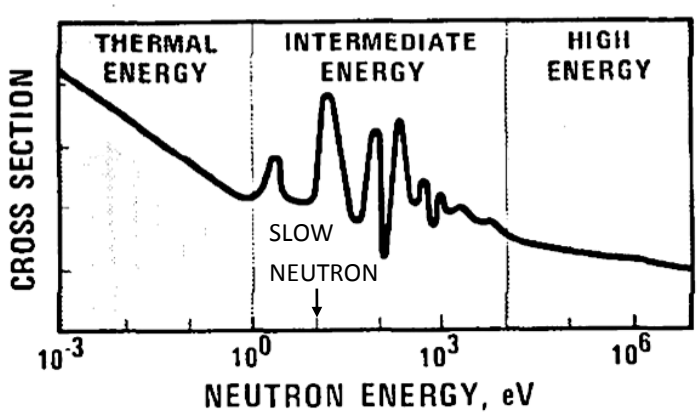


Fig 1.7 The energy dependence of neutron capture cross sections for many nuclei [33].

The energy of neutrons not only affects the transmutation probability, but also the type of transmuted product. Fig 1.8 demonstrates some possible pathways in tungsten [34]. Nuclear reactions are described in Eq 1.8-1.12 accordingly. Given substantial periods of time, one would expect a tungsten-based PFC to undergo significant compositional changes. Fig 1.9 illustrates such changes for tungsten, after 5 years of first-wall fusion power plant service. Pure tungsten becomes mostly (94 at.%)W-(3.8 at.%)Re-(1.4 at.%)Os-(0.8 at.%)Ta, and includes gas products He (30 appm) and H (80 appm) [30].

$$(n,\gamma)\ reaction:\ {}^{74}_{184}W + n \rightarrow {}^{74}_{185}W + \gamma \qquad Eq\ 1.8$$

$$(n,2n)\ reaction:\ {}^{75}_{187}Re + n \rightarrow {}^{75}_{186}Re + 2n \qquad Eq\ 1.9$$

$$\beta - decay:\ {}^{74}_{185}W \rightarrow {}^{75}_{185}Re + \beta \qquad Eq\ 1.10$$

$$(n,p)\ reaction:\ {}^{75}_{185}Re + n \rightarrow {}^{74}_{185}W + p \qquad Eq\ 1.11$$

$$(n,\alpha)\ reaction:\ {}^{75}_{185}Re + n \rightarrow {}^{73}_{182}Ta + {}^{2}_{4}He \qquad Eq\ 1.12$$

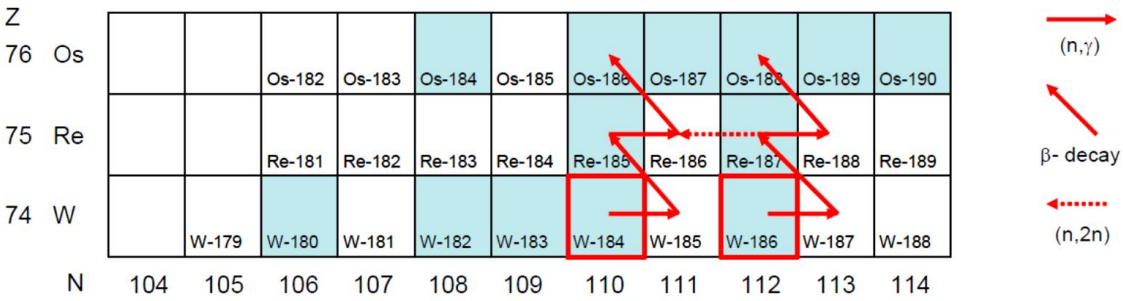


Fig 1.8 Re and Os production pathways through tungsten neutron-induced transmutation. Stable isotopes are shaded [34].

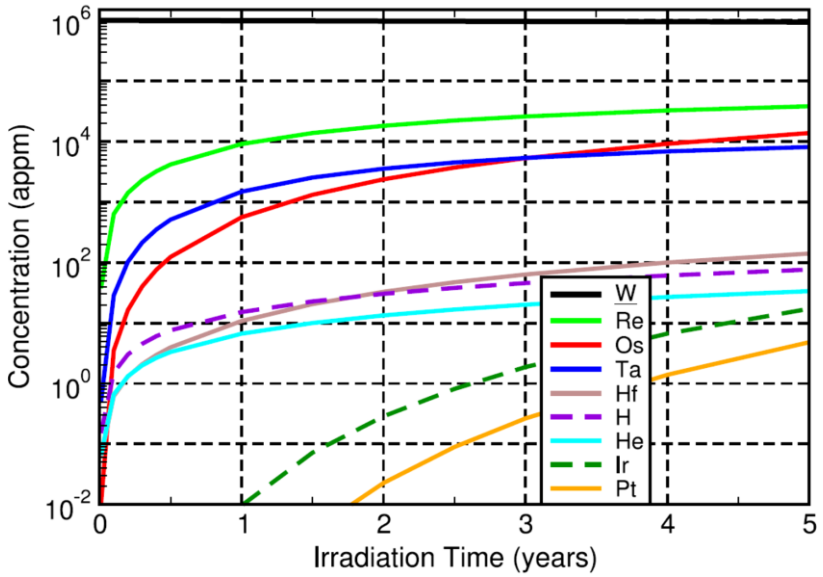


Fig 1.9 Transmutation of W during a 5-year irradiation under first-wall fusion power plant conditions [30].

Another source of radiation damage originates from the bombardment of gas ions in the plasma. This is crucial for the divertor, where He ash from the D-T reactions would be diverted towards it and expedite the erosion of surface through blistering [1].

1.1.3. Configurations of radiation damages

This section focuses on configurations of defects in radiation damaged crystalline materials. The displacement damage route creates pairs of SIAs and vacancies which may then cluster into complex geometries. An SIA can be imaged as an equivalent of a 'crowdion' (Fig 1.10), which is an extra particle in the close packed chain of atoms introducing local deformation [35]. An analogy can be made to a mono-vacancy, i.e. as 'voidions' [36].

At above a threshold concentration, the radiation-induced point defects cluster to form loops or voids. Fig 1.11 illustrates the formation of loops, through the insertion of extra platelets of either interstitials or vacancies into a perfect lattice [37]. These loops are prismatic, i.e. they are pure edge and their slip planes adopt a cylindrical topology [38]. A void is an important configuration for vacancy clusters. Calculations of the formation energy suggested that it being always more stable than vacancy loops [39]. In fact, when transmutation is also considered, the production of voids becomes facilitated due to large amounts of gas production (He, H). Stable complexes of H-V and He-V are formed and lead to higher density of voids [40].

Radiation-induced precipitates are the third major category of defect configuration. Transmutation introduces impurity (solute) atoms in the matrix (solid solution) [30]. With the increase of dose, solutes may be locally enriched or depleted, leading to the change of their concentration in the region. Once it exceeds the solubility limit, precipitation occurs [24]. The geometry of the precipitates and the parent phase may differ, i.e. coherent if the perfect registry were preserved; semi-coherent if misfit dislocations were formed at interfaces to reduce the strain energy; or incoherent if there were no matching of the interface [41]. Fig 1.12 demonstrates the microstructure in fast neutron irradiated W-10%Re alloy. In addition to voids, needle-shaped precipitates were formed (σ phase, coherent) [42, 43] .

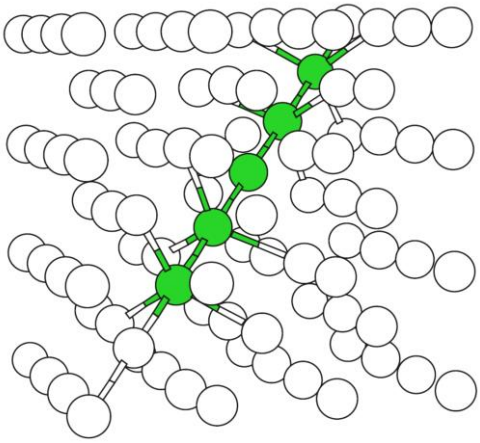


Fig 1.10 Illustration of a 111 crowdion, i.e. along [111] direction in bcc lattice [44].

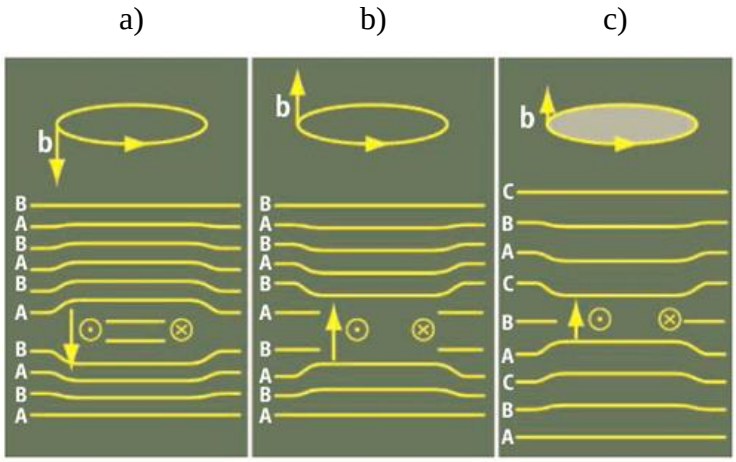


Fig 1.11 Prismatic dislocation loops illustrated with the stacking sequence of planes: In a) and b), the stacking sequence is preserved by either insertion of two layers of interstitial or vacancies, forming interstitial or vacancy type loops; in c) the stacking sequence is disturbed and the loop becomes faulted [37].

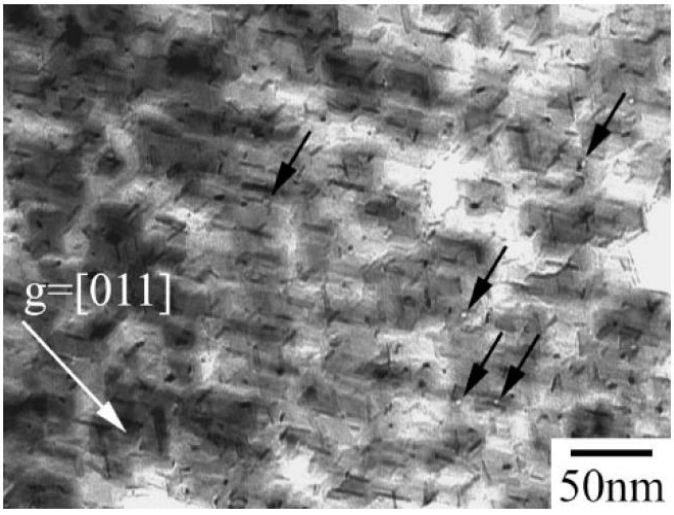


Fig 1.12 Voids (black arrow) and precipitates in neutron irradiated W-10%Re alloy [42].

1.2. Overview of radiation damage studies on tungsten

1.2.1 Sources of irradiation

Sources of irradiation include fusion neutrons (D-T 14.1 MeV), fission neutrons and ions[2]. This section aims at a brief comparison of their principles of production, damage profile and rate, energy spectrum, transmutation and generation of radioactive waste.

Fusion neutrons can be obtained from two approaches: one is accelerator-based; the other is plasma-based. The former speeds up deuterium nuclei to hundreds of kilovolts, which fly onto a rotating tritium target and release 14.1 MeV neutrons [45]. Such facilities are widely spread over the world (25 facilities by the year 2000, funded by the International Atomic Energy Agency IAEA alone [46]). But most of which generate a low neutron flux ($< 10^{12}$ n/cm^2/s [47]) and are therefore restricted to studying cross sections of nuclear reactions, chemical analysis and radiography. In the case of ITER, the neutron production rate at 14.1 MeV will achieve the level of 10^{13} n/cm^2/s [48]. This is one to a few orders of magnitude higher than what accelerator-based sources can deliver. As a consequence, the time required to achieve irradiation doses equivalent to 2-5 years of reactor service from the accelerator-based approach becomes unrealistically long. The second approach deals with the available lab-scale TOKAMAKs. Although they seem an obvious option for a test facility, they run under short pulses (tens of seconds) where future commercialized fusion reactors are expected to run continuously [1]. Also, precise and convenient control of irradiation dose, dose rate and temperature can be hard to achieve.

The majority of experimental knowledge on neutron irradiations in materials comes from fission neutron[3] [49] data due to easier access and damage build up [50]. The damage

[2] Sources may also include protons and electrons. Due to the scope and emphasis of this thesis, they are not discussed here.

profiles in both fusion neutron and fission neutron irradiated specimens are uniform, but the level of displacement damage is no longer equivalent due to the large difference in neutron energy spectrum[4]. On a fusion neutron spectrum (ITER), over 65% neutrons generated have energies higher than 100 keV. In contrast, a typical fission neutron spectrum only contains about 20% [51]. In addition, although both sources generate radioactive products, the radiochemistry in fission neutron irradiated materials is much more complex. Radioactive isotopes of elements are formed not only through transmutation, but also from the splitting of parent nucleus into fragments. The chemical composition of the target material changes drastically once these energetic fragments enter by bombardments.

Ion irradiations are frequently applied in the radiation damage studies of bcc-metals. While high energy heavy/self-ions are used to mimic the displacement damage introduced by PKAs of fusion neutrons, the effects of transmutation are investigated by implanting model alloys (e.g. W-Re-Os for tungsten [42]) with heavy/self-ions and/or gas ions (D^+/He^+). These ion irradiations can be performed on single beams, sequentially; or carried out on dual or triple beam facilities to unveil the synergies of the various sources of fusion neutron radiation damage (e.g. the Jannus platform in France [52]). On a general basis, radiation damage in ion irradiations builds up around four orders of magnitude faster, but the depth of damage does not go beyond a few μm due to strong electronic stopping [24, 53]. Moreover, ion beams can be easily incorporated with in-situ facilities, where the process of radiation damage is monitored in real time. Table 1.2 summarizes the comparison among irradiation sources.

---

[3] Nuclear fission is the splitting of an atomic nucleus into fragments (lighter nuclei that are different from the parent and bombarding neutrons) by capturing a neutron.

[4] A neutron energy (flux) spectrum gives information on the quantities of neutrons generated per unit area and time for a particular energy.

Table 1.2 Comparison of irradiation sources [51].

	Fusion neutron	Fission neutron	Self-ion
Damage profile	Uniform	Uniform	≤ a few μm
Damage rate (dpa/s)	10^{-7}-10^{-8}	10^{-7}-10^{-8}	10^{-3}-10^{-4}
Neutron energy spectrum	~ 65% (> 0.1 MeV)	~ 20% (> 0.1 MeV)	N/A
Max. PKA energy in W	50-300 keV	≤ (50-300 keV)	~ MeV
Source of radioactive products	Transmutation	Transmutation Fragments from split nuclei	N/A

1.2.2. Fission neutron radiation of tungsten

Quite a few works on fission neutron irradiated tungsten have been reported in the past, but the focus lay on obtaining quantitative information on the nature and distribution of the defects (field ion microscopy, FIM), as well as their recovery behaviour (electrical resistivity measurements). On one hand, even though the irradiation conditions covered a substantial range of temperature (60-500°C) and dose (10^{21}-10^{26} n/m^2, > 1 MeV), these irradiations were carried out in different reactors and therefore the neutron energy spectra were different [54-59]. Consequently, one may not draw much conclusion on the influence of irradiation dose and temperature on the damage microstructure. On the other hand, investigations on the recovery behaviour of the neutron damage induced defects were systematic. Van Bueren [60] divided the annealing of radiation damage defects in tungsten into five main stages I to V, numbered from low to high temperature. Each stage represents a distinct recovery stage, during which a certain variety of defect species reaches a maximum rate of annihilation. Numerous attempts were made on defining the range of each stage, the migrating species and their concentration, and finally determining the correspondent activation energy and kinetics. Some papers have also indicated the existence of a sixth stage, characteristic of high dose or

high temperature irradiations, but data on defect types and their migration energy are not available [61-63]. Table 1.3 summarizes the key results of investigations on defect recovery process in neutron irradiated tungsten.

Tanno et al. and He et al. reported the only available works on damage microstructure and mechanical properties studies of fission neutron irradiated tungsten [42, 64-66]. Irradiations were performed consistently on JMTR and JOYO (fast neutron test reactors from Japan Atomic Energy Agency, JAEA), over a range of dose (10^{24}-10^{26} n/m^2, or 0.15-1.54 dpa) and temperature (400-750°C) that are relevant to ITER conditions. Both pure W and W-Re-Os model alloys were tested, in order to investigate not only the displacement damage, but also effects of transmutation elements.

In pure tungsten, TEM observations suggest the presence of both voids and dislocation loops (see Fig 1.13). With the increase of irradiation temperature from 538°C to 750°C, there are indications that void number density dropped over an order of magnitude from ~ 10^{23} /m^3, while the average size doubled to ~ 5 nm, despite of the slight difference in dose (i.e. 1.54 dpa versus 0.96 dpa) [65]. Also, void lattices in alignment with [001] directions were discovered under high dose and high temperature conditions (750°C, 1.54 dpa) [42]. The dislocation loops in neutron irradiated tungsten were found thermally unstable, and TEM micrographs suggest they probably disappeared between 600 and 750°C [65, 66]. For a test piece irradiated at 538°C up to a dose of 0.96 dpa, dislocation loop number density was around 10^{22} m^{-3} and the average loop diameter was around 5 nm. Meanwhile, the co-existing voids in the microstructure were smaller (by a factor of 2) and denser (by a factor of 10) [65].

In W-xRe-yOs model alloys, where x = 0~26 wt.% and y = 0~5 wt.%, voids, dislocation loops as well as radiation-induced precipitates e.g. (σ, ReW) and (χ, Re_3W) were identified (see Fig 1.13) [42, 66]. The influence of the alloy concentration, dose and

temperature can be summarized into the following three points. First, the increase of the concentration of transmuted elements in tungsten was found to favour the suppression of loop and void formation. For example, in W-xRe specimens irradiated at 600°C, up to a dose of 0.15 dpa, He et al. found that the increase of Re concentration has led to the decrease of both void and loop population. Particularly when x = 26, no voids or loops were observed [66]. Second, in the low alloy concentration grades, voids exhibited enhanced stability in comparison with loops, but no lattice formation was discovered. Third, with the increase of irradiation temperature, the precipitates tend to increase in size, but drop in number density. For instance, the comparison between 0.96 dpa / 538°C and 1.54 dpa / 750°C irradiated W-10Re showed that the length range of precipitates varied from 2-18 nm to 2-28 nm, while the number density dropped from 8.4×10^{23} /m^3 to 4.2×10^{23} /m^3. The authors interpreted it as the nucleation of precipitates being dominant at 538°C, while additional growth process was facilitated at 750°C [65].

The damage defects, such as voids, dislocation loops and precipitates (hard brittle phase) can all be sources of radiation-induced hardening. The fact that hardness increase was found nearly always higher in the W-xRe-yOs grades suggested that precipitates in the damage microstructure make a larger contribution to hardening. Moreover, for the higher concentrations of transmutation elements, an enhanced level of radiation hardening was found [42, 65]. Examples are illustrated in Fig 1.14. Furthermore, there were indications that hardness increased with increasing dose at constant irradiation temperature. Also, the rate of hardness increase at lower temperatures significantly exceeded that of elevated temperatures (e.g. 500-538°C versus 750°C). Available data points at constant dose (~ 0.5 dpa) did not demonstrate pronounced effects of temperature variation [65].

Table 1.3 Stages of defect annealing in irradiated tungsten [54, 55, 67].

Stage	Temperature (°C)	Activation energy (eV)	Type of defect
I	< −170	0.06	< −230°C Point defect recombination −230 ~ −170°C Free interstitial migration
II	−170 ~ +130 or −170 ~ +350	0.25 → 1.7	Not interpreted
III	+130 ~ +450 or +350 ~ +450	1.7 → 1.9	SIAs, impurities, vacancies
IV	+450 ~ +650 or +450 ~ +800	3.1 → 3.3	Bivacancies, impurities, impurities complexes.
V	+650 ~ +1000 or +800 ~ +1000		Vacancies
VI	+1000 ~ +1500	No data	Not interpreted

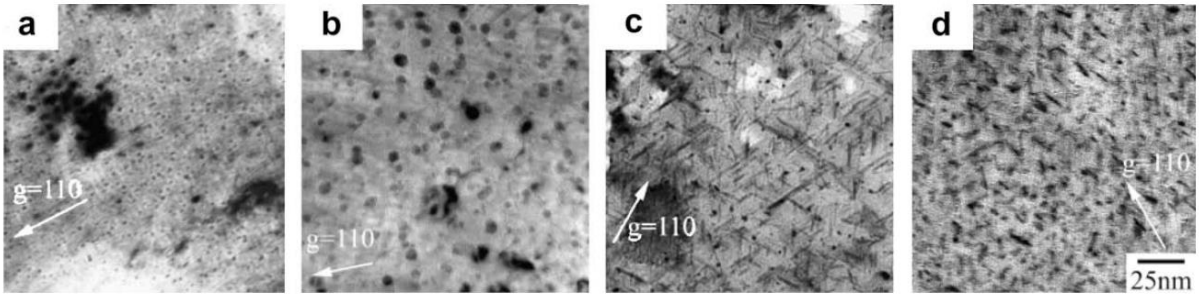


Fig 1.13 TEM micrographs illustrating the formation of a) voids, b) dislocation loops and c, d) precipitates in neutron irradiated W, W-26Re and W-3Os alloys [64].

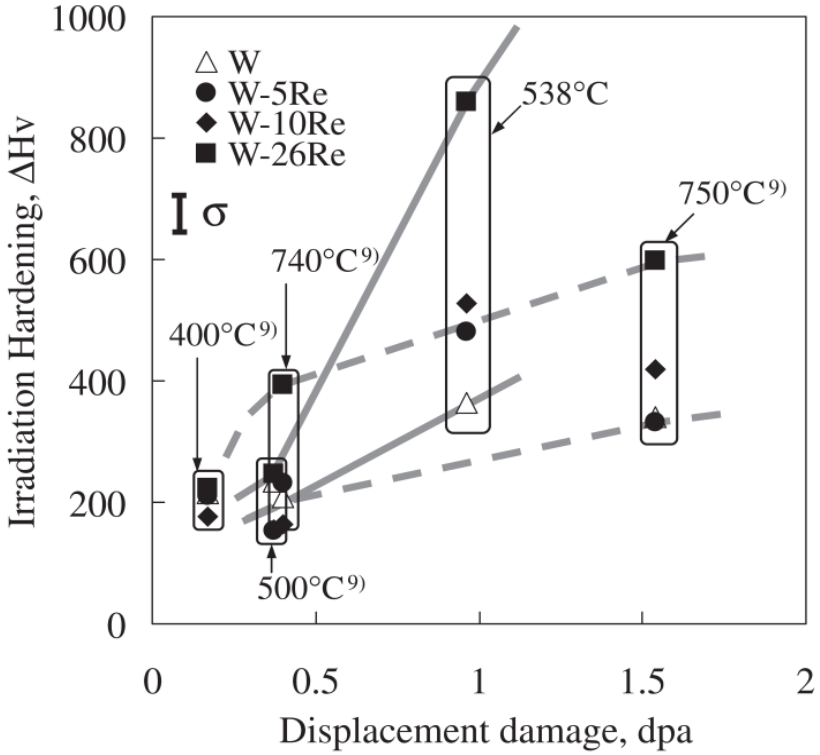


Fig 1.14 Hardness test results of W-xRe alloys irradiated in JOYO [65].

1.3.2. Heavy/self-ion irradiation of tungsten

High energy self-ions simulate the displacement damage of PKAs introduced by fusion neutrons. Systematic research of the radiation damage in tungsten among literature has been limited to the scope of room temperature and below. The status of the test pieces were not in the form of bulk either. Instead, thin foils (TEM) and needles (FIM) were adopted for characterization.

Häussermann irradiated two grades of tungsten with Au^+ ions over a range of ion energy (20-70 keV) and irradiation dose ($\leq 5\times10^{17}$ ions/m^2) at 300 K and characterized the damage microstructure with TEM [68, 69]. Based on diffraction contrast analysis, he claimed that the damage microstructure consisted of predominantly ½<111> dislocation loops as well as a small fraction of faulted ½<110> loops, all of which were vacancy type (also reported by Jäger et al. [70]). No <100> loops were found. He did not comment on any evidence of voids either. Additionally, he found that chemical composition may affect the size distribution of dislocation loops, illustrated in Fig 1.15. In the ORSAM grade (doped with Al_2O_3, K_2O and SiO_2), the average loops reached Φ = 45.6 Å and the maximum value reached ~150 Å. Meanwhile, in the un-doped Plansee grade, loops were about 30% smaller in general. The average size was only Φ = 27.7 Å and the maximum did not exceed 100 Å. Furthermore, he went on to demonstrate the influence of foil orientation on the defect yield in the ORSAM grade W, illustrated in Fig 1.16. Irradiations near a low-index orientation resulted in a much lower defect density, which can be attributed to the greater loss of loops to the foil surface and the channelling effects of the incident ions.

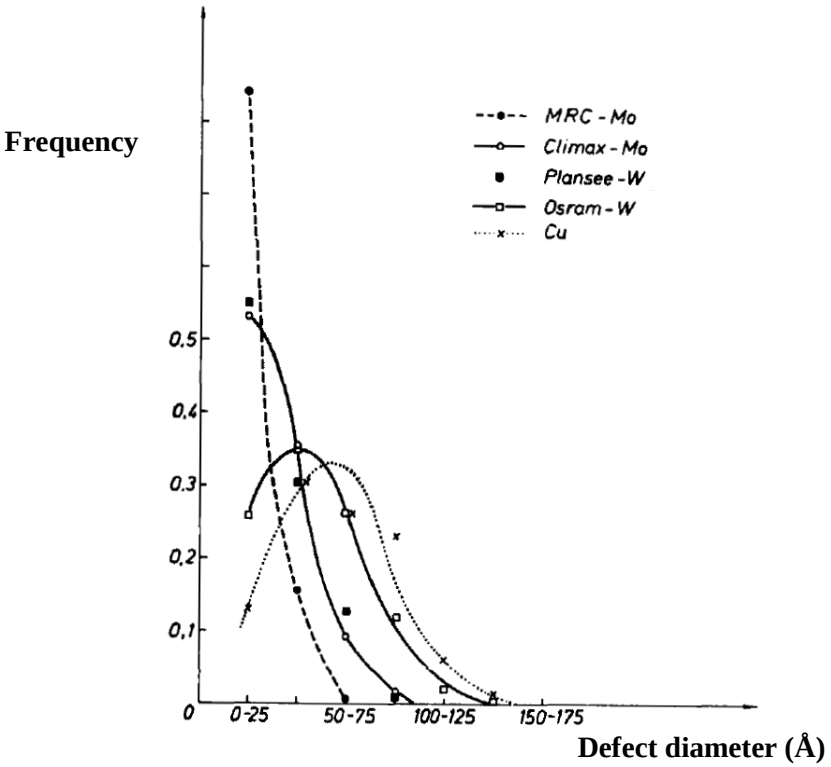


Fig 1.15 Size distributions of irradiated tungsten illustrating the effect of doping. ORSAM-W: average loop size Φ = 45.6 Å, maximum ~150 Å; Plansee -W: average loop size Φ = 27.7 Å, maximum ~100 Å [69].

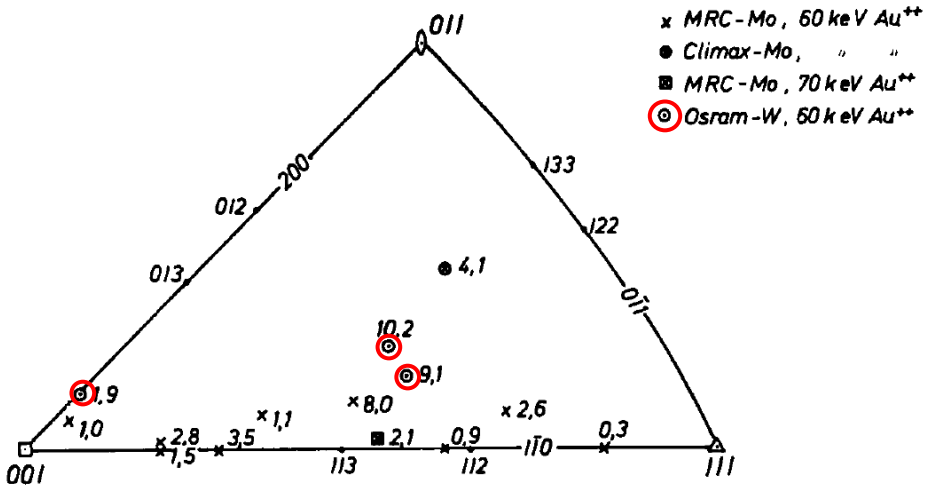


Fig 1.16 Defect yields in tungsten as a function of the irradiation direction (or equivalently the grain orientation), unit: $\times 10^2$ [69].

The effects of irradiation dose and temperature on the defect characteristics were further touched on using field ion microscopy (FIM). Bobkov et al. [71] irradiated commercially pure tungsten (Russian grade VA-3[5]) [72] with 50 keV W^+ ions at 300 K. Post-irradiation defect analysis was conducted at 78 K with FIM. The defect types and their features are summarized in Table 1.4, as a function of irradiation dose. No interstitial clusters were found. The authors argued that it might have been a result of the migration of interstitials to the surface or the capture by impurities. The absence of interstitial clusters inhibited defect recombination and up to 80% of vacancies induced by the irradiation were retained. Vacancy cluster volume (the integration of size and quantity) was found to increase with dose, and cascade overlap was first observed around 10^{17} W^+/m^2. Swelling levels were estimated accordingly. For 5×10^{18} W^+/m^2, the damage layer swelled up to 7%.

Scanlan et al. investigated the mobility of SIAs in 20 keV W^+ ion irradiated high purity tungsten (impurity level ≤ 150 appm) at temperatures between 8-18 K and post-irradiation annealed between 15-120 K, which is particularly useful in understanding the damage microstructure evolution in tungsten [73]. Within the range of irradiation temperature, SIAs were immobile and followed the trend illustrated in Fig 1.17, showing a linear increase of SIA concentration with increasing ion dose. SIAs became mobile at ~ 28 K and underwent long range migrations at Stage I (≈ 20-100 K [55]) over distances of ~ 200 Å. Continuous recovery of the damage microstructure was observed between 15-120 K and the migration barrier for a SIA was estimated to be ~ 0.085 eV. Furthermore, irradiations on impure tungsten grades suggested that impurities could strongly hinder the Stage I recovery by forming immobile impurity-SIA complexes.

[5] VA-3 grade: Ni, Mn, Ti, Cu, Mg, each < 200 ppm; V, Mo: each < 500 ppm; Al: 200-600 ppm; Si: 200-300 ppm.

Table 1.4 FIM analysis of defects produced for 50 keV W^+ irradiation at 300 K [71].

Dose W^+/m^2	Defect type	Features
10^{16}	Va, I, Va-clusters	Va-cluster size (300Va), volume~$10^3 a_w^3$, separated by 25Å Va-cluster size (10~30Va) Va concentration: 30±10 at.% Small voids ~10Å
10^{17}	Va, I, Va-clusters	Va-cluster size (1000Va), volume~$3\times10^3 a_w^3$ Cascade overlap observed Single interstitials at 10~50Å distance from the Va-cluster Total number(I)=1% Total number(Va) Small voids ~10Å
5×10^{18}	Va, I, Va-clusters	Va-cluster volume~$1\text{-}5\times10^4 a_w^3$ Cascade overlap observed Small voids ~10Å

* Lattice parameter of pure tungsten: a_w=3.1585Å.

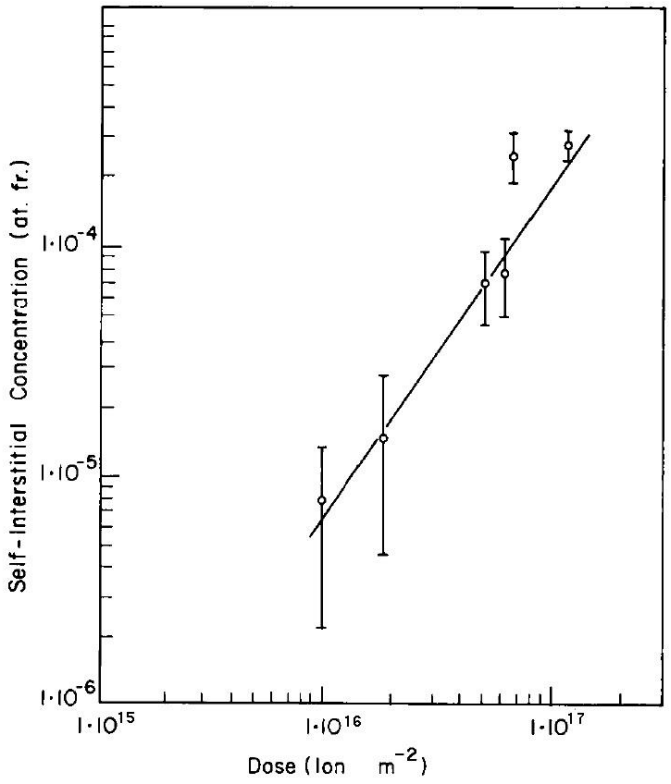


Fig 1.17 The atomic fraction of self-interstitial atoms as a function of the ion dose. Irradiation condition: 20 keV W^+ ions, 8-18 K [73].

1.4. Research goals of this thesis

This thesis aims at filling in the gaps of current understanding on the radiation damage response of tungsten and approaches the problem by studying the displacement damage produced by the PKAs of fusion neutrons. Self-ions were implanted with well-defined irradiation parameters on tungsten and alloys, and the damage microstructures were characterized with the aid of transmission electron microscopes (TEMs). The research goals of this thesis can be summarized into five key points. (1)-(3) are related to the implantation of bulk samples, providing comprehensive understanding on the post-irradiation damage features. (4) deals with the study of microstructural evolution path with complementary in-situ thin-foil irradiation experiments. Finally (5) represents some preliminary efforts on the thermal stability study of radiation damage in tungsten.

1) *What defect species can be identified in the damaged microstructure of tungsten within the resolution of conventional TEMs? (e.g. dislocation loops, voids).*

2) *If dislocation loops were present, what are their Burgers vectors, nature (interstitial or vacancy type), number density as well as size and spatial distribution? If voids were present, what are their number density as well as spatial and size distribution?*

3) *What are the effects of irradiation temperature, dose, impurity level, alloying elements and grain orientation on the defect species and their characteristics in tungsten?*

4) *What dynamic behaviours of damage defects are present in tungsten during irradiations? How do defects interact or react, and how do these affect the final damage microstructural features, taking into account the influence of irradiation temperature, dose, alloying element and grain orientation?*

5) *How stable is the radiation damage produced in tungsten? What is the relationship between annealing parameters (temperature, time) and the damage microstructural features (e.g. defect number density, size distribution)? What dynamic mechanisms contribute to the microstructural changes observed during annealing?*

Chapter 2

Materials and methods

2.1. Introduction

The electron microscopy study of radiation damage in W/W-alloys described in this thesis covers a wide range of chemical compositions and an extensive matrix of radiation conditions, including both temperature and dose variables. Acquiring reliable data on the damage microstructure depends heavily on the quality of specimens prepared. In the next few sections, a detailed description of specimen preparation techniques will be presented, illustrating how raw materials were mechanically polished, heat treated, electropolished, ion irradiated and finally thinned down to electron transparency. Microscopy techniques for characterizing the radiation induced defects (e.g. dislocation loops and voids) are demonstrated with case studies.

2.2. Tungsten and alloy specimens

Pure tungsten [74] (ultra high purity grade UHP-W and commercial grade CG-W) and three major types of tungsten alloys were studied: W-Re, W-Ta and W-V. The UHP-W was used as a reference material, as proposed in the ITER material scheme for the fabrication of plasma-facing divertor components [75]. The materials were produced by Plansee Group using a powder metallurgy route. The consolidation of the products was achieved by either hot rolling or hot forging.

The rationale for selecting the various types of tungsten based alloys was as follows (using UHP-W as a reference material in each case): 1) to evaluate the influence of impurity levels on radiation damage microstructure in tungsten (CG-W); 2) to study effects of transmutation element Re with model alloy [42] (W-5wt.% Re); 3) to seek for and validate ductilizing strategies of tungsten by adding Ta and V. Table 2.1 summarizes the chemical compositions and the fabrication route of all materials studied. The impurity levels are taken from the Plansee Group website [74]. Contents of the alloying elements are nominal values.

Table 2.1 Chemical compositions and fabrication route of the W/W-alloys investigated.

Material	Fabrication	W (wt.%)	Re (wt.%)	Ta (wt.%)	V (wt.%)	C (μg/g)	O (μg/g)
UHP-W[6]	PM. HR	>99.9999	-	-	-	<10	<5
CG-W	PM. HR	>99.95	-	-	-	<30	<20
W-5Re	PM. HR	95	5	-	-	<30	<20
W-1Ta	PM. HF	99	-	1	-	<30	<20
W-5Ta	PM. HF	95	-	5	-	<30	<20
W-5V	PM. HF	95	-	-	5	<30	<20

* PM: powder metallurgy; HR: hot rolled; HF: hot forged.

Microstructures of selected materials in the as-received state are shown in Fig 2.1. All hot-worked materials exhibit a predominant texture, e.g. {100} <011>[7] for pure tungsten grades [76]; a "cube" texture {100} <001> for W-5Re [76, 77]; and {110} <uvw>[8] for W-5Ta and W-5V. Grain sizes in W/W-alloys are severely anisotropic. Take UHP-W for example, grain sizes measured 0.5 μm × 3 μm × 15 μm [76]. Grain elongations are found lower in the alloyed samples. Dimensions along the elongated direction typically do not exceed 5 μm.

[6] If not specified, W always refers to UHP-W. Purity level specified is based on the typical maximum concentrations of H, C, N, O and Si.

[7] Most grains had {100} planes aligned in parallel with the foil surface, but formed a 45º angle with the rolling direction, i.e. R.D. // <011>.

[8] Preferred crystallographic direction w.r.t. the R.D. is not known due to unavailability of EBSD data in the literature. The preferred crystal planes are based on TEM observations in this work.

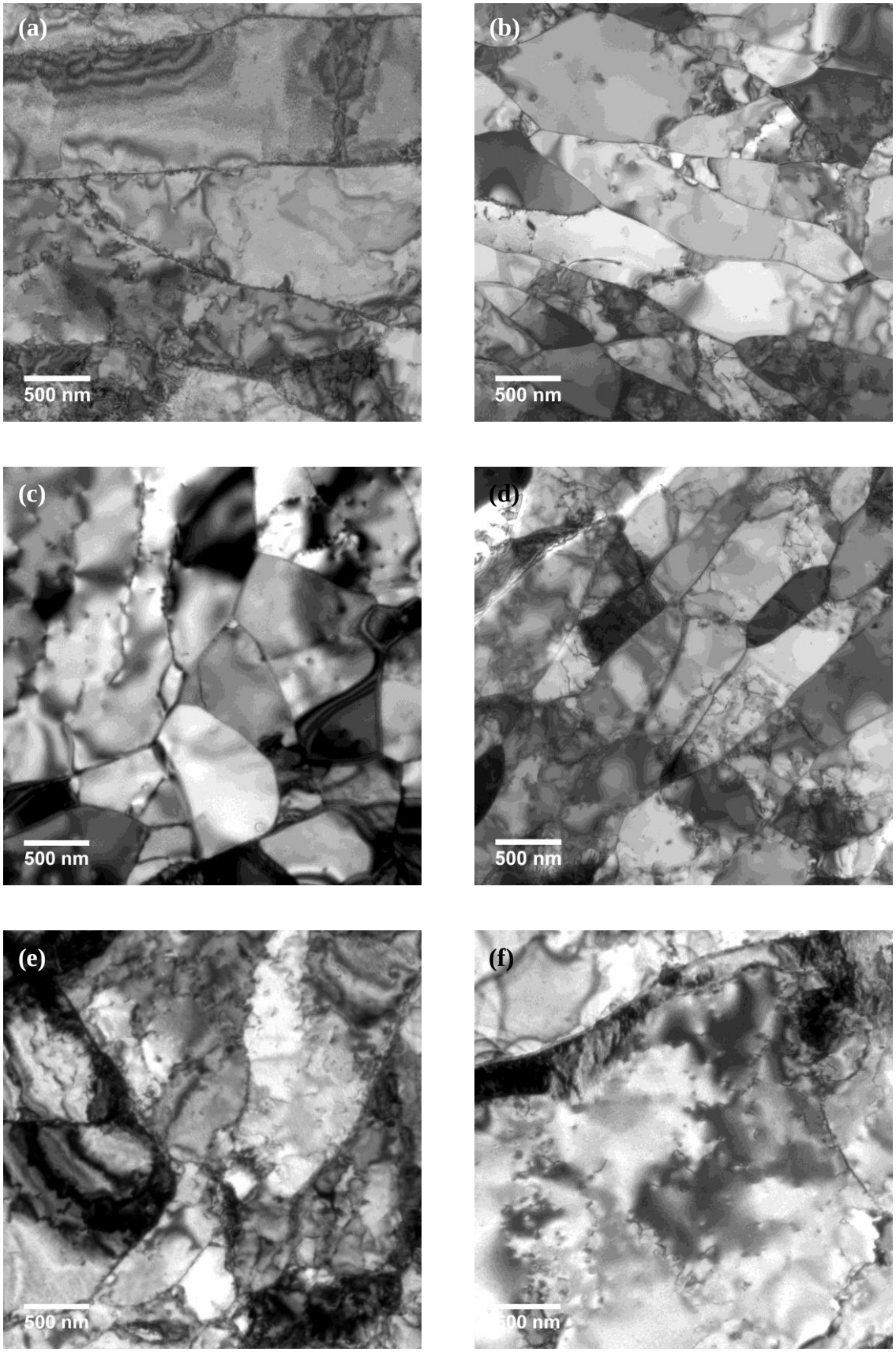


Fig 2.1 Microstructure of selected materials in the as-received state: a) UHP-W; b) W-5Ta; c) W-5Re; d) W-5V and e, f) CG-W.

2.3. Irradiation facilities and conditions

Self-ion irradiations were adopted to simulate the displacement damage produced by the primary knock-on atoms of fast neutrons, in both bulk specimens and electron-transparent thin foils. Bulk implantations involved MeV energy W^+ ions and were carried out at the National Ion Beam Center, University of Surrey, UK and the Ion Beam Laboratory, Sandia National Laboratories, USA.

Fig 2.2 shows the beam line at Surrey. W^+ ions are electrostatically accelerated in the tandem Van de Graaff accelerator (Fig 2.2 a), directed and focused in the target chamber (vacuum level ~10^{-6} Pa) and impinge onto the heatable top plate at an incident angle of $\theta = 90°$ (Fig 2.2 b, 2.2 c), on which has been mounted the target holder (Fig 2.2 d). The heating stage may run implantations up to 500°C, controlled and calibrated by the thermocouple wire embedded in one of the rails on the top plate. Temperature calibrations performed by Hardie [78] indicated the range of uncertainty to be ± 25°C. The dose and dose rates were controlled by an arrangement of four small-diameter Faraday cups located at the four corners of the sample mask.

The implants at Sandia were done on the 15 RT beam line of 6 MV EN Tandem. A Faraday cup installed between the SNICS source and the upstream of the sample calibrated the (non-rastered) beam current. Temperature was applied using a button heater that was integrated into a custom sample mount. The sample was held in place using a cylindrical Ta clamp with no adhesive used. A k-type thermocouple was spot welded onto the sample and gave temperature measurements. A proportional-integral-derivative (PID) feedback system controlled the heating [79]. Details of the uncertainties of temperature measurement were not available.

To complement the bulk implantations, which provide information only on the final-stage damage microstructure, in-situ irradiations on pre-thinned TEM foils were conducted at Argonne National Laboratory, using the IVEM-Tandem facility [80]. An ion accelerator is incorporated with a 300 kV TEM (Hitachi 9000NAR) capable of digital recording at high frame rates (15 fps). This allows direct observation of the formation and evolution of radiation damage in the studied materials. A double-tilt heating stage ensures that the diffraction conditions (e.g. weak-beam dark-field) needed to image nanoscale defects could be precisely set up while the specimen is being heated (up to 1000°C) in a Ta furnace. A pair of Cr-Al thermocouple wires measures the furnace temperature, which has been adopted as the irradiation temperature. The estimates of uncertainty of irradiation temperature measurement took into account the temperature gradient between the furnace (equivalently the peripheral region of the foil) and the area of interest (thin region of the foil) as well as the electron beam heating. The two aspects counterbalance on similar orders of magnitude, i.e. a few degrees. Therefore, the uncertainty in temperature in the thin area of the sample is estimated to be no more than 5°C. The thermal response to the W^+ ion beam is even less [81]. A Faraday cup installed at the entrance of the TEM column measures the dose. The configuration of this in-situ irradiation facility is illustrated in Fig 2.3. Note that the ion beam direction is 30° away from the 300 keV electron beam due to engineering limitations. As a consequence, a compromise was made by tilting the TEM foil about 15° in order to achieve a high incidence angle (75°) for the ion beam and not to sacrifice too much of the microscopy quality.

Table 2.2 below provides a complete list of irradiations completed for the materials studied. The ion dose has been converted to dpa values in the right column. From this section onwards, dose will be referred to in dpa units.

Table 2.2 Summary of irradiation conditions on W/W-alloys.

Material	Ion energy (keV)	Temperature (°C)	Dose (W^+m^{-2})	dpa	dpa/s
UHP-W	150 / Argonne	25, 300, 500, 600, 800	10^{16}	0.01	5×10^{-4}
			10^{18}	1.0	
	2000 / Surrey	300	3.3×10^{17} 10^{18} 3×10^{18} 2.5×10^{19}	0.5 1.5 4.5 37.5	3×10^{-4}
		500	3.3×10^{17} 10^{18} 3×10^{18}	0.5 1.5 4.5	
	1900 / Sandia	750	10^{18}	1.5	
CG-W	2000 / Surrey	300	3.3×10^{17} 10^{18}	0.5 1.5	
		500	3.3×10^{17} 10^{18} 3×10^{18}	0.5 1.5 4.5	
W-1Ta	2000 / Surrey	300	10^{18}	1.5	
		500	10^{18} 3×10^{18}	1.5 4.5	
W-5Ta	150 / Argonne	500, 600, 800	10^{18}	1.0	5×10^{-4}
	2000 / Surrey	300	3.3×10^{17} 10^{18}	0.5 1.5	3×10^{-4}
		500	10^{18} 3×10^{18}	1.5 4.5	
W-5V	150 / Argonne	500, 800	10^{18}	1.0	5×10^{-4}
	2000 / Surrey	500	10^{18}	1.5	3×10^{-4}
W-5Re	150 / Argonne	500	10^{16}	0.01	5×10^{-4}
		500, 600, 800	10^{18}	1.0	
	2000 / Surrey	300	3.3×10^{17} 10^{18}	0.5 1.5	3×10^{-4}
		500	3.3×10^{17} 10^{18} 3×10^{18}	0.5 1.5 4.5	

In order to assess damage levels in the different experiments, damage profiles were calculated using SRIM 2008.03 [82] ("full cascade option"), see Fig 2.4. Estimates of the radiation dose in displacement per atom (dpa) units were then made for the peak regions of the profile as described below. The displacement threshold energy (E_d) quoted for the dpa level estimation was an average over all crystallographic directions. Dudarev [83] gave an estimate of 55.3 eV based on Maury et al.'s [17] measurements of threshold for Frenkel pair production in tungsten subject to 1.4-1.8 MeV electron irradiation using the Jan and Seeger model[9] [84]. The value given here seems consistent with the ASTM standard, in which the range of E_d is recommended to be between 40 and 90 eV [85].

Here is an example describing the dpa level estimation for 2 MeV W^+ ions in the peak damage region, based on equation 2.1 and Fig 2.4 b):

$$dpa_{peak} = \frac{N_{displacement}\Phi}{N_w} \qquad Eq\ 2.1$$

The number of displacements $N_{displacement}$ given by SRIM is 1.0×10^{11} displacements·m^{-1}·ion^{-1}. N_w is the atomic density and has the value 6.35×10^{28} atoms·m^{-3} (the lattice parameter for tungsten is 3.155 Å) [86]. For a known dose $\Phi = 3.3\times10^{17}$ ion·m^{-2}, the peak damage level in dpa is therefore approximately 0.5 dpa.

[9] The model averages the displacement threshold energy over all the directions of the initial velocity of the primary knock-on atom, thus removing the crystallographic anisotropy of defect production in the NRT model (theoretical basis of the SRIM code).

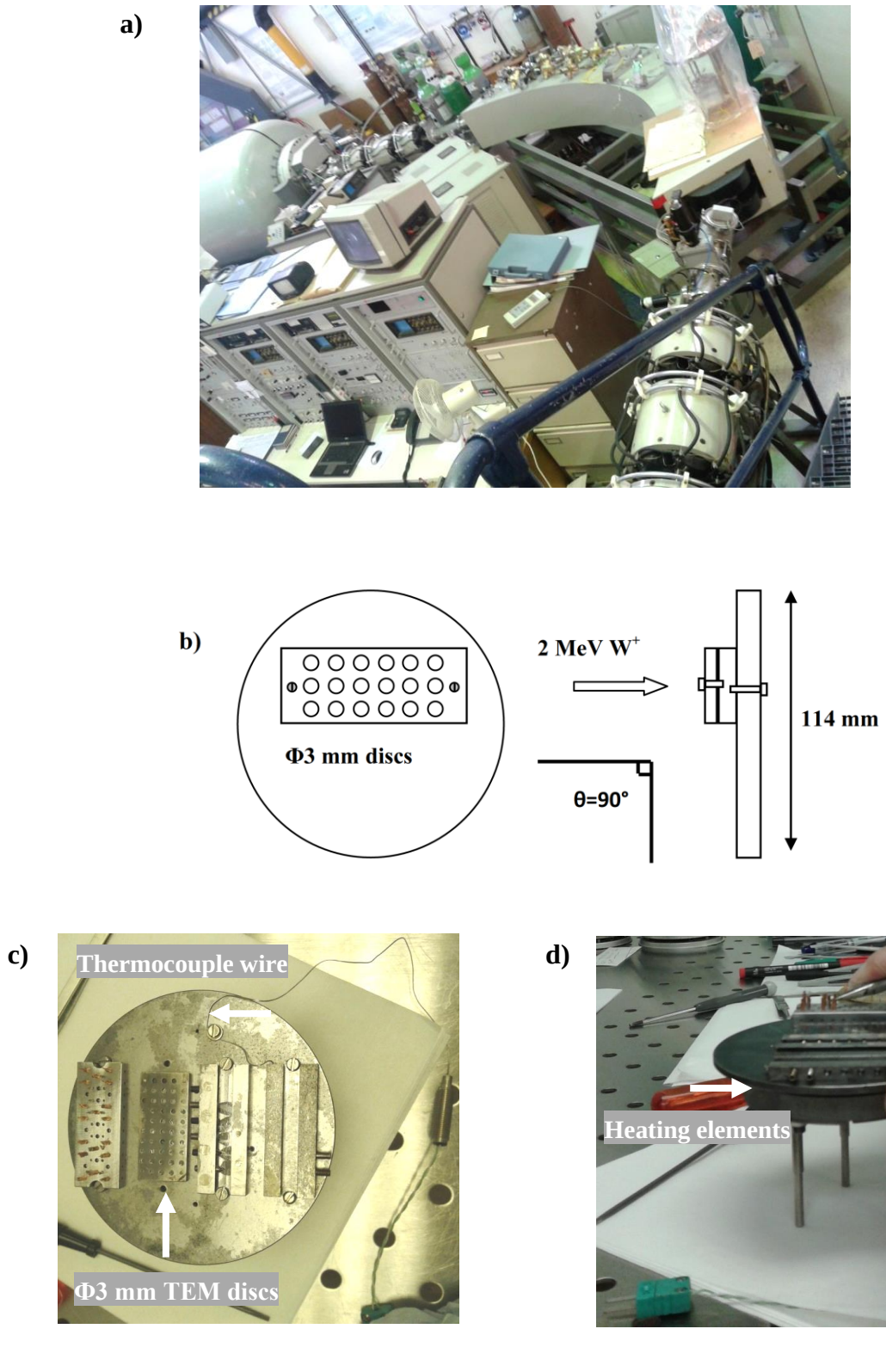


Fig 2.2 Ion implantation at the National Ion Beam Center, University of Surrey: a) Van de Graff Accelerator; b) geometry of the W^+ ions with respect to the specimens (not drawn to scale); c) planar view of the top plate holding materials to be irradiated; d) top plate being mounted onto a heatable target holder.

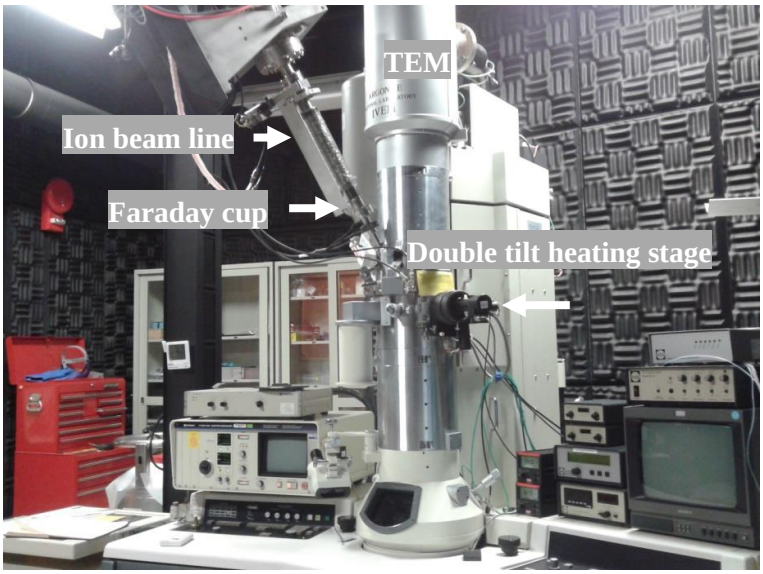


Fig 2.3 Configuration of the in-situ irradiation facility at Argonne National Laboratory.

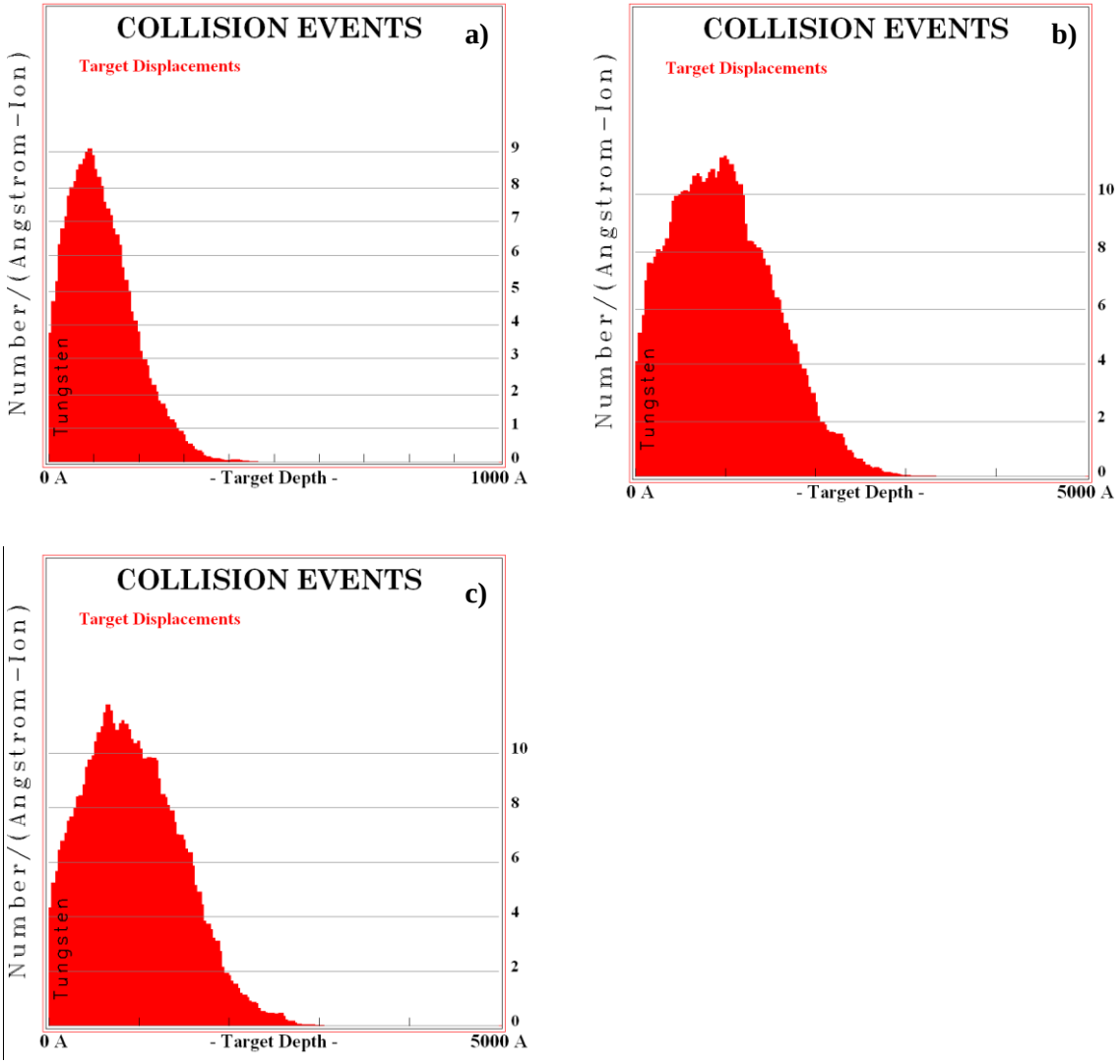


Fig 2.4 Damage profile calculations based on SRIM 2008: a) 150 keV W^+ ions; b) 2 MeV W^+ ions and c) 1.9 MeV W^+ ions. Displacement threshold energy: 55.3 eV [83].

2.4. Post-irradiation in-situ annealing experiments

Systematic annealing experiments were performed on the irradiated UHP-W specimens obtained from the Argonne ion beam facility. The UHP-W discs were pre-irradiated at R.T. with 150 keV W^+ ions, up to a dose of 1.0 dpa, at a rate of 6.25×10^{14} $W^+m^{-2}s^{-1}$ (5×10^{-4} dpa/s). The damaged microstructures were then in-situ annealed at 300°C, 500°C and 800°C respectively for 120 min. The rate of temperature ramp-up was around 25°C/min.

2.5. Sample preparation

2.5.1. General pre-irradiation treatments

Preparing Φ3 mm discs was the first step. Pure tungsten was supplied as sheets (≤ 0.15 mm) and the discs were obtained by punching. The alloys came available as chunks typically $10\times20\times50$ mm^3 in size and were first sliced into sheets of thickness 0.5 mm and were then cut into individual 3 mm discs, in both cases by spark erosion [87]. Slicing was performed using an electrode in the form of a wire, whist discs were produced using an electrode in the form of a hollow tube (inner diameter close to 3 mm, usually made of Cu). The second step was mechanical polishing of the discs to a mirror-like finish. All discs were thinned to ~ 80 μm with diamond lapping films (grit sizes 15, 9, 6, 3 and 1 μm). The third step was to encapsulate the discs in two layers of quartz tube. A spring-like scaffold made of tungsten was inserted into the inner tube in order to provide support at temperatures higher than 1200°C when quartz softens. This ensured that the specimen discs did not come into contact with the quartz. The inner tube was evacuated to a vacuum better than 10^{-6} Pa. In the fourth step, the quartz tubes were annealed in Ar atmosphere for 20 hours at 1400°C. Double layer encapsulation ensured that the discs were protected from oxidation. Fig 2.5 illustrates how the discs were encapsulated and their surface quality after the heat treatment. The last step of sample preparation prior to irradiation was to dip the discs in an electropolishing bath and remove

damaged surface layers to achieve a ‘clean’ microstructure, free of near-surface dislocations from mechanical polishing which would be effective sinks for point defects produced during the irradiation [88]. Fig 2.6 illustrates the bath-type electropolishing set up. A dedicated pair of tweezers, with its tips coated with Pt, clamps the peripheral area of the Φ3 mm disc and dips it completely into the electrolyte. The opposite end of the tweezers is connected to the anode of the (D.C.) power supply. The conditions for electropolishing vary between materials. Details of parameters and recipes are summarized in Table 2.3 in § 2.5.2. For all specimens, at least 2 μm of material was removed per surface during the bath-type electropolishing, at a rate of ~1μm/min. The numbers were taken from thickness measurements with a micrometer.

Fig 2.7 shows the state of microstructure in all materials after annealing and bath-type electropolishing, but prior to the irradiation (compared with Fig 2.1). The types of texture in the materials remained unchanged and became more pronounced. Remarkable grain growth was observed in pure tungsten grades (quasi-symmetric: 50-500 μm) and W-5Re (quasi-symmetric: 10-100 μm), while no evidence of recrystallization was found [76, 77]. Also, there seemed very little indications of grain growth in W-5Ta and W-5V. The majority of grains imaged were almost free of dislocations, implying a desired series of heat treatment was achieved. This is crucial for the quantitative analysis of the damage microstructure. Some degree of grain growth provides convenience for electron microscopy.

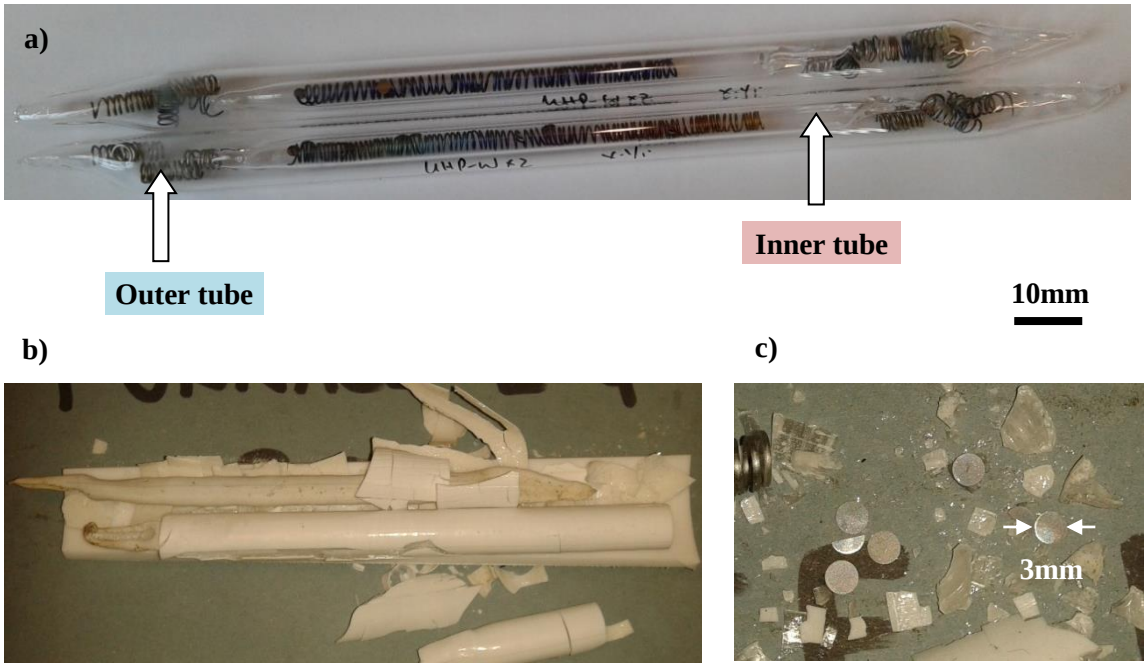


Fig 2.5 a) double-layer encapsulation of discs; b) the inner evacuated quartz tube retained its integrity after the heat treatment; c) disc surface quality after the heat treatment. Good surface quality is essential for subsequent successful electropolishing.

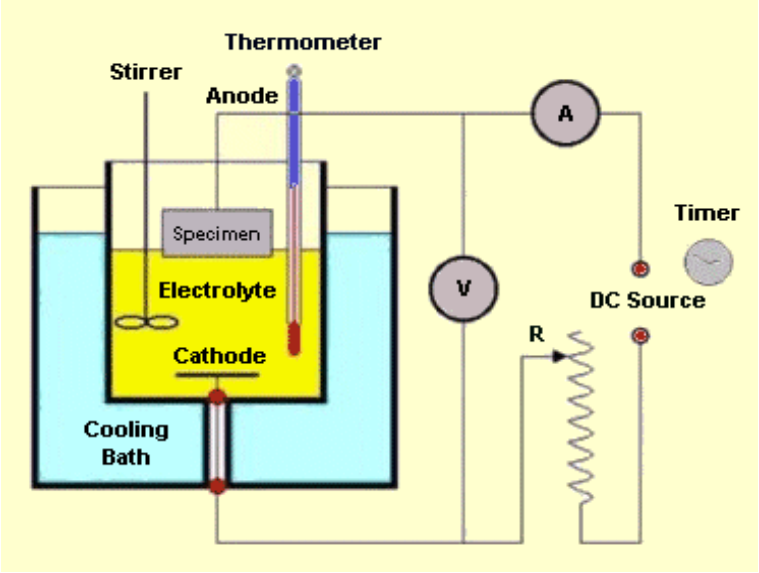


Fig 2.6 A schematic drawing of the bath-type electropolishing method [89].

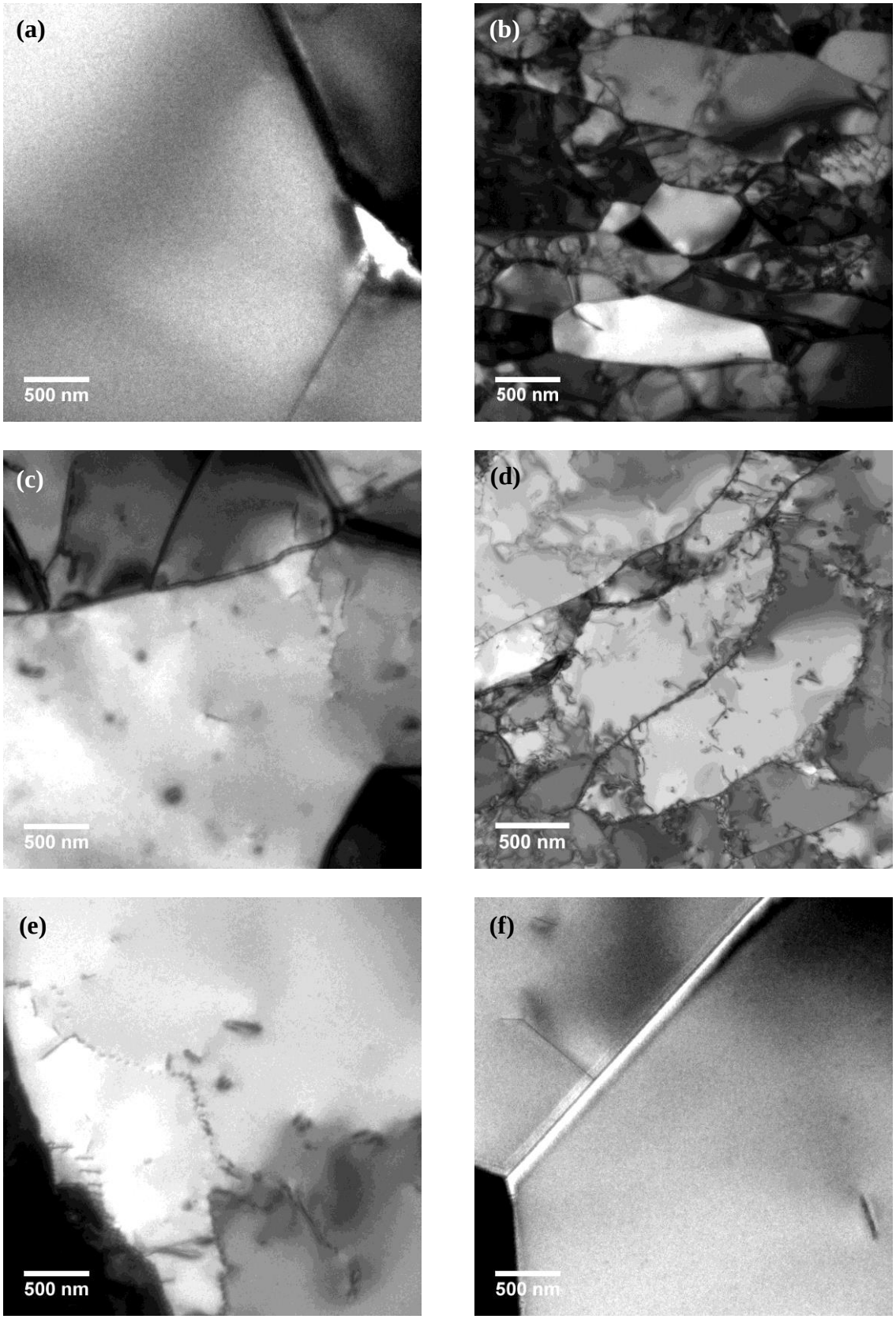


Fig 2.7 Microstructure of selected material grades in the annealed state (1400°C / 20 hrs). a) UHP-W; b) W-5Ta; c) W-5Re; d) W-5V and e, f) CG-W. Compare with Fig 2.1.

2.5.2. TEM samples for bulk irradiations

The damage profile calculated by SRIM demonstrates that those irradiations with 1.9 or 2.0 MeV W^+ ions produces a peak damage region located 50-150 nm beneath the top surface, which is also the range of thickness of good quality thin foils obtained for microscopy. Therefore it was expedient to prepare TEM foils of irradiated samples by directly covering the implanted layer with a protective paint coating (Lacomit, Agar Scientific) and back-thinning the disc in a jet electropolishing device (TENUPOL-5, Struers), illustrated in Fig 2.8. The electropolishing of W/W-alloys in general involved two types of electrolytes, regardless of bath-type or jet-type. For pure W, W-Re and W-V grades, 0.5 wt.% NaOH in distilled water was used. For W-Ta grades, 12.5 vol.% H_2SO_4 and 1.5 vol.% HF in methanol was used. Owing to the high corrosion resistant behaviour of Ta, HF was added to effectively remove the passivation layer [90]. Good quality electropolishing requires a balance between the rate of formation of a passivation layer and its removal by aggressive ions in the electrolyte [91]. In practical terms, it can be achieved by plotting the variation of current density against voltage during the electropolishing (Fig 2.9). In this diagram, the polishing region is the featured plateau where current density remains constant with the voltage increase. A summary of suitable electropolishing parameters for all material grades is presented in Table 2.3.

2.5.3. TEM samples for in-situ irradiation/annealing

Sample preparation in this case was very similar to the back-thinning approach, in terms of electropolishing set up and parameters. Annealed sample discs were directly loaded into the jet polisher TENUPOL and thinned from both sides. Since no protective lacomit paint was applied, the light stop preset value was set to 24-28. The resulting thin wedge region is close to the mid-plane of the disc foil and ready for (in-situ) ion irradiation.

Table 2.3 Back-thinning parameters (TENUPOL) for W/W-alloys[10].

Material	Electrolyte	Temperature	Voltage	Current density	[11]Light stop preset/actual
UHP-W CG-W W-Re alloy	0.5wt.% NaOH in distilled water	0-5°C	14V	1700-2600 A/m^2	18-20/28-36
W-Ta alloy	12.5vol% H_2SO_4 1.5vol% HF in methanol	-40°C	8V		
W-5V	0.2wt.% NaOH in distilled water	0-5°C	15V	1100-1400 A/m^2	

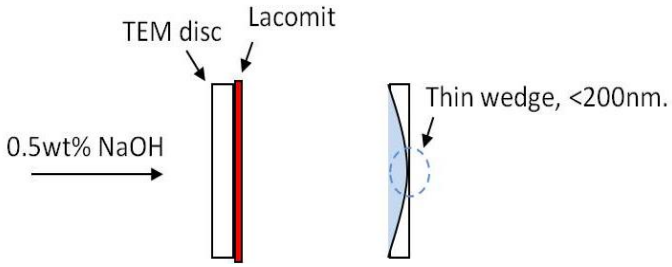


Fig 2.8 A schematic diagram illustrating the back-thinning approach.

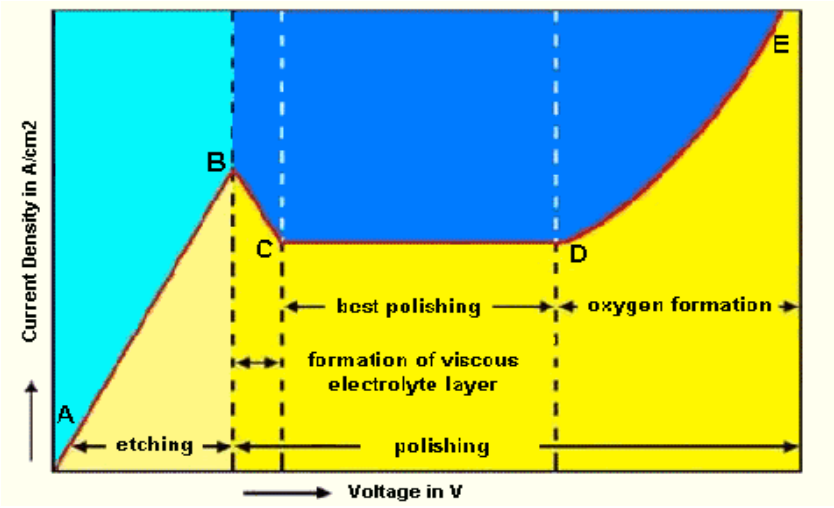


Fig 2.9 Variation of current density with voltage during electropolishing [89].

[10] For bath-type electropolishing, all parameters were kept the same except the temperature, being room temperature to increase the polishing speed.

[11] Electropolishing in a TENUPOL is controlled by an infrared light source, stopping the process as soon as the first light can pass through the established hole. In the back-thinning approach, the layer of lacomit may affect this light measurement. Presetting a small light stop value is in favour of preparing good quality thin foils.

2.6. Transmission electron microscopy techniques

2.6.1. Image rotation calibration

In a TEM, a change in the strength of the intermediate lenses allows a convenient switch from diffraction mode (selected area) to image mode, but often at the cost of introducing an image rotation [29]. Hence, it is crucial to calibrate the rotation angle of the diffraction pattern with respect to the micrograph, in order to correctly orientate the diffraction vectors for subsequent dislocation analysis. The calibration of the image rotation angle θ was performed using a MoO_3 crystal, which is pseudo-orthorhombic (a = 3.963 Å, b = 13.855 Å, c = 3.696 Å) with long straight edges corresponding to [001] [92]. A double exposure was carried out for each combination of camera length and magnification to superimpose the diffraction pattern and the image on a single photographic plate. The angle θ was measured counter-clockwise from diffraction spot to image direction.

Two models of microscopes were used for diffraction contrast analysis of dislocations, i.e. Hitachi H-9000 NAR and Philips CM20. The lens design of the former instrument eliminates the rotation angle issue, i.e. θ = 0° and therefore the calibration was carried out only on the Philips CM20. Combinations of two camera lengths (500 mm and 1000 mm) and four magnifications (38 kx, 50 kx, 88 kx and 115 kx) were calibrated, corresponding to the most commonly used imaging parameters in the diffraction contrast analyses. An additional inversion of the image by the objective lens was confirmed for all magnifications, by defocusing in the diffraction mode until the image occurred. Hence, a total of (θ + 180°) was rotated for aligning diffraction vectors on the TEM micrographs. Fig 2.10 illustrates the calibrations for a camera length of 500 mm on the Philips CM20 and all the calibrated values are summarized in Table 2.4.

Table 2.4 The calibration of image rotation angles for Philips CM20[12].

Magnification	Camera length 500 mm	Camera length 1000 mm
38 kx	-352°+180°= -172°	/
50 kx	-356°+180°= -176°	-354°+180°= -174°
88 kx	-15°+180°= +165°	-10°+180°= +170°
115 kx	-28°+180°= +152°	-27°+180°= +153°

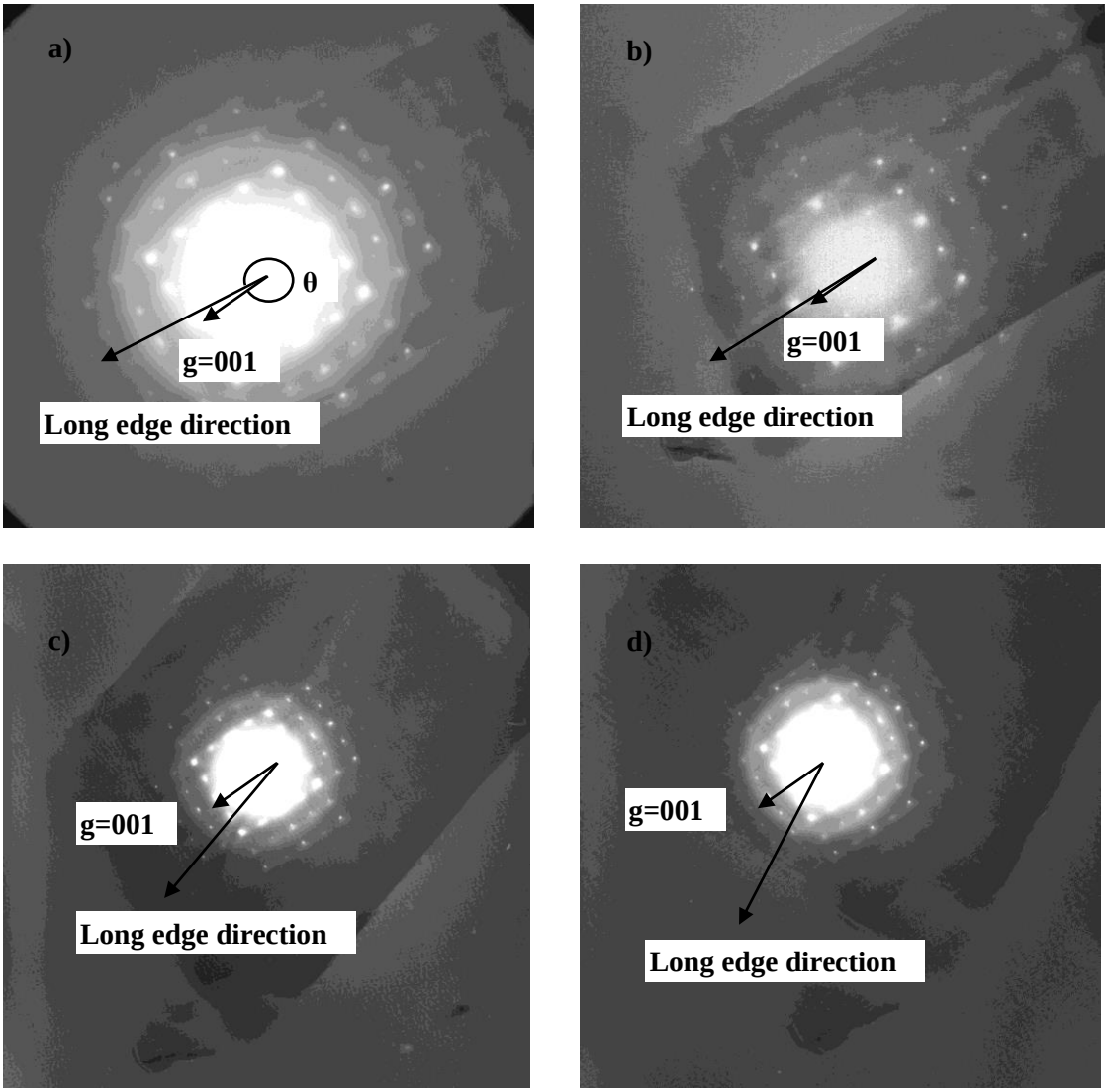


Fig 2.10 Micrographs and superimposed diffraction patterns of a MoO_3 crystal, taken in a Philips CM20 microscope (200 kV) at a constant camera length of 500 mm. Magnifications: a) 38 kx; b) 50 kx; c) 88 kx and d) 115 kx.

[12] Positive rotation angle corresponds to a clockwise rotation from diffraction to image, whereas negative rotation angle corresponds to an anti-clockwise rotation.

2.6.2. Foil thickness measurement

The characterization and analysis of radiation defects often require measurements of the volume number density, which is obtained from measurements of the areal density and the local foil thickness. There are two established techniques available for in-situ thickness measurement, i.e. electron energy loss spectroscopy (EELS) and convergent beam electron diffraction (CBED). EELS achieves an accuracy of 10% whereas CBED gives about 5% [93]. Each method will be demonstrated with an example in the following paragraphs.

To obtain foil thickness from an energy-loss spectrum, samples were viewed in a JEOL 3000F microscope. Regions previously examined in other instruments in diffraction contrast experiments were identified and the simple Log-Ratio Method was applied. In this model, the specimen thickness is given by equation 2.2, where λ is the total mean free path for all inelastic scattering, I_t is the integrated intensity of the whole spectrum and I_0 is the integrated intensity of the zero-loss peak (Fig 2.11). λ can be estimated from equations 2.3 - 2.5 [93], where λ is given in nm, the collection semi angle β in mrad, the incident electron energy E_0 in keV and the mean energy loss E_m in eV. F is the dimensionless relativistic factor.

$$t = \lambda \ln\left(\frac{I_t}{I_0}\right) \qquad Eq\ 2.2$$

$$\lambda = \frac{106F(E_0/E_m)}{\ln(2\beta\, E_0/E_m)} \qquad Eq\ 2.3$$

$$F = \frac{1 + E_0/1022}{(1 + E_0/511)^2} \qquad Eq\ 2.4$$

$$E_m = 7.6Z^{0.36} \qquad Eq\ 2.5$$

For the current set up, E_0 = 297 keV, hence F = 0.516; β = 10 mrad; E_m = 35.79 eV (Tungsten, Z = 74) and 34.71 eV (Vanadium, Z = 23). Therefore, λ is estimated to be 89 nm for W and 91 nm for W-5V. Due to the fact that the difference in atomic number Z between W, Ta and Re is small, λ was assumed constant, regardless of composition. Fig 2.12 illustrates how

typically an EELS foil thickness measurement is presented. The "compute thickness" procedure in the Gatan EL/P software first generates a thickness map (Fig 2.12 a), then a line profile is then drawn across the site of interest, demonstrating the thickness variation along the chosen direction (Fig 2.12 b). Note that the vertical axis of this line profile has been converted from the log-ratio of intensities to absolute thickness, while the horizontal axis represents the lateral range that has been measured.

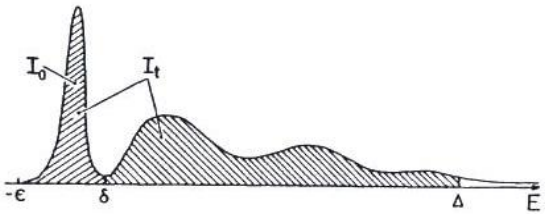


Fig 2.11 The integrals involved in measuring the foil thickness by the Log-Ratio method. I_0 is the integrated intensity of the zero-loss peak while I_t is the integrated intensity of the entire spectrum [93].

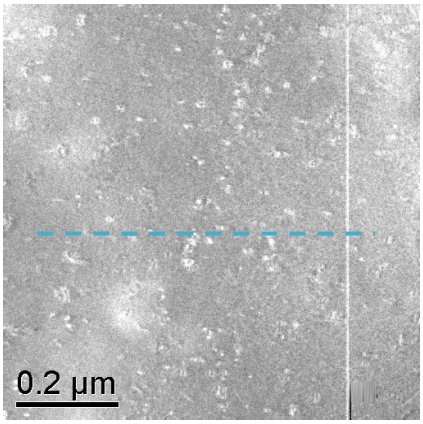


Fig 2.12 a) Computed thickness map from the EELS spectrum in irradiated tungsten.

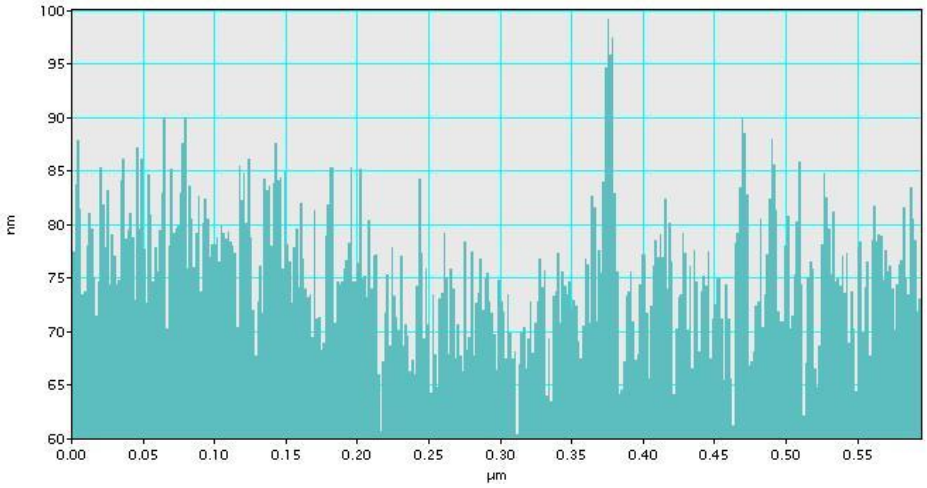


Fig 2.12 b) Line profile of the thickness map shown above (λ = 89 nm).

The measurement of foil thickness by CBED is illustrated in Fig 2.13, also for irradiated tungsten. These experiments were performed on a Philips CM20 microscope, operating at 200 kV. Kossel-Möllenstedt (K-M) fringes in a zero order Lauer zone (ZOLZ) CBED pattern was taken under two-beam conditions with (200) strongly excited. The foil thickness t can be extracted by graphical means, based on equations 2.6 and 2.7 [94]:

$$\frac{s_i^2}{n_k^2} + \frac{1}{\xi_g^2 n_k^2} = \frac{1}{t^2} \qquad Eq\ 2.6$$

$$s_i = \lambda \frac{\Delta\theta_i}{2\theta_B d^2} \qquad Eq\ 2.7$$

where n_k is an integer; λ is the electron beam wavelength (0.0025 nm); d is the lattice parameter (pure W, 3.1565 Å); $\Delta\theta_i$ represents K-M fringe spacing and θ_B is the Bragg angle for the diffracting (hkl) plane. Analysis proceeds as follows. Assign arbitrarily n=1 to the first fringe in Fig 2.13 a), which corresponds to an excitation error s_1. Then assign n=2, 3, ... to the following fringes. Plot (s_i^2/n_k^2) versus $(1/n_k^2)$. If the result is a straight line, the arbitrary assignment is appropriate and the thickness t can be derived from the intercept value, i.e. intercept = $(1/t^2)$. If not, reassign n=2 to the first fringe and iterate until a straight line is obtained. In this example, a straight line plot was achieved by assigning n=3 to the first fringe and gave an estimated foil thickness t of (168±14) nm. Although CBED-based measurements are considered of higher accuracy, they are limited to thick regions. Often the area of interest does not produce a sufficient number (at least three) of K-M fringes and the thickness t cannot be reliably extracted from the graphical plot. This is a particular difficulty with the alloyed samples. As a result, the majority of thickness measurements involved in this project was performed using EELS.

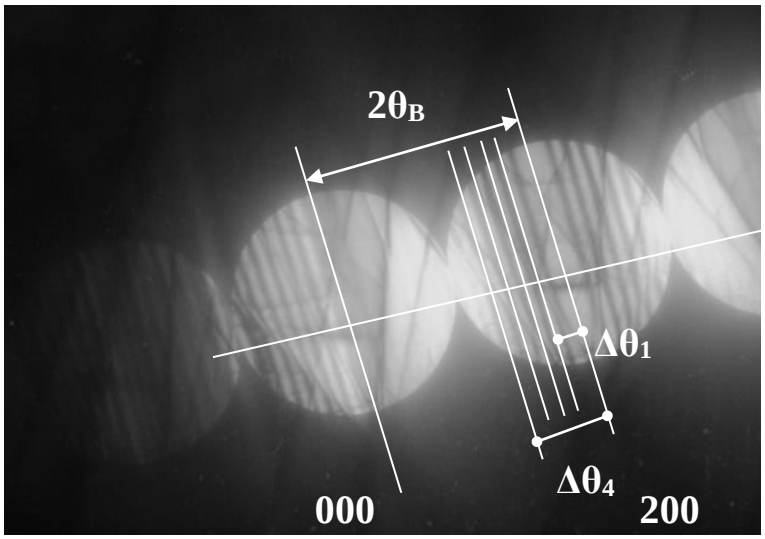


Fig 2.13 a) Kossel-Möllenstedt fringes in a ZOLZ CBED pattern was taken under two-beam conditions with (200) strongly excited in irradiated tungsten.

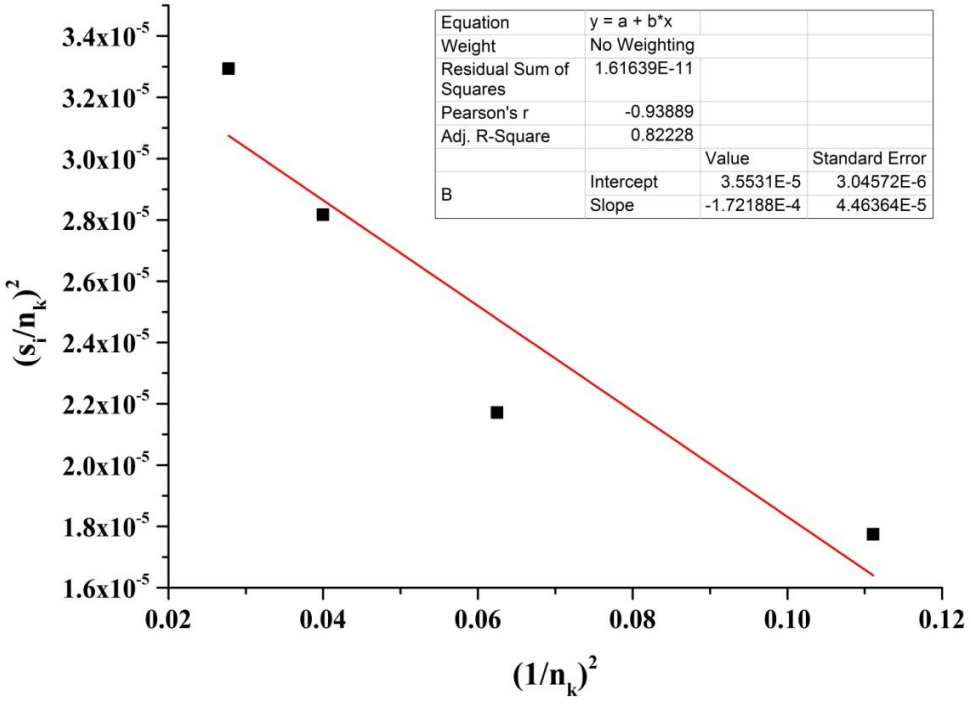


Fig 2.13 b) (s_i^2/n_k^2) is plotted against$(1/n_k^2)$. The first fringe has been assigned with n=3. Intercept = 3.5531×10^{-5} (nm^{-2}). Foil thickness t = (168±14) nm.

2.6.3. Dislocation loop characterization

Dislocation loops in this project were characterized by identifying their Burgers vectors and nature (interstitial or vacancy). The methods used are described in detail in the book by Jenkins and Kirk [95]. A sample analysis is demonstrated (see Figs 2.14 - 2.18) for UHP-W irradiated with 150 keV W^+ ions at 800°C at a dose of 1.0 dpa. All specimens in this project were primarily intended for irradiation and characterization of those grains close to **z** = [001]; other orientations were investigated only for exploring grain orientation effects on irradiation damage in W-5Ta and W-5V alloys. In the Argonne in-situ irradiations, channelling was avoided since the direction of the incident ions was not precisely parallel to the [001] direction.

Prior to the analysis of individual loops, it is important to clarify the following points. First, micrographs recorded on films on the Philips CM20 were printed emulsion-up, so that they appear as seen on the microscope screen. Second, diffraction vectors were placed on the micrographs taking account of image rotation and inversion as described in § 2.6.1. Third, a set of crystallographic axes (reference) was defined. In this case, **z** = [001] was defined as the upward-drawn normal (pointing out of the paper). Reflections near this pole were then assigned indices. In Fig 2.14, $\mathbf{g_1}$ was assigned 200. This choice was arbitrary. $\bar{2}00$, 020 or $0\bar{2}0$ could also have been chosen due to the four-fold symmetry at this orientation. Once this choice was made, all the remaining diffraction spots were indexed consistently using a Thompson tetrahedron.

The determination of the Burgers vectors of dislocation loops is described as follows. Dislocation loops in bcc materials are expected to have Burgers vectors of type ½<111>, <100> and perhaps ½<110> [96]. In particular, ½<111> and ½<110> loops have been reported in thin foil experiments on tungsten, irradiated by 60 keV Au^+ ions [68]. In the

diffraction contrast analysis throughout this project, it was assumed that loops with all three major types of Burgers vectors could be present. Each type of loop Burgers vector has several variants as a result of symmetry. For example, ½<111> has four variants, i.e. $\pm\frac{1}{2}[\bar{1}11]$, $\pm\frac{1}{2}[1\bar{1}1]$, $\pm\frac{1}{2}[11\bar{1}]$ and $\pm\frac{1}{2}[111]$. To determine the particular variant of a dislocation loop, the invisibility criterion **g.b** = 0 was applied. Sufficient constraints were obtained to derive the Burgers vector of a loop without ambiguity. In Table 2.5, eight independent diffraction vectors have been selected over **z** = [001], $[\bar{1}13]$ and [012]. Applying these to Fig 2.16, it can readily be concluded that the loops circled in blue have **b** = $\pm\frac{1}{2}[\bar{1}11]$.

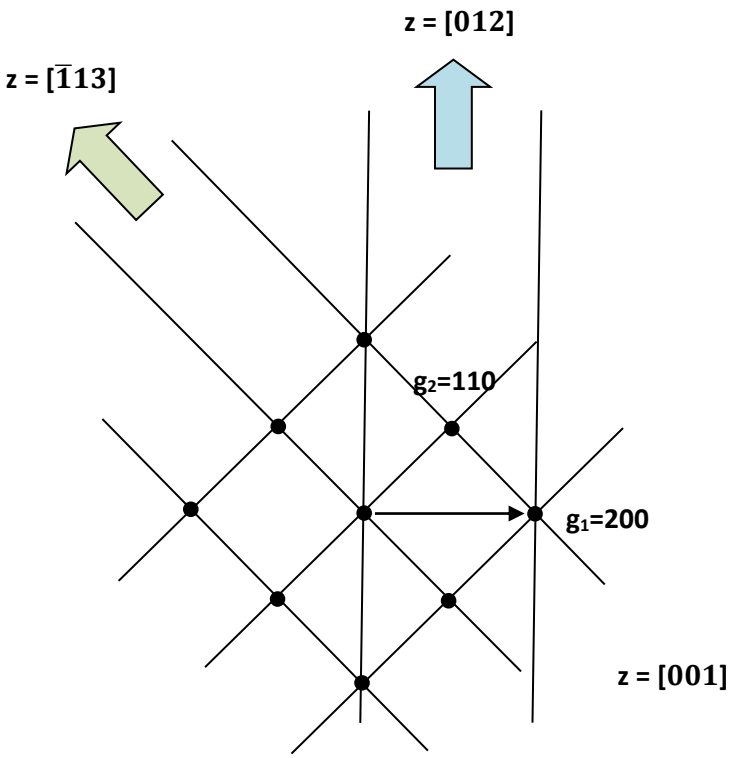


Fig 2.14 Indexing the diffraction spots at **z** = [001]; the relative geometry of $[\bar{1}13]$ and [012] with respect to [001].

Table 2.5 Values of **g.b** for Burgers vector determination in a bcc - lattice.

h	k	l	½[111]	½[-111]	½[1-11]	½[11-1]	½[110]	½[1-10]	½[101]	½[-101]	½[011]	½[0-11]	[100]	[010]	[001]
0	2	0	1.0	1.0	-1.0	1.0	1.0	-1.0	0.0	0.0	1.0	-1.0	0.0	2.0	0.0
1	1	0	1.0	0.0	0.0	1.0	1.0	0.0	0.5	-0.5	0.5	-0.5	1.0	1.0	0.0
1	-1	0	0.0	-1.0	1.0	0.0	0.0	1.0	0.5	-0.5	-0.5	0.5	1.0	-1.0	0.0
2	0	0	1.0	-1.0	1.0	1.0	1.0	1.0	1.0	-1.0	0.0	0.0	2.0	0.0	0.0
2	-1	1	1.0	-1.0	2.0	0.0	0.5	1.5	1.5	-0.5	0.0	1.0	2.0	-1.0	1.0
1	-2	1	0.0	-1.0	2.0	-1.0	-0.5	1.5	1.0	0.0	-0.5	1.5	1.0	-2.0	1.0
3	2	-1	2.0	-1.0	0.0	3.0	2.5	0.5	1.0	-2.0	0.5	-1.5	3.0	2.0	-1.0
1	2	-1	1.0	0.0	-1.0	2.0	1.5	-0.5	0.0	-1.0	0.5	-1.5	1.0	2.0	-1.0

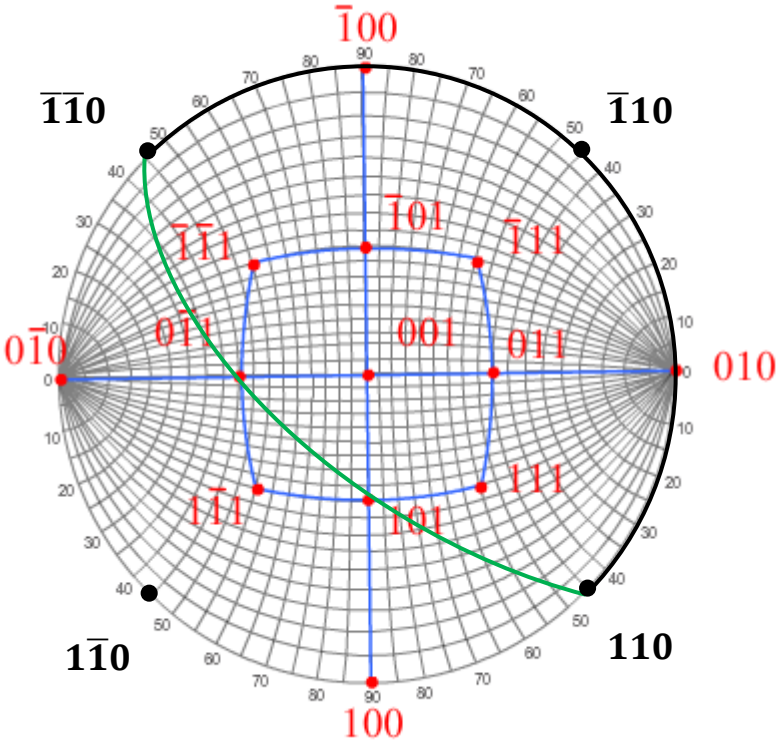


Fig 2.15 The (001) stereographic projection of a body-centred cubic lattice [97].

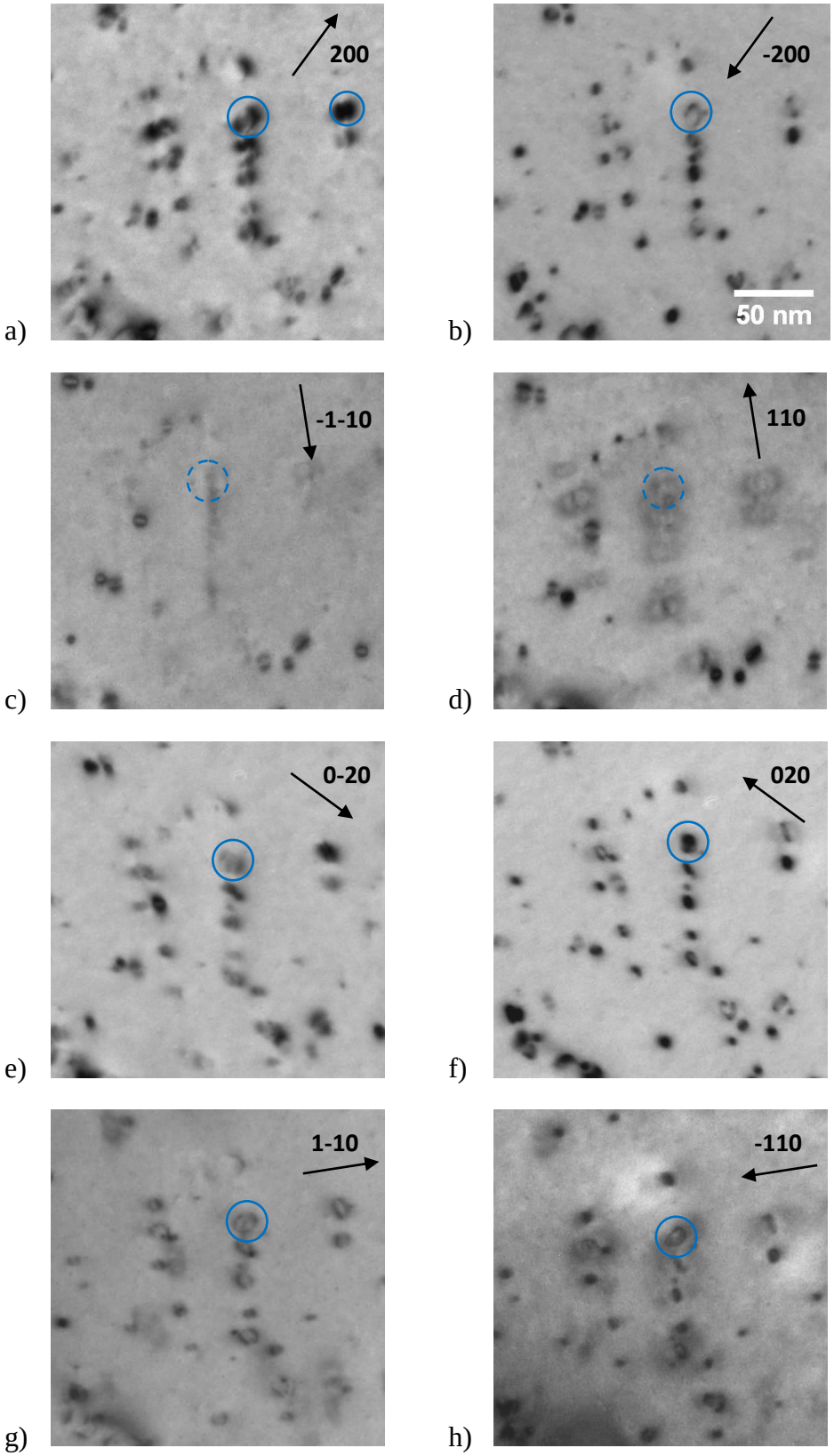


Fig 2.16 a-h) Kinematical-bright field micrographs taken close to **z** = [001] in UHP-W, irradiated at 800°C, up to 1.0 dpa, using the diffraction vectors indicated.

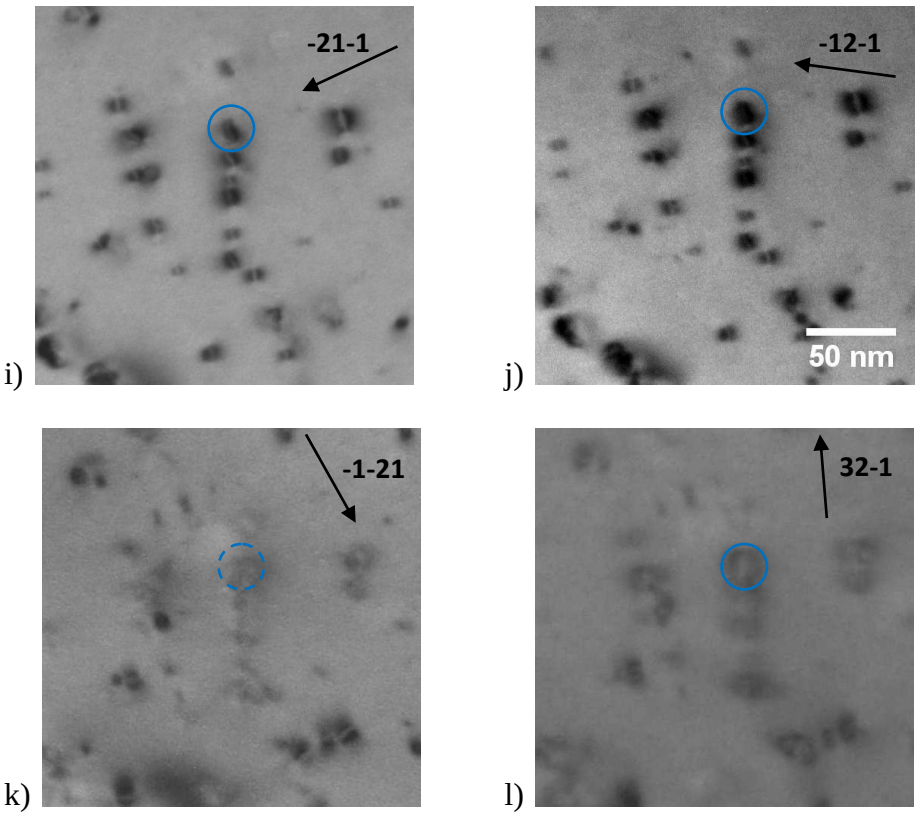


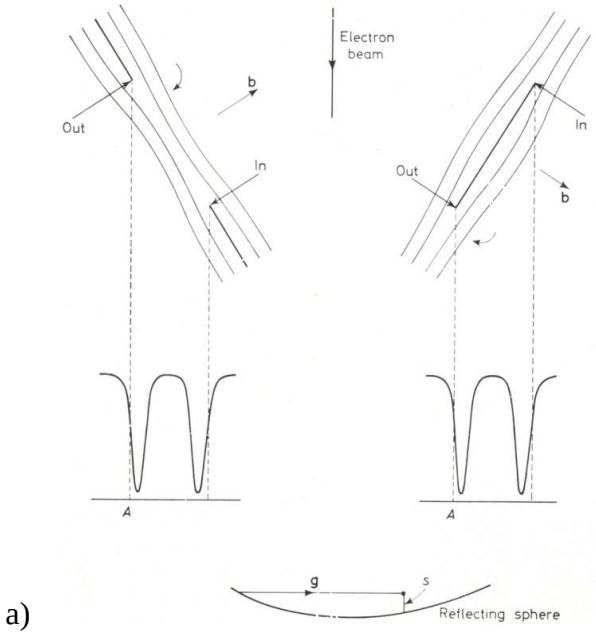
Fig 2.16 i-l) Kinematical-bright field micrographs taken close to **z** = [012] and [$\bar{1}$13] in UHP-W, irradiated at 800°C, up to 1.0 dpa, using the diffraction vectors indicated.

The vacancy or interstitial nature of these labelled loops in Fig 2.16 was deduced by performing inside-outside contrast analysis, using an established technique originally introduced by Groves and Kelly [98] , later amended by Eyre and co-workers [99]. In this technique, inside (outside) contrast is assigned to cases when the loop image size shown is smaller (larger) than the real size. To fully characterize the nature of a dislocation loop, it is necessary to know the inside-outside contrast for a ±**g** pair; the axis of **b**; the loop habit plane (plane normal **n**) or the sense of inclination. However, it is difficult or impossible to determine the habit plane or sense of inclination of very small loops. In this case a simplified procedure may be used, when only the inside-outside contrast behaviour and the axis of **b** are known. It is important to discuss under what conditions this simplification remains valid. Consider loops with **b** = ½<111>. It is generally accepted that such loops nucleate on {110} planes. They may subsequently rotate towards the edge orientation, i.e. on {111} planes [96].

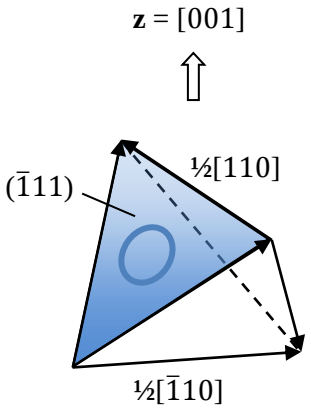
In the damage microstructure of tungsten, there may therefore contain a mixture of pure edge loops and loops with some shear components. The simplified procedure assumes that certain non-edge loops lying in 'safe orientations' show the same inside-outside contrast behaviour as edge-loops with the same Burgers vector. Such loops would lie within the area of a stereographic projection, with boundaries defined by **n.z** = 0 (edge-on orientation, black curve) and **n.b** = 0 (pure shear orientation, green curve), illustrated in Fig 2.15.

Referring back to the **b** = ±½[$\bar{1}$11] loops in Fig 2.16, the possible nucleation planes are ($\bar{1}$01), (011) and ($\bar{1}$10), according to the stereographic projection in Fig 2.15. In the following the extreme case where loops have retained their nucleation planes as habit planes is considered. The ±**g** pairs were recorded close to **z** = [001]. Two of the habit planes of **b** = ±½[$\bar{1}$11] loops, i.e. ($\bar{1}$01) and (011), lie at an angular distance of 35° with respect to the [$\bar{1}$11] pole, while ($\bar{1}$10) is at the border of an edge-on orientation. What this implies is that if the nucleation planes were ($\bar{1}$01) and (011) for **b** = ±½[$\bar{1}$11] loops, we are within the safety limit for producing a correct sense of inside-outside contrast. If the nucleation planes have rotated towards {111}, we will fall further within the safety limit. For **b** = ±½[$\bar{1}$11] loops nucleated on ($\bar{1}$10), imaging near the **z** = [001] means we are right on the safety limit. In practice, it would not be a big problem since only loops exhibiting double arc features were analysed, i.e. loop habit planes were not far from the plane of the foil. Therefore, the edge-on oriented loops were not taken into account. Alternatively, an angular limit can be defined to assure "safe contrast" behaviour. An upper limit to the acute angle φ_m between **b** and **n** can be assigned, considering whether the loops were pure edge or contained shear components. A crystal orientation **z** can then be selected, for which $\measuredangle$(**b, z**) < 90°- φ_m. In this scenario, φ_m is assigned with 35° and therefore $\measuredangle$(**b, z**) < 55°. This is a convenient criterion for selecting crystal orientations for 'safe contrast' imaging. Having confirmed that the simplified inside-

outside contrast procedure remains valid for the loops analysed in Fig 2.16, the nature of the **b** = ±½[$\bar{1}$11] loops can be determined. The labelled loops show inside contrast in **g** = $\bar{2}$00, 020 and $\bar{1}$10 and outside contrast in the opposite reflections. Since the images were obtained in kinematical bright-field conditions with positive deviation parameter ($\mathbf{s_g}$>0) and inside contrast corresponds to (**g.b**) $\mathbf{s_g}$ <0, it can be concluded that **b** = −½[$\bar{1}$11]. Since **b.z** < 0, these loops are therefore interstitial [95]. Fig 2.17 illustrates the analysis with a Thompson tetrahedron, where inside contrast under **g** = $\bar{1}$10 confirms the loops to be interstitial.



a)



b)

Fig 2.17 a) Inside contrast effect, a combined result of loop nature and its sense of inclination in the foil [29]. b) Orientation of the Thompson Tetrahedron for **g** = $\bar{1}$10.

The determination of the nature of <100> loops must be performed with extra care. Any <100> loop identified in images taken close to **z** = [001], i.e. **b** = ±[100] or ±[010], would likely be close to an edge-on orientation (**n.z** = 0). Hence, the method previously applied for determining ½<111> loop nature fails and the sense of inclination for the dislocation loop must be known in addition to the inside-outside contrast for a ±**g** pair and the axis of **b** [95]. The procedure is demonstrated with <100> loops observed in UHP-W. In Fig 2.18 a-d), two red-circled loops are identified as **b** = ±[100]. Comparing the contrasts shown in **g** = ±200 conditions, both loops show outside contrast under **g** = $\bar{2}00$, and so are assigned **b** = [$\bar{1}$00]. Next, a series of images was obtained by tilting along the ($\bar{1}$10) band (equivalent to anti-clockwise on x-drive) to reveal their sense of inclination.

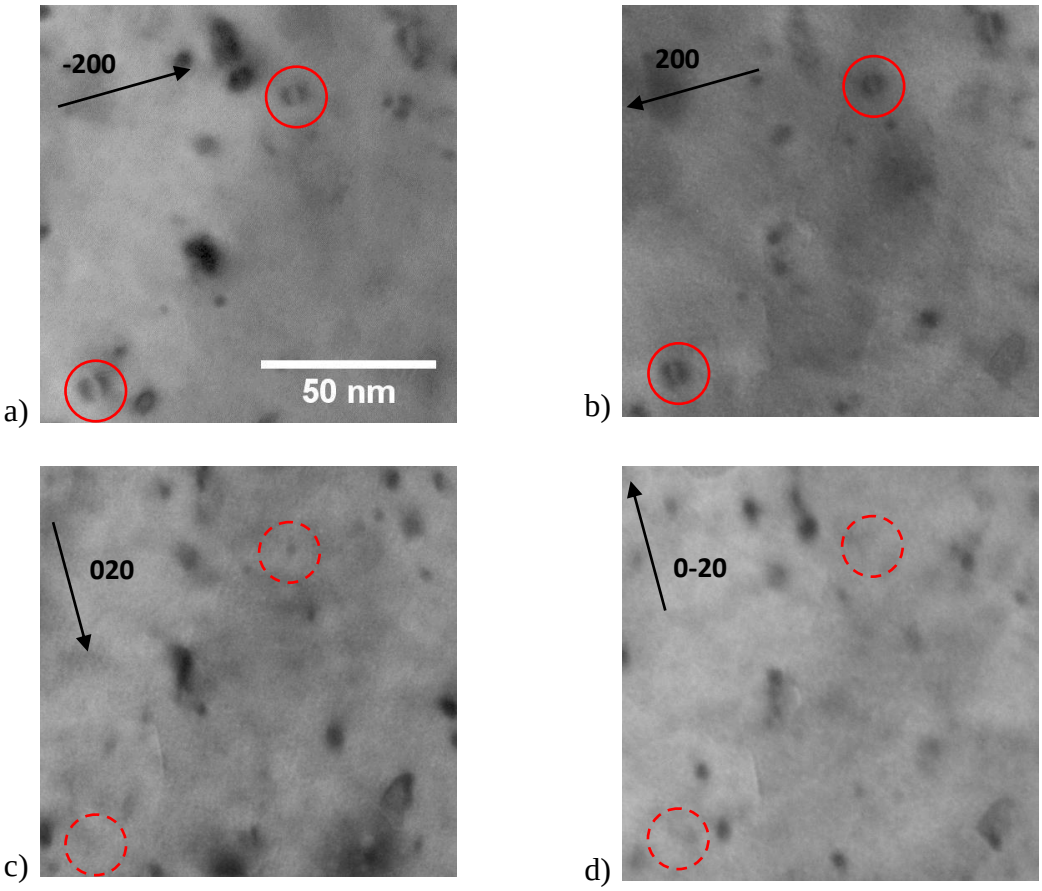


Fig 2.18 a-d) Kinematical bright field micrographs taken close to **z** = [001] in UHP-W, irradiated at 600°C, up to 1.0 dpa.

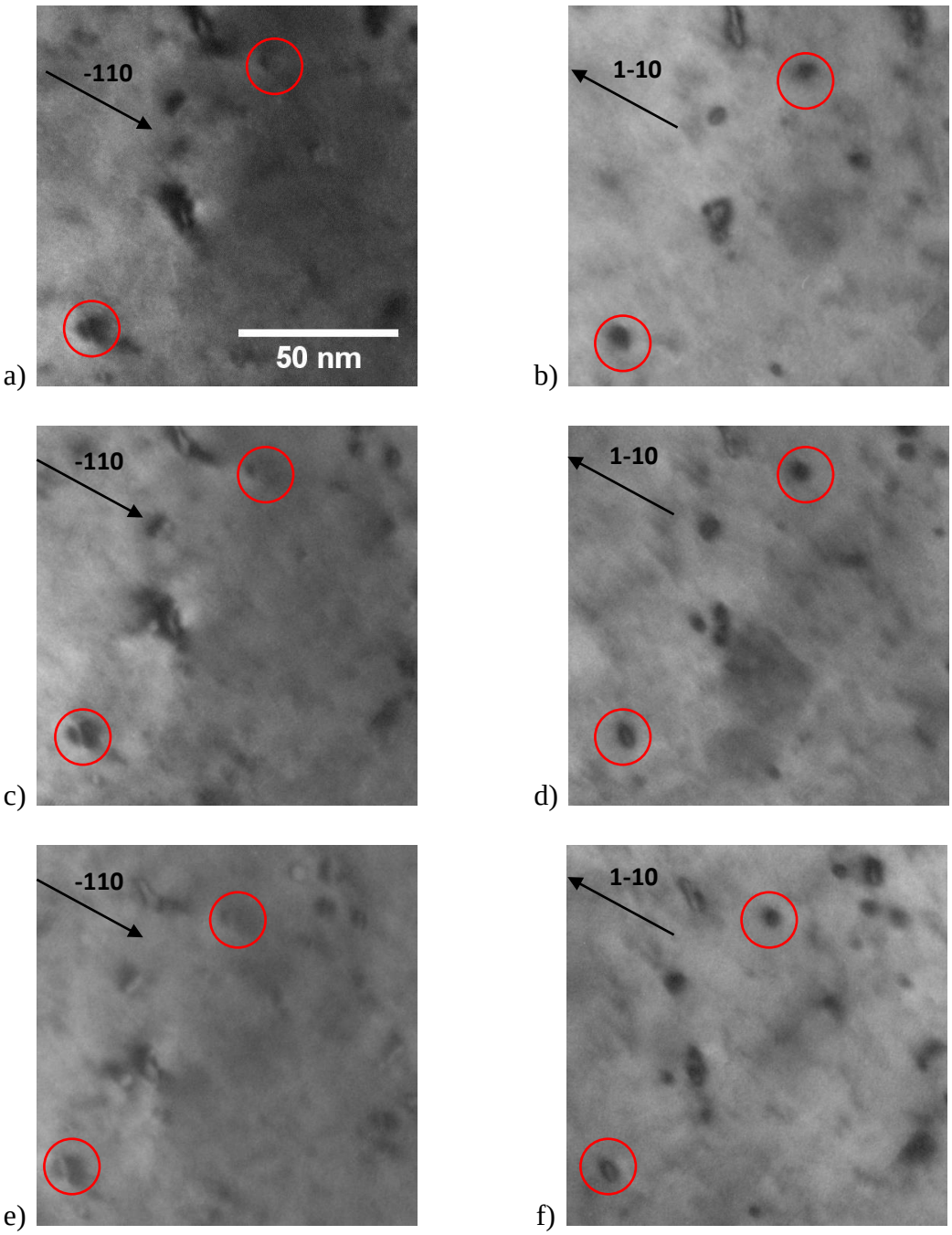


Fig 2.19 Kinematical-bright field micrographs taken along the $(\bar{1}10)$ band in UHP-W, irradiated at 600°C, up to 1.0 dpa. The crystal was tilted close to poles of a-b) **z** = [001]; c-d) **z** = [114] and e-f) **z** = [113].

With increasing tilt angle along the $(\bar{1}10)$ band, it is apparent that the image sizes of the labelled loops increase (Fig 2.19: a → c → e or b → d → f). This may be confirmed by comparing the new double arc contrast features displayed in Fig 2.19 d) and f), with those seen in Fig 2.19 b). This increase in loop size as a consequence of tilting indicates that the sense of inclination follows the geometry depicted in Fig 2.20, from which one can

subsequently derive the nature of the loops. Fitting this geometry into the illustrative diagram in Fig 2.17, where **g** = 200 corresponds to "inside-contrast", it can be concluded that the **b** = [$\bar{1}$00] loops analyzed are of interstitial nature.

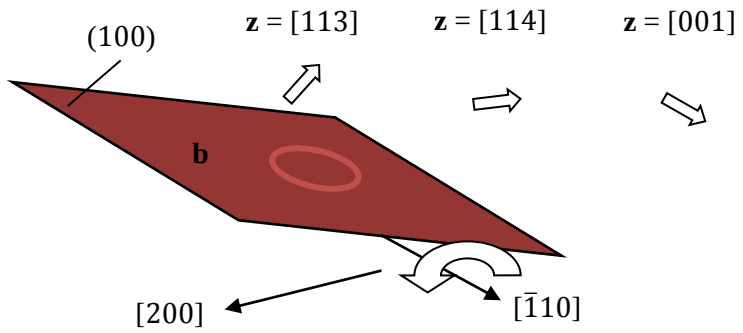


Fig 2.20 Relative geometry of the labelled loops in Fig 2.19.

Note that both of the inside-outside contrast methods described above fail for loops of size ≤ 5 nm, which appear as dots and not double-arcs in diffraction contrast images under weak-beam dark-field or kinematical-bright field conditions. In these cases, the black-white contrast method may be used to extract the nature of small loops, based on both the intensity (visibility) and the shape of the diffraction contrasts. The details of the technique will be described in Ch 4, where it is applied to deal with the nature determination of loops formed at the early stage of irradiation damage.

2.6.4. Void characterization

The imaging of small voids (< 5nm) is found best in out-of-focus conditions. Defocus is introduced to give rise to phase shift between the electron waves traversing through the matrix and the void. Fresnel fringes form accordingly close to the edge of the void, but their intensity varies with the degree of under focus or over focus of the objective lens. In bulk irradiated samples, voids can be confirmed by recording a through-focal-series in bright field condition.

However, caution is required for void characterization from thin-foil irradiations since surface craters and small voids essentially exhibit the same contrast. An example of such is illustrated in Fig 2.21 on an irradiated UHP-W specimen (150 keV W^+). Void-like features were observed and the sizing of which was carried out in under focus condition (approximately -1 μm). The only reliable method to distinguish surface craters from voids is to perform stereo measurements, which provide the depth information of observed contrast features [95]. In this project, stereo measurements were not included and therefore the possibility of the features being surface craters may not be eliminated. It is commonly accepted that surface craters are more likely to form when the deposited energy density in the displacement cascade is high, i.e. large E_{PKA} and large ion mass [100, 101]. Meanwhile, void formation may require excess amount of vacancies and stabilizing agents such as gases in the vicinity of the foil surface [24]. Due to the scope of this thesis, the possibility of voids in irradiated tungsten subject to high temperature and high dose has been proposed but further investigation is required to confirm their presence in the damage microstructure.

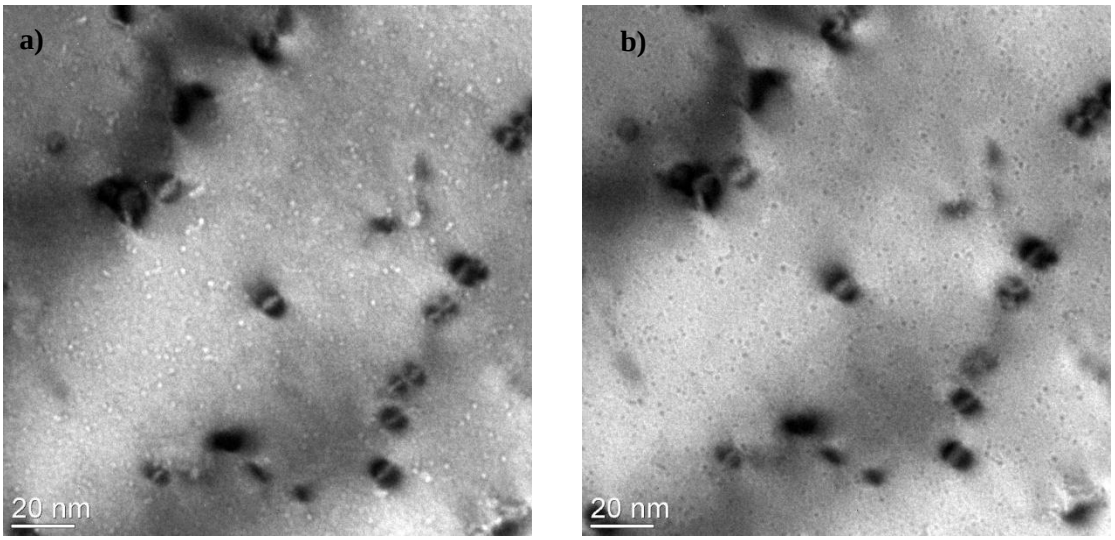


Fig 2.21 Out-of-focus images of voids in UHP-W irradiated with 150 keV W^+ ions at 800°C, to a dose of 1.0 dpa: a) Δf = -896 nm, best contrast is achieved and the voids appear as white dots surrounded by dark fringes; b) Δf = +896 nm, voids appear as dark dots surrounded by bright fringes.

2.7. Technical notes of data processing with Image J

2.7.1. The counting of loops

The counting of loops assumes that each local intensity maximum on the micrograph represents a loop. The software finds the local maxima by acquiring a noise tolerance parameter, measured in grey scale. Maxima are therefore ignored if they do not stand out from the surroundings by more than this parameter. In practice, the value is given arbitrarily, winded down gradually from 255 (maximum intensity in grey scale). During each step, the eye makes a judgment whether all loops have been picked up. The process iterates until all loops can be counted.

The uncertainty of counts arises when dealing with loops with intensities comparable to that of the background noise. The range of which is estimated from the fluctuation of the background intensity. Fig 2.22 a) and b) illustrates the estimation. A loop-free area (as-judged by eye) is selected with a line drawn through (Fig 2.22 a). Then, an intensity line profile is generated as shown in Fig 2.22 b). The magnitude of the grey scale fluctuation is around 10. Hence, the noise tolerance parameter is also assigned with a ±10 variation. If one defines the grey scale intensity of a loop comparable to that of the background as I, then loop counts correspondent to noise tolerance parameters I-10 and I+10 will be sought for. The difference between the counts represents the range of uncertainty.

The same noise tolerance parameter value has been assigned for all counting of loops in this thesis, since all micrographs adopted for loop number density analysis were recorded under weak-beam dark-field conditions ($\mathbf{g} = \pm 200/020,\ 3-4\mathbf{g}$) using similar exposure parameters.

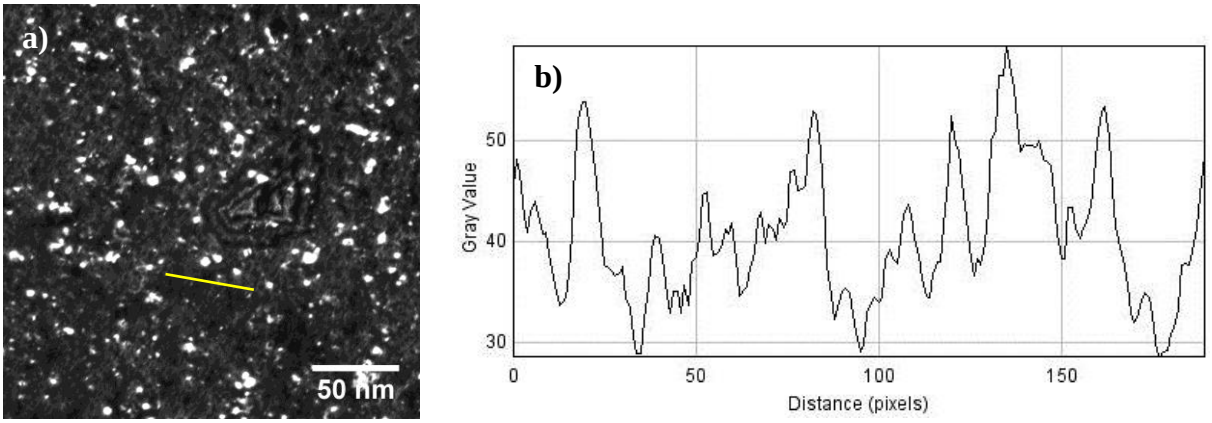


Fig 2.22 Estimation of the range of loop count uncertainty: a) a sample micrograph for image processing, obtained from an irradiated W-5Re specimen under weak-beam dark-field condition; b) Image J generates a line profile of the selected background region (marked yellow). The intensity fluctuates around ±10 in arbitrary grey value units.

2.7.2. Loop size distribution

Loop sizing may vary with the strength of diffraction. Quantitative analysis of overall loop size distributions in this thesis were averaged among data obtained from pairs of weak-beam dark-field images of the same areas of interest taken in $\mathbf{g} = \pm 200/020, 3-4\mathbf{g}$.

Selected micrographs, typically 4 to 8, were converted from grey scale to a binary format. Each visible loop was assumed to be a particle-like feature possessing a circularity value between 0 and 1. The range of loop dimensions was binned at a step size of 1 nm for loops between 1 and 10 nm, and all loops larger than 10 nm were grouped as one category. As a consequence of the difficulty of distinguishing loop boundaries from the background noise (or resolution limit of diffraction contrast), loops that were smaller than 1 nm were not taken into account in the overall size distribution analyses. The statistics of loop size were then obtained by analysing the range of areas equivalent in $(\text{pixel})^2$ for all particle-like objects picked up by the software. The error bars show the standard deviation of the frequency for each binned loop size category.

Despite of the convenience on loop sizing following this automated procedure, a few notes must be born in mind on the interpretation of acquired loop size measurements. First, it is the conversion of raw grey scale data to binary format (foreground 255, background 0), where any intensity less than an automated threshold[13] (computed based on the isodata algorithm developed by Ridler and Calvard [102]) would be taken to 0 after the conversion. Typically, threshold values of micrographs in this thesis are found to be ~ 50% of the maximum foreground value 255.

Fig 2.23 demonstrates the conversion of image formats with two examples, i.e. a large/bright loop (~ 11 nm) and a small/faint loop (~ 3 nm) seen in irradiated pure tungsten. The grey scale contrast, binary format contrast and respective line profiles of selected loops are summarized from a) to f). Boundaries of loop are defined as points where the grey scale intensity sees a sharp change in gradient. In the case of a large/bright loop, the systematic error of loop sizing due to image conversion is ~ 10%. However, a larger degree of underestimation of loop size is found when dealing with small/faint loops, as a result of applying the same intensity threshold. Systematic sizing error increases to ~ 35%. Generally speaking, size measurements following this method for loops larger than 4 nm can be regarded as accurate reproductions of the true size.

[13] The isodata algorithm of automatic thresholding.
The grey scale histogram is initially segmented into a foreground part (also known as object) and a background part using a starting threshold value, e.g. half the maximum dynamic range. Then, the averages of the pixels at or below the threshold and pixels above are computed. The averages of those two values are then calculated. The threshold is then incremented and the process repeats until the following relation is satisfied:
threshold > ½ (average foreground + average background).

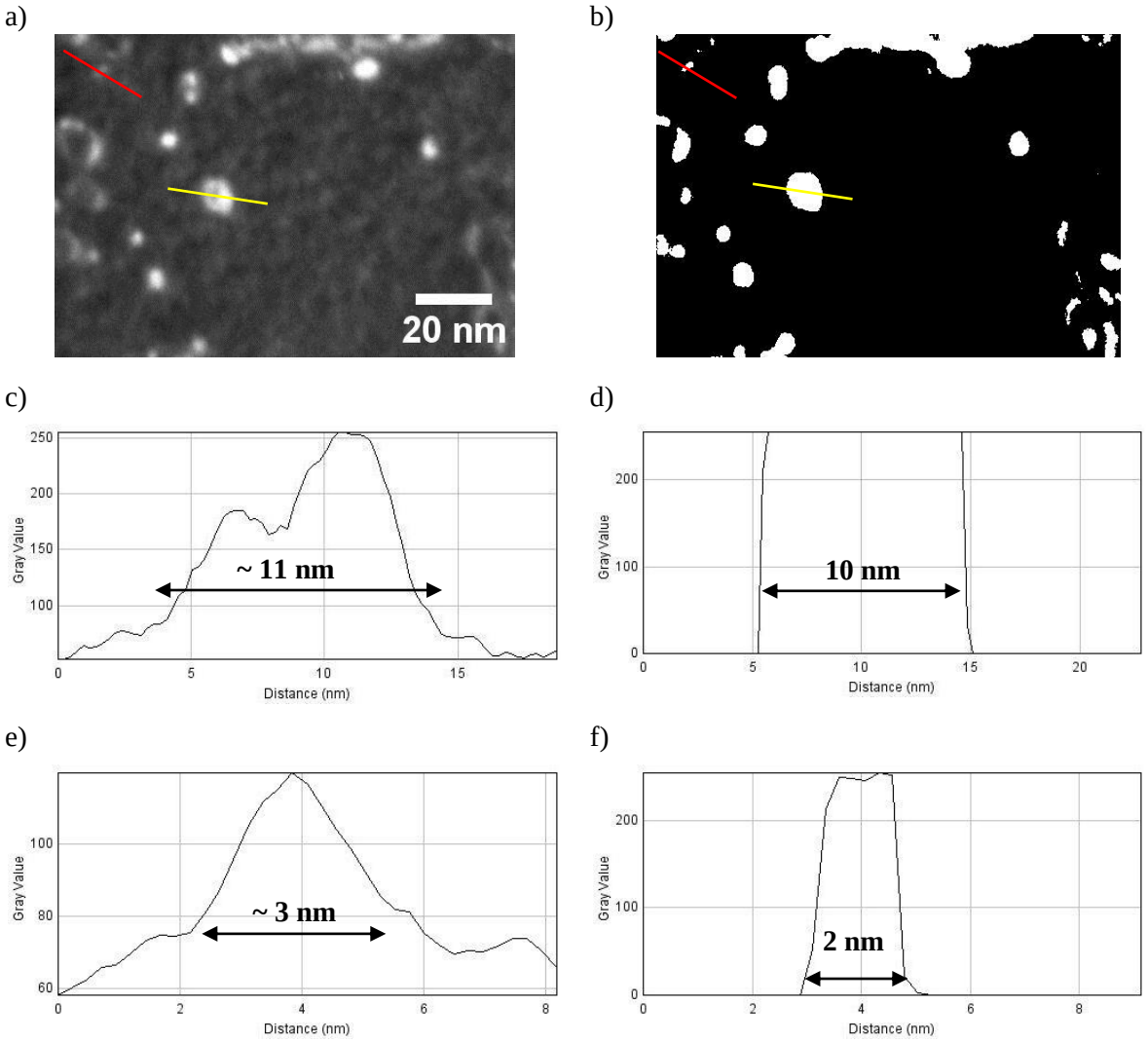


Fig 2.23. Demonstration of loop sizing in an irradiated UHP-W specimen: a) grey scale image; b) binary format of the image; c and d) line profiles of a large/bright loop (marked yellow) in grey and binary format respectively; e and f) line profiles of a small/faint loop (marked red) in grey and binary format respectively.

The second point to bear in mind is the challenge of sizing individual loops at high doses. The separation distance among loops may be so small that they were mistaken for one single large loop. This may be the major cause for the large standard deviations found in overall loop size distributions presented in this thesis, the "> 10 nm" category in particular. Finally, one need to note that only one diffraction condition was adopted for sizing analysis and the overall size distributions shown in the results chapters do not distinguish between loops of type ½<111> or <100>. ½<111> loops would have been present in both micrographs, with individual loops showing outside contrast in one and inside in the other. It

was not possible however to correlate the measured sizes of individual ½<111> loops. Loops of <100> would have been present in only one of the micrograph pairs ([100] in **g** = 200 and [010] in **g** = 020), with one variant showing inside contrast in one micrograph, and the other showing outside contrast in the other. Overall therefore image size changes due to inside-outside contrast changes would have been averaged out for both ½<111> and <100> loop populations.

2.7.3. Loop Burgers vectors analysis

In principle, the Burgers vectors of dislocation loops should be deduced according to § 2.6.3. Owing to the high loop number densities in various cases, it was not usually possible to perform one-to-one correlation for all loops in micrographs recorded in different diffraction conditions. Therefore the problem was treated by analysing the different loop number densities seen in micrographs (as described in § 2.7.1.) taken with **g** = $\pm 200 / 020$ and $\pm 110 / 1\bar{1}0$, assuming that all variants of ½<111> and <100> loops are produced in equal quantities. If **g** = 200 or 020, all variants of loops with **b** = ½<111> will be seen, but only one variant of **b** = <100> remains visible, i.e. **b** = [100] or [010]. If **g** = 110 or $1\bar{1}0$, two of four ½<111> variants will be seen, ½[111] and ½[$11\bar{1}$] or ½[$1\bar{1}1$] and ½[$\bar{1}11$] respectively, and two of the three <100> variants, **b** = [100] and [010]. It then follows that if the number density of a ½<111> variant were assigned x, and a <100> variant y, then in **g** = $\pm 200 / 020$, a total loop number density of (4x+y) would be expected; and in **g** = $\pm 110 / 1\bar{1}0$, (2x+2y). By counting the total number of loops visible in each micrograph x and y can be found. In practice not just one but several (typically 8) micrographs recorded under equivalent diffraction conditions were counted in each condition in order to improve statistics. The fraction of ½<111> loops is then 4x/(4x+3y), which is plotted against irradiation temperature and dose for a selection of materials in the following results chapters.

Chapter 3

Bulk Irradiated Tungsten and alloys

3.1. Introduction

Bulk self-ion irradiations of tungsten and alloys were carried out as an analogue of fusion neutron damage in TOKAMAK reactors. MeV-energy W^+ ions were implanted at different combinations of dose (0.5 ~ 37.5 dpa) and irradiation temperature (300 ~ 750°C), in pure tungsten grades and tungsten-based alloys (W-(1,5) wt.% A, A = Ta, Re, V). The dose rate was held constant, at around 2×10^{14} $W^+m^{-2}s^{-1}$ (3×10^{-4} dpa/s). The experiments were aimed at gaining a systematic understanding of the radiation response of the materials including the effects of dose, irradiation temperature, material composition and grain orientation. Grains in **z** = [001] were chosen for comparison across all materials and irradiation conditions due to annealing texture, but in CG-W and W-5Ta, radiation damage features at different grain orientations were also investigated. The layout of this chapter begins with detailed descriptions of the damage microstructures in **z** = [001] oriented grains of UHP-W, CG-W, W-5Re, W-(1,5) Ta and W-5V in sequence (§ 3.2.1 - 3.2.5), followed by a case study on non **z** = [001] oriented grains of W-5Ta in § 3.2.6, and finishes with the quantitative analyses of the radiation damage described in § 3.3.1 - 3.3.3.

3.2. Radiation damage microstructures

Microstructure characterizations in this section refer solely to the dislocation loops induced by the ion irradiation. The imaging conditions used were kinematical-bright field and weak-beam

dark-field ($\mathbf{g} = 200, 3 - 4\mathbf{g}$). Evidence of voids in the damage microstructure was also sought, but systematic investigations were not performed due to limitations of time.

3.2.1. (300, 500, 750°C) / (0.5, 1.5, 4.5, 37.5 dpa) irradiated UHP-W

Results of irradiations performed at three temperatures are presented here. The 750°C irradiation was carried out with ions of slightly lower energy (1.9 MeV), but is included for comparison with the rest of the 2 MeV W^+ ion irradiations. TEM micrographs of the damage microstructures at 300, 500 and 750°C are shown in Figs 3.1-3.3 respectively. Overall loop size distributions in UHP-W as a function of dose and temperature are illustrated in Fig 3.4.

At 300°C, an increase in dose from 0.5 dpa to 1.5 dpa resulted in a substantial increase in loop number density and a moderate increase in loop size. Note that the loop number density directly observable from the micrographs refers to area number density. The foil thicknesses were similar in the various micrographs presented so that this qualitative trend is valid. However, the foil thickness will be considered in § 3.3.1, where loop volume number density will be adopted for comparison across the various material compositions. A further increase in dose to 37.5 dpa resulted mostly in an increase in loop size while the loop number density appeared to remain constant. Additionally, loop strings and rafts[14] made up of small dislocation loops were observed.

At 500°C, dislocation loops had larger size and lower number density, compared with the same doses at 300°C. Also the increase in irradiation temperature seemed to have lowered the dose threshold for loop strings and rafts to occur, now seen at doses as low as 1.5 dpa. The directionality of loop strings was quite well defined, with projected directions mostly parallel to <110>.

[14] Raft: A planar cluster of small dislocation loops.

At 750°C, the loop number density in UHP-W irradiated to a dose of 1.5 dpa was strikingly lower than at the other two irradiation temperatures, along with a distinct increase in loop size. The damage microstructure seemed populated with rafts of loops as well as individual loops.

In all of the irradiated UHP-W specimens, evidence of the coexistence of ½<111> and <100> loops was found (fractions given in Fig 3.25 a). This observation is explicitly illustrated in the UHP-W specimen irradiated at 750°C (Fig 3.3). Several examples of loops are circled, in red for ½<111> and yellow for <100>. Dashed circles correspond to contrast extinction described by the invisibility criterion **g**.**b** = 0.

Quantitative analysis of the overall loop size distributions in UHP-W irradiated at various conditions were made from pairs of weak-beam dark-field images of the same areas of interest (360 nm by 360 nm) taken in **g** = 200 and **g** = 020. Typically 4-8 micrographs were included in the analysis. The highlights of results are summarized as follows. The fractions of loops of size ≥ 4 nm at 300°C were ~21%, ~23% and ~25%, respectively for 0.5, 1.5 and 37.5 dpa; at 500°C they were ~27% for 0.5 dpa and ~ 30-40% for 1.5 and 4.5 dpa; at 750°C (1.5 dpa) this fraction increased to ~46% (see Fig 3.21). It seems therefore that irradiation temperature has a larger influence on loop size than dose (the extreme examples being UHP-W irradiated at 300°C / 37.5 dpa and 750°C / 1.5 dpa).

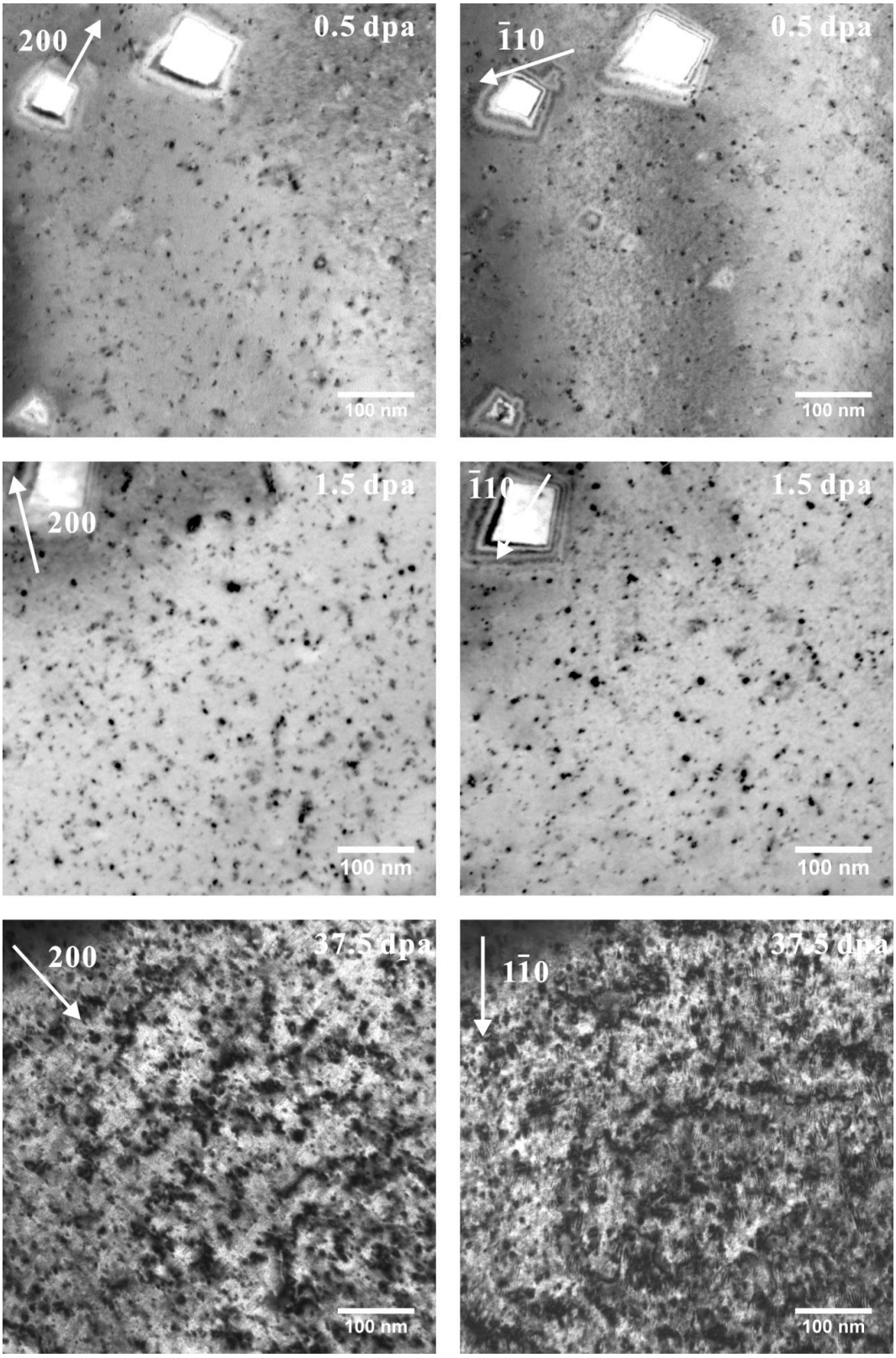


Fig 3.1 UHP-W irradiated with 2 MeV W^+ ions at 300°C at doses of 0.5, 1.5 and 37.5 dpa.

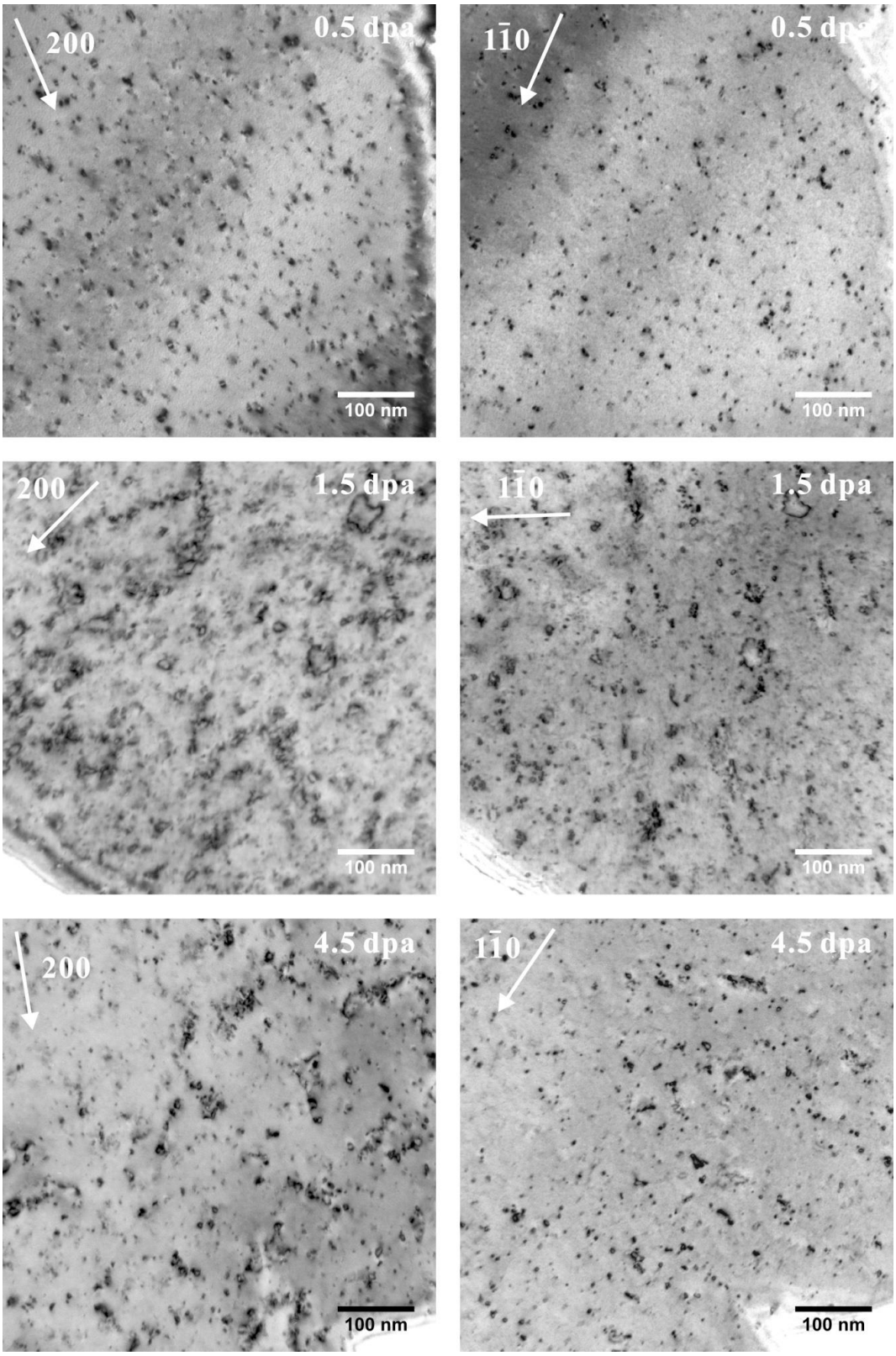


Fig 3.2 UHP-W irradiated with 2 MeV W^+ ions at 500°C at doses of 0.5, 1.5 and 4.5 dpa.

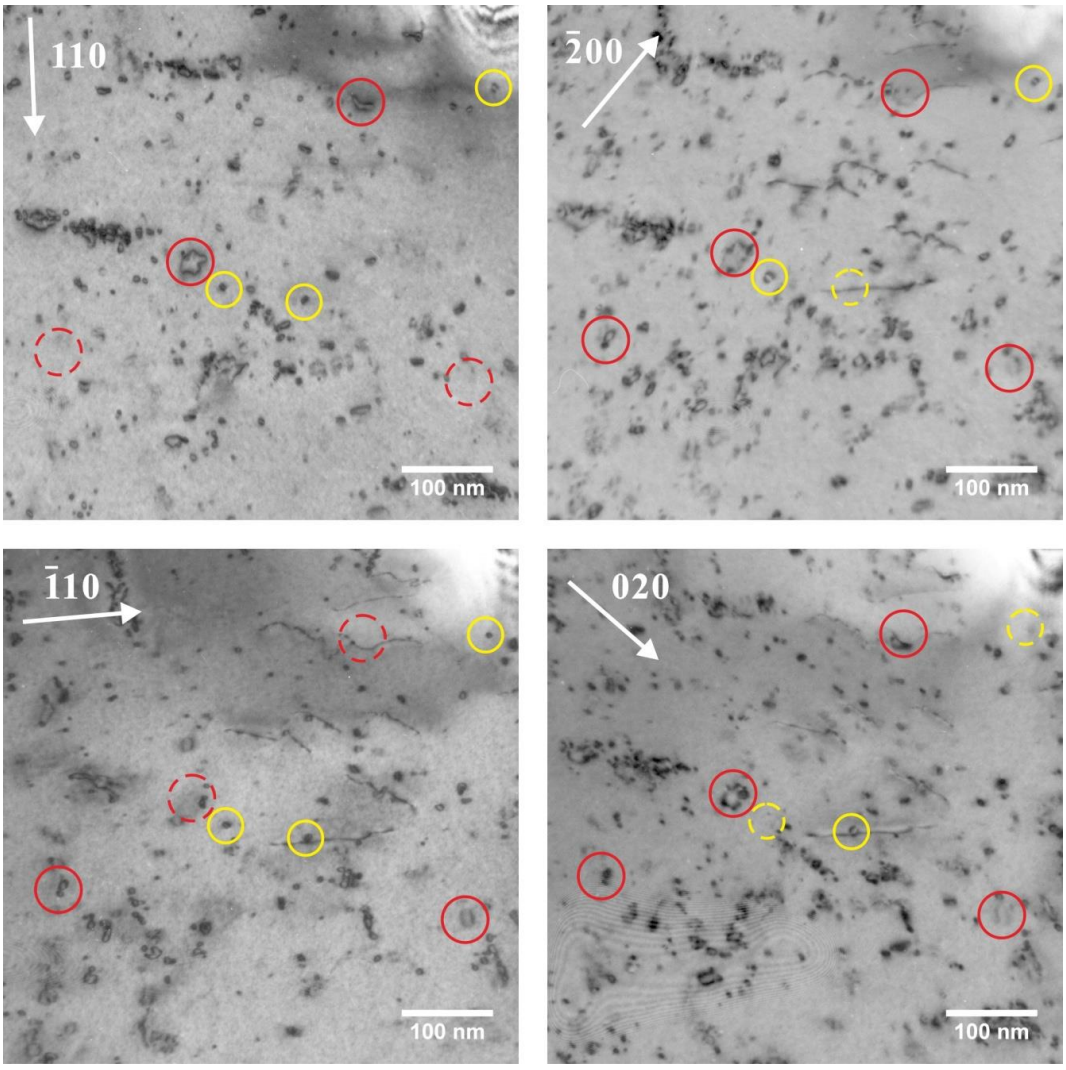


Fig 3.3 UHP-W irradiated with 1.9 MeV W^+ ions at 750°C at a dose of 1.5 dpa. Circles illustrate the coexistence of ½<111> (red) and <100> (yellow) dislocation loops in the material.

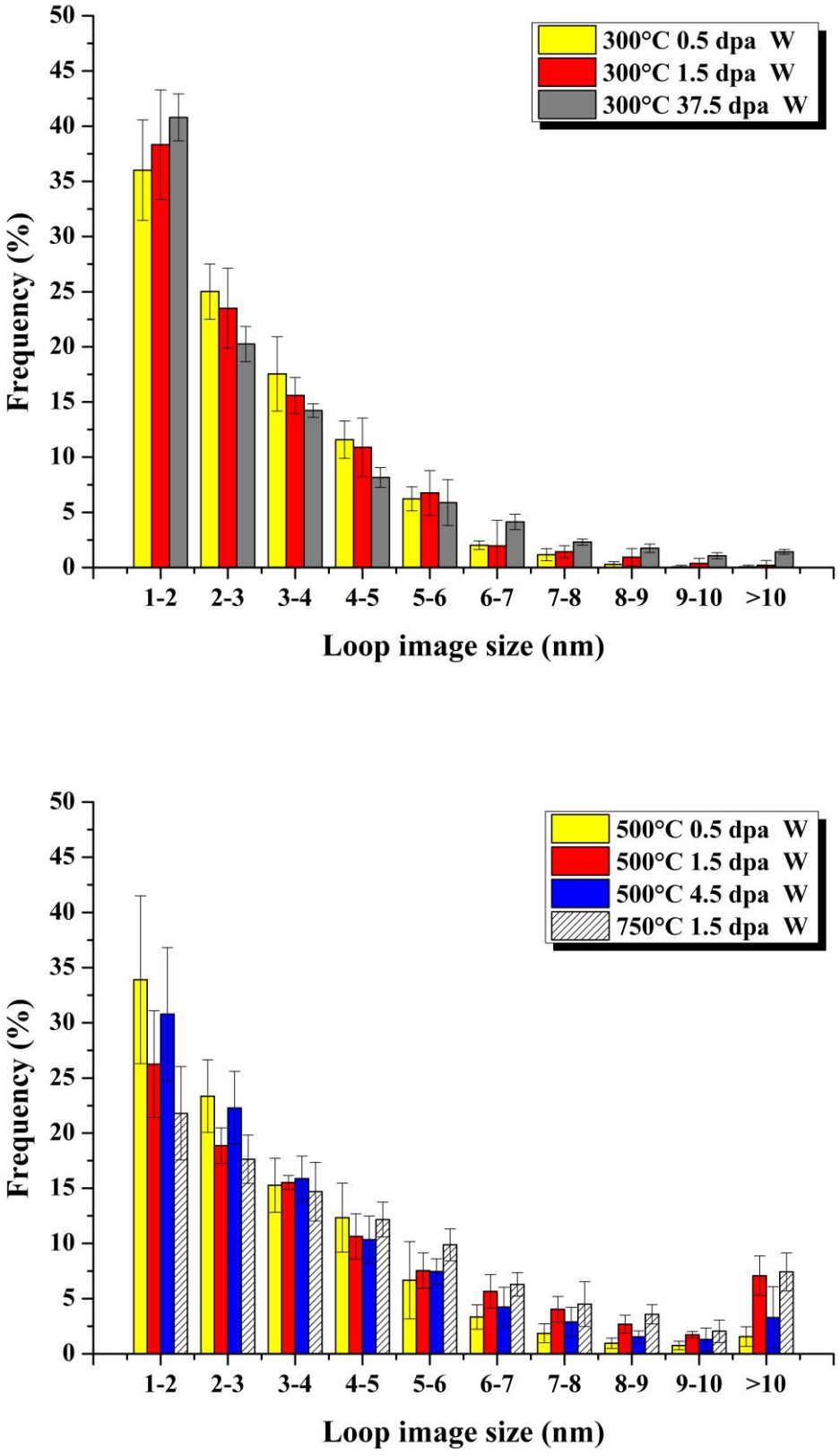


Fig 3.4 Overall loop size distributions in 2 MeV (1.9 MeV) W^+ ion irradiated UHP-W specimens in **z** = [001] orientation.

3.2.2. (300, 500°C) / (0.5, 1.5, 4.5 dpa) irradiated CG-W

The general features of damage microstructures in CG-W were similar to the trends found in UHP-W (Fig 3.5 and 3.6). At constant dose, an increase in irradiation temperature from 300°C to 500°C led to a reduction in loop number density, but favoured loop growth. At constant irradiation temperature, both loop number densities and loop image sizes increased with dose (0.5 dpa to 4.5 dpa). Loop strings and rafts were observed at doses of 1.5 dpa and beyond, at both 300°C and 500°C. The coexistence of ½<111> and <100> loops was also found in the irradiated CG-W specimens (fractions given in Fig 3.24 b). The Burgers vector analysis of these loops on the sample irradiated at 500°C, at a dose of 0.5 dpa in Fig 3.7 is demonstrated.

Detailed analyses of the overall loop size distributions in irradiated CG-W specimens are presented in Fig 3.8. The plots for the 300°C irradiations exhibit large error bars and it seems difficult to draw definite conclusions on the influence of dose. The plots do however gave an estimate of the fraction of loops with diameters larger than 4 nm, which is around 24-30% at both doses. The plots for the 500°C irradiations clearly indicate two trends: 1) Loop size distributions shift to larger sizes with increasing irradiation temperature; 2) Significant loop growth occurred between 0.5 dpa and 1.5 dpa, but little further growth occurred on an increase in dose to 4.5 dpa. The fraction of loops with ≥ 4 nm was ~25% for 0.5 dpa and ~35% for both 1.5 dpa and 4.5 dpa.

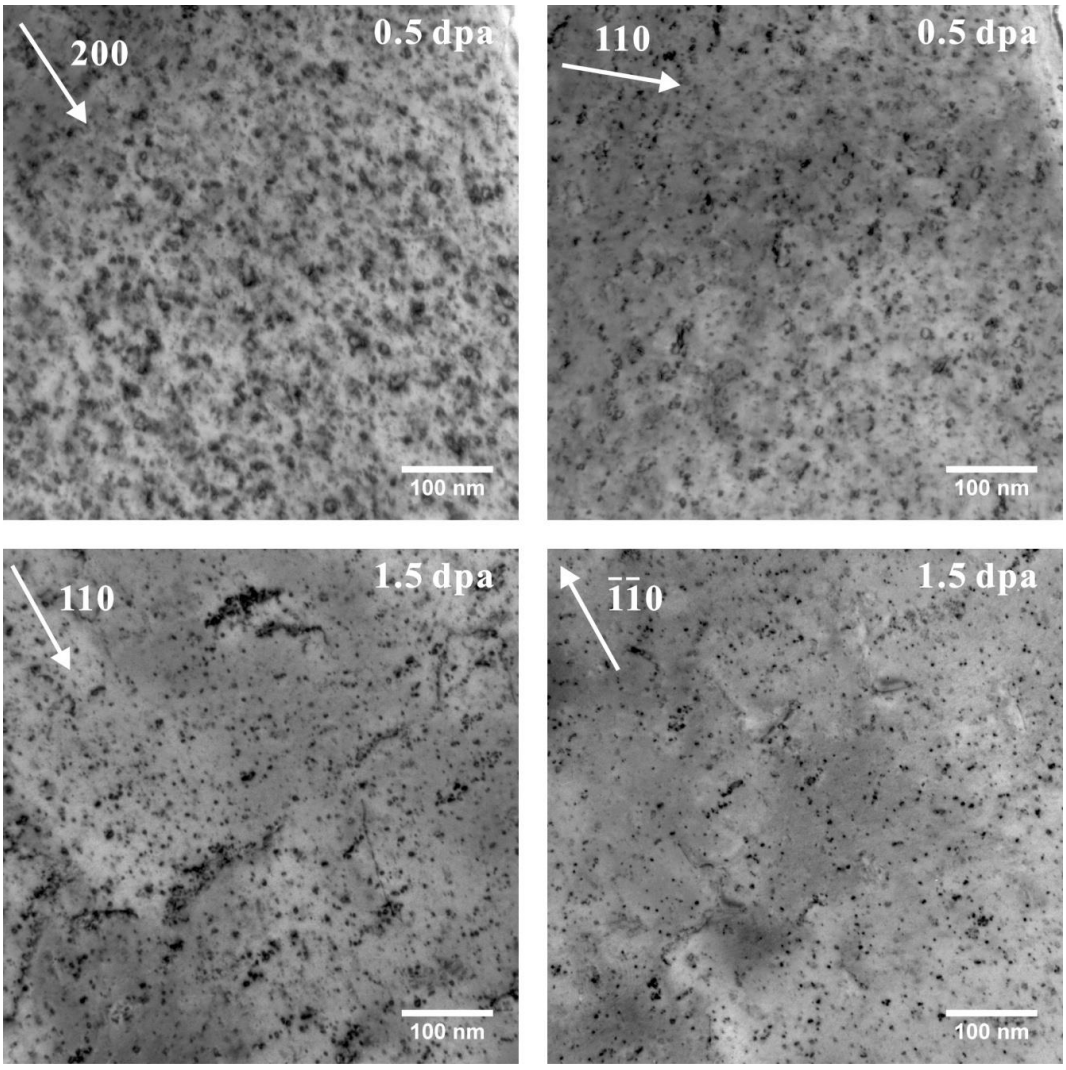


Fig 3.5 CG-W irradiated with 2 MeV W^+ ions at 300°C at doses of 0.5 and 1.5 dpa.

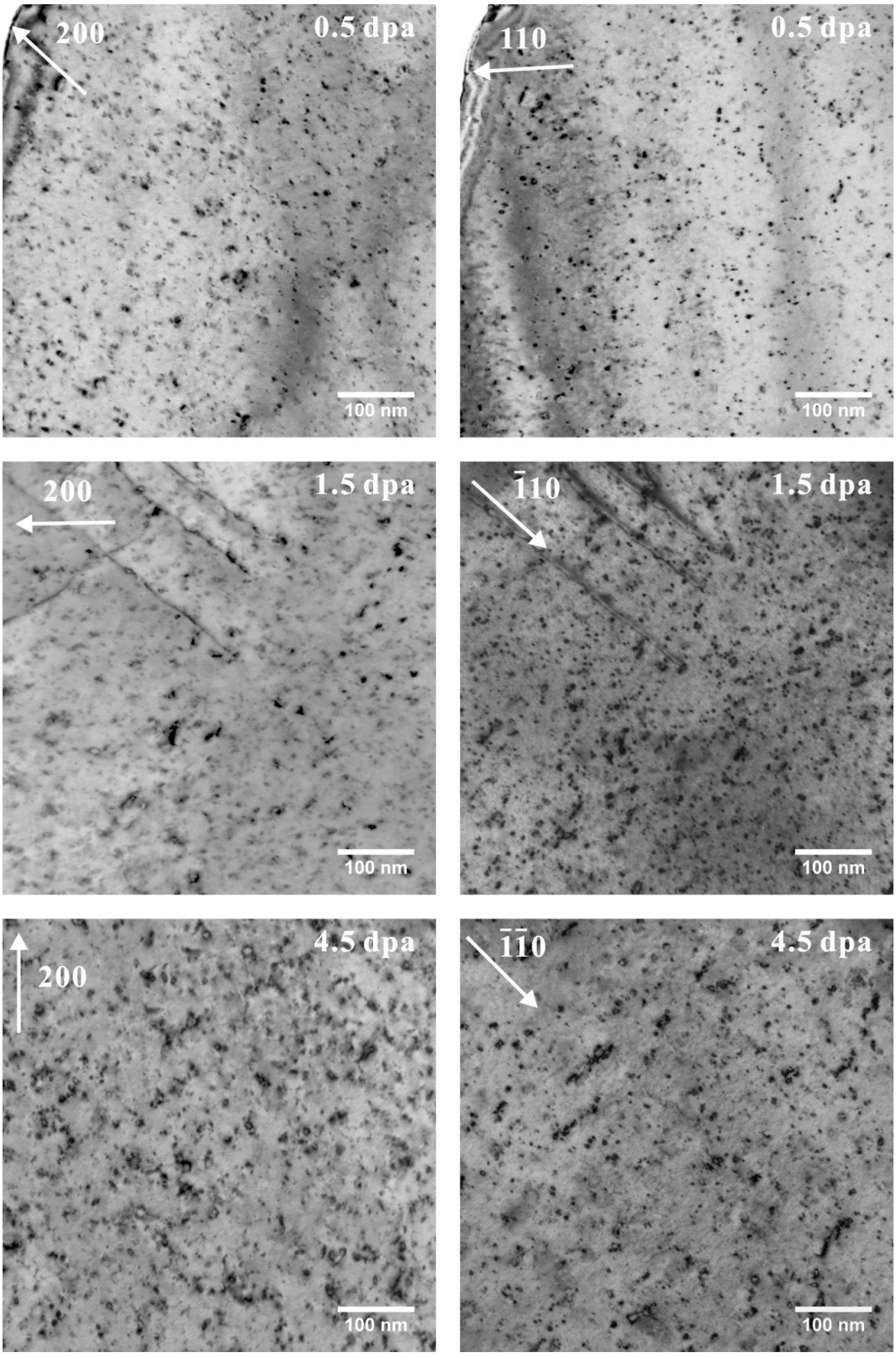


Fig 3.6 CG-W irradiated with 2 MeV W^+ ions at 500°C at doses of 0.5, 1.5 and 4.5 dpa.

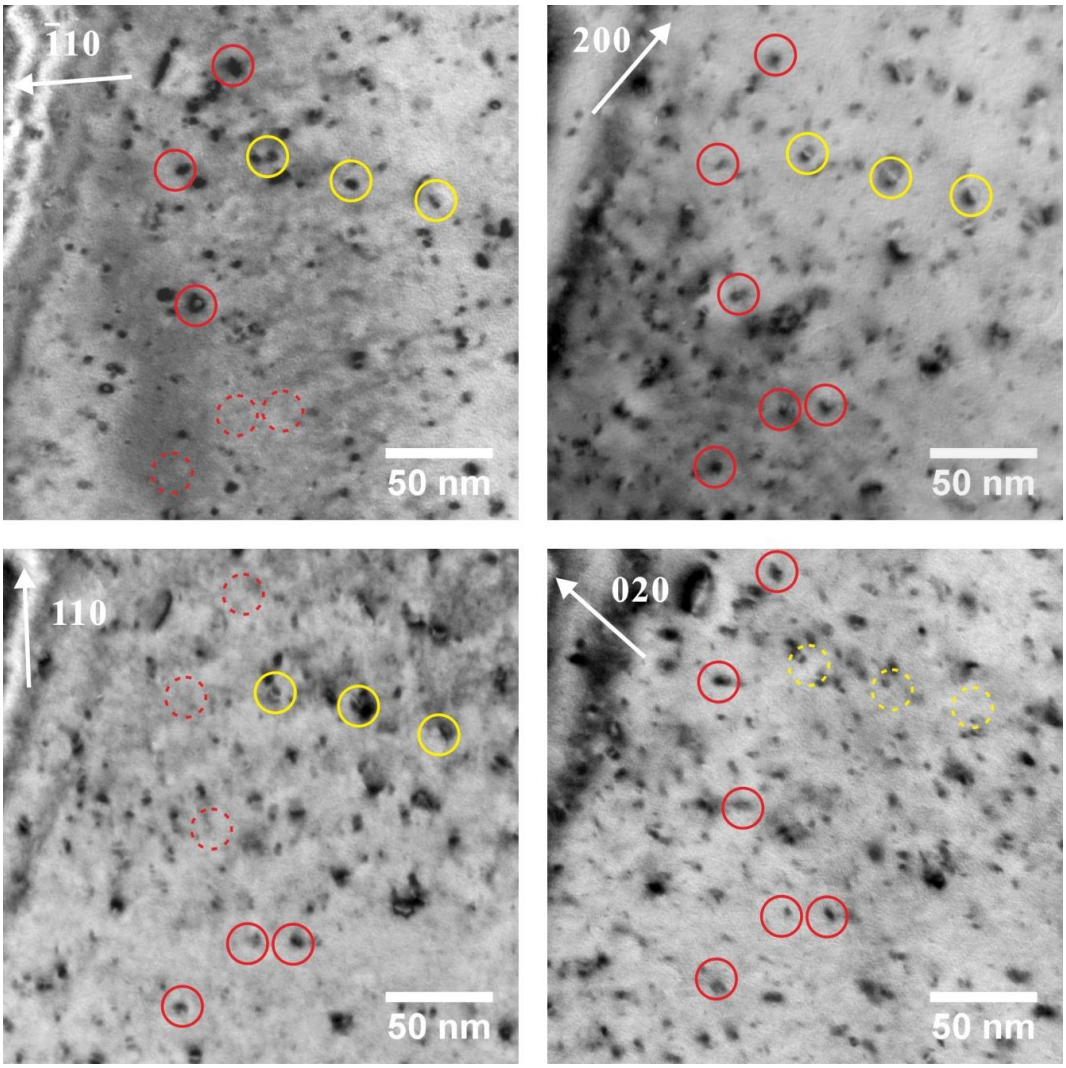


Fig 3.7 CG-W irradiated with 2 MeV W^+ ions at 500°C at a dose of 0.5 dpa. Circles illustrate the coexistence of ½<111> (red) and <100> (yellow) dislocation loops in the material.

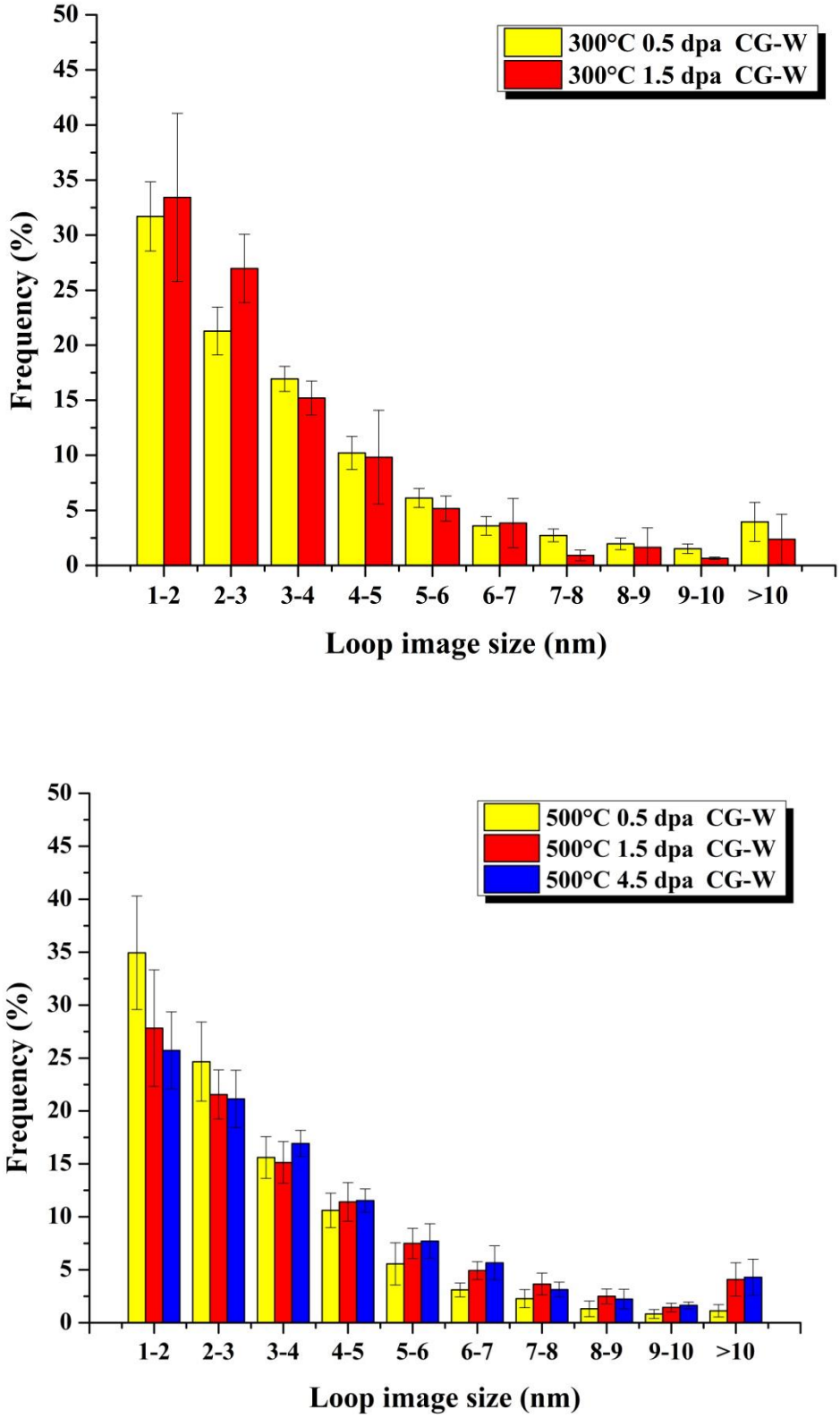


Fig 3.8 Overall loop size distributions in 2 MeV W^+ ion irradiated CG-W in **z** = [001].

3.2.3. (300, 500°C) / (0.5, 1.5, 4.5 dpa) irradiated W-5Re

Micrographs of damage microstructures in irradiated W-5Re are presented in Figs 3.9 - 3.10. At 300°C, dislocation loops increased significantly in number and size between 0.5 dpa and 1.5 dpa. At 500°C, the loop number density exhibited signs of saturation with an increase of dose from 0.5 to 4.5 dpa. Increases in loop size did not become pronounced until 4.5 dpa. No clear signs of string or rafts were found in any of the irradiated W-5Re specimens. Both ½<111> and <100> loops were present in the damage microstructure (fractions are given in Fig 3.24 c). The observation with a case study on W-5Re irradiated at 500°C up to a dose of 0.5 dpa is illustrated (Fig 3.11).

The overall loop size distributions in irradiated W-5Re are presented in Fig 3.12. At 300°C, the fractions of loops ≥ 4 nm were ~9% and ~20% for 0.5 and 1.5 dpa irradiations respectively. At 500°C, the fractions of loops ≥ 4 nm were ~17%, ~22% and ~33% for 0.5 dpa, 1.5 dpa and 4.5 dpa irradiations respectively (see also Fig 3.21). The effect of increasing dose on loop sizes was more prominent at 300°C. To achieve an equivalent increase in the fraction of loops larger than 4 nm, one needs to increase the dose by a factor of 3 at 300°C but by a factor of 9 at 500°C. The influence of irradiation temperature seemed discernible only at low doses (e.g. 0.5 dpa). At around 1.5 dpa, little difference was found between W-5Re specimens irradiated at 300°C and 500°C, regarding the fraction of ≥ 4 nm loops. In these experiments therefore dose seems to have a relatively larger influence on dislocation loop size than irradiation temperature. Note that this observation is different from that of UHP-W, where loop size was influenced more by irradiation temperature than dose.

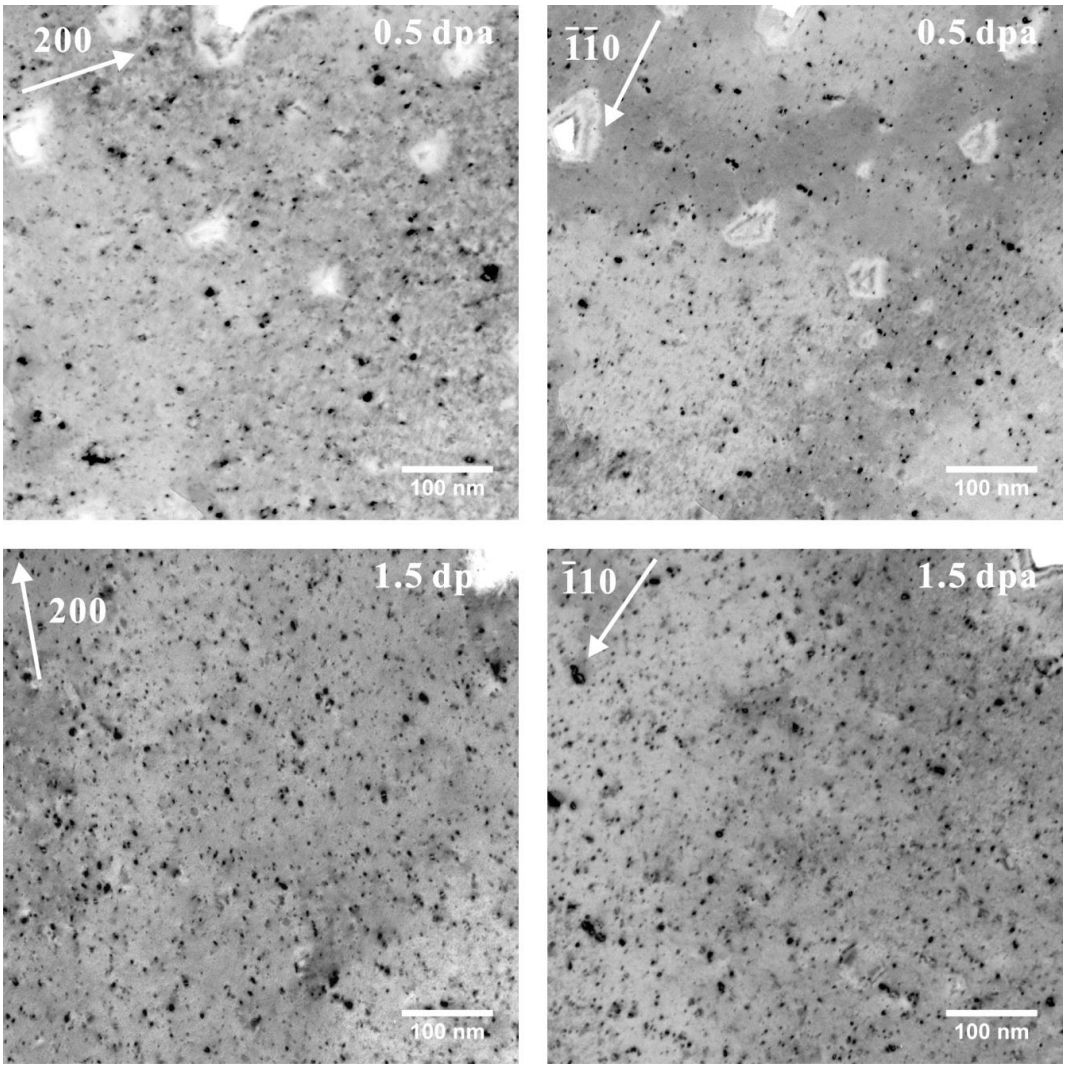


Fig 3.9 W-5Re irradiated with 2 MeV W^+ ions at 300°C at doses of 0.5 and 1.5 dpa.

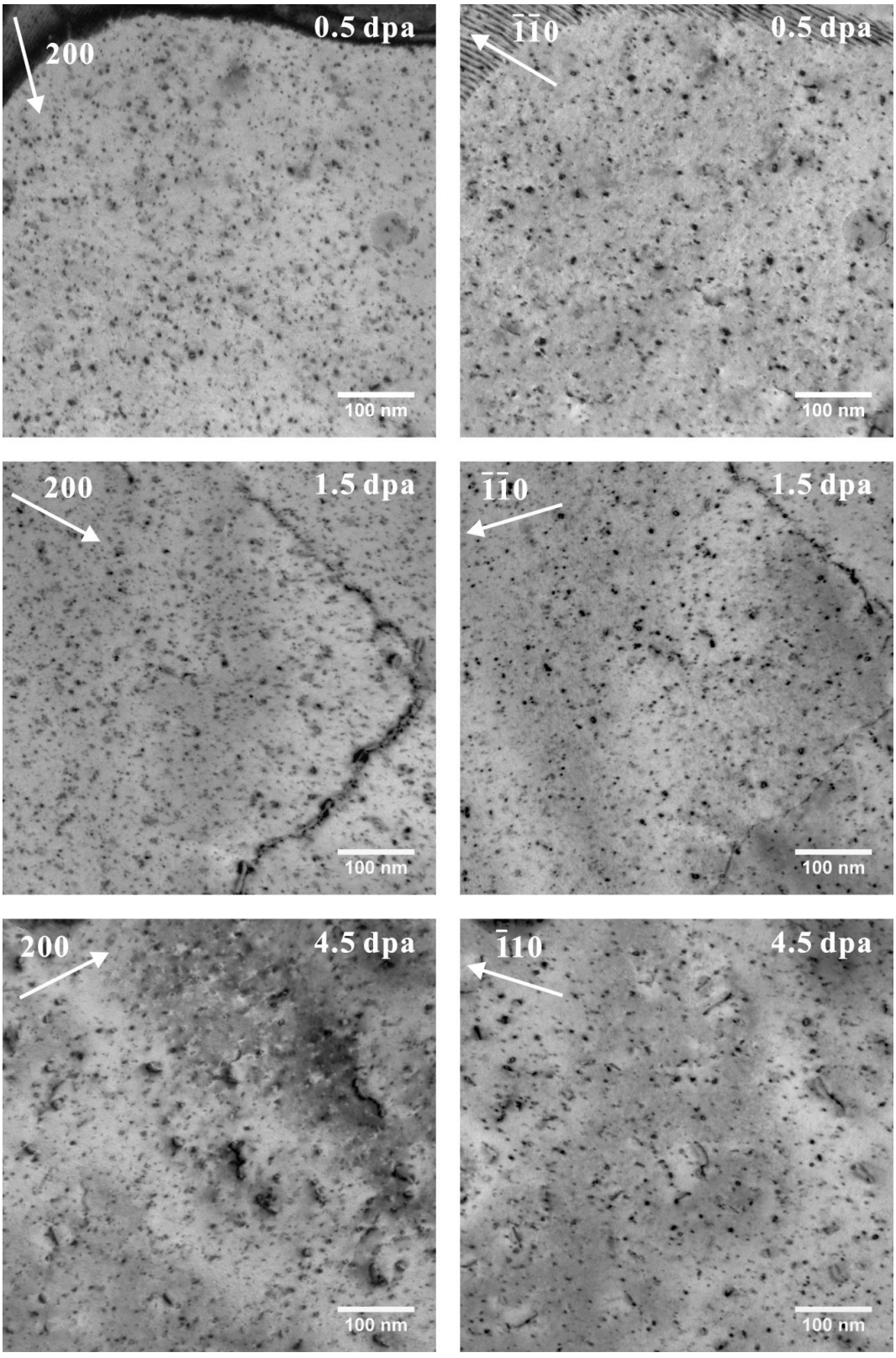


Fig 3.10 W-5Re irradiated with 2 MeV W^+ ions at 500°C at doses of 0.5, 1.5 and 4.5 dpa.

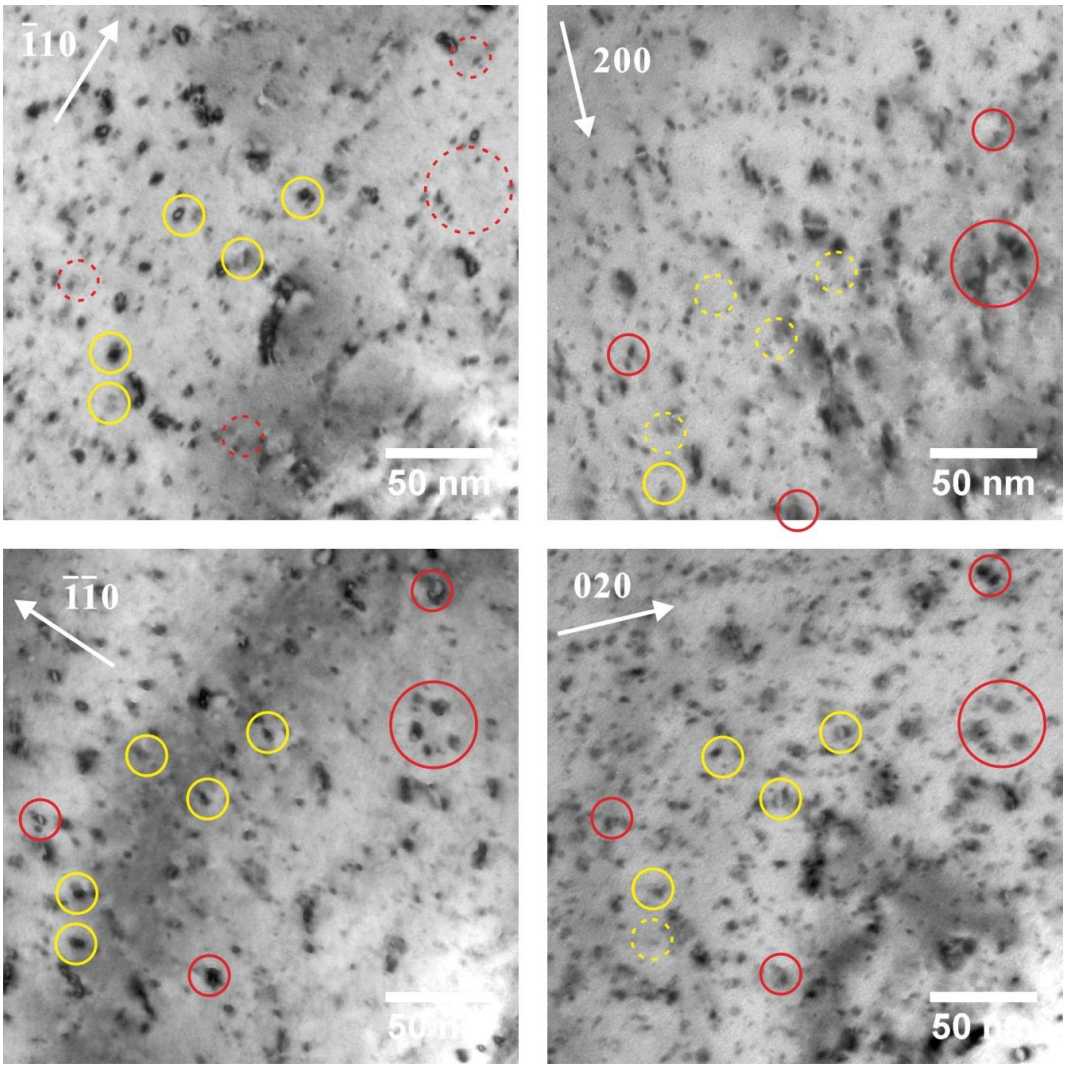


Fig 3.11 W-5Re irradiated with 2 MeV W^+ ions at 500°C at a dose of 0.5 dpa. Circles illustrate the coexistence of ½<111> (red) and <100> (yellow) dislocation loops in the material.

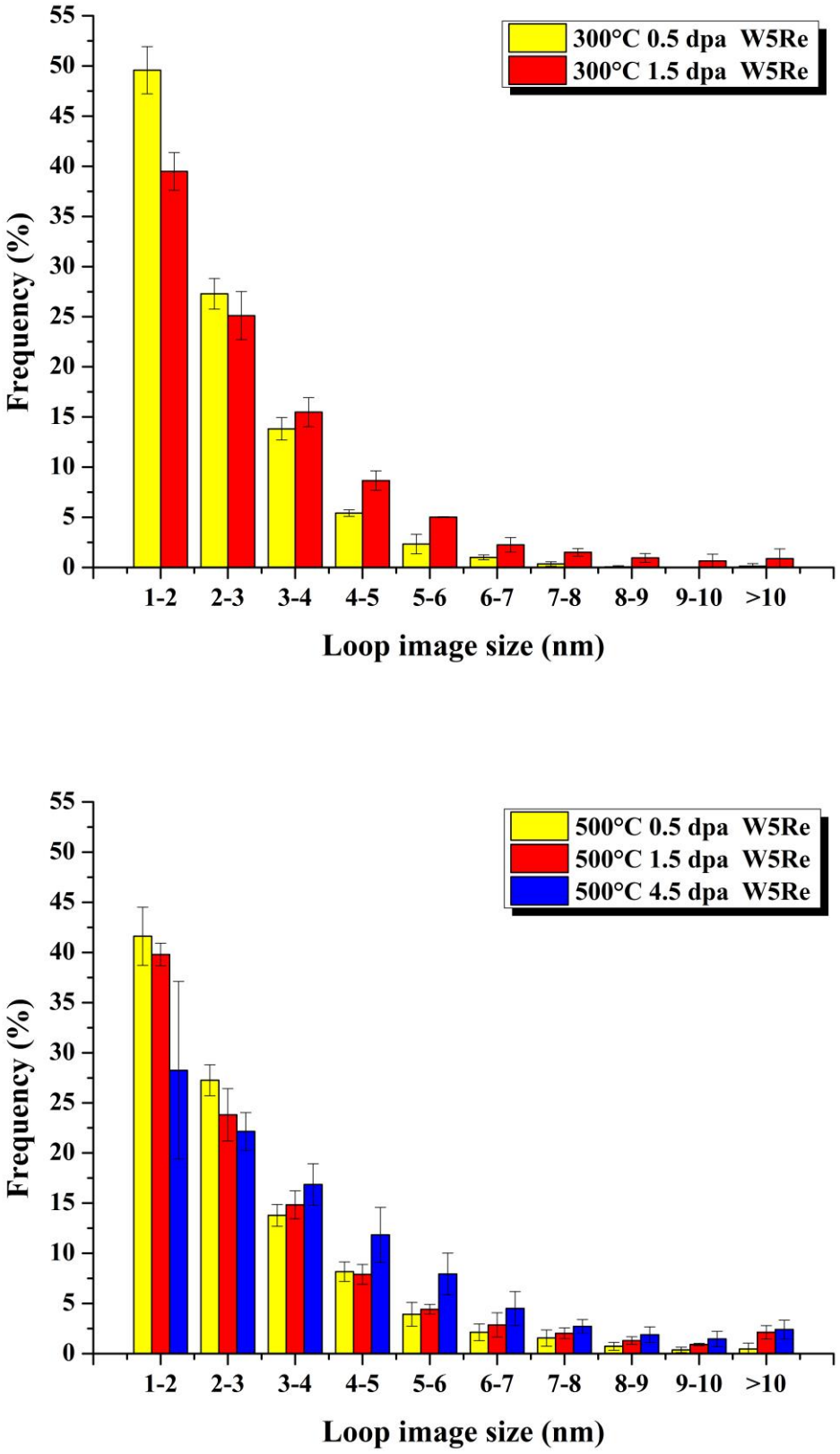


Fig 3.12 Overall loop size distributions in 2 MeV W^+ ion irradiated W-5Re in **z** = [001].

3.2.4. (300, 500°C) / (0.5, 1.5, 4.5 dpa) irradiated W-(1, 5)Ta

The influence of Ta concentration was investigated in addition to irradiation dose and temperature. Figs 3.13-3.16 present the damage microstructures of W-(1,5)Ta. In W-1Ta, an increase in dose and temperature favoured loop growth. The damage microstructures at 300°C in W-1Ta featured randomly distributed loops. Raising the temperature to 500°C led to the accumulation of small loops, forming strings and rafts. However, a dose increase at 500°C did not produce significant changes in the population of loop strings and rafts. The projected directions of loop strings observed were mostly in parallel to <110>. In W-5Ta, the higher concentration of Ta has resulted in a higher loop number density and a distinct increase of 1-2 nm loops, compared with W-1Ta irradiated under the same conditions. Evidence of loops forming strings and rafts has also been found, displaying a similar manner of directionality as those found in W-1Ta. Both ½<111> and <100> loops were present in the irradiated W-1Ta and W-5Ta (fractions given in Fig 3.24 d). An example is given in Fig 3.17, demonstrating the presence of loops of the two types in W-5Ta, irradiated at 300°C, to a dose of 0.5 dpa. Lastly, Fig 3.18 summarizes the overall loop size distributions in irradiated W-Ta alloys. The influence of dose, temperature and the alloying content on the fraction of loops larger than 4 nm is as follows (see also Fig 3.21). In W-1Ta, the fractions are ~21%, ~33% and ~40% for 300°C/1.5 dpa, 500°C/1.5 dpa and 500°C/4.5 dpa respectively. In W-5Ta, the fractions are ~20% for both 0.5 dpa and 1.5 dpa at 300°C; ~38% and ~39% for 1.5 dpa and 4.5 dpa at 500°C respectively. It can be concluded that temperature has a greater influence than dose on loop sizes. The effect of increased Ta concentration appeared negligible for ≥ 4 nm loops.

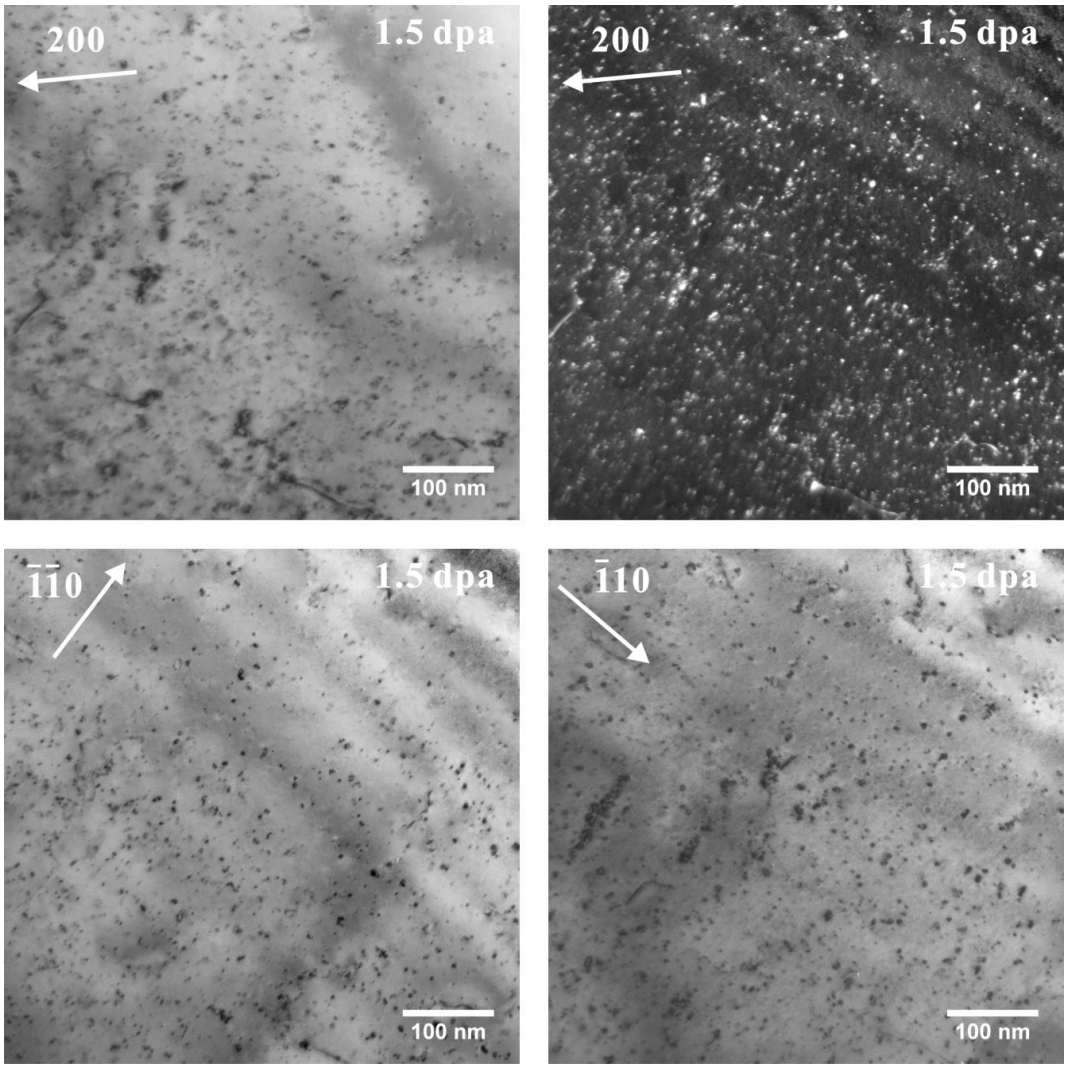


Fig 3.13 W-1Ta irradiated with 2 MeV W^+ ions at 300°C at a dose of 1.5 dpa.

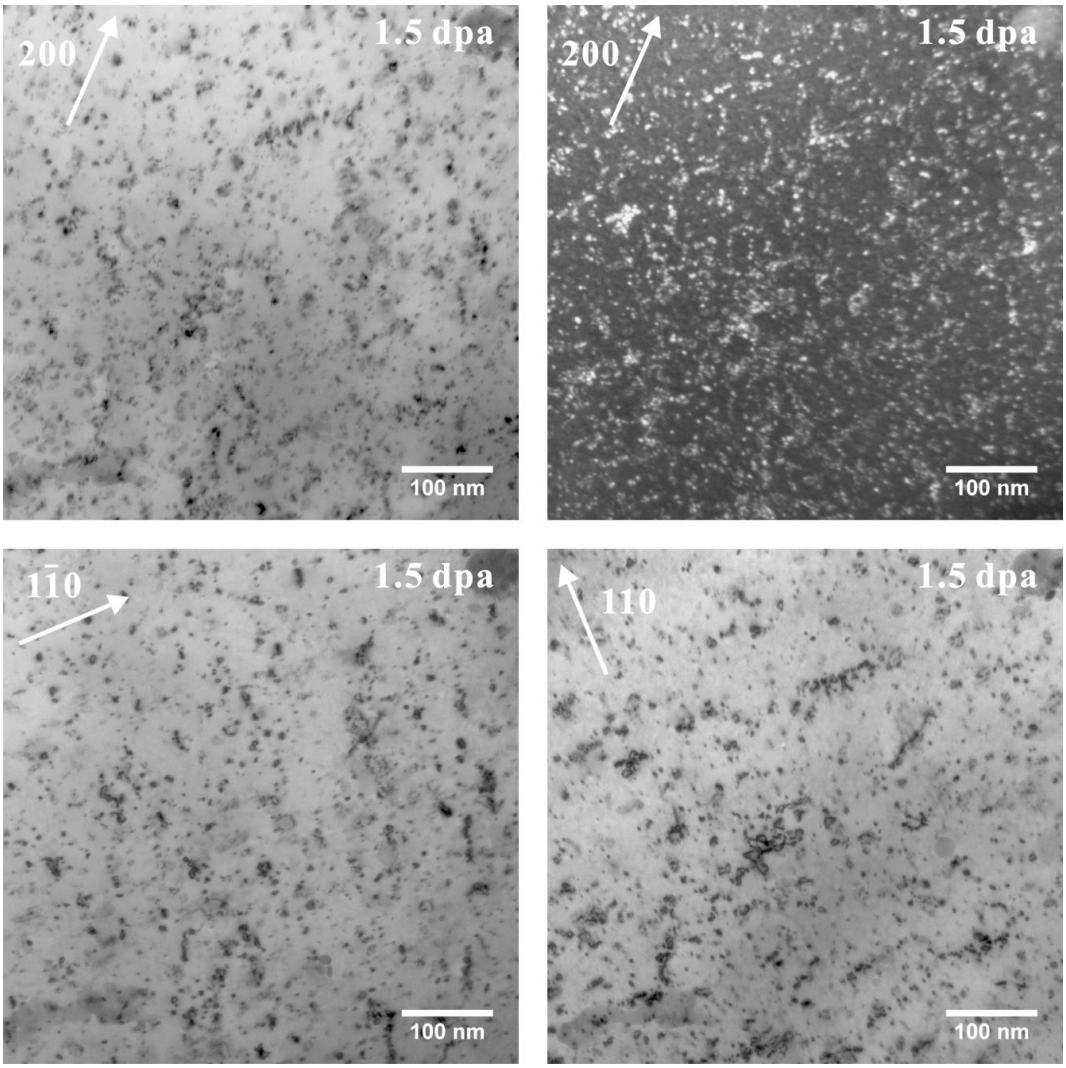


Fig 3.14 a) W-1Ta irradiated with 2 MeV W^{+} ions at 500°C at a dose of 1.5 dpa.

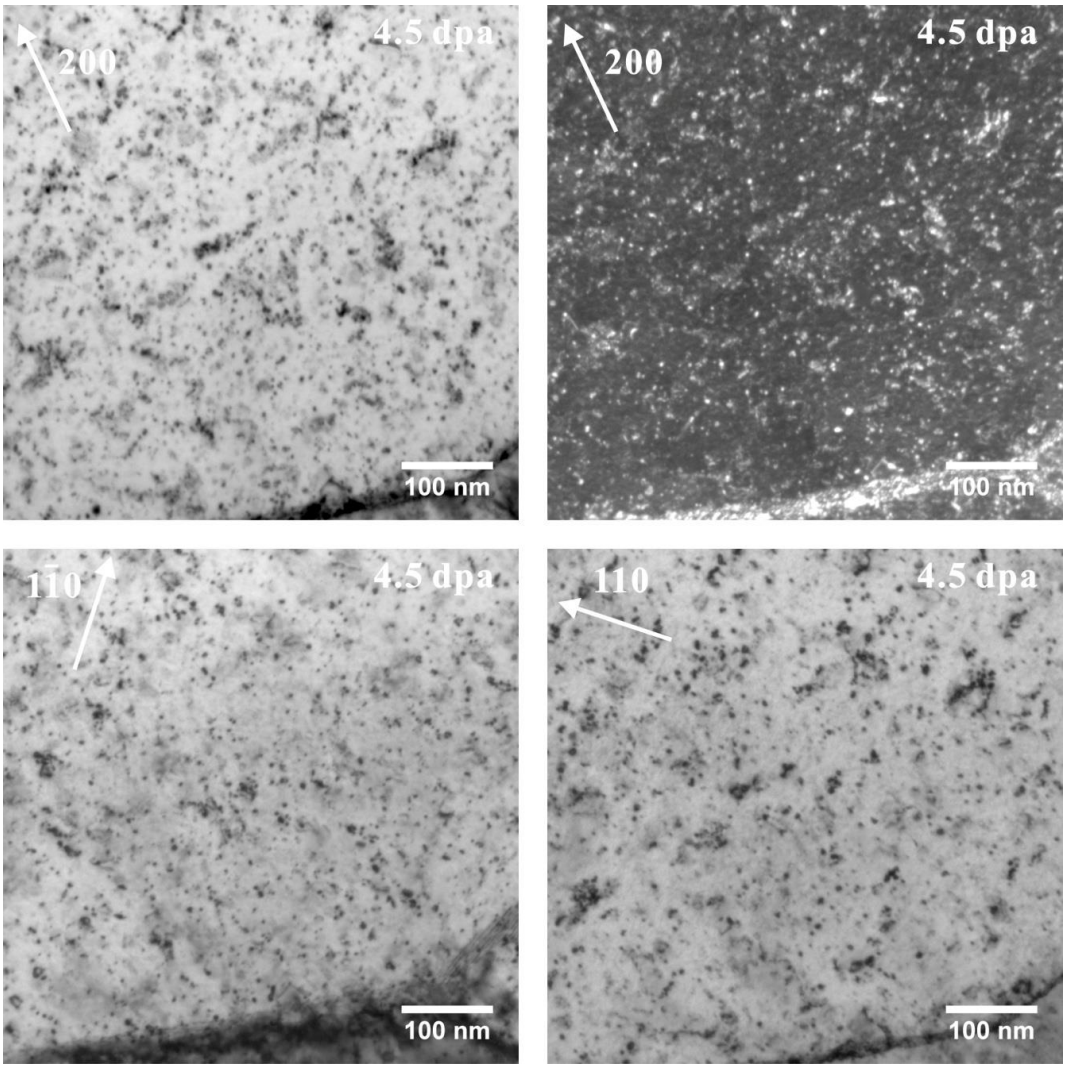


Fig 3.14 b) W-1Ta irradiated with 2 MeV W^+ ions at 500°C at a dose of 4.5 dpa.

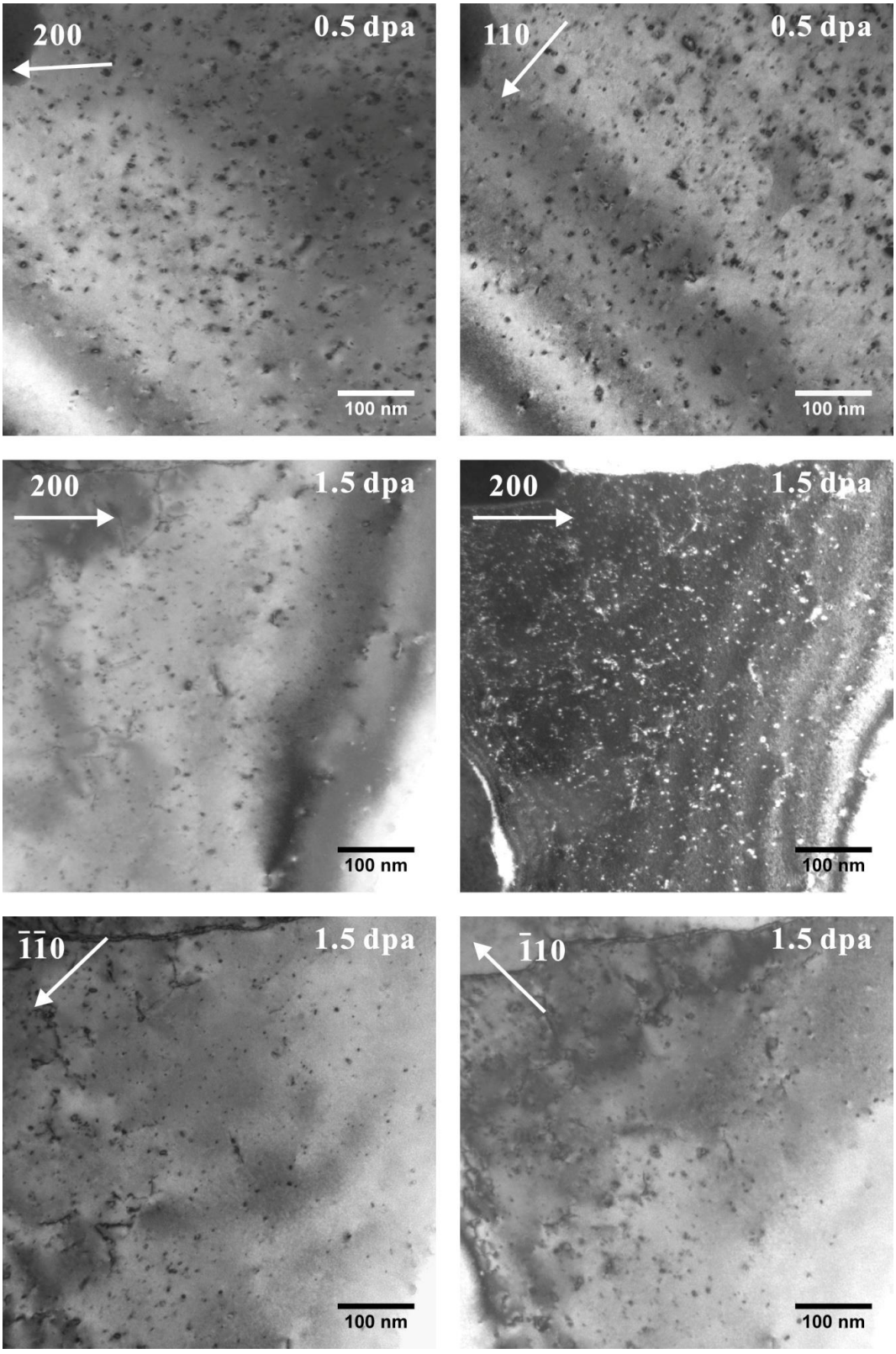


Fig 3.15 W-5Ta irradiated with 2 MeV W^+ ions at 300°C at doses of 0.5 and 1.5 dpa.

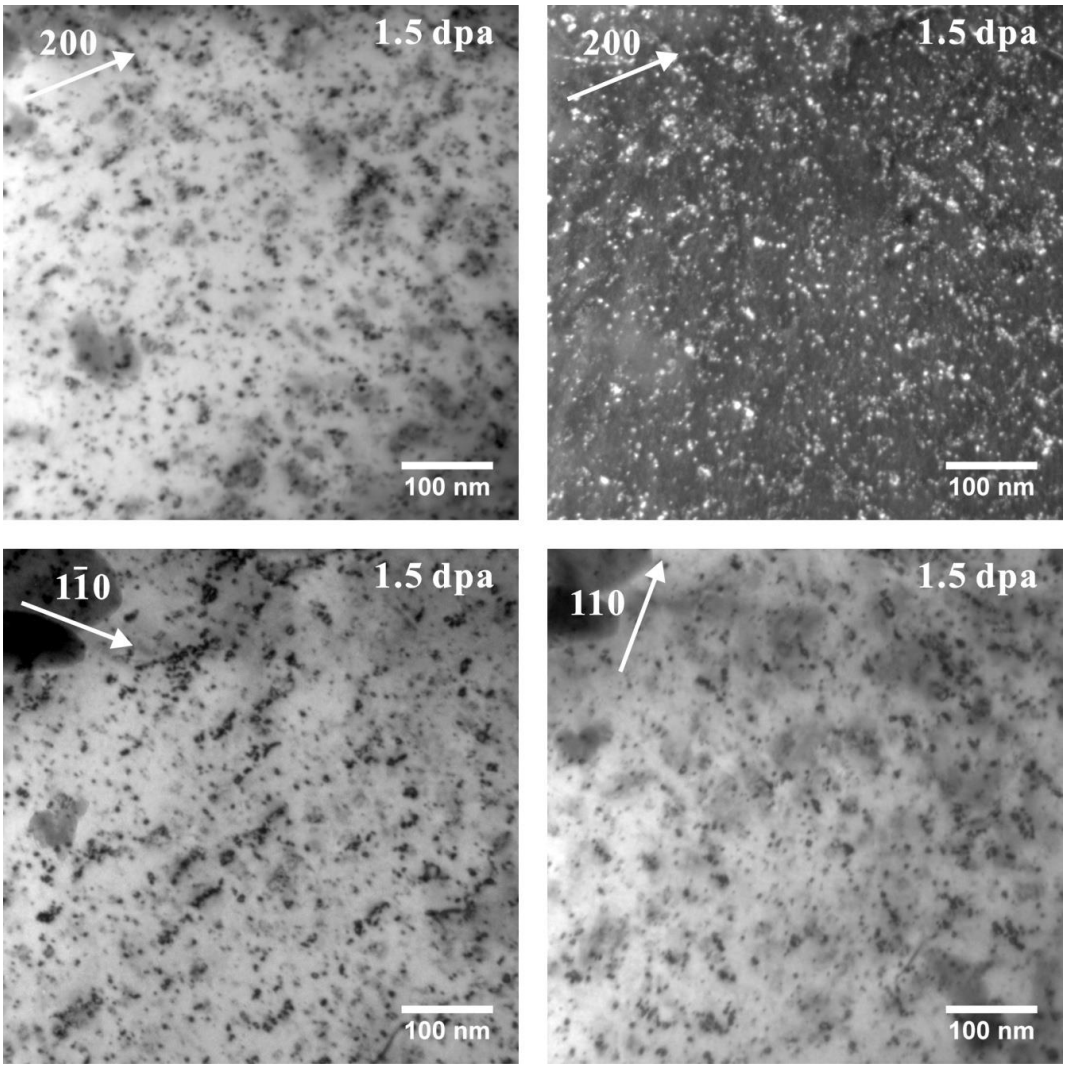


Fig 3.16 a) W-5Ta irradiated with 2 MeV W^+ ions at 500°C at a dose of 1.5 dpa.

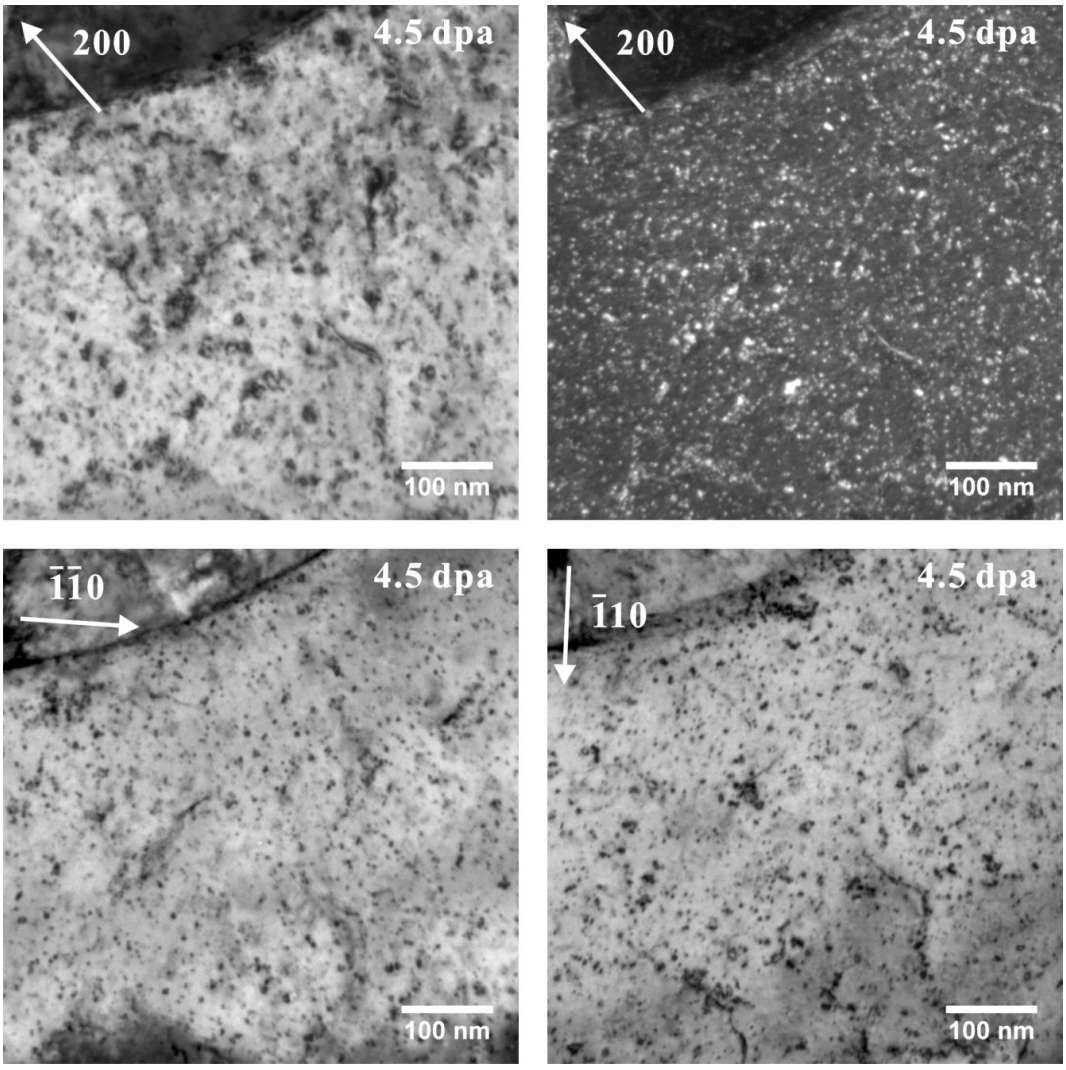


Fig 3.16 b) W-5Ta irradiated with 2 MeV W^+ ions at 500°C at a dose of 4.5 dpa.

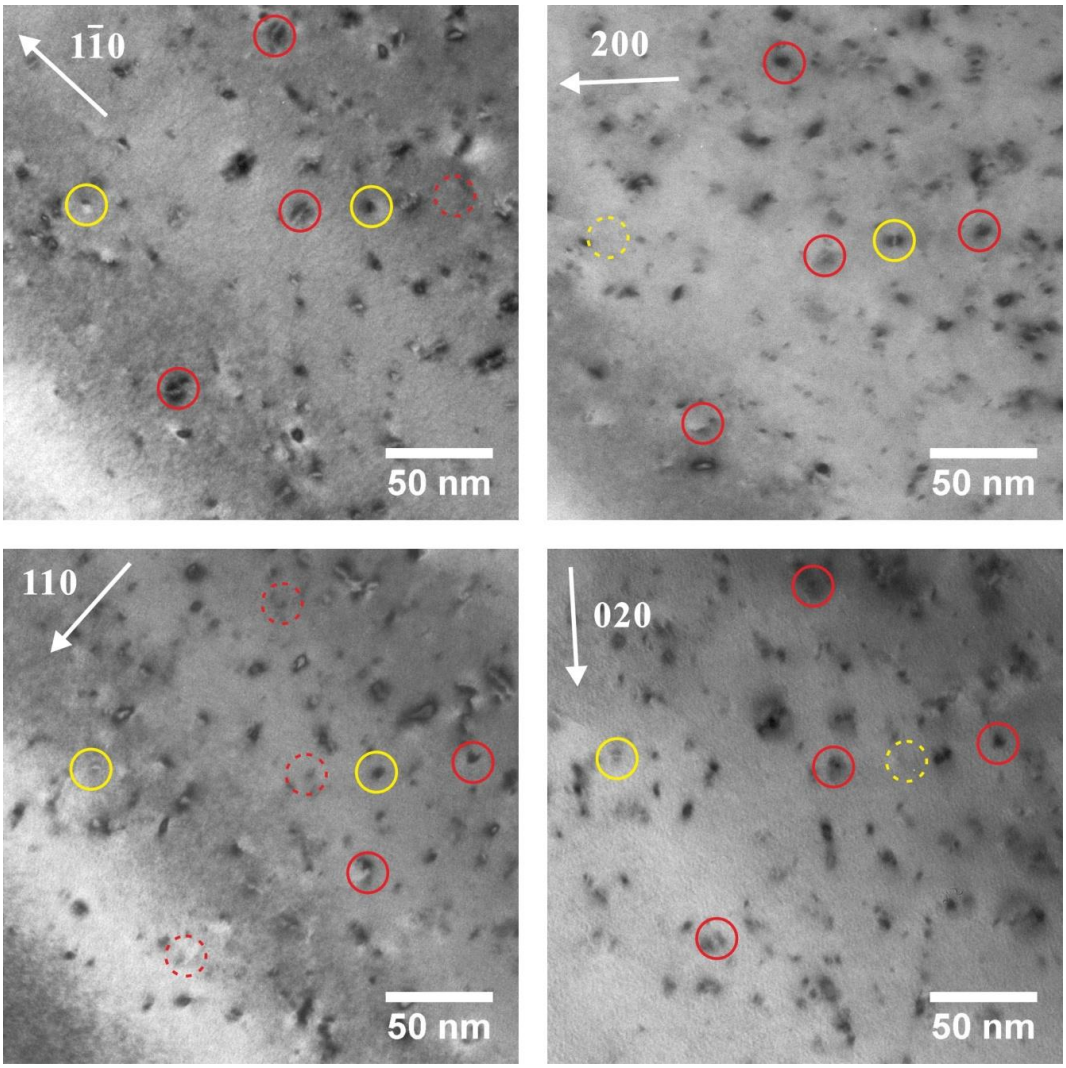


Fig 3.17 W-5Ta irradiated with 2 MeV W^+ ions at 300°C at a dose of 0.5 dpa. Circles illustrate the coexistence of ½<111> (red) and <100> (yellow) dislocation loops in the material.

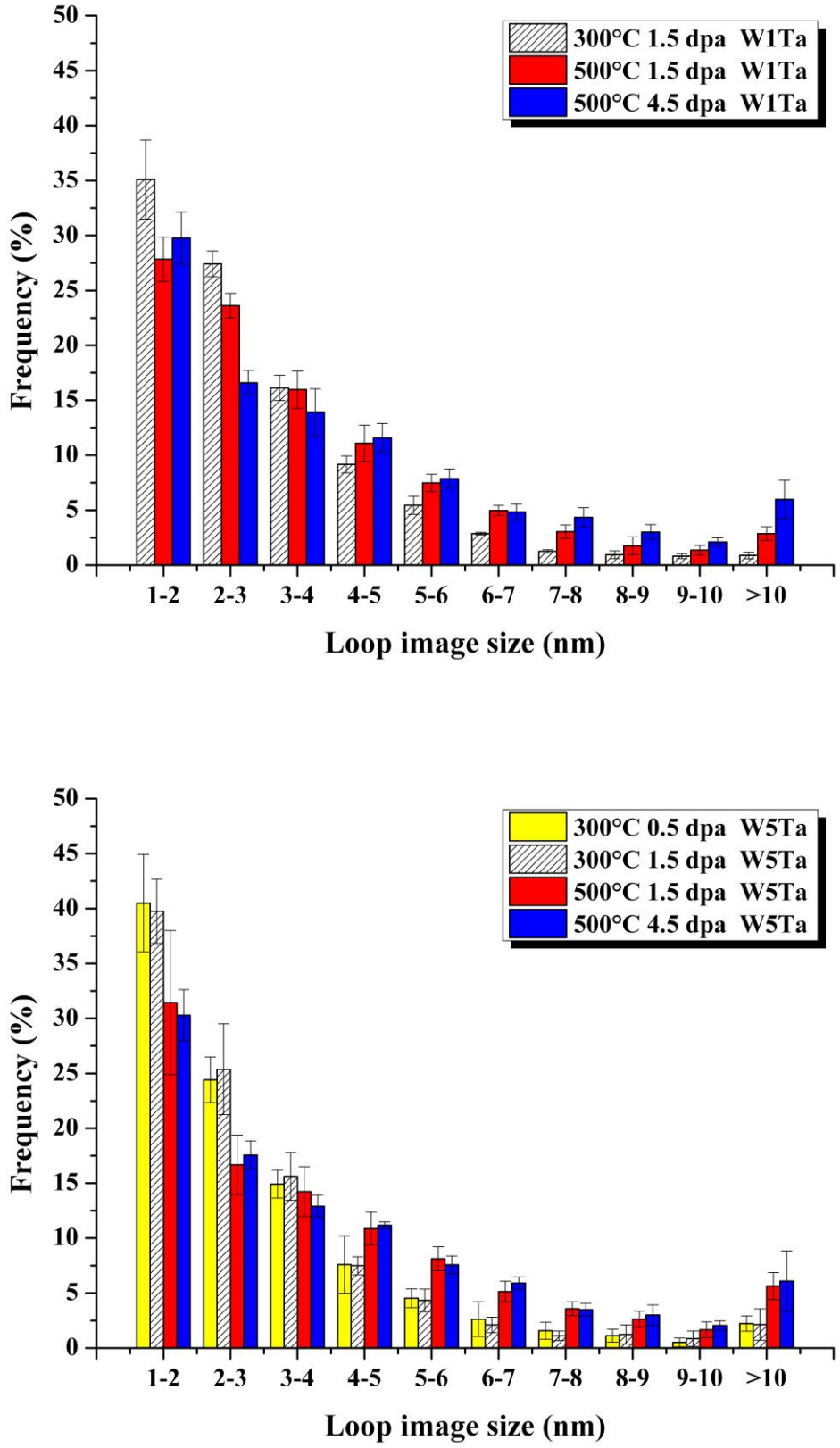


Fig 3.18 Overall loop size distributions in 2 MeV W^+ irradiated W-(1,5)Ta in **z** = [001].

3.2.5. (500°C / 1.5 dpa) irradiated W-5V

The effect of V-alloying in tungsten was briefly examined at the irradiation condition of 500°C and 1.5 dpa. The damage microstructure shown in Fig 3.19 features a much higher loop number density and smaller loop sizes in comparison with UHP-W irradiated at the same condition. In Fig 3.20, the overall loop size distribution in W-5V is plotted along with that of UHP-W, W-5Ta and W-5Re irradiated at the same condition. The fractions of loops with diameters larger than 4 nm are ~39% in UHP-W, ~38% in W-5Ta, ~22% in W-5Re but only ~20% in W-5V.

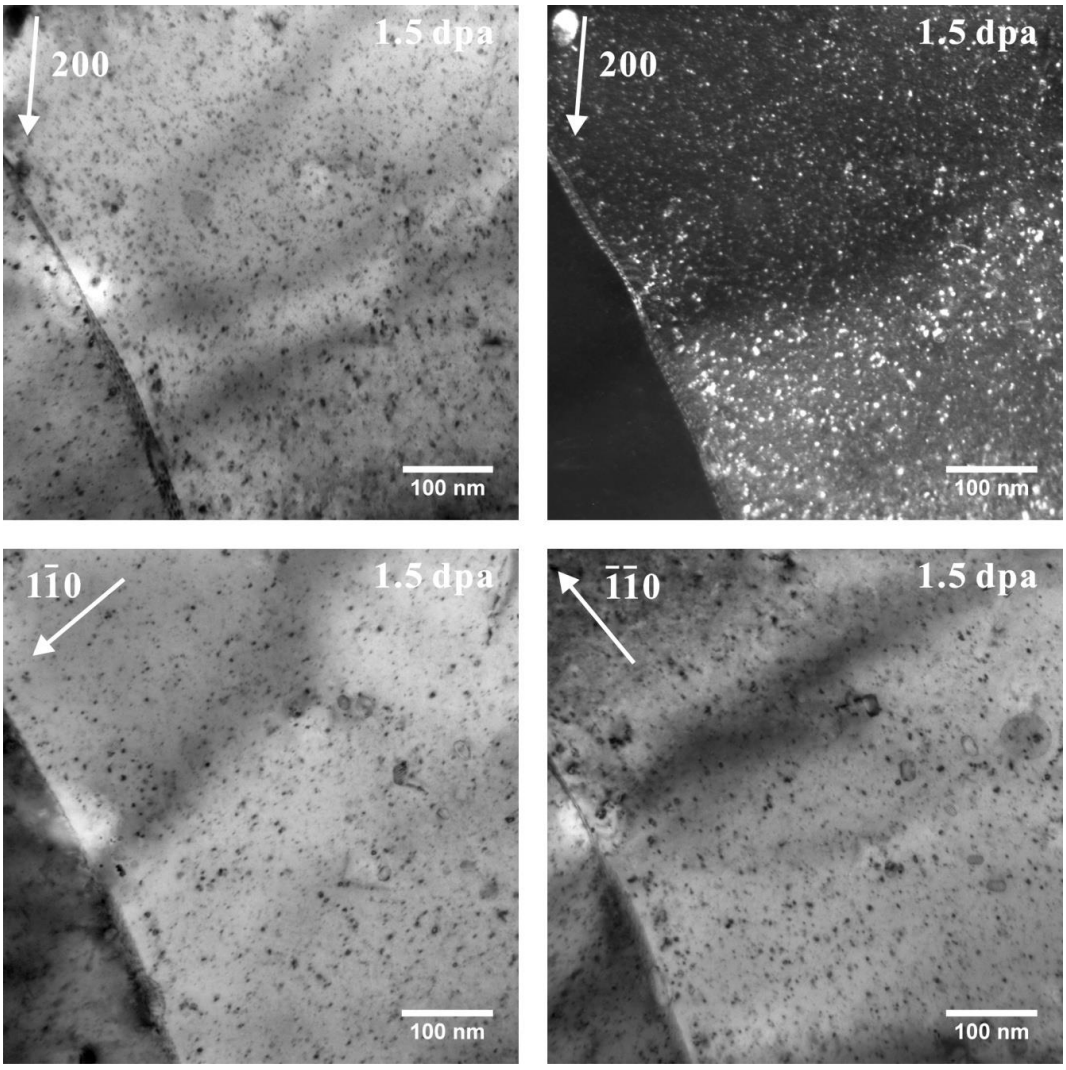


Fig 3.19 W-5V irradiated with 2 MeV W^+ ions at 500°C at a dose of 1.5 dpa.

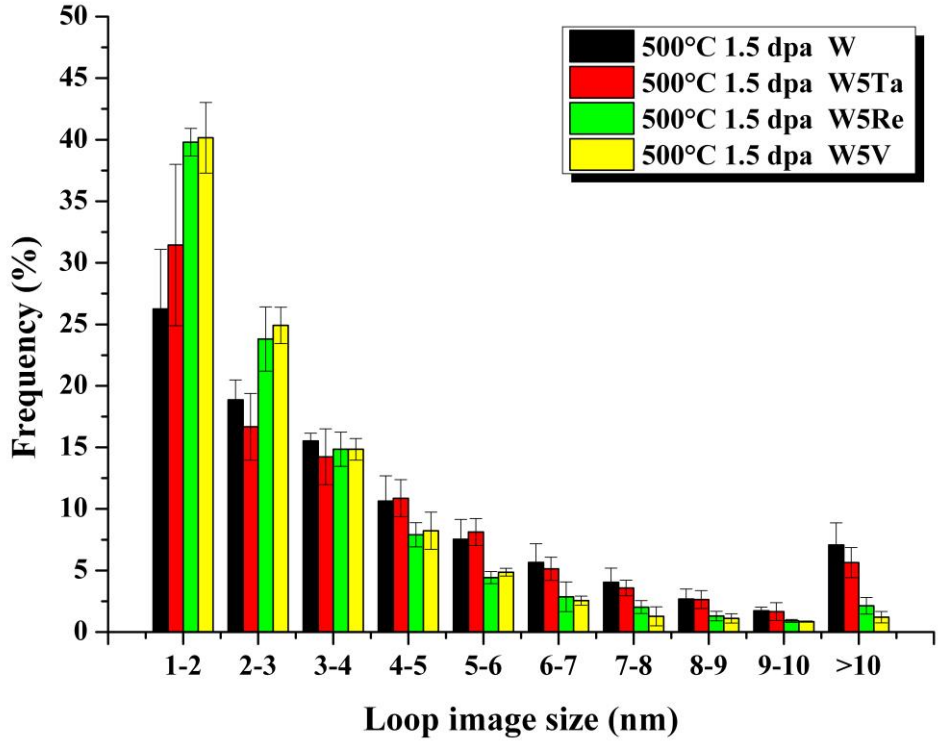


Fig 3.20 Comparison of overall loop size distribution between irradiated (500°C / 1.5 dpa) W-5V and UHP-W/W-5Ta/W-5Re in **z** = [001] orientation.

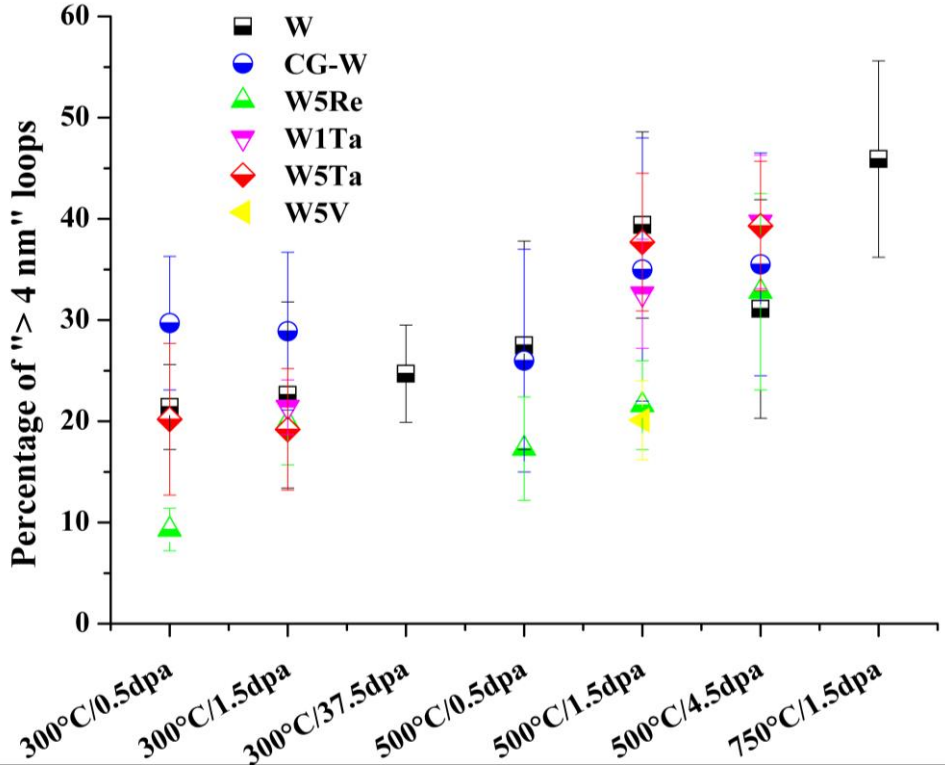


Fig 3.21 A summary of the fractions of loops larger than 4 nm with respect to irradiation conditions and material grades.

3.2.6. Damage microstructures in non z = [001] grains

The grain orientation may also influence the appearance of damage microstructures in tungsten and its alloys. Two case studies are explicitly presented here, one on CG-W and the other on W-5Ta.

In Fig 3.22, the damage microstructure (500°C / 0.5 dpa) in a grain in CG-W with normal **z** = $[\bar{1}13]$ is characterised by short strings made up of ½<111> dislocation loops, as determined by a contrast experiment using the diffraction vectors **g** = $1\bar{2}1$ and $1\bar{1}0$. In fact, the invisibility criterion pins down the variants of the observed ½<111> loops as $\pm$½$[\bar{1}11]$ and $\pm$½$[1\bar{1}1]$ (§ 2.6.3). The strings typically did not go beyond 50 nm in length and were spatially well separated, and surrounded by individual loops of smaller size. In Fig 3.23, damage microstructures are presented from two orientations in W-5Ta specimens irradiated at 300°C. Loops in foils with normal **z** = [111] and **z** = [011] both seemed to align in parallel in preferred directions ([110] in the foil with **z** = [111]; and [100] and $[21\bar{1}]$ in the foil with **z** = [011]), and coalesced into strings up to hundreds of nanometres in length. Comparing the two orientations at 0.5 dpa, loop strings in the foil with **z** = [111] exhibited a shorter length than in the foil with **z** = [011] and almost no connectivity. Some loop strings found in the **z** = [011] foil seemed partially connected. With an increase in dose from 0.5 dpa to 1.5 dpa, the damage microstructure in W-5Ta at the **z** = [011] orientation portrayed a well-developed network of loop strings, due to the intersection of which residing in different orientations. In other words, an increase in irradiation dose promoted an increase in the length and connectivity of loop strings.

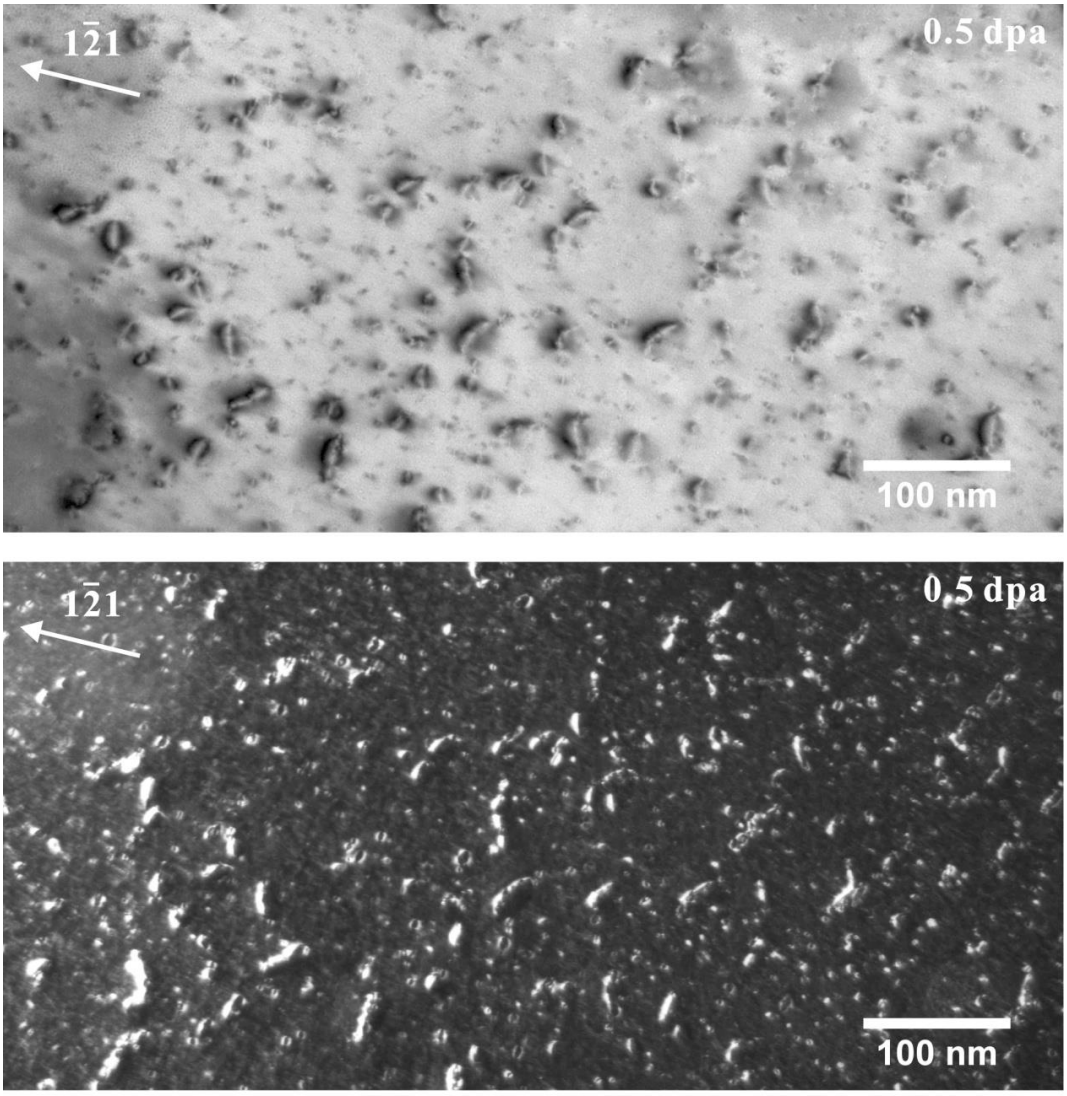


Fig 3.22 Microstructure in CG-W, irradiated in **z** = $[\bar{1}13]$ orientation at 500°C, up to a dose of 0.5 dpa.

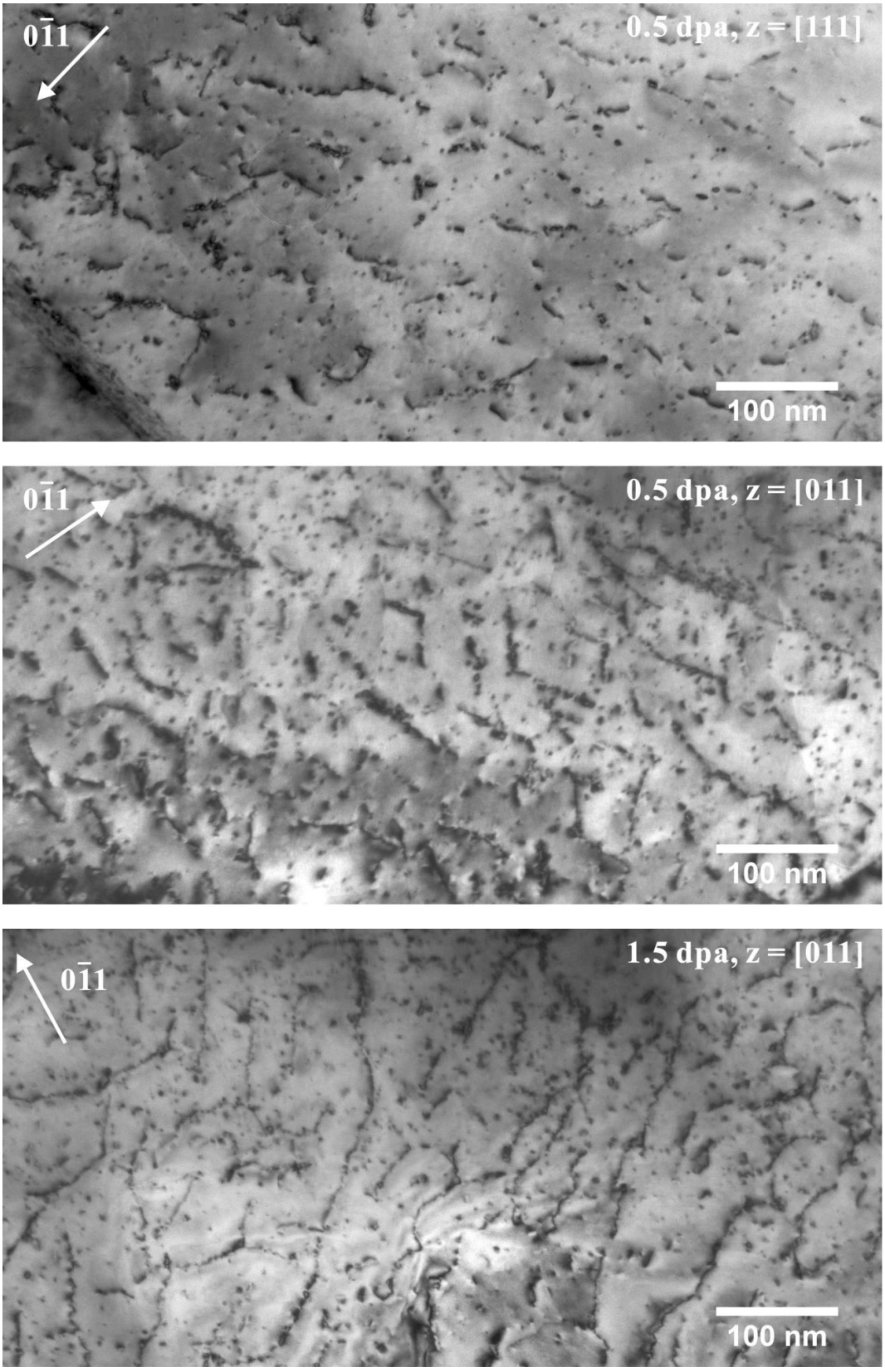


Fig 3.23 Microstructure in W-5Ta, irradiated in non **z** = [001] orientations at 300°C.

3.3. Quantitative characterizations

Quantitative diffraction contrast analyses were only performed in grains of **z** = [001] orientation for all material compositions. The effects of irradiation temperature, dose and alloying elements will be demonstrated in three aspects, i.e. dislocation loop number density, loop Burgers vector and loop nature. Due to limited time, voids were not systematically searched; but none were seen in preliminary searches.

3.3.1. Dislocation loop number densities

Dislocation loop volume number densities were deduced from measurements of foil thickness using EELS (§ 2.6.3) and area number densities as found in weak-beam dark-field micrographs (**g** = $\pm 200/020, 3-4\mathbf{g}$). For all specimens, the areas of interest were selected only from regions of relatively uniform thickness as indicated by thickness fringes. This allows the convenience of treating the foil volumes as 'cuboids', rather than 'wedges'. In addition, areas of the same size were cropped from original micrographs to reduce the occurrence of systematic error, in this case 482 by 482 $(nm)^2$. Further details of image processing can be found in § 2.7.1.

Fig 3.24 (a-e) shows the loop number densities in different materials as a function of irradiation temperature and dose. The same trends seem to apply for all figures from a) to d): (1) with increasing irradiation temperature, the loop number density drops; (2) with increasing irradiation dose, the loop number density increases. The following text describes these trends in further detail, in correlation with chemical composition.

In UHP-W (Fig 3.24 a), at a dose of 1.5 dpa, the loop number density decreased almost linearly with increasing irradiation temperature, at a rate of ~10^{20} /m^3/°C. At constant irradiation temperature, an increase in dose had much less effect on the dislocation loop population. In particular at 300°C, an increase of in dose by a factor of 75 just barely doubled

the loop number density. This is an indication that the damage in UHP-W may have saturated at somewhere above 1.5 dpa at 300°C, and above 4.5 dpa at 500°C.

The trends seen in CG-W specimens (Fig 3.24 b) did not diverge much from the UHP-W grade at the lowest dose, i.e. 0.5 dpa. However, at higher damage levels the dislocation loop population was noticeably boosted. At 300°C and 1.5 dpa, there were about 33% more loops in CG-W compared to UHP-W. Saturation in loop density was also found in CG-W. At 500°C, a tripling in dose from 1.5 dpa to 4.5 dpa led to a negligible increase in the loop number density.

In W-5Re (Fig 3.24 c) specimens irradiated at 300°C, an addition of 5 wt.% Re led to large increases in loop number densities compared with UHP W, by ~67% at a damage level of 1.5 dpa. However, the effect of alloying was much smaller at 500°C: it was hardly noticeable at low dose (0.5 dpa), and there was only a ~36% increase in loop number density at 1.5 dpa. The loop number densities were found to saturate at doses beyond 1.5 dpa at 300°C and 4.5 dpa at 500°C.

Two concentrations of W-Ta alloys were studied, i.e. 1 and 5 wt.%. Fig 3.24 d) shows that in alloys irradiated at 300°C to a dose of 1.5 dpa, adding just 1 wt.% of Ta resulted in ~60% increase in loop number density, equivalent to the increase caused by the addition of 5 wt% Re. In 5 wt.% Ta at the same irradiation condition, the increase in loop number density relative to UHP-W was ~116% and so the increase was not proportional to alloying concentration. Large increases in loop densities were also seen at an irradiation temperature to 500°C. At a dose of 1.5 dpa, increases of ~25% and ~64% in loop number density relative to UHP-W were exhibited in 1 wt.% Ta and 5 wt.% Ta respectively. Due to limited doses covered in these experiments, it has not yet been found when damage saturates in these alloys.

Data for the W-5V alloy was only available for irradiation at 500°C to a dose of 1.5 dpa. Fig 3.24 e) has been plotted so that a variety of materials can be compared in terms of loop number density for this specific irradiation condition. It is apparent that all of the alloying elements (Re, Ta, V) as well as impurities may contribute to an increase of loop number density. Moreover, it seems that CG-W, 1 wt.% Ta and 5 wt.% Re fall in the same category in terms of their effect on the loop number density, which is to cause an increase of about ~30%; while 5 wt.% Ta and 5 wt.% V elevate this value to ~70%. Of all materials investigated, the highest loop number density was found in W-5V.

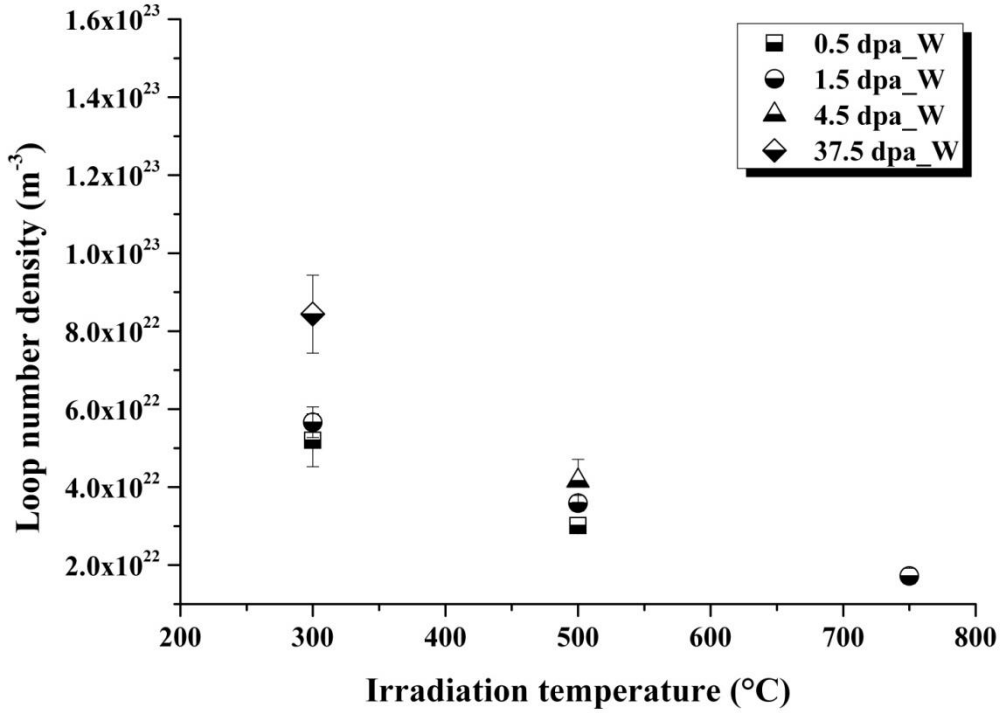


Fig 3.24 a) Loop number densities in UHP-W, w.r.t. irradiation temperature and dose.

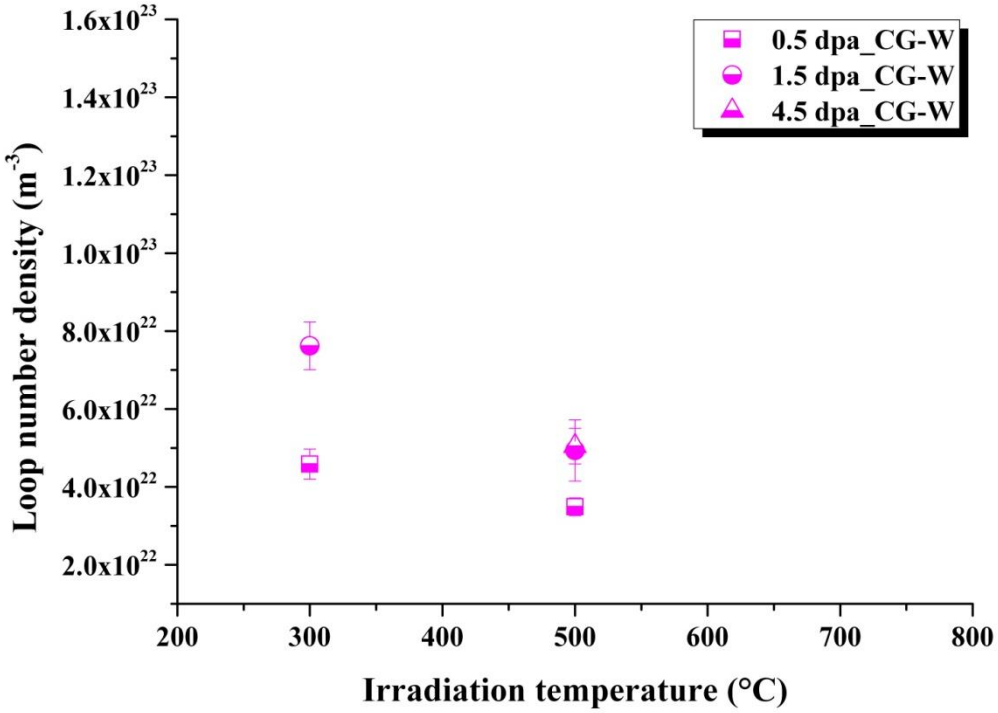


Fig 3.24 b) Loop number densities in CG-W, w.r.t. irradiation temperature and dose.

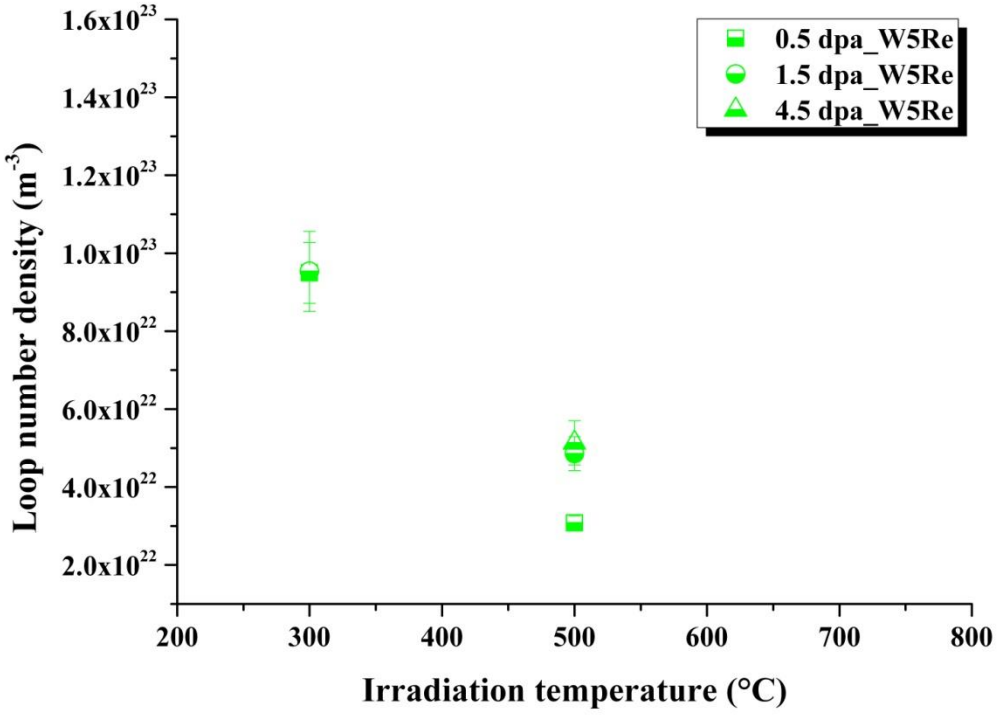


Fig 3.24 c) Loop number densities in W-5Re, w.r.t. irradiation temperature and dose.

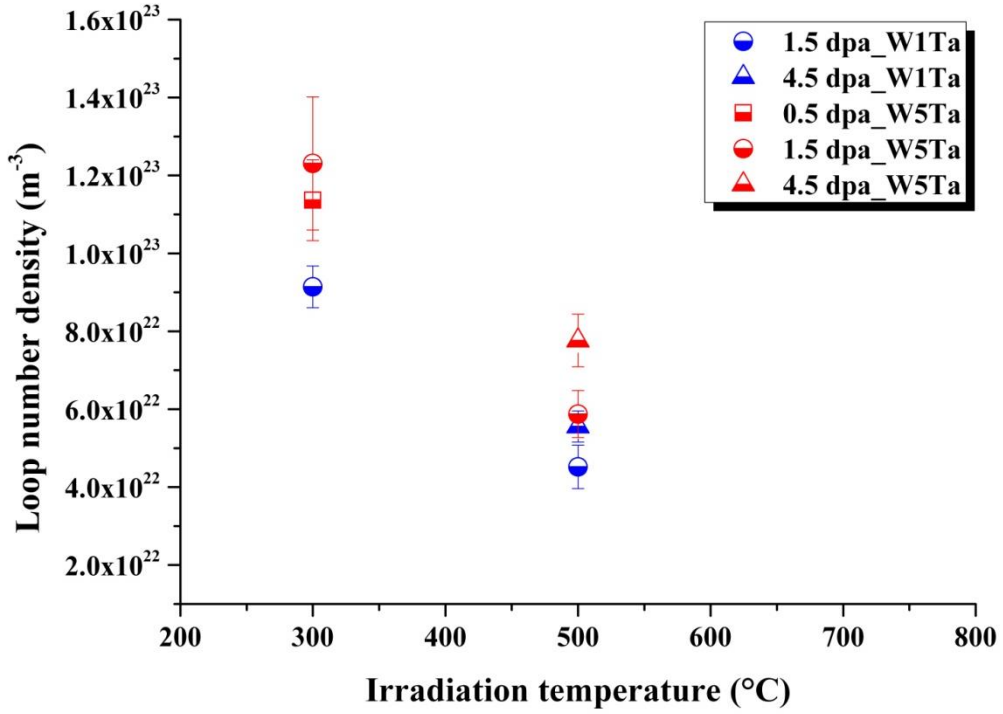


Fig 3.24 d) Loop number densities in W-Ta alloys, w.r.t. irradiation temperature and dose.

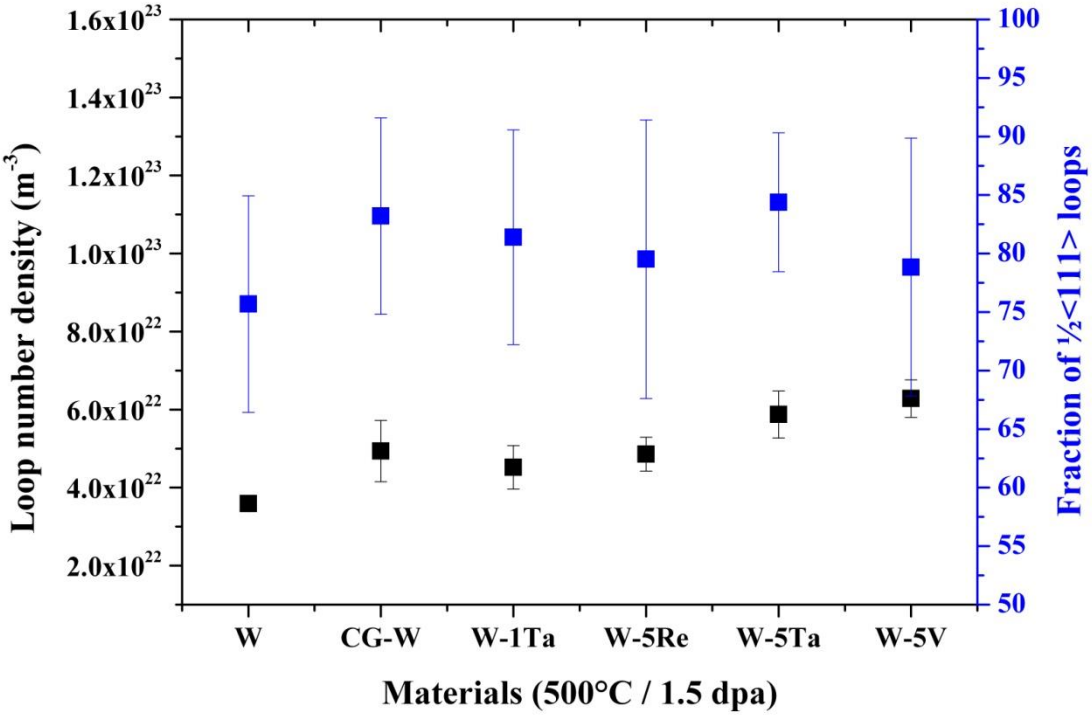


Fig 3.24 e) Loop number densities in W-5V, w.r.t. irradiation temperature and dose.

3.3.2. Dislocation loop Burgers vector characterization

It has been demonstrated that the damage microstructures in W and W-alloys consist of a mixture of ½<111> and <100> loops. In this section, this is quantitatively analysed by generating plots of the fraction of ½<111> loops at various irradiation parameter and material compositions.

In many cases, e.g. high irradiation dose samples, loop Burgers vector analysis through one-to-one correlation was not possible and many visible loops could not be included in the sampling body. In order to gain sufficient statistics on the geometries of loops seen, a loop number density based method described in § 2.7.3 replaced the standard approach demonstrated in § 2.6.3. Inevitably this is bound to generate larger errors, but one can still be confident about several trends reflected in the plots of Fig 3.25. First, the ½<111> configuration dominates regardless of irradiation conditions and chemical composition. Further, at constant dose the fraction of ½<111> loops increases with irradiation temperature; while at constant irradiation temperature, there seems to be a weak tendency for an increase in the fraction of ½<111> loops with dose. In the next few paragraphs, the trends in the different materials will be covered in detail.

In UHP-W samples (Fig 3.25 a) irradiated to a dose of 1.5 dpa, the fraction of ½<111> loops increased markedly from ~79% to ~90% between irradiation temperatures from 300°C to 750°C. An increase in dose at constant temperatures had a much weaker impact on the fraction of ½<111> loops. At 300°C, no significant differences could be found for doses ranging from 0.5 dpa to 37.5 dpa. At 500°C, an order of magnitude increase in dose merely increased the fraction of ½<111> loops from ~72% to ~85%.

At 300°C, CG-W (Fig 3.25 b) specimens behaved very similarly to UHP-W. A noticeable difference was only seen at 500°C. From 0.5 dpa to 1.5 dpa, the fraction of

½<111> loops increased from ~77% to ~83%, although this fraction then changed little. The influence of irradiation temperature diverged slightly from what was observed in UHP-W. At 0.5 dpa, not much change was found. At 1.5 dpa, a moderate increase in the fraction of ½<111> loops from ~77% at 300°C to ~83% at 500°C was seen.

In general, the fractions of ½<111> loops in W-5Re (Fig 3.25 c) were lower than their UHP-W counterparts. An increase in irradiation temperature again produced more ½<111> loops. However, the fraction of ½<111> loops looked to be largely independent of dose, especially at 300°C.

In W-Ta, neither dose and temperature nor the concentration of Ta (1-5 wt.%) had much impact on the fraction of ½<111> loops (Fig 3.25 d). The value sat constantly within a range of 80-85%.

Finally, Fig 3.24 e) shows data from W-5V irradiated to 1.5 dpa at 500°C and compares the fraction of ½<111> loops across a range of materials at the same irradiation condition. It is quite convincing to conclude that in all the non-ultra pure tungsten grades, i.e. CG-W and W-alloys, the fraction of ½<111> loops tend to be about 5-10% higher than in the UHP-W specimens.

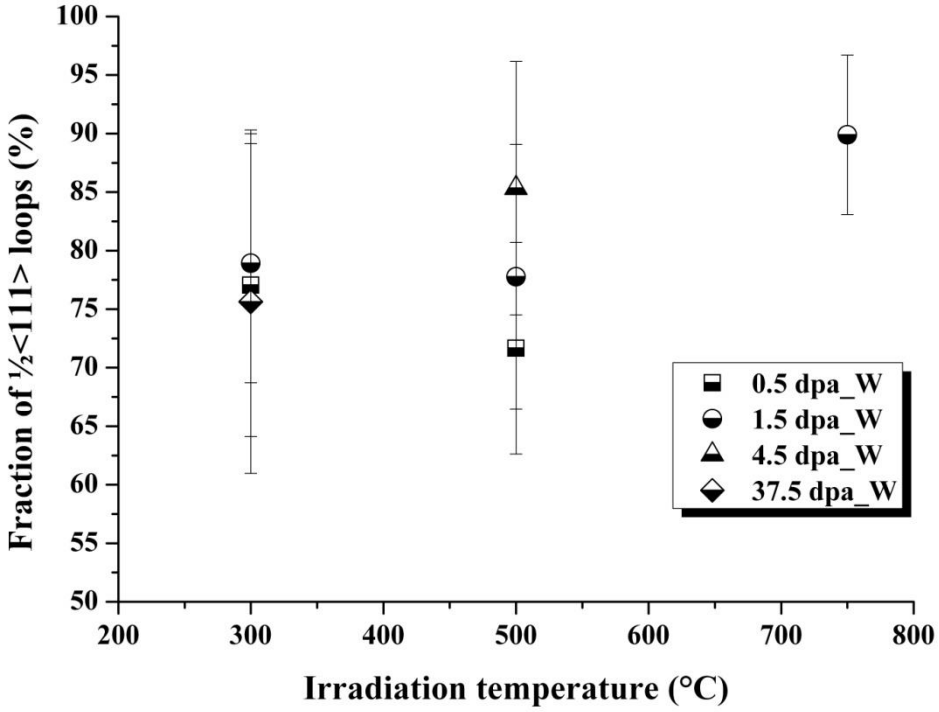


Fig 3.25 a) Fraction of ½<111> loops in UHP-W, w.r.t. irradiation temperature and dose.

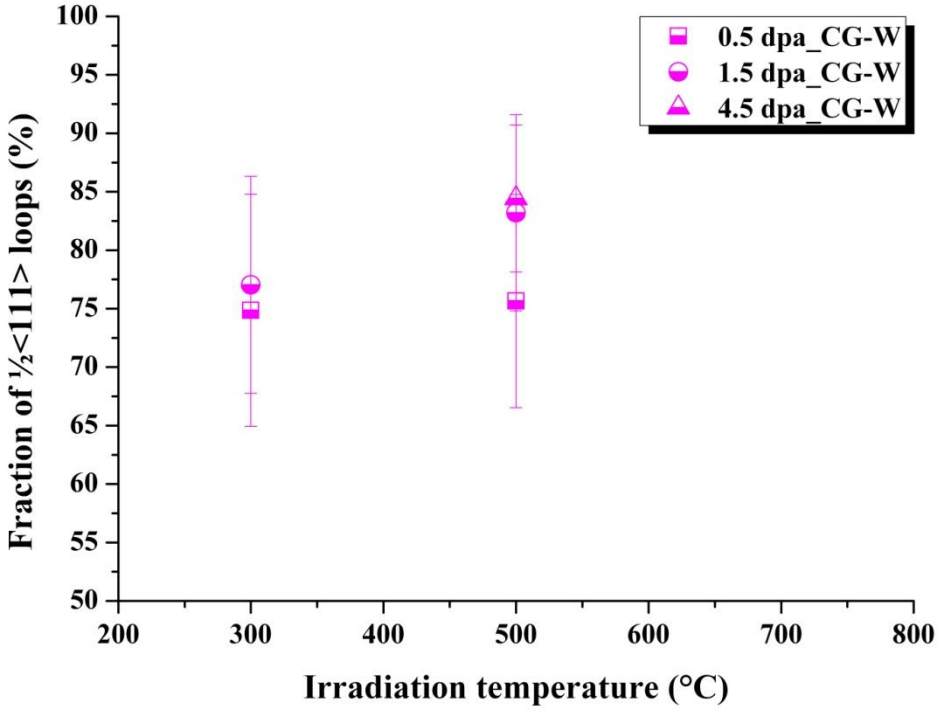


Fig 3.25 b) Fraction of ½<111> loops in CG-W, w.r.t. irradiation temperature and dose.

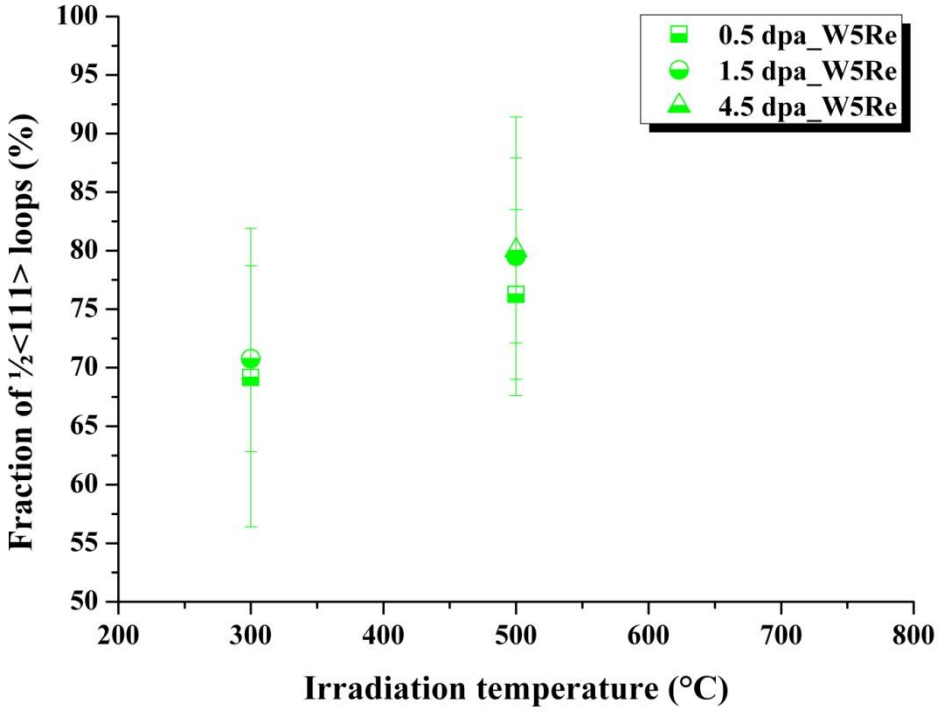


Fig 3.25 c) Fraction of ½<111> loops in W-5Re, w.r.t. irradiation temperature and dose.

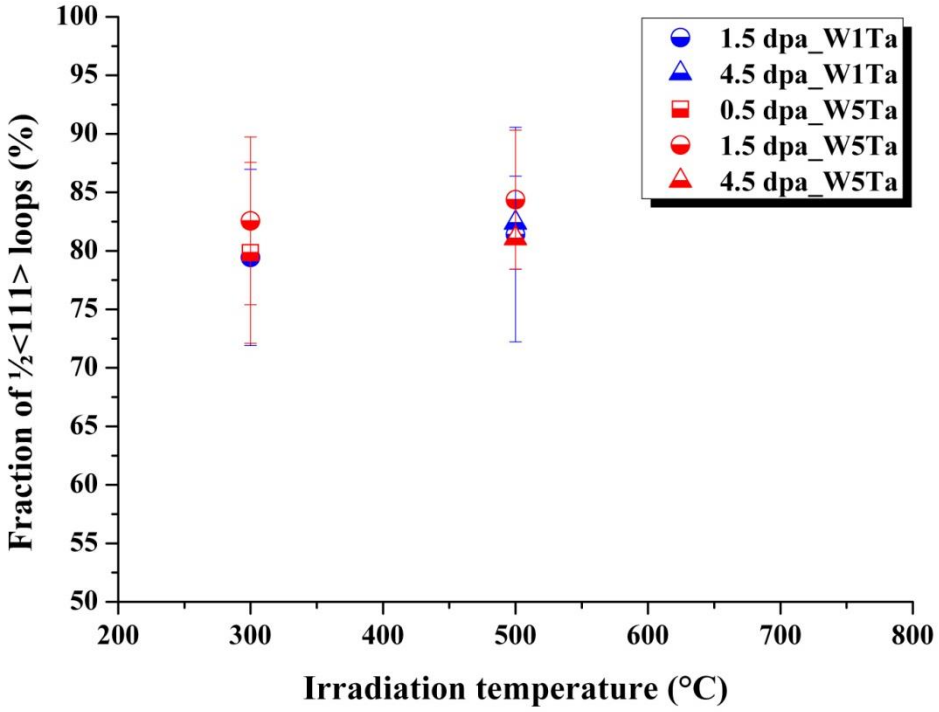


Fig 3.25 d) Fraction of ½<111> loops in W-Ta, w.r.t. irradiation temperature and dose.

3.3.3. Dislocation loop nature analysis

This section refers to grains with **z** = [001] orientation only. The statistics of loop nature were extracted from their inside-outside contrast behaviour, but approached differently for ½<111> and <100> loops (see § 2.6.3). Loops ≤ 4 nm were not considered for nature analysis, due to the difficulty in distinguishing inside contrast from outside contrast. Error bars were extracted from the number of loops in the analysed population which fell into the 4-5 nm size category.

According to the previous sections, a typical damage microstructure in the materials and irradiation conditions covered in this chapter consisted of at least 60% ½<111> loops, in addition to a minority of <100> loops. Unlike ½<111> loops, where the nature of loops can be worked out from the axis of **b** and the inside-outside contrast produced by a ±**g** pair, <100> loops with large edge component lie close to edge-on in foil orientations close to **z** = [001] and the sense of inclination of loops is further required to correctly deduce their nature. The sense of inclination can be found by the change in shape of loops during high-angle tilting along designated Kikuchi bands. This essentially pushes up the lower size bound for <100> loops which are suitable for nature analysis. As a consequence of loop scarcity and size limitations, the nature analyses for <100> loops were performed only in the UHP-W specimen irradiated at 750°C at a dose of 1.5 dpa.

The analysis of dislocation loop nature divides into three parts. The first part will focus on pure tungsten (ultra high purity and commercial grade), the second on W-5Re and the third on W-(1,5)Ta alloys. W-5V alloy is not considered for loop nature determination due to restricted loop size in the "500°C / 1.5 dpa" data set. All data will be presented as plots illustrating the fraction of interstitial-type loops with respect to irradiation temperature and dose, and the normalized size distributions of all analysed loops.

The UHP-W data set is the most complete. Shown in Fig 3.26 is the fraction of ½<111> loops with interstitial nature, plotted against irradiation temperature and dose. It appears that an increase in either temperature or dose leads to a higher fraction of ½<111> interstitial loops. However, the increment with dose was less at the higher temperature, i.e. at 300°C there was an increase in the fraction of interstitial loops from 53.5% to 76.0% between 0.5 dpa and 1.5 dpa, while at 500°C the increase was from 86.2% to 100%. Additionally, the fraction of interstitial loops saturated at 500°C, at doses above 1.5 dpa. At 750°C, where only data for 1.4 dpa was available, the fraction of interstitial loops dropped but the error bar has been substantially reduced due to the increased sampling body of > 5 nm loops. On the whole, the trend in UHP-W for the fraction of ½<111> loops with interstitial nature to increase with temperature remains valid.

Additional information can be found in Fig 3.29 a) regarding the nature and size evolution of ½<111> loops. At 300°C, a dose increase (× 3 times) had little effect on the loop sizes, but distinctly increased the fraction of interstitial-type loops. At 500°C, the loop size distributions began to flatten out and the peak size category shifted towards larger sizes. The influence of dose on loop size remained subtle. However, as dose increased, vacancy-type loops disappeared from the loop populations. If present at all, the vacancy-type loops do not exceed a size of 9 nm, while interstitial loops in the > 10 nm size category are present in considerable numbers.

Another interesting observation comes from the “750°C / 1.5 dpa” data set. The loop nature-size distributions for both ½<111> and <100> loops are shown in Fig 3.29 b). For ½<111> loops, the size distribution has flattened out further compared with irradiations at 500°C. In particular, the number of loops in > 9 nm size categories has almost doubled, compared with the “500°C / 1.5 dpa” plot. Moreover, vacancy-type loops are present beyond

the > 10 nm size category, which appeared to be a unique feature for irradiations above 500°C. For <100> loops, although the statistics are poor, the nature-size distribution has shown one important point: the <100> loops in the damage microstructure of UHP-W are predominantly of interstitial type. The fact that the peak size category in <100> loops is 8-9 nm also suggests that <100> loops are larger than ½<111> loops on average.

The dependence of the fraction of ½<111> loops with interstitial nature in CG-W with temperature and dose was similar to that of UHP-W, see Fig 3.26. However, an increase in temperature from 300°C to 500°C at a dose of 0.5 dpa resulted in only a third of the increase seen in UHP-W in absolute values. Saturation of the fraction of ½<111> loops with interstitial nature also occurred around 1.5 dpa at 500°C. Generally, the fractions of ½<111> loops with interstitial nature in CG-W was about 20% lower than its counterpart UHP-W. The loop nature-size distributions in CG-W (Fig 3.30) do not show any distinct indications of flattening out towards larger dimensions with increases in irradiation temperature or dose. A slight increase in fractions of interstitial loops in particular loop size categories has been observed. Taking the 500°C irradiations for example, the fraction of interstitial loops in the 5-6 nm size category steadily built up from 44.4% to 47.1% as the dose increased by an order of magnitude. Also, the sizes of vacancy-type loops were restricted to less than 7 nm, and no loops of either nature were found with diameters larger than 9 nm.

Fig 3.27 and Fig 3.28 compare the fraction of ½<111> loops with interstitial nature in UHP-W with W-5Re, W-1Ta and W-5Ta. All three alloys revealed two features in common: 1) at constant temperature, an increase in dose has little effect on the fraction of interstitial loops; 2) at 300°C, the fraction of interstitial loops in the alloys were consistently higher than in UHP-W, while at 500°C the opposite was true. In W-5Re, the number of interstitial loops decreased from ~80% to ~70% between these temperatures. In W-Ta grades, none of the

irradiation or compositional parameters seemed to have a pronounced effect and the fraction of interstitial loops settled around 75%. Figs 3.31-3.33 summarize the loop nature-size distributions for all the ½<111> loops analysed in W-5Re and W-(1,5)Ta alloys. In these alloys, loop size distributions do not show a flattening-out tendency with increases in temperature nor in dose. Rather, the highlights lie in the individual size categories. For example, the total fraction of loops in the 5-6 nm size category has been found to increase gradually with temperature and dose in both W-5Re and W-5Ta. More strikingly, this increase has been found to be due substantially to an increase in the number of vacancy-type loops, as opposed to the "wiping out" of vacancy loops found in UHP-W.

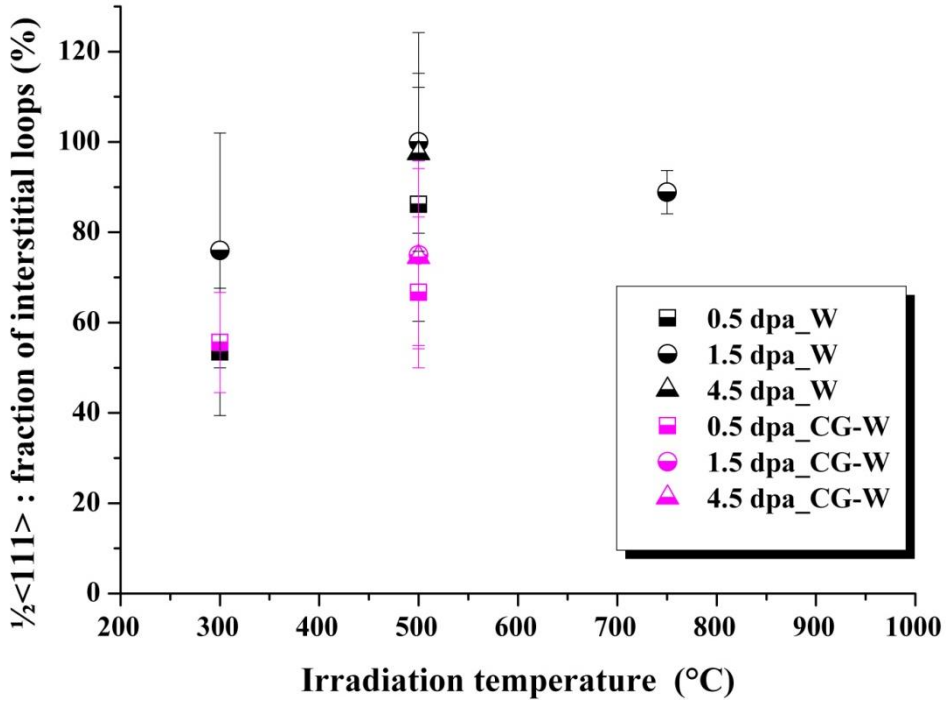


Fig 3.26 The fraction of interstitial loops among loops with **b** = ½<111> in UHP-W and CG-W, as a function of irradiation temperature and dose.

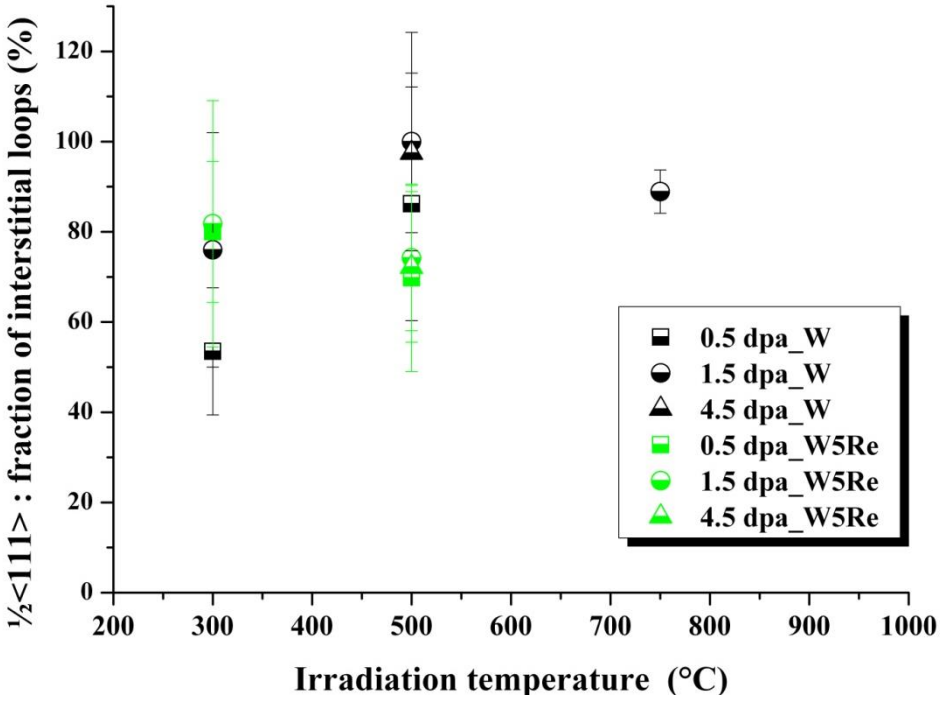


Fig 3.27 The fraction of interstitial loops among loops with **b** = ½<111> in UHP-W and W-5Re, as a function of irradiation temperature and dose.

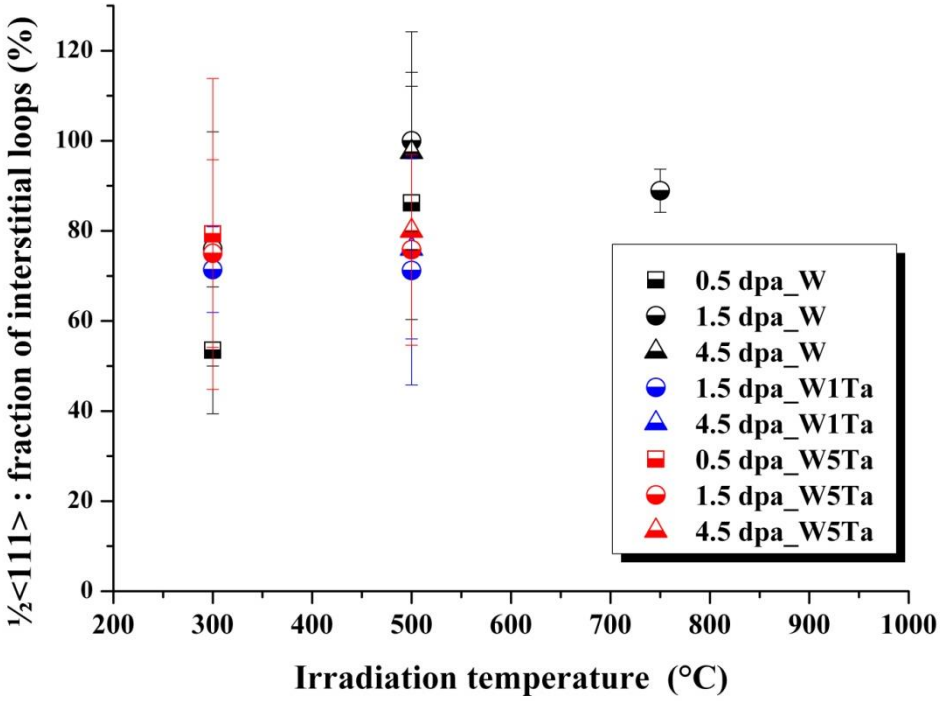


Fig 3.28 The fraction of interstitial loops among loops with **b** = ½<111> in UHP-W and W-(1, 5)Ta, as a function of irradiation temperature and dose.

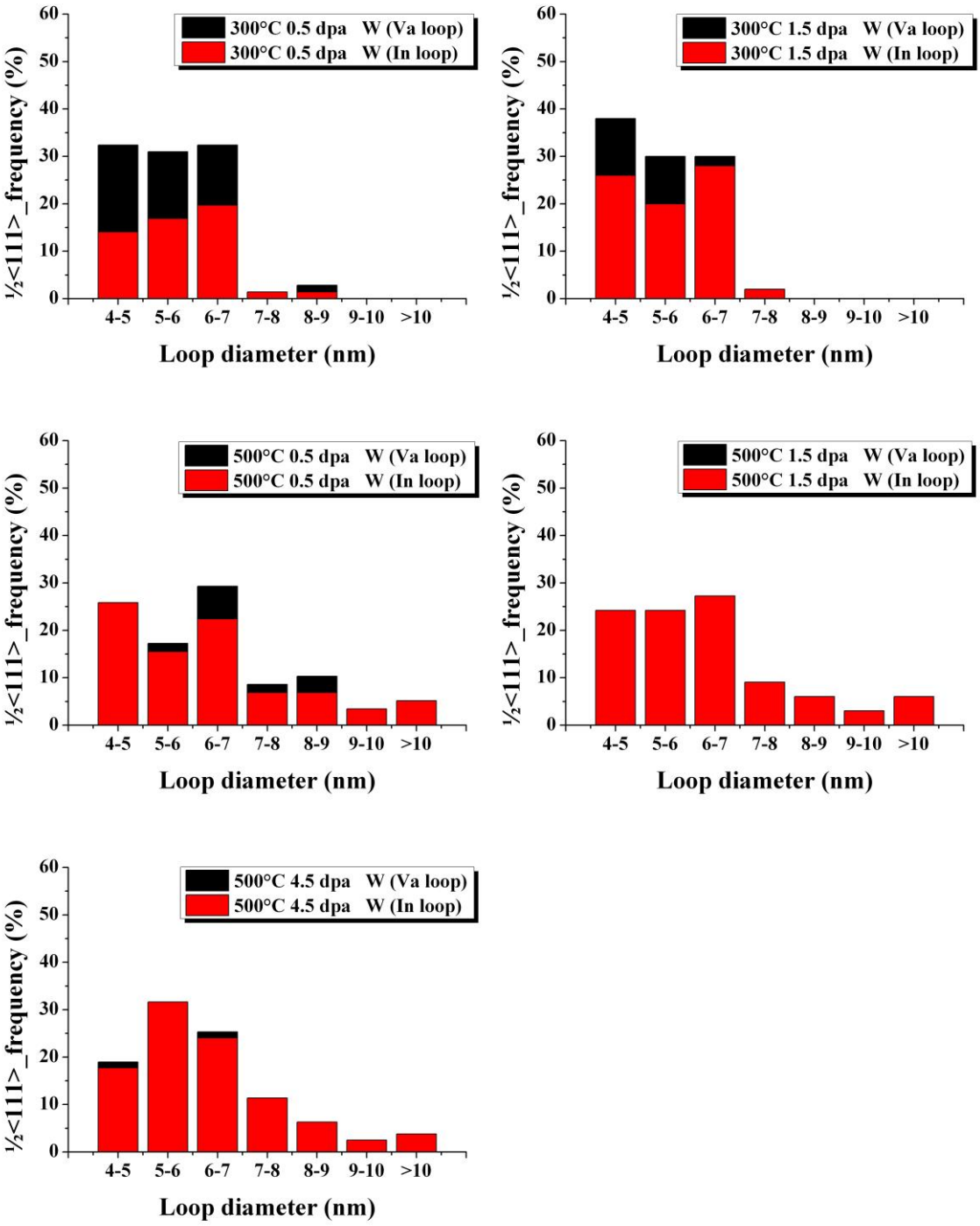


Fig 3.29 a) The size distributions of interstitial/vacancy-type ½<111> loops in UHP-W, normalized against the total sampled ½<111> loop population (typically 50-70 loops). Irradiation conditions: 300-500°C; 0.5-4.5 dpa.

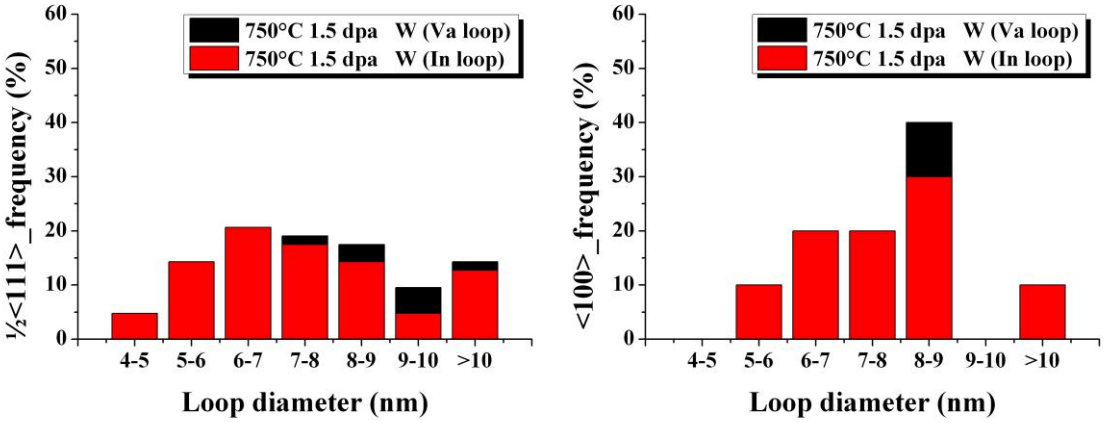


Fig 3.29 b) The size distributions of interstitial- and vacancy-type loops in UHP-W irradiated at 750°C at a dose of 1.5 dpa. The plots are normalized against the total sampled ½<111> (63 loops) or <100> (10 loops) loop population.

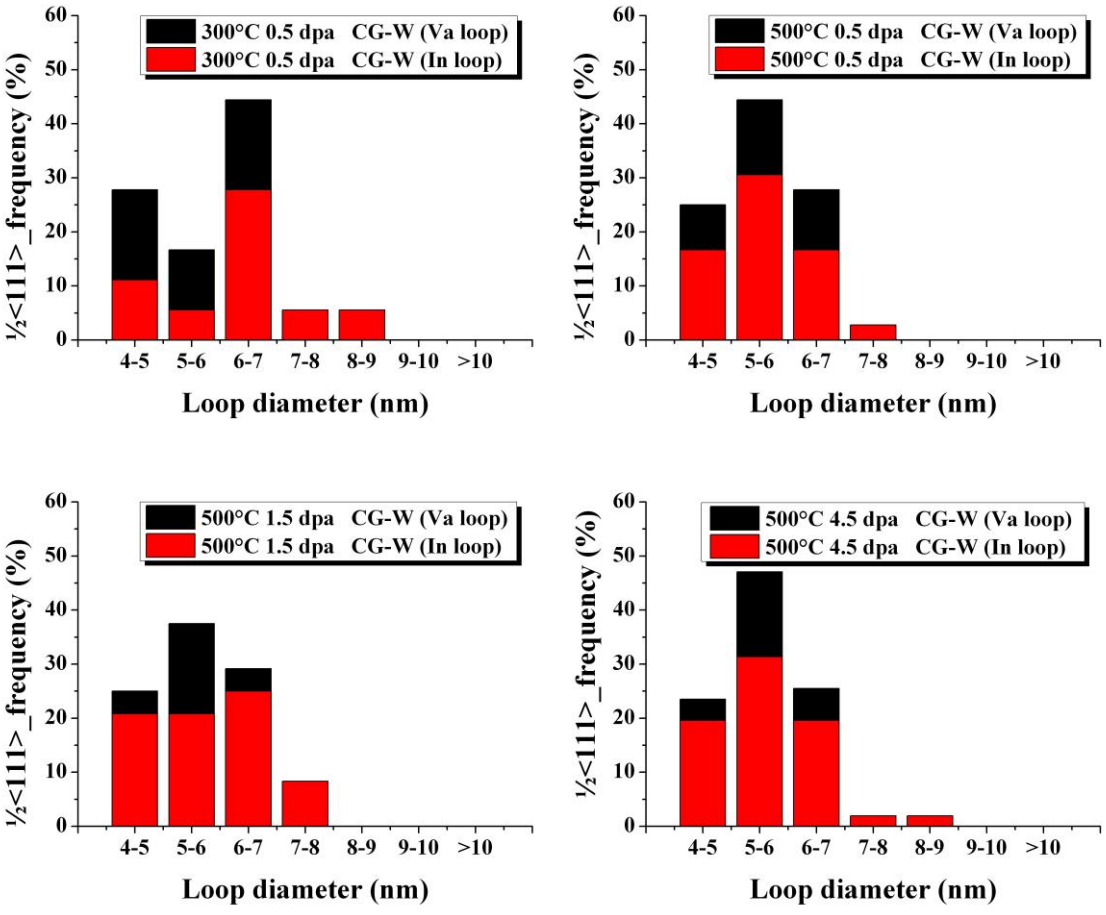


Fig 3.30 The size distributions of interstitial- and vacancy-type ½<111> loops in CG-W, normalized against the total sampled ½<111> loop population (typically 50-70 loops). Irradiation conditions: 300-500°C; 0.5-4.5 dpa.

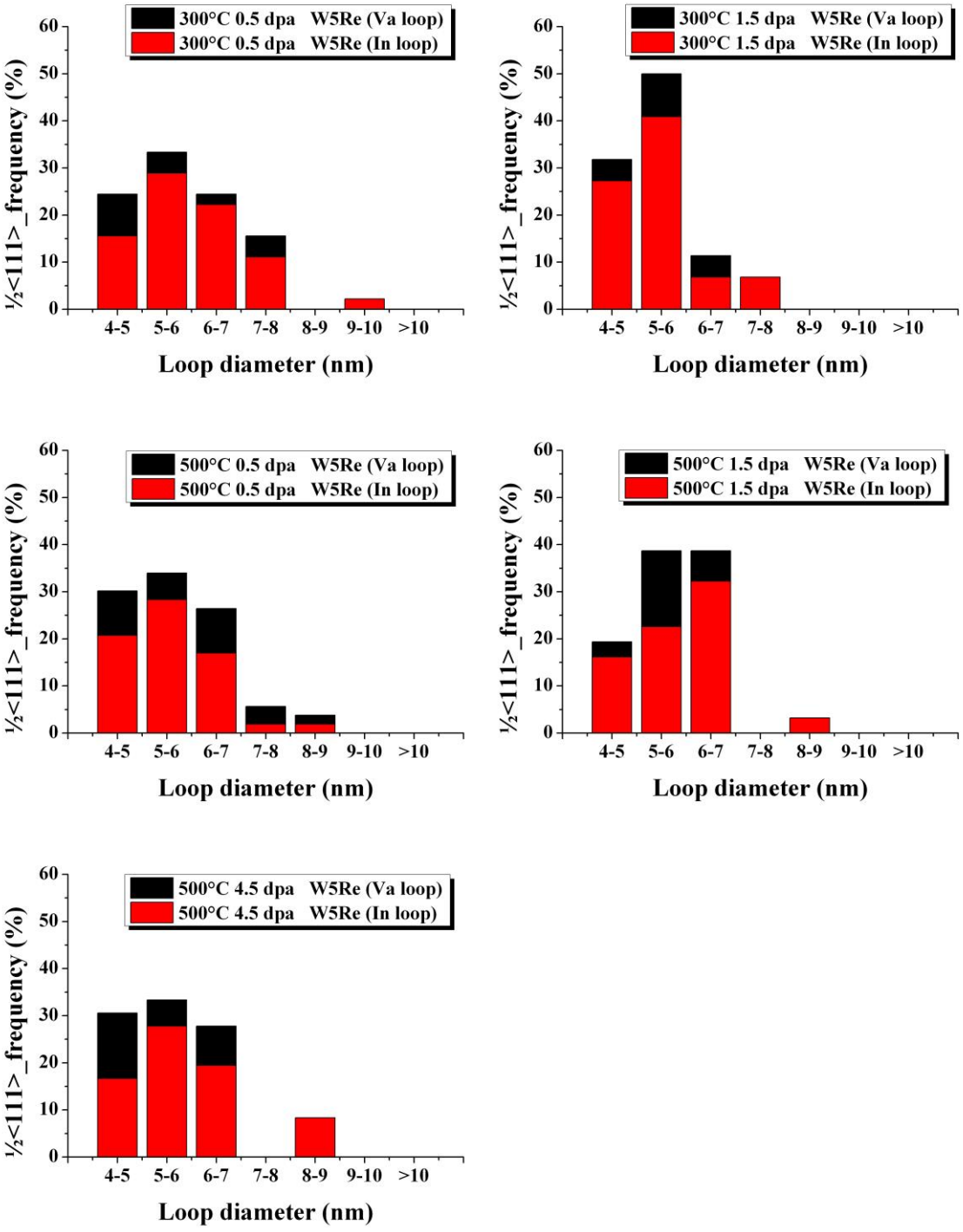


Fig 3.31 The size distributions of interstitial- and vacancy-type ½<111> loops in W-5Re, normalized against the total sampled ½<111> loop population (typically 50-70 loops). Irradiation conditions: 300-500°C; 0.5-4.5 dpa.

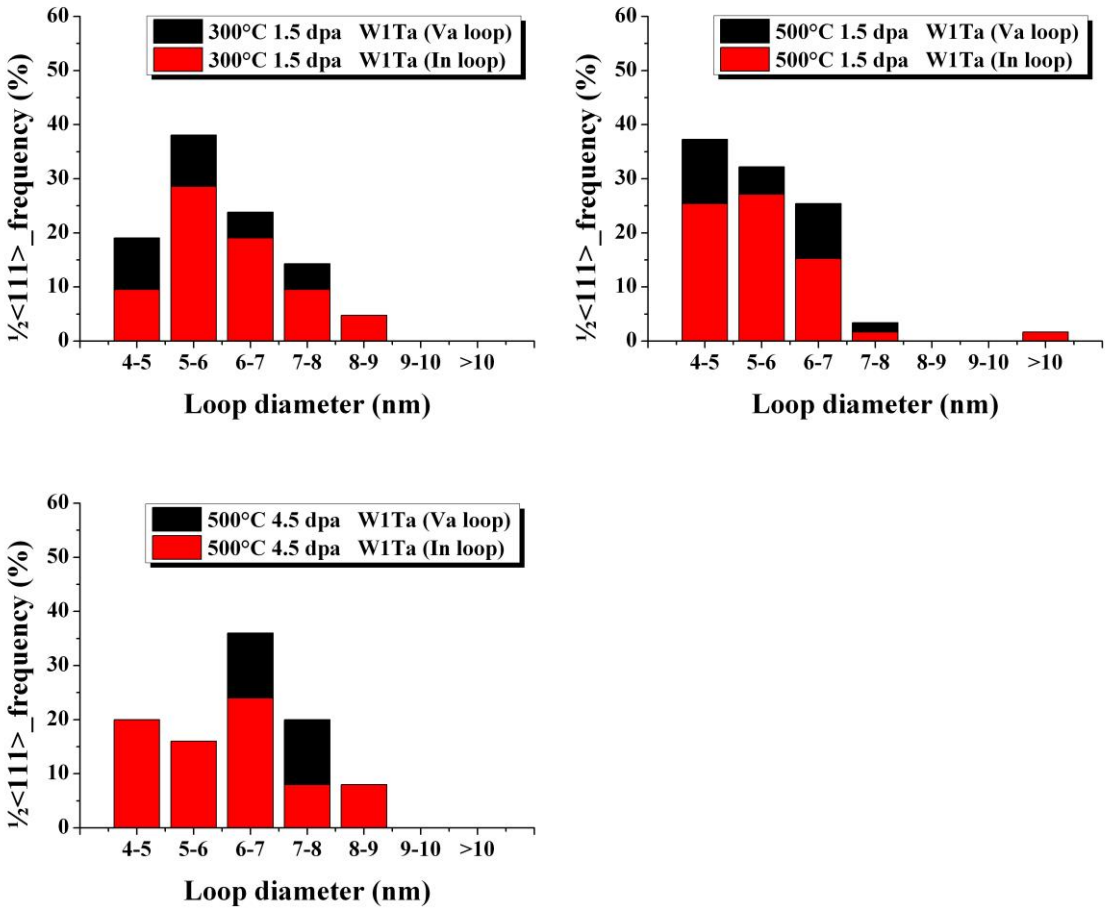


Fig 3.32 The size distributions of interstitial- and vacancy-type ½<111> loops in W-1Ta, normalized against the total sampled ½<111> loop population (typically 50-70 loops). Irradiation conditions: 300-500°C; 1.5-4.5 dpa.

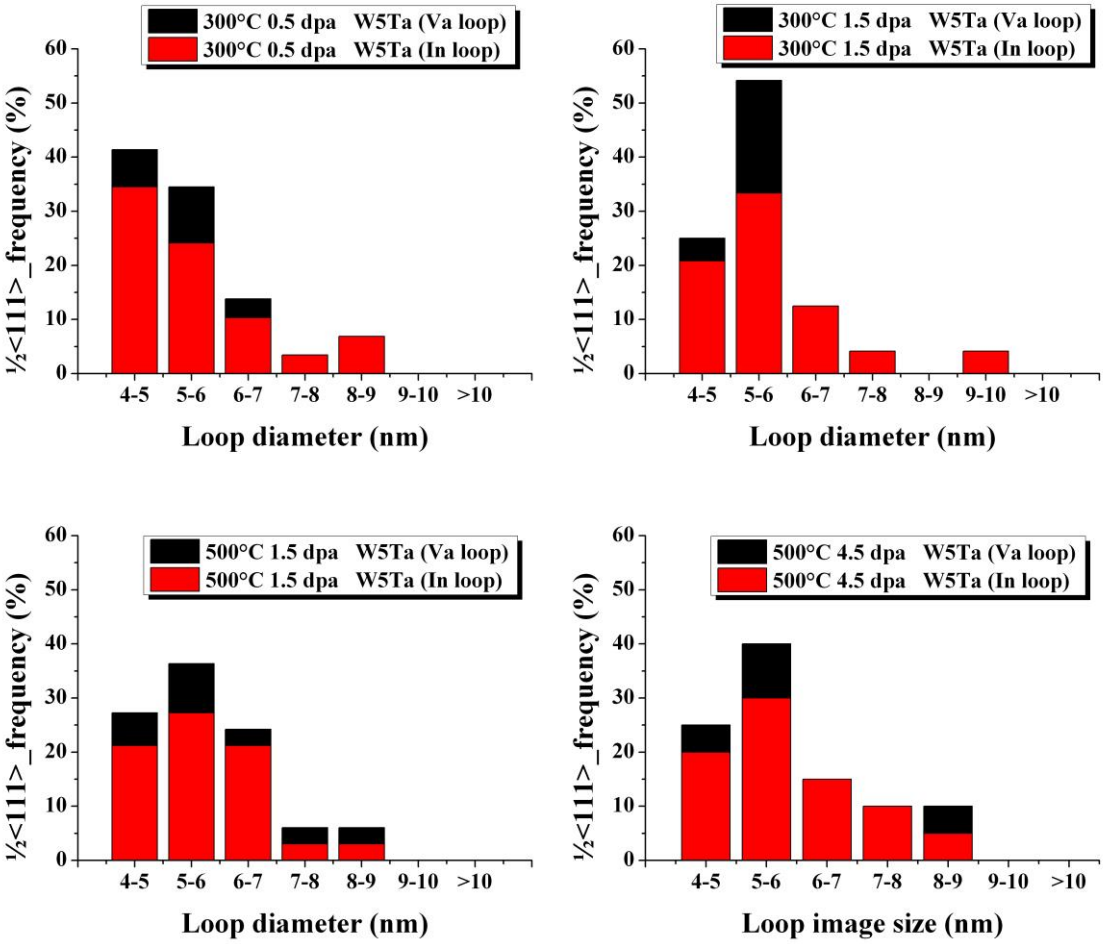


Fig 3.33 The size distributions of interstitial- and vacancy-type ½<111> loops in W-5Ta, normalized against the total sampled ½<111> loop population (typically 30-50 loops). Irradiation conditions: 300-500°C; 0.5-4.5 dpa.

Table 3.1 Summary of results on bulk implantations of W/W-alloys

Material / Irradiations	Overall microstructure	Loop density	Loop size	Loop geometry ½<111> + <100>	Loop nature (interstitial)
UHP-W, **z** = [001] 300°C, 0.5-37.5dpa 500°C, 0.5-4.5dpa 750°C, 1.5dpa	Loop raft/string formation: T ≥ 500°C or dose > 1.5 dpa. Uniform otherwise.	T↑, density ↓ Dose ↑, density ↑ No saturation.	T ↑, size ↑ Dose ↑, size ↑	T ↑ or Dose ↑, ½<111> (%) ↑.	T ↑ or Dose (0-1.5 dpa) ↑, I-loop (%) ↑; Dose (> 1.5 dpa), Not sensitive.
CG-W, **z** = [001] 300°C, 0.5-1.5dpa 500°C, 0.5-4.5dpa	Loop raft/string formation: Dose ≥ 1.5 dpa. Uniform otherwise.	T↑, density ↓ Dose ↑, density ↑ No saturation.	T ↑ or Dose (0-1.5 dpa)↑, size ↑; Dose (> 1.5 dpa), Not sensitive.	T ↑ or Dose (0-1.5 dpa) ↑, ½<111> (%) ↑.	T ↑, I-loop (%) ↑; Not dose sensitive
W-5Re, **z** = [001] 300°C, 0.5-1.5dpa 500°C, 0.5-4.5dpa	Uniform loop distribution.	T↑, density ↓ Dose ↑, density ↑ Saturation observed.	T ↑, size ↑ Not very sensitive to dose	T ↑ or Dose (0-1.5 dpa) ↑, ½<111> (%) ↑.	Not sensitive to dose and T.
W-1Ta, **z** = [001] W-5Ta, **z** = [001] 300°C, 0.5-1.5dpa 500°C, 1.5-4.5dpa	Loop raft formation: T ≥ 500°C and dose > 1.5 dpa. No loop string formation.	T↑, density ↓ Dose ↑, density ↑ No saturation.	T ↑, size ↑ Not very sensitive to dose	Not sensitive to dose and T.	Not sensitive to dose and T.
W-5V, **z** = [001] 500°C, 1.5dpa	Uniform loop distribution.	Strongest effect on loop density (V>Ta>Re, Im)	Strongest suppression effect (V>Ta>Re,Im).	/	/
Non "**z** = [001]" W/W-alloys 300°C, 0.5-1.5dpa 500°C, 0.5-4.5dpa	Loop strings form, and may evolve further into networks under low T and high dose conditions.	/	/	/	/

Chapter 4

In-situ Irradiated Tungsten and Alloys

Many of the micrographs shown in the figures of this chapter have been extracted from video recordings. In most cases the trends described are better appreciated by viewing the videos directly, especially those involving loop and string motion, and interactions. For this reason, the original recordings of the case studies covered have been placed on the DVD attached to the thesis as an appendix.

4.1. Introduction

In-situ irradiations of tungsten and alloys with 150 keV W^+ ions contribute to the understanding of damage behaviour with respect to temperature, dose and composition variables. They have enabled monitoring of the evolution of damage and so to provide answers to fundamental questions such as: How do loops nucleate? How do they accumulate, migrate and interact? What are the features of the final damage microstructures and how did these develop? The layout of this chapter has been defined according to these questions. § 4.2 describes the early-stage (≤ 0.01 dpa) damage development in UHP-W between R.T. and 800°C (~10^{16} W^+m^{-2}). § 4.3 and 4.4 describe how the microstructures evolve from 0.01 dpa to 1.0 dpa in UHP-W and W-alloys. Finally § 4.5 presents in detail the quantitative analyses of post-irradiation microstructures at 1.0 dpa. Possible artefacts introduced by the electron beam and surface attraction are specified and their impact on the microstructure is evaluated.

4.2. Early stage radiation damage in tungsten (0.01 dpa)

Early damage formation in UHP-W was investigated with all grains close to the **z** = [001] direction. Imaging conditions during the irradiation were all set to weak-beam dark-field ($\mathbf{g} = 200, 3-4\mathbf{g}$). Fig 4.1 and 4.2 compare the nucleation and development of defects in UHP-W at R.T. and 800°C, respectively. At R.T., loops were produced within 0.07s of the start of the irradiation. They appeared abruptly from one frame to the next and did not grow measurably within the time frame of the experiment. Similar features were also observed in the irradiations performed between 300°C and 600°C. At 800°C, the first signs of loop formation did not occur until ~1s after the start of the irradiation. Most loops gained increased brightness and size within ~0.3s upon nucleation and were remained stable until the irradiation was terminated. The selection of 0.01 dpa was to ensure that the damage seen would originate from individual cascades only. The dose limit has been deduced based on an estimate of the cascade size. At a dose rate of 6.25×10^{14} $W^{+}m^{-2}s^{-1}$, the threshold for visible damage can be estimated as $\leq 4.20\times10^{13}$ $W^{+}m^{-2}$. If the cascade size were ~10 nm, cascades would not overlap significantly below ~10^{16} ions m^{-2}. This has been confirmed in Fig 4.3. At doses below 10^{16} ions m^{-2}, a linear relationship between dose and loop number density applies for all three temperatures plotted, implying that no interference of cascades were present.

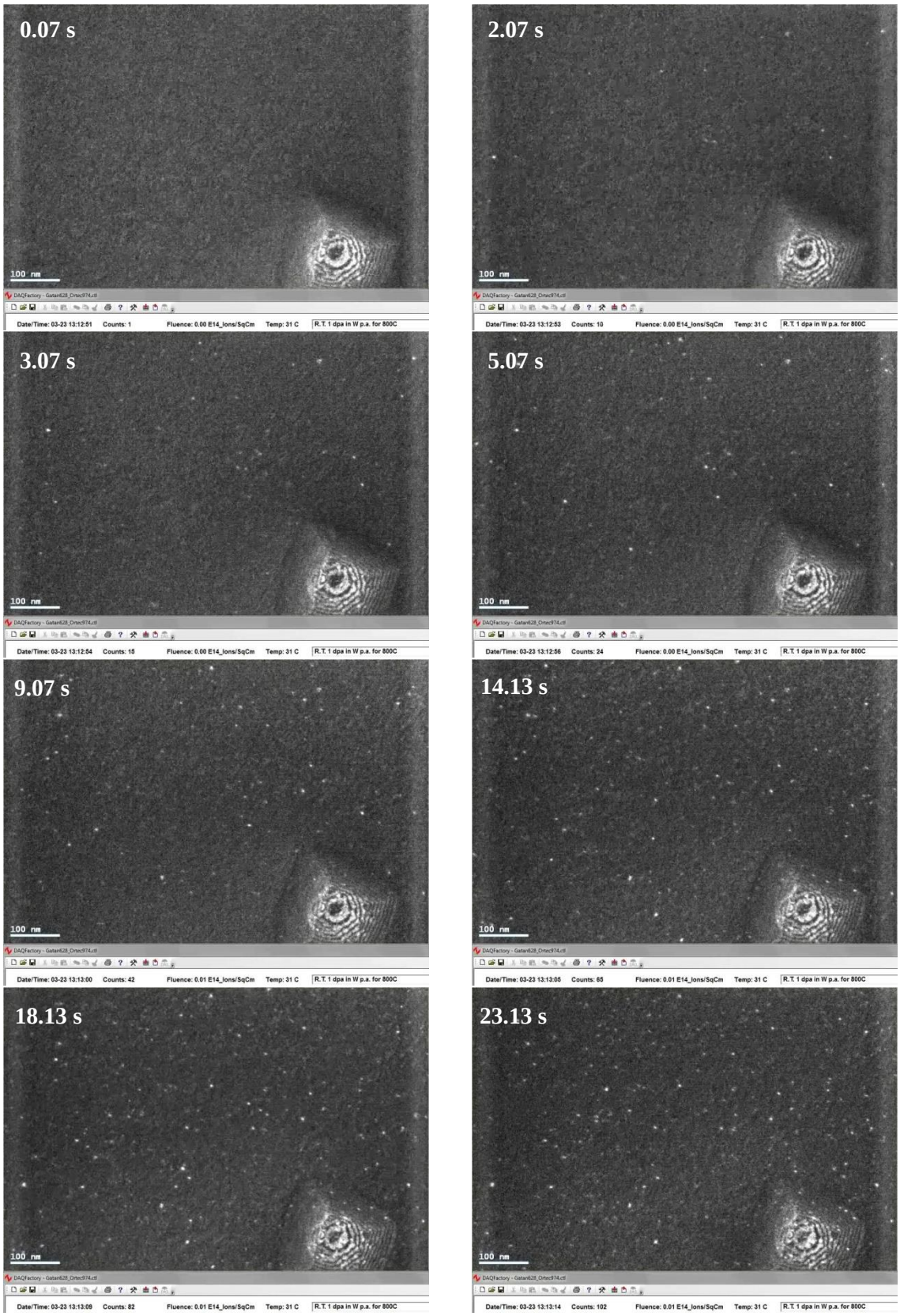


Fig 4.1 Damage development in UHP-W, irradiated up to 0.01 dpa at R.T. **z** = [001].

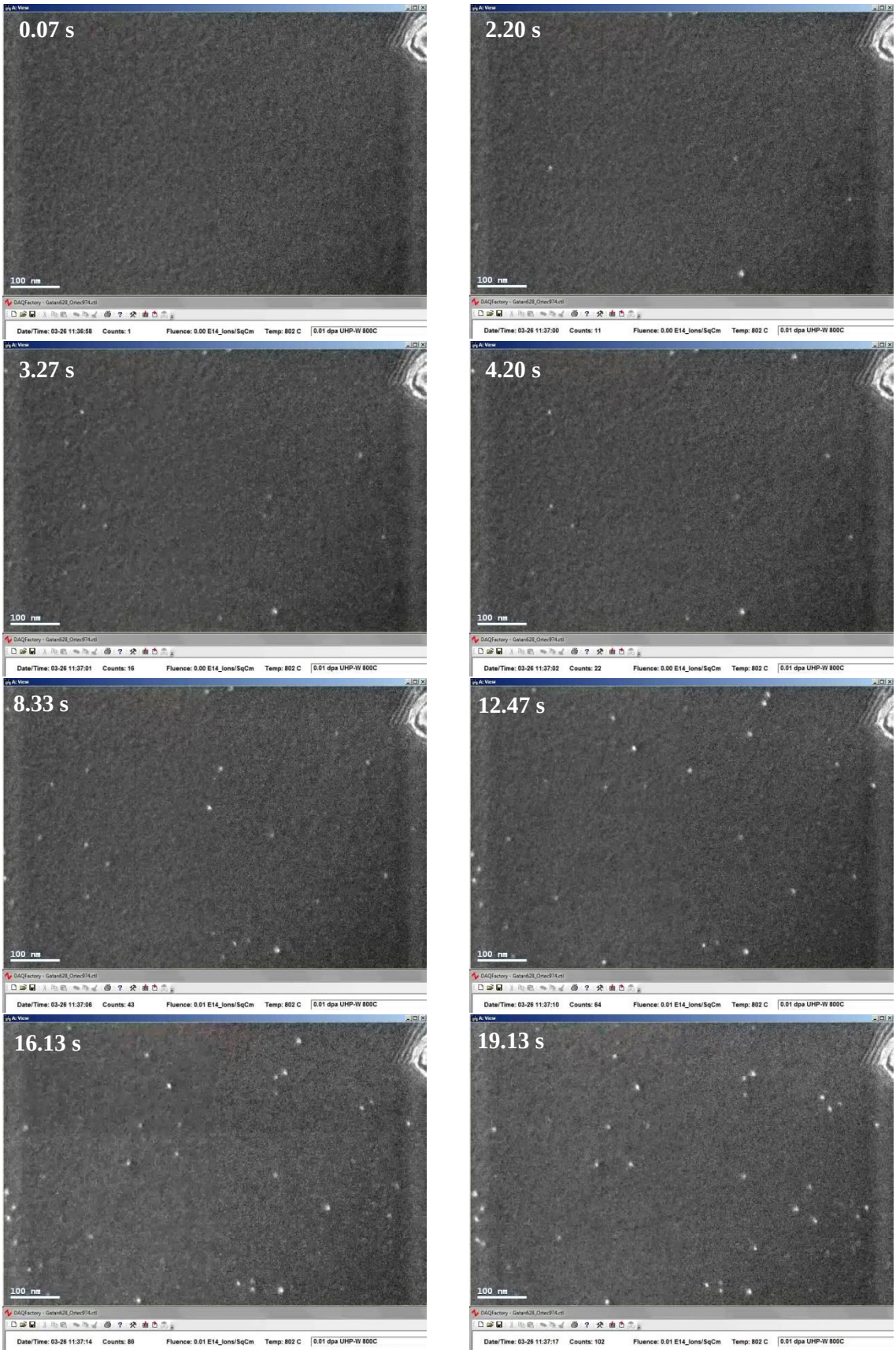


Fig 4.2 Damage development in UHP-W, irradiated up to 0.01 dpa at 800°C. **z** = [001]. (See Appendix, video 1).

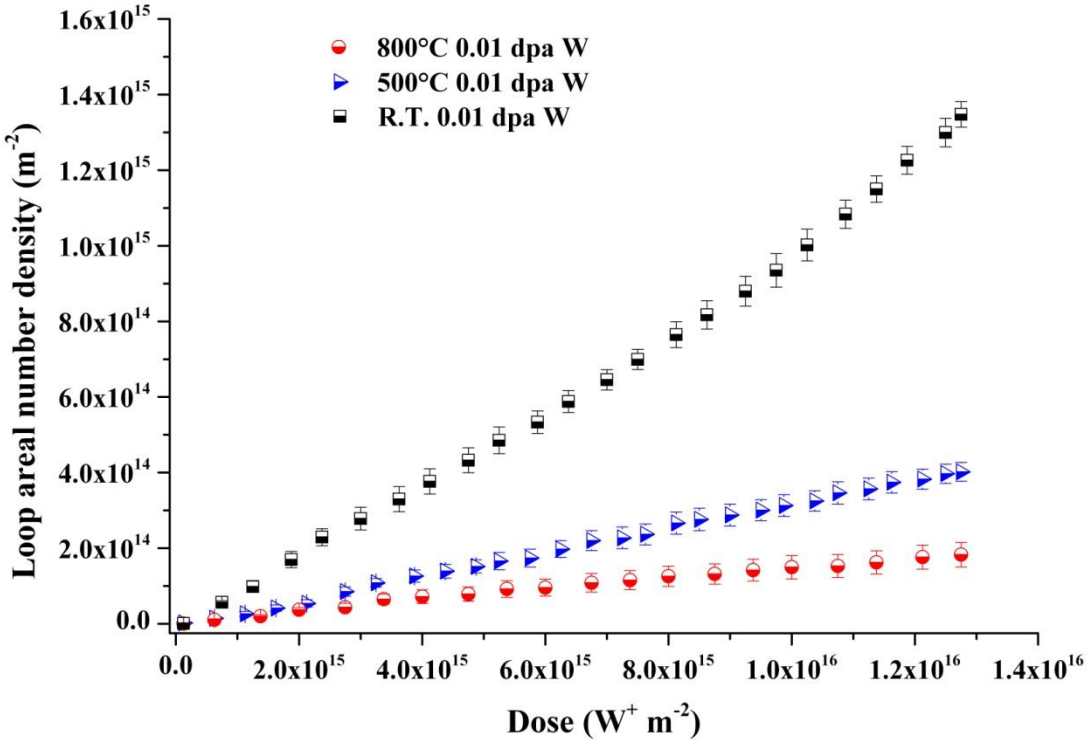


Fig 4.3 Dose and temperature dependence of loop areal number density in UHP-W, irradiated up to 0.01 dpa.

4.2.1. Defect yield and size distribution

At the terminating dose of 0.01 dpa in this experiment, the damage microstructures shown in Fig 4.4 suggested their strong dependence on temperature. The population of loops decreased while their average size gained increase, when the irradiation temperature rose from R.T. to 800°C. At a characteristic transition temperature of ~500°C, the rate of these changes accelerated. Quantitative descriptions of these trends are presented in Fig 4.5 and 4.6.

Two parameters have been introduced to characterize the early stage radiation damage, i.e. the defect yield (this section) and the cascade collapse efficiency (§ 4.2.3). The defect yield is defined as the ratio between the number of visible loops per unit area and the ion dose [103]. In other words, it measures how effectively bombarding ions introduce visible loops in the material. It can be seen in Fig 4.5 that even at R.T., the efficiency of the bombardment by 150 keV W^{+} ions was very low, only about 3%. With an increase in

temperature, the defect yield decreased further, and eventually dropped to ~0.2% at 800°C. Also presented in Fig 4.5 is the loop average image size, plotted against the irradiation temperature. At around 500°C, the rate of increase of loop sizes increased from 2.9×10^{-3} nm/K to 1.4×10^{-2} nm/K.

Loop image size distributions were obtained from measurements of weak-beam dark-field micrographs such as those shown in Fig 4.6. Similar numbers of loops (50-100) were measured under each irradiation condition. With increasing irradiation temperature, there was a consistent trend for the maximum loop sizes to shift to larger values, illustrated in Fig 4.6. Between R.T. and 300°C, loops with 1-2 nm diameters dominate in the microstructure; at 500°C, the largest fraction of loops is in the 4-5 nm category. At 800°C, 7-8 nm loops prevail over other size categories. Focusing on the predominating loop size categories, the abrupt jump from 1-2 nm to 4-5 nm at 500°C seems to agree quite well with observations in Fig 4.5. Another important observation is that once the loops had nucleated and became visible in the microscope, they tended to retain their original dimension throughout the time scale of the low dose (0.01 dpa) irradiation experiments.

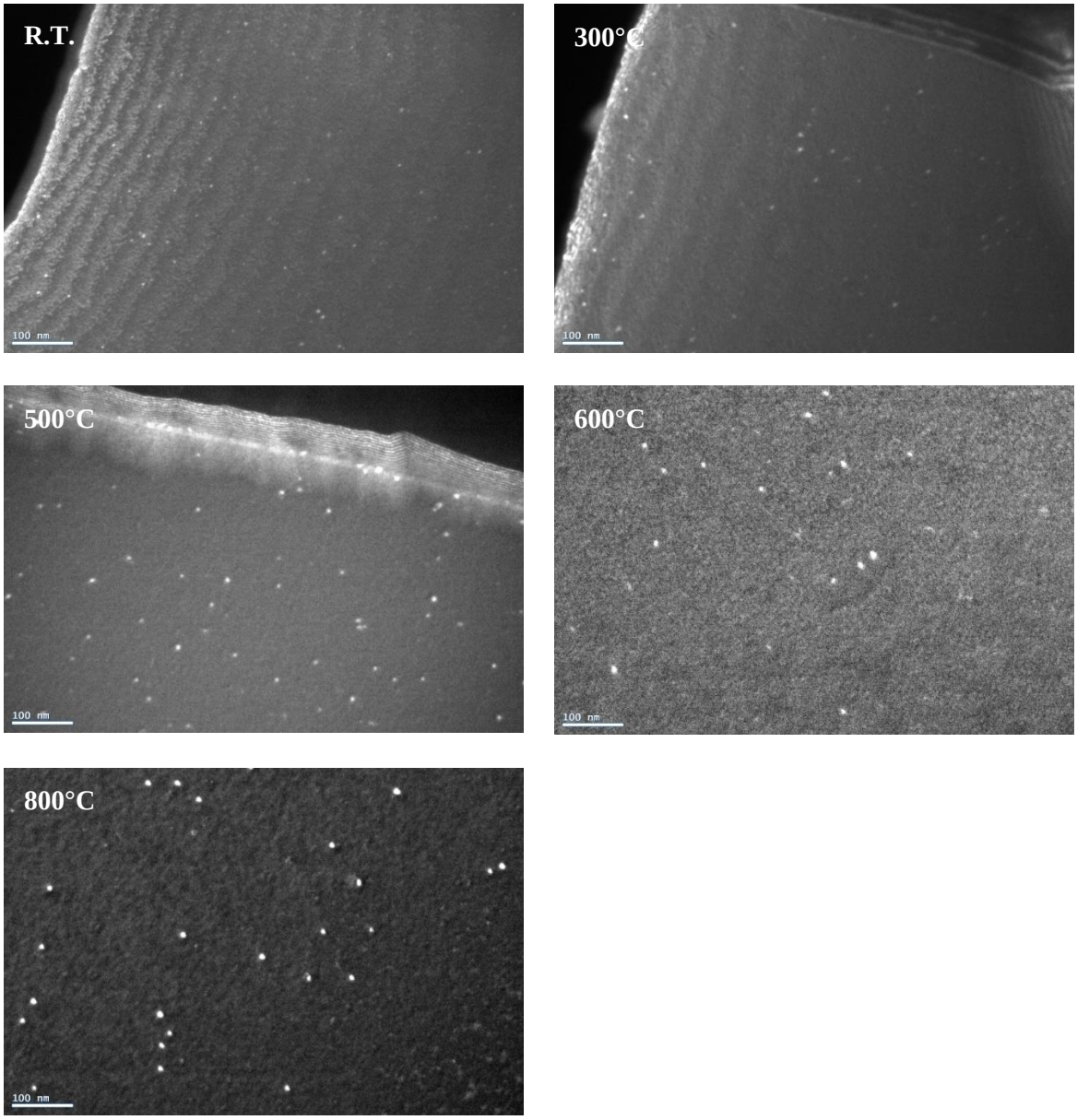


Fig 4.4 Damage microstructures imaged under weak-beam dark-field ($\mathbf{g} = 200, 3-4\mathbf{g}$) diffraction conditions in 0.01 dpa irradiated UHP-W. Temperature range: R.T.- 800°C.

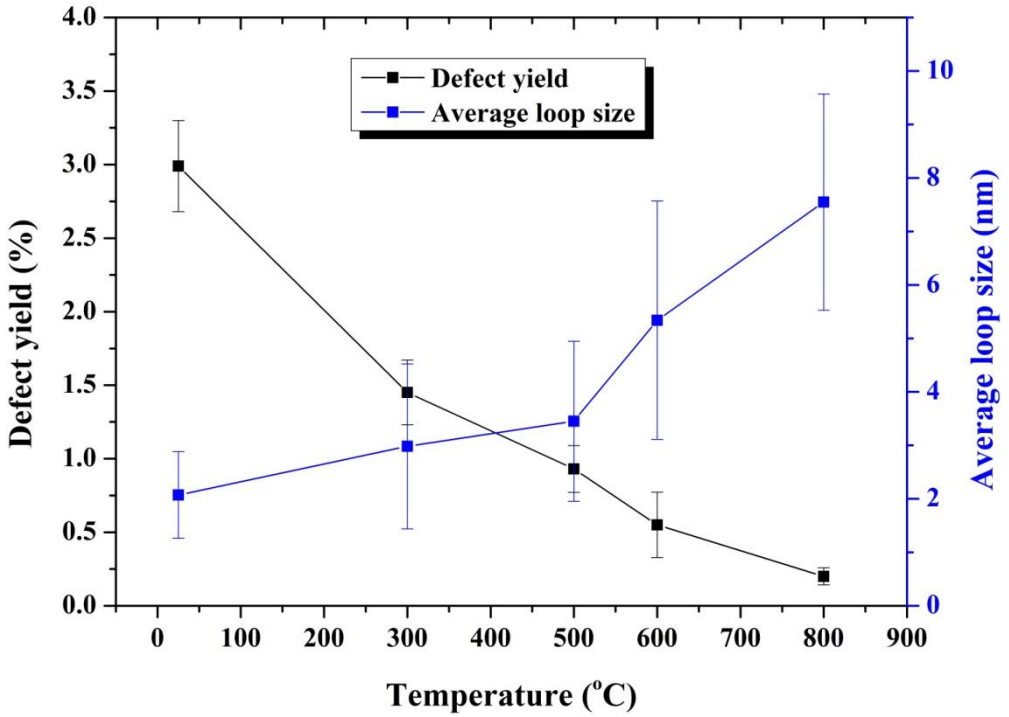


Fig 4.5 Temperature dependence of defect yield and average loop size in 0.01 dpa irradiated UHP-W.

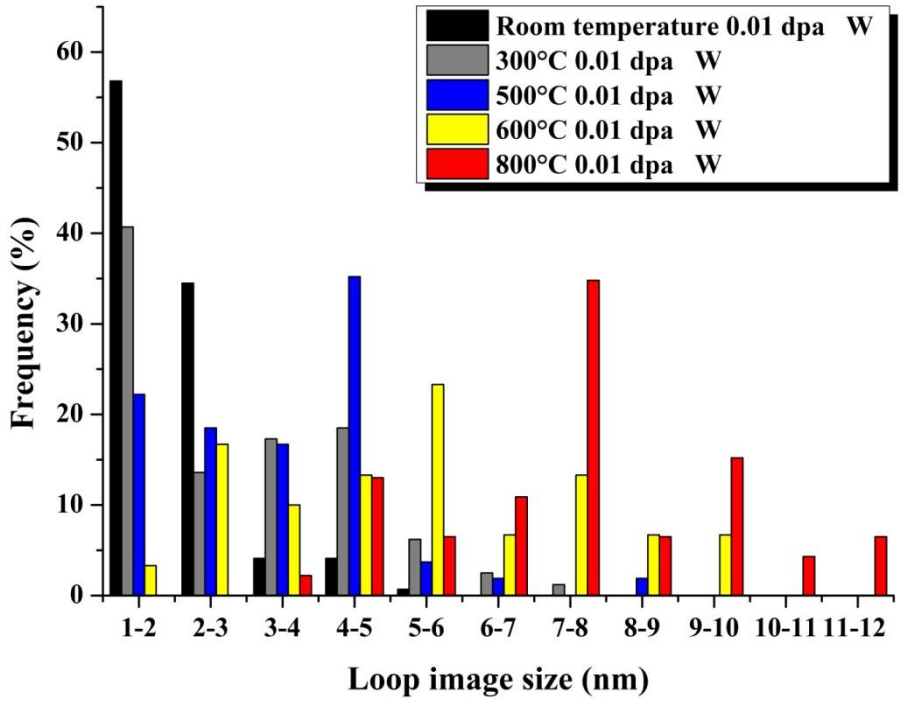


Fig 4.6 Loop image size distributions in 0.01 dpa damaged UHP-W, as a function of temperature.

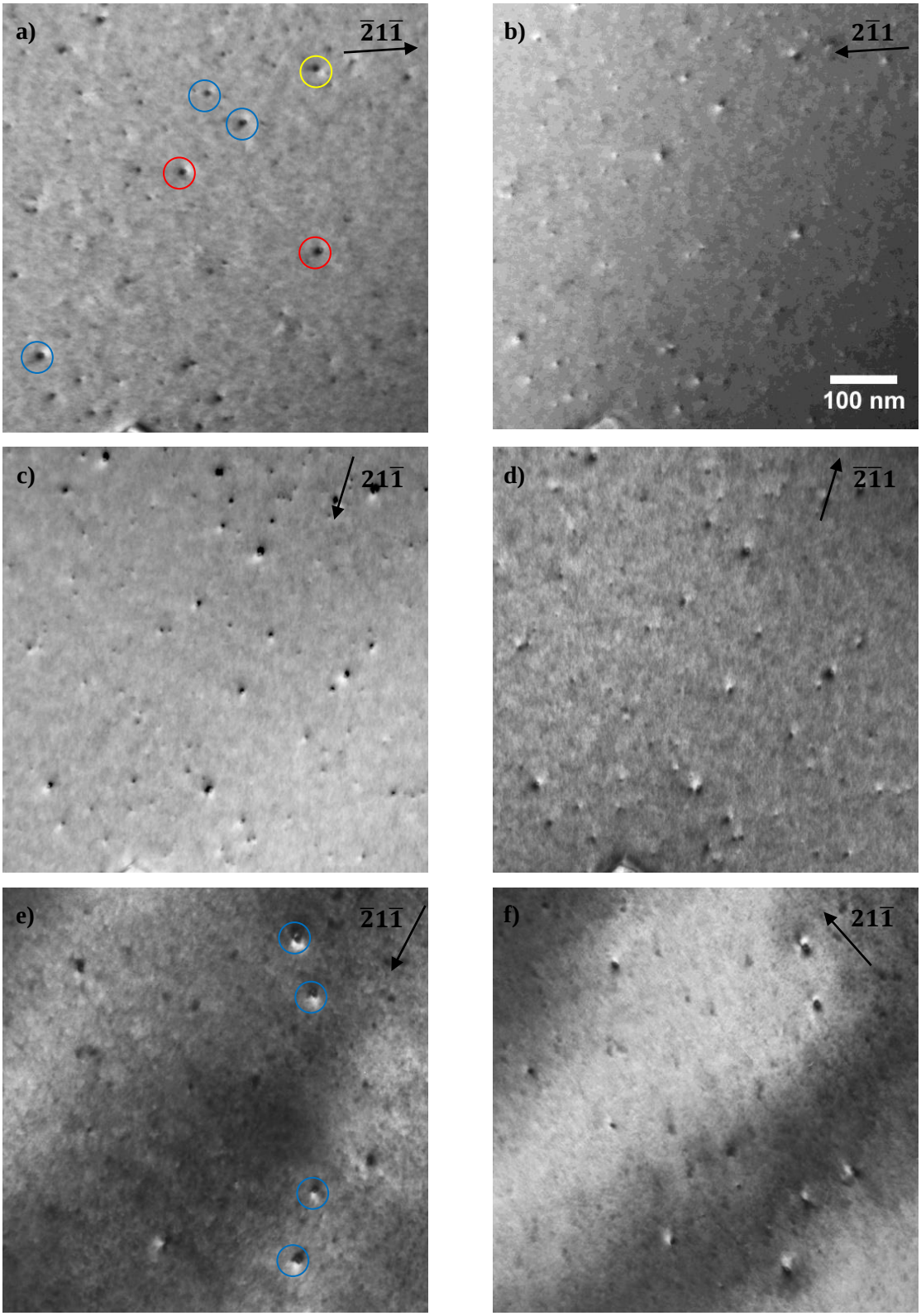


Fig 4.7 Black-white contrast micrographs taken close to **z** = [011], under two-beam dynamical dark-field conditions. a-d) R.T.; e-f) 800°C 0.01 dpa irradiated UHP-W. Pure edge ½<111> loops (blue) and <100> loops (yellow); sheared ½<111> loops (red).

4.2.2. Loop Burgers vector and nature determination

Acquiring loop Burgers vectors **b** and natures needed post irradiation analyses based on the black-white diffraction contrast theory [104, 105]. Two specimens, i.e. R.T. and 800°C irradiated UHP-W were selected, each irradiated to a dose of 0.01 dpa.

The post-irradiation analyses shown in Fig 4.7 were performed on a Philips CM20 (200 kV) microscope after the specimen had been returned to Oxford. The TEM foils have been flipped so that the irradiated surface faces downwards, to obtain stronger contrast intensities [68]. The foil was tilted to the $[011]$ zone and images of the same area were taken, using in turn the reflections **g** = $\pm(\bar{2}1\bar{1})$ and $\pm(21\bar{1})$. A considerable proportion of the loops showed strong black-white contrast. The Burgers vectors of these loops were determined by the shapes of contrast figures which depend on the value of |**g.b**|. For example, in Fig 4.7 a) where **g** = $\bar{2}1\bar{1}$, nearly all loops with well defined contrast exhibited an image feature of black-white lobes with interface structure, suggesting that |**g.b**|>1. The possible Burgers vectors of loops must therefore be either $\pm$½$[1\bar{1}1]$ or $\pm[100]$.

To determine the nature of loops observed at very low doses with sufficient confidence, a variant of the well-known technique of **l**-vector analysis was used [104]. SRIM estimation shows that in 150 keV W^+ irradiation the damage profile extends over a depth of 30 nm. An area outside the electron beam was selected and the local foil thickness was derived from an Electron Energy Loss Spectrum (EELS) using the Log-ratio method; the thickness was in the range 65-70 nm (Fig 4.8). The damage is thus expected to be confined to the bottom half of the foil. It should be noted that the validity of the conventional black-white diffraction contrast method relies on the presence of distinct layer structures within about $1.25\xi_g$ (ξ_g = extinction distance) of both upper and lower foil surfaces, so that foils at least $2.5\xi_g$ thick must be used. However, the calculated extinction distance for $\{211\}$ reflections of

a 200 kV electron beam is 40.6 nm, which means that in the present case layers from the upper surface and the lower surface would overlap [104]. As a result, the layer structure required for loop nature determination was instead defined by image simulations. The TEMACI software was used, where the loop contrast is derived from numerical solutions of the Howie-Basinski equations [106]. Images of loops at depths of 48-64 nm were simulated and are shown in Fig 4.9. The simulations were performed for vacancy type loops with Burgers vector [100] and ½<111> (all four variants included) in a 66 nm thick foil with normal **z** = [011] imaged in **g** = $\bar{2}1\bar{1}$. The loop size was 1 nm. The results of image simulations confirmed two points. First, the **g.l** >0 criterion applied for all loops with strong contrast intensities, where **l** is the black-white contrast vector, indicating that the nature of early stage damage in UHP-W is due to the collapse of vacancies into dislocation loops. Second, three types of loop morphology were found in the damage microstructure and examples of each were labelled as circles in Fig 4.7. Namely, the pure edge **b** = ½[$1\bar{1}1$] loops are in blue, **b** = ½[$1\bar{1}1$] loops with shear components are in red (habit plane on (101) or ($1\bar{1}0$)) and the pure edge **b** = [100] loops are in yellow.

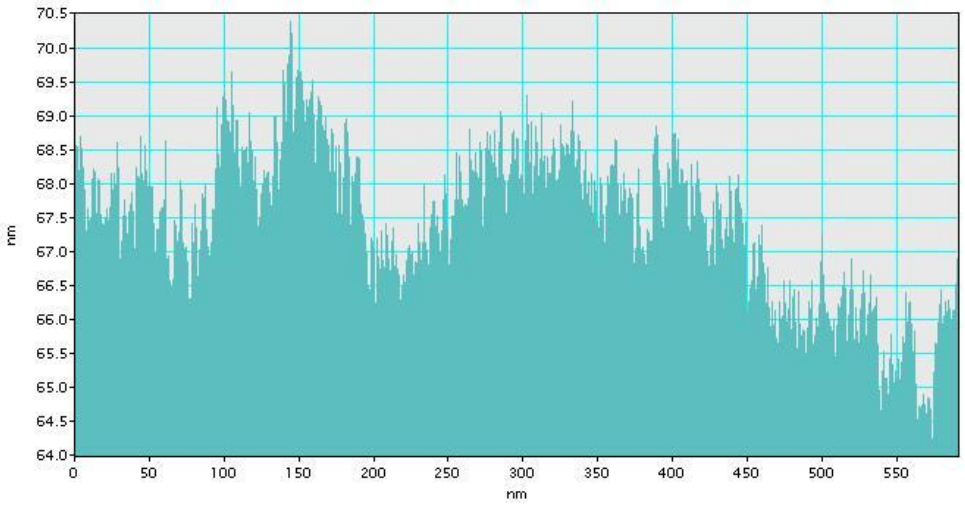


Fig 4.8 Foil thickness of R.T. 0.01 dpa damaged tungsten foil, derived from an EELS spectrum using the Log-ratio method. X-axis: lateral range; Y-axis: site thickness.

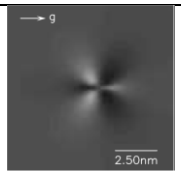
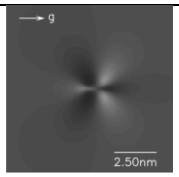
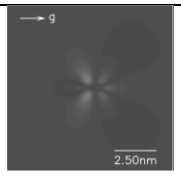
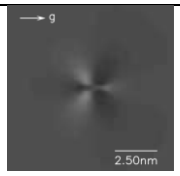
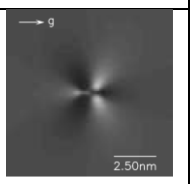
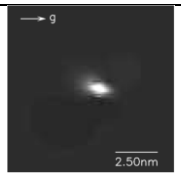
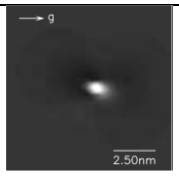
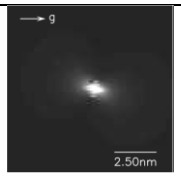
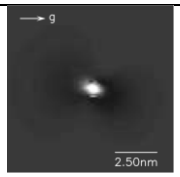
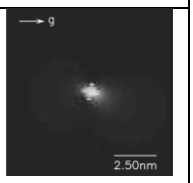
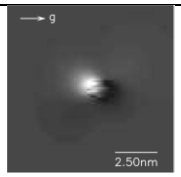
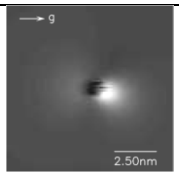
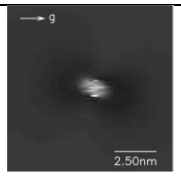
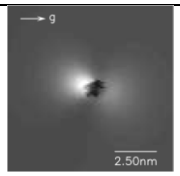
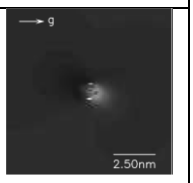
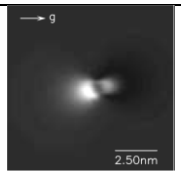
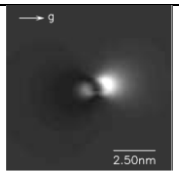
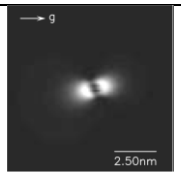
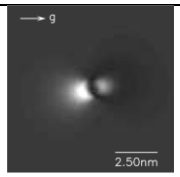
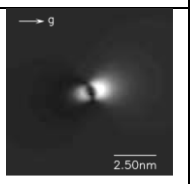
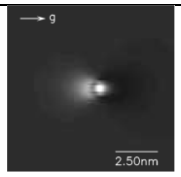
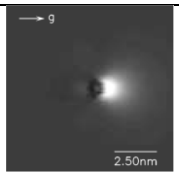
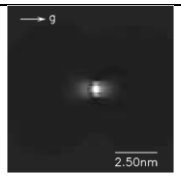
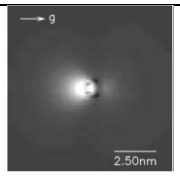
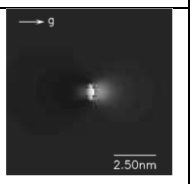
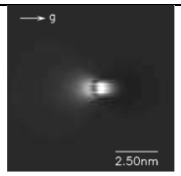
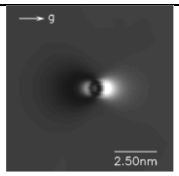
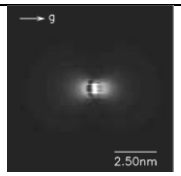
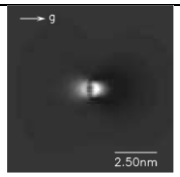
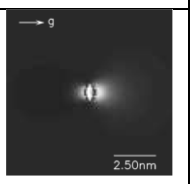
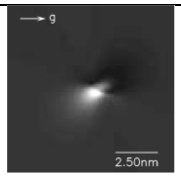
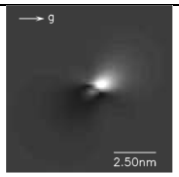
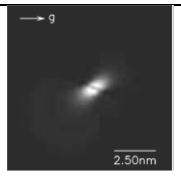
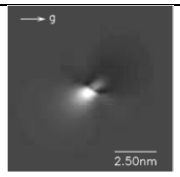
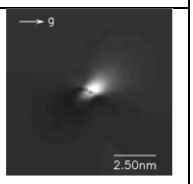
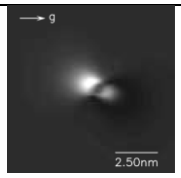
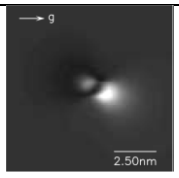
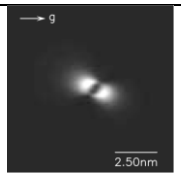
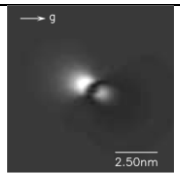
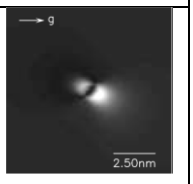
Depth	48 nm	52 nm	56 nm	60 nm	64 nm
b = ½[11$\bar{1}$] **n** = [11$\bar{1}$]					
b = ½[$\bar{1}$11] **n** = [$\bar{1}$11]					
b = ½[111] **n** = [111]					
b = ½[1$\bar{1}$1] **n** = [1$\bar{1}$1]					
b = ½[1$\bar{1}$1] **n** = [101]					
b = ½[1$\bar{1}$1] **n** = [1$\bar{1}$0]					
b = ½[1$\bar{1}$1] **n** = [0$\bar{1}$1]					
b = [100] **n** = [100]					

Fig 4.9 Results of simulations on the black-white contrasts of vacancy loops in tungsten. The simulations are for a **b** = [100] loop and four variants of **b** = ½<111> loops in a foil of 66 nm with **z** = [011]. Loop depth 48 - 64 nm; loop diameter 1 nm; loop normal **n**; diffraction condition **g** = $\bar{2}1\bar{1}$.

4.2.3. Cascade collapse efficiency

The SRIM calculations in Fig 2.4 predict that every 150 keV W^+ ion hitting the sample produces ~1200 vacancies in the local region. Based on this figure and the loop size measurements, it is possible to evaluate which portion of these vacancies is preserved in the form of a visible vacancy-type dislocation loop. In past literatures, the term "cascade collapse efficiency" has been introduced for this purpose [103, 107]. The cascade collapse efficiency is defined as the ratio between the total number of vacancies retained per visible loop and the SRIM-calculated number of vacancies generated in the cascade. Loops are assumed to have perfect circular shapes. Cascade collapse efficiencies are plotted in Fig 4.10 and are seen to increase with irradiation temperature. At 800°C in particular, ~96% of the vacancies in individual cascades are preserved in the form of a vacancy loop. As expected, the cascade collapse efficiency increases sharply beyond 500°C, in agreement with the observed loop size increase.

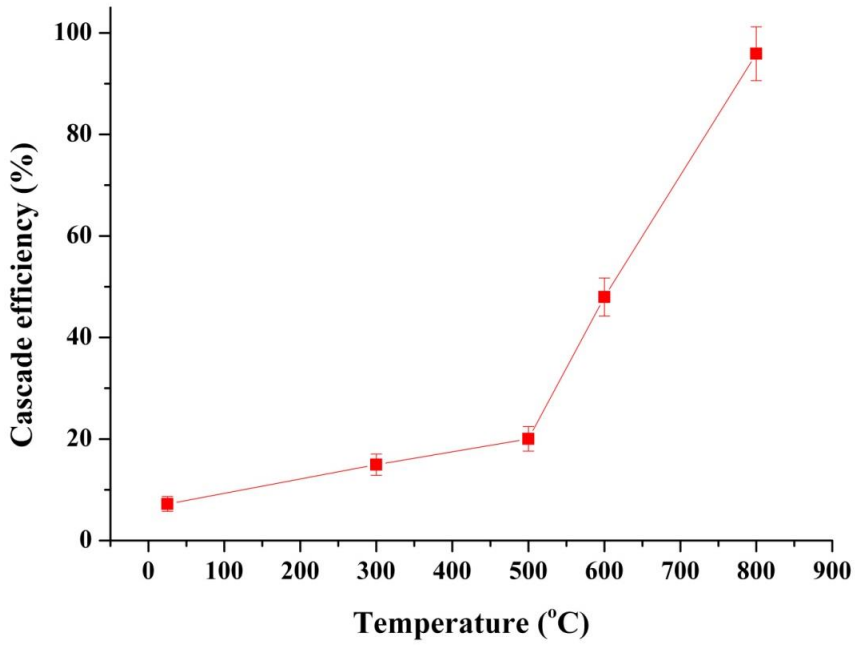


Fig 4.10 Cascade collapse efficiency as a function of irradiation temperature in 0.01 dpa irradiated UHP-W.

4.2.4. The fate of vacancies in the cascade

The cascade collapse efficiencies obtained in § 4.2.3 suggest that if collapse occurs the growing loop becomes increasingly effective in pulling in vacancies at higher temperature. At 800°C, the collapse efficiency may approach unity. However, it is also important to consider the fate of vacancies produced in the cascades which do not collapse. Indeed, since defect yields are low in all cases most cascades do not collapse to loops. Fig 4.11 is a plot of the product of loop areal number densities and loop areas (integrated from the size distribution histogram of equal-sized area of interest) as a function of irradiation temperature. Since the dose in each case was the same the total number of vacancies produced would also be the same. The declining trend of the product with increasing temperature implies that vacancies must be present in some form other than dislocation loops. The higher the temperature, the greater the portion of vacancies not present in loops. The low defect yields and the trend for yields to decrease with temperature suggest that dislocation loops is not the most stable form of agglomerated vacancies, or the recombination of vacancies with interstitials is facilitated.

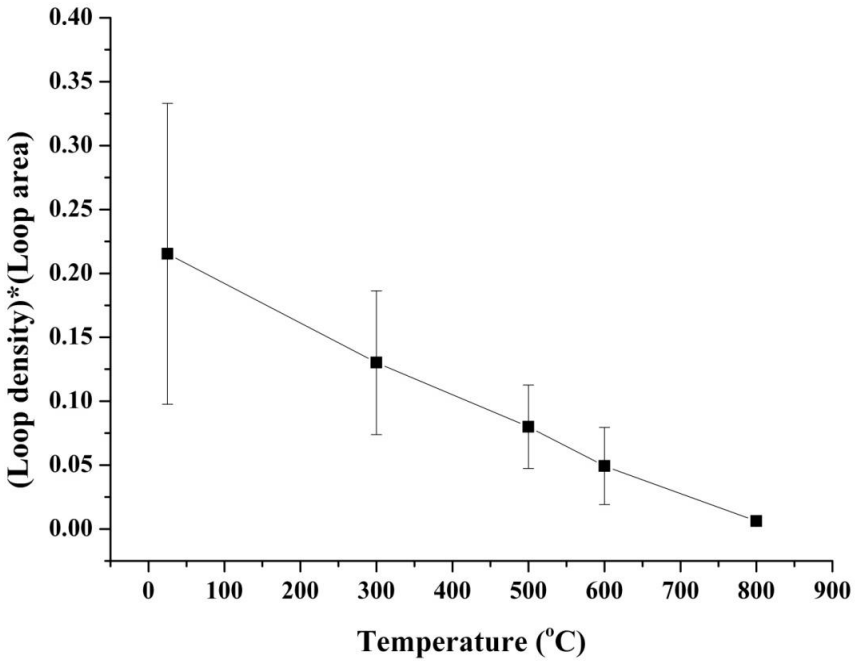


Fig 4.11 Product of loop areal number density and integrated loop area as function of temperature in 0.01 dpa irradiated UHP-W.

4.3. Microstructure evolution in tungsten (from 0.01 dpa to 1.0 dpa)

Microstructure evolution in irradiated tungsten depends on various parameters, i.e. dose, irradiation temperature, alloying elements and irradiation direction (grain orientation). The influence of each impact factor will be demonstrated in § 4.3.1 through 4.3.4, based on quantitative features such as loop number densities and loop image sizes.

4.3.1. Microstructure evolution as a function of dose and temperature

The irradiation dose and temperature are the two fundamental parameters for determining the damage microstructure. Micrographs taken under weak-beam dark-field diffraction conditions ($\mathbf{g} = 200, 3-4\mathbf{g}$) are presented in Fig 4.12, demonstrating the evolution of loop coalescence into strings[15] in UHP-W, at doses $\geq 4.0\times10^{17}$ W^+ m^{-2} and temperatures ≥ 600°C.

Fig 4.13 shows the loop number density against dose for different irradiation temperatures (300-800°C), in areas under the electron beam. The irradiations were completed close to $\mathbf{z}$ = [001]. At constant irradiation temperature, the loop number density increased with dose; while at constant dose, higher irradiation temperatures resulted in lower loop number densities. Moreover, the total loop number density seemed to saturate in the range of $(4.0 - 6.0)\times10^{17}$ W^+ m^{-2} at above 600°C. Fig 4.14 illustrates explicitly in the case of UHP-W irradiated at 800°C, how the loop image size shifted towards the larger end with the increase of irradiation dose. The fraction of 2-3 nm loops remained almost constant while the dose increased from 0.1 dpa to 0.8 dpa. Moreover, the increase of loop size was not perfectly gradual, i.e. > 10 nm loops were present whereas 7-10 nm loops were missing in the 0.2 dpa loop size distribution, suggesting that abnormal growth might have occurred for some loops.

---

[15] Definition of a string: a group of loosely attached dislocation loops, typically of the same Burgers vector and nature.

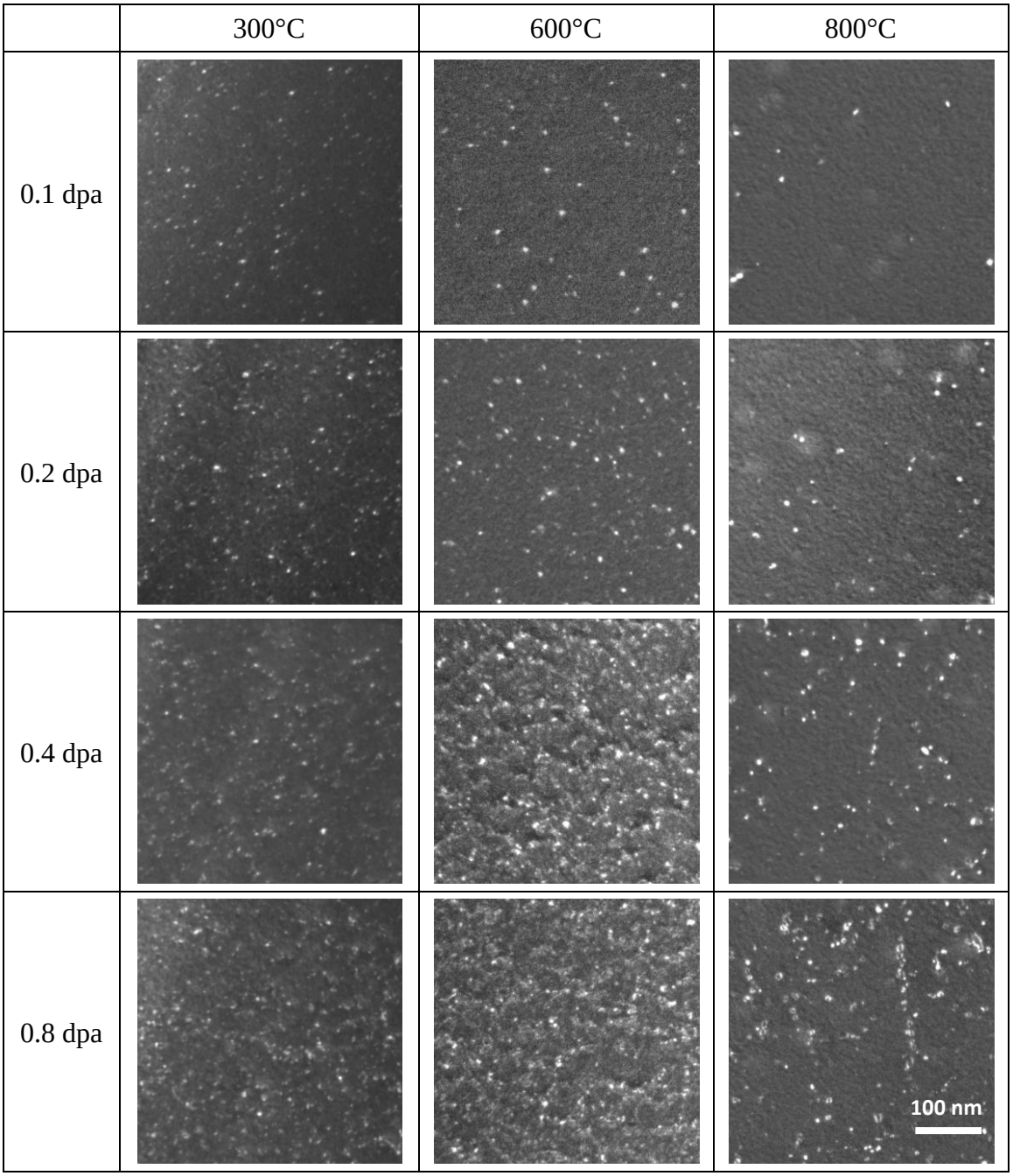


Fig 4.12 The microstructure evolution in UHP-W with increasing dose and temperature (WBDF, **g** = 200, 3-4**g**).

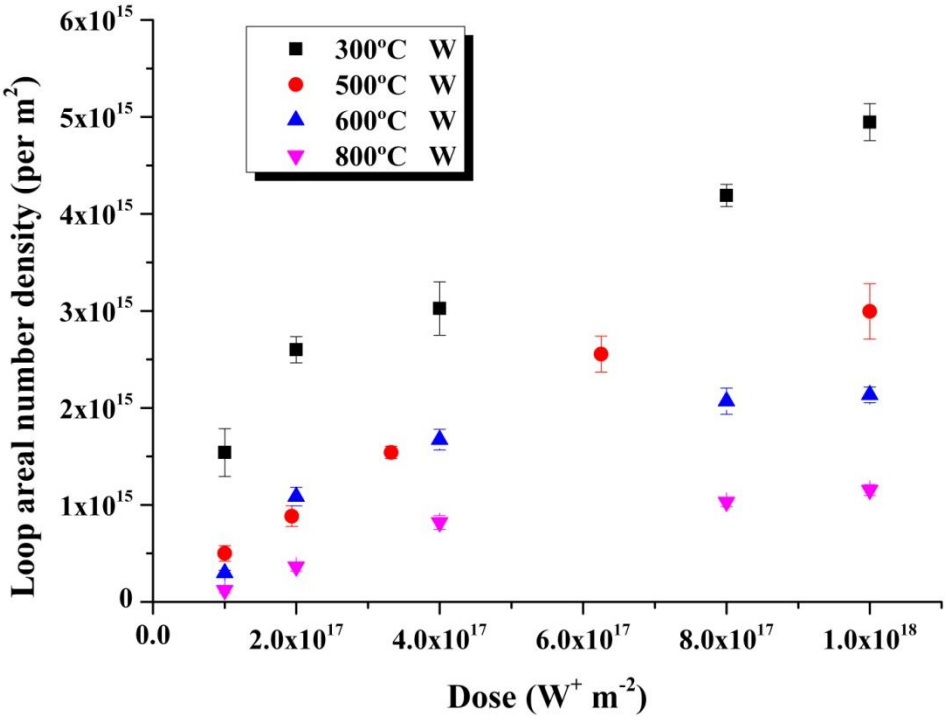


Fig 4.13 Loop areal number density in UHP-W as a function of dose and temperature.

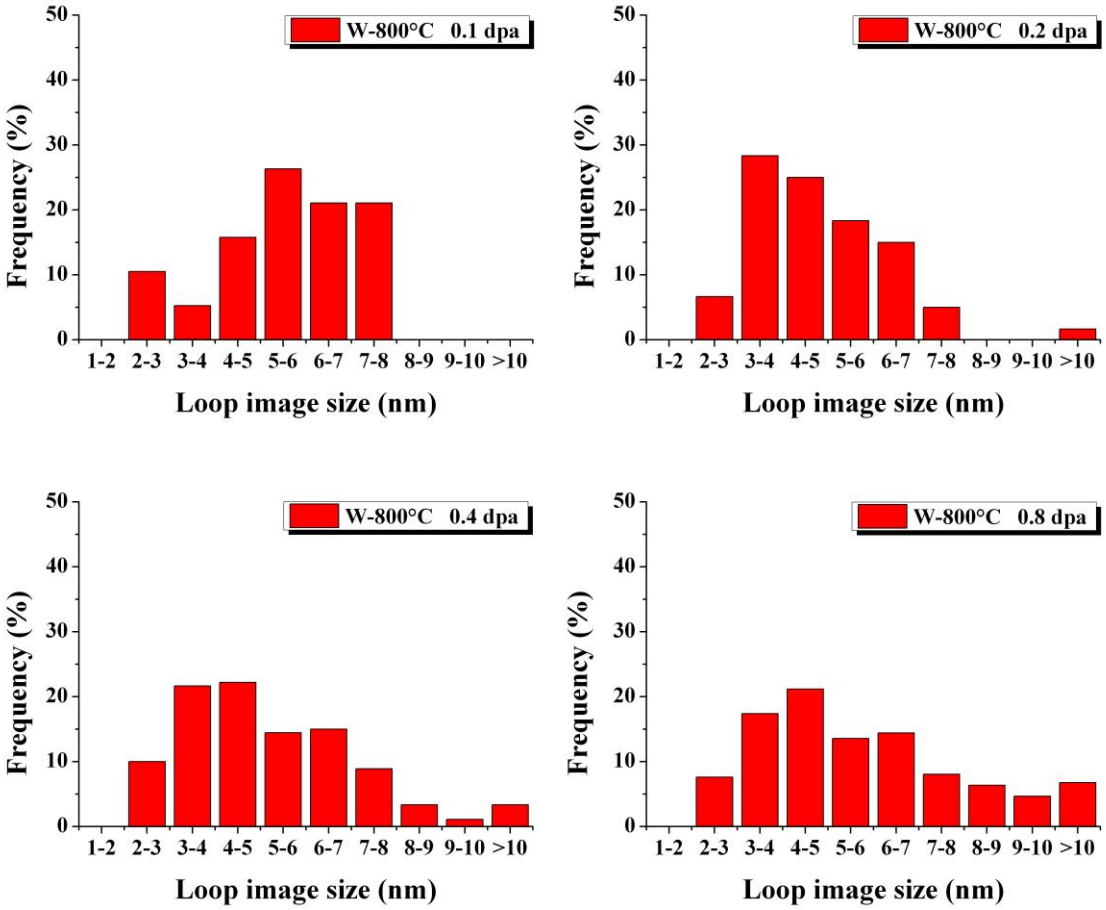


Fig 4.14 The overall loop image size distributions in UHP-W, irradiated at 800°C to doses of 0.1 dpa, 0.2 dpa, 0.4 dpa and 0.8 dpa.

4.3.2. Microstructure evolution as a function of alloying elements (Re, Ta, V)

The effects of alloying elements (5 wt.% Re, Ta, V) in tungsten are explored by tracing the evolution of loop areal number density with the accumulation of irradiation dose at three irradiation temperatures, i.e. 500°C, 600°C and 800°C. Most irradiations for such comparison were carried out close to the **z** = [001] orientation, except W-5Ta (800°C, **z** = [113]), labelled with a '*'.

Fig 4.15 shows the following trends for irradiations at 500°C: 1) loop areal number densities were higher in the W-alloys than in UHP-W throughout the dose range (10^{17}-10^{18}) $W^{+}m^{-2}$; 2) loop density in W-5Re and W-5Ta saturated at ~6×10^{17} W^{+} m^{-2}, but not in W-5V; 3) the saturation of loop number density in W-5Ta resulted in a turnover on the effectiveness of alloying elements on the damage microstructure, i.e. at doses lower than 6×10^{17} W^{+} m^{-2}, Ta>V>Re; at doses above 6×10^{17} W^{+} m^{-2}, V>Ta>Re.

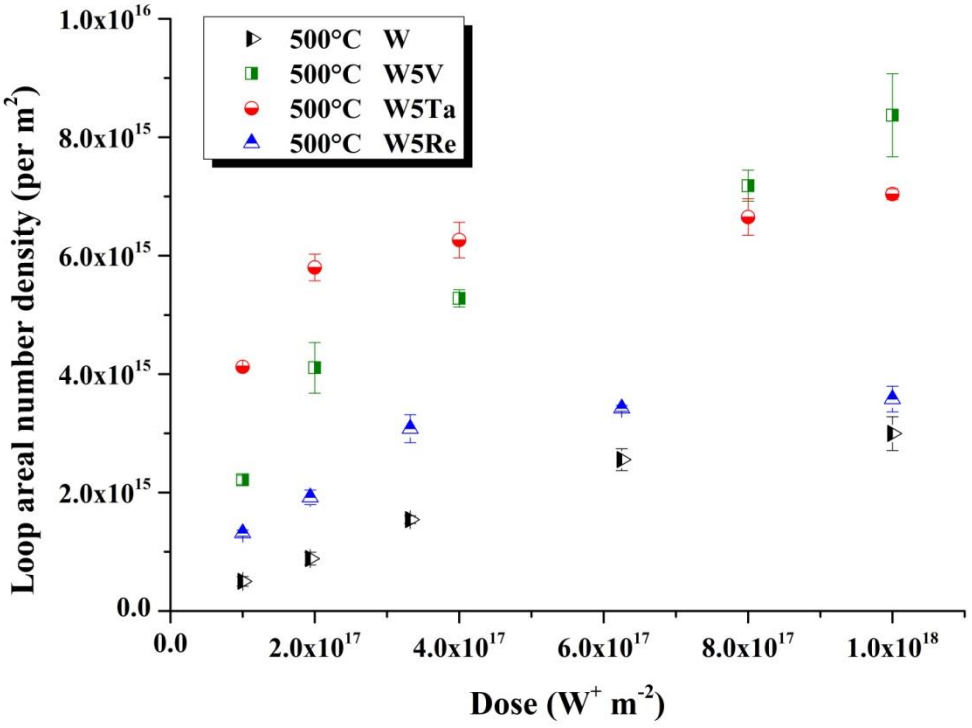


Fig 4.15 Effects of alloying elements on the loop areal number density at 500°C.

The damage evolution trends for W-alloys at 600°C are illustrated in Fig 4.16. At 10^{17} W^{+} m^{-2}, there was no distinguishable difference between the three types of alloy, but all of them gave rise to higher loop number densities compared to UHP-W. At doses beyond 10^{17} W^{+} m^{-2}, V had a larger effect on the microstructure than Re and Ta; and the difference between Ta and Re was barely discernible, i.e. V>Ta≈Re. Both W-5Ta and W-5Re showed loop density saturation at doses higher than 4×10^{17} $W^{+}m^{-2}$. No saturation was discovered in W-5V up to the final dose 10^{18} W^{+} m^{-2}.

At 800°C, higher number densities of loops were again present in the W-alloys than in UHP-W (Fig 4.17). Loop number densities saturated at a dose of ~4×10^{17} W^{+} m^{-2} for UHP-W, W-5Ta and W-5Re. A limitation with this data set was that during the irradiation, W-5Ta and W-5V were irradiated in a non-[001] direction, as finding (001)-grains was very difficult. Therefore, comparing the loop number density data between W-5Ta and W-5Re required extra caution. The resemblance displayed between the two materials at 600°C and the considerable difference exhibited at 800°C suggest a possible influence of grain orientations on damage development. This is described below. Finally, the W-5V data was not included in the plot because massive dislocation networks were produced instead of individual loops in the irradiated (011)-grain.

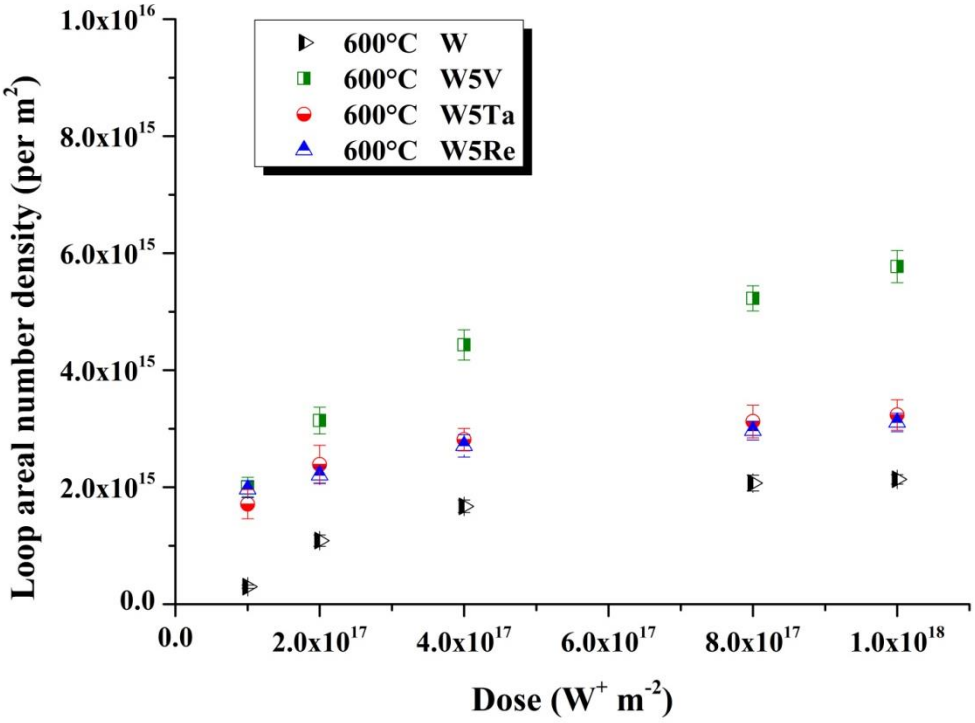


Fig 4.16 Effects of alloying elements on the loop areal number density at 600°C.

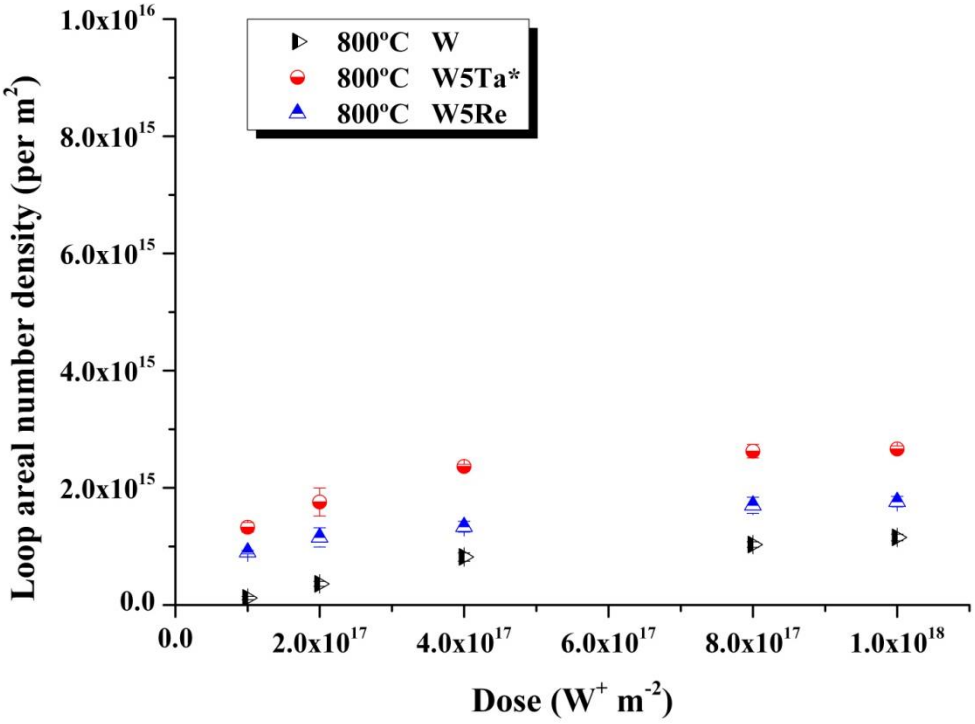


Fig 4.17 Effects of alloying elements on the loop areal number density at 800°C.

4.3.3. Microstructure evolution as a function of grain orientation

The effect of grain orientation was studied. It was found that **z** = [011] and **z** = [111] grains favour the formation of loop string networks, whereas in **z** = [001] foils, the damage microstructure featured more isolated loops. Examples are shown in Fig 4.18. It is important to note that loop strings were also observed in **z** = [001] foils, however only in UHP-W at temperatures ≥ 600°C, without any network formation. On the contrary, irradiations at the other two grain orientations seemed to lower the temperature threshold for loop strings/networks to form, based on similar observations at 500°C in W-5Ta (**z** = [011] and [111]). The materials investigated were polycrystalline and it was therefore possible to analyse the damage microstructure of irradiated non (001)-grains, but outside the electron beam. Analysis of the strings seen in Fig 4.18 reveals that the majority lay close to the [100] direction. Moreover, many small loops were found embedded within the networks. The process of string network formation is illustrated in W-5V, irradiated at 800°C in **z** = [011] (Fig 4.19). The network evolved by the nucleation of small loops (same **b** and nature) which joined into short strings, and then coalesced. At 0.2 dpa, a directionality of loop strings appeared: the projected direction of some strings lay close to the [100] direction, whereas others lay at an angular distance (< 30°) with respect to this direction. Later in Fig 4.27, combined video frame analysis and image simulations show that loop segments/strings may have contained shear components. Network formation did not occur until ~0.4 dpa, when the loop strings reached moderate length (tens of nm) and density. The curly shapes of loop strings were consequences of the string- string/loop interactions. On the whole, the connectivity of the strings increased with dose. Unlike W-5Ta irradiated to 1.0 dpa, few individual loops were seen embedded in the networks of UHP-W.

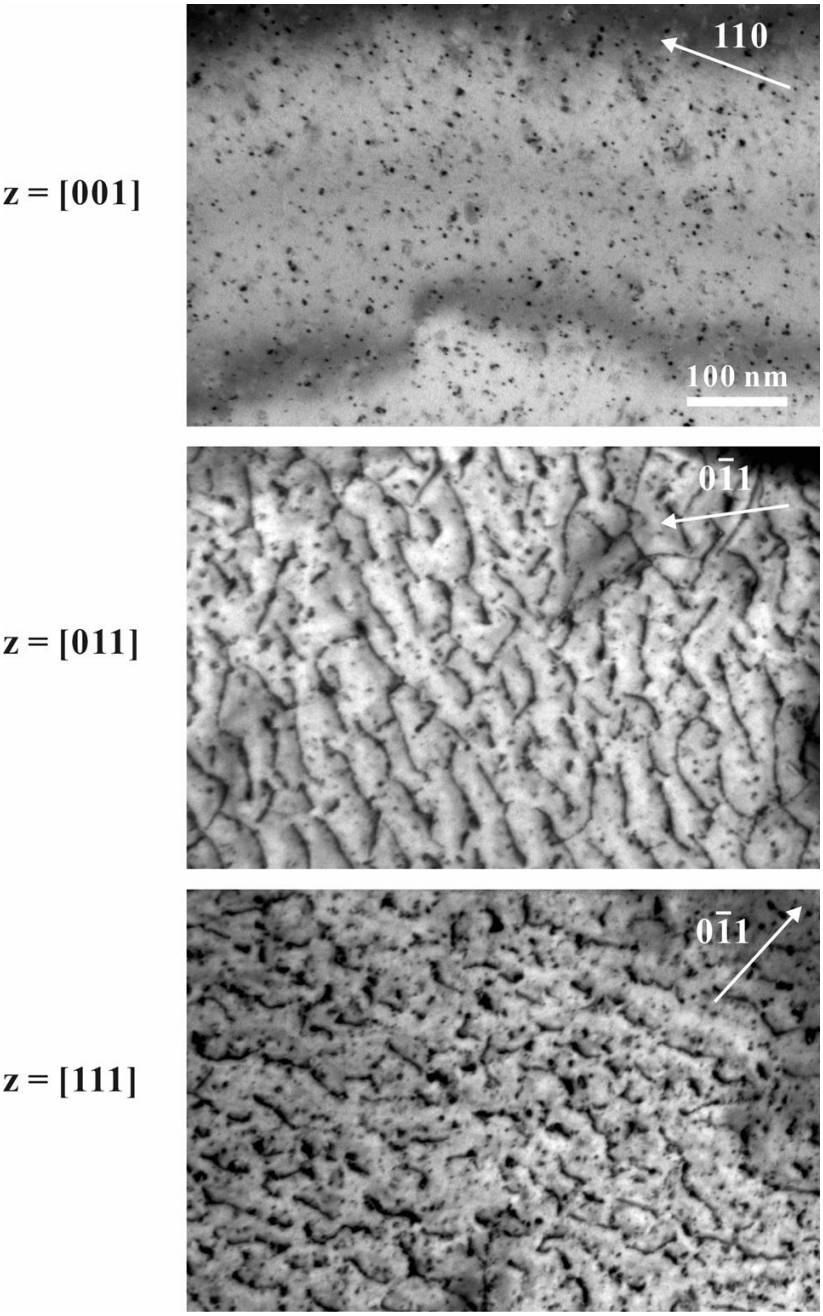


Fig 4.18 Radiation damage microstructure varies with respect to grain orientations, illustrated with the W-5Ta specimen, irradiated at 500°C up to 1.0 dpa.

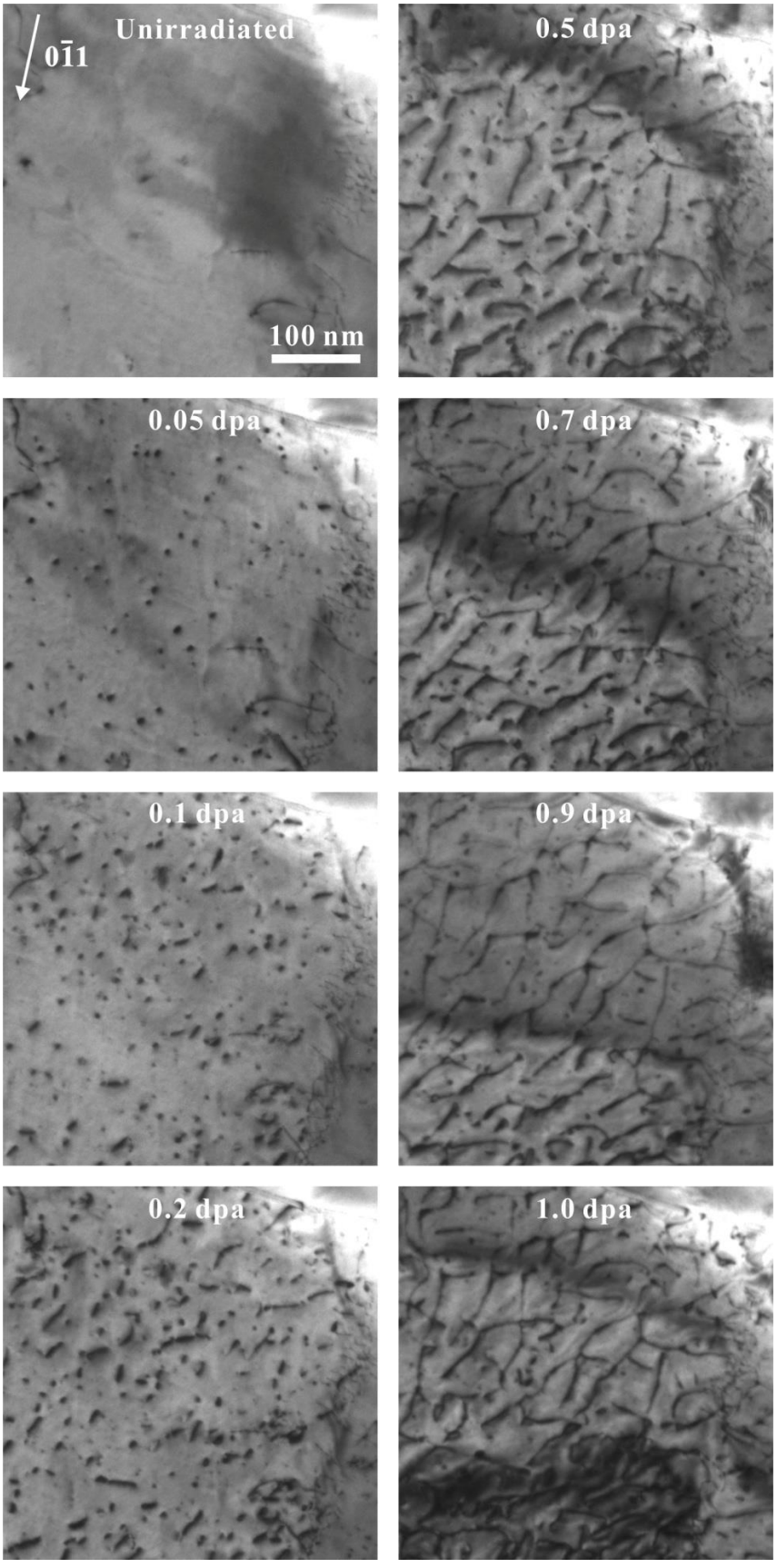


Fig 4.19 Loop network formation in W-5V, irradiated at 800°C in **z** = [011] orientation.

4.4. Dynamic behaviour of observable point-defect clusters in tungsten and alloys

The key sources of understanding the evolution of damage microstructure in tungsten come from observations of loop dynamic behaviour. At moderate doses, the damage microstructure evolved by movements of individual loops, and loop elastic interactions and reactions (absorption and coalescence) with close neighbours. At higher doses, some loops gathered to form strings, as seen in examples shown in § 4.3, loop-string interaction and string-string interaction thus become dominant in controlling the microstructure development. In § 4.4.1 - 4.4.4, various examples will be presented to illustrate the four categories of loop dynamic behaviour listed above.

4.4.1. The motion of individual loops

Individual loops were found to exhibit hopping motions in the irradiation experiments of this thesis. This behaviour occurred in all materials studied. However, holding the irradiation temperature but blocking the 150 keV W^+ ion beam seemed to make a large difference between W and W-alloys. During such in-situ annealing experiments (lasting a few minutes, more details in Ch 5), pronounced loop hopping behaviour was observed only in UHP-W. In order to characterize the hopping of loops, the term "loop displacement" has been adopted, referring to the relative displaced distance of the loop from its site of origin.

Fig 4.20 shows an example of loop hopping in UHP-W during an 800°C irradiation in the **z** = [001] orientation. The loop in hopping motion is labelled with (→) in Fig 4.20. The (projected) hopping direction of the loop is found to be parallel to <110>, which indicates that the Burgers vector of the loop is **b** = ½<111> [108]. In the first 25s of hopping motion, the loop displaced within (-20 nm, +10 nm), and its size remained ~4 nm. It then underwent a sudden growth to ~7.5 nm in the interval from 25.40s to 25.47s. Simultaneously, the displacement range dropped to (-10 nm, 0). A quantitative picture of the process is illustrated

in Fig 4.21, where the loop displacement and its image size (diameter) are plotted against elapsed time. Each cycle demonstrated some difference in either the absolute hopped distance or the length of intervals between hops. For instance, during the intervals between 0-2.5s, the loop seemed to have been pinned quite strongly, suggesting that a cluster of point defects (e.g. vacancies, impurity atoms) though invisible for TEM observation, may be blocking it from hopping further to -20 nm. However in the interval between 12.5-15s, the loop seemed to hop smoothly in the range of (-20 nm, +10 nm), suggesting that at this time there were no cluster-like obstacles in its path of hopping, and that the previously existing clusters may have either migrated elsewhere or annihilated with defects of the opposite nature. Similar explanation may account for the large hop (~15 nm) of the loop observed between 26s and 28s, despite of its gain in size. Hence, it is important to note that the 1D motion of an individual loop reflects the dynamic influence of the changing environment, due to the continuous bombardment of energetic W^+ ions. Hops may be initiated or caused by the nearby impact of W^+ ions, as a result of detrapping of the loop from obstacles (e.g. impurities, clusters) [109]. With the increasing loop size, detrapping becomes more difficult, which is probably why the loop remained stationary from 28s onwards.

Apart from the size of the dislocation loop, another significant factor affecting the magnitude of hopping distances is the temperature. This will be carefully demonstrated in Fig 5.12, where the irradiation dose and the post-annealed time were kept comparable for UHP-W specimens.

The role of alloying elements on the hopping motion of loops was explored by comparing the annealing behaviour of UHP-W and W-alloys irradiated to identical doses at the same temperature. The magnitudes of loop displacements, the frequency of hopping events and the number of loops exhibiting hopping behaviour were all significantly lower in

the W-alloys, in comparison with the UHP-W. This implies that the loop hopping was strongly restricted by the alloying atoms.

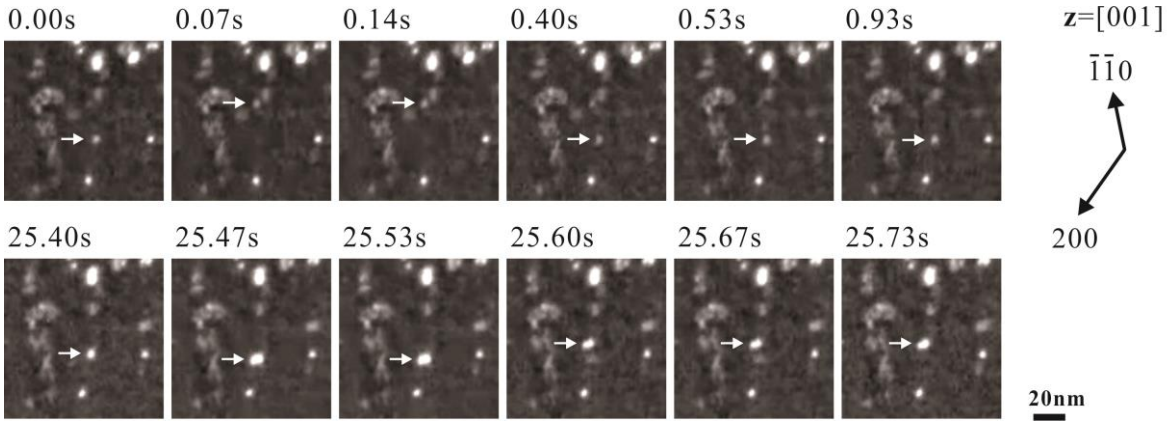


Figure 4.20 The image sequence of loop hopping in UHP-W (800°C) and its variation of displacement with respect to time and size. (See Appendix, video 2).

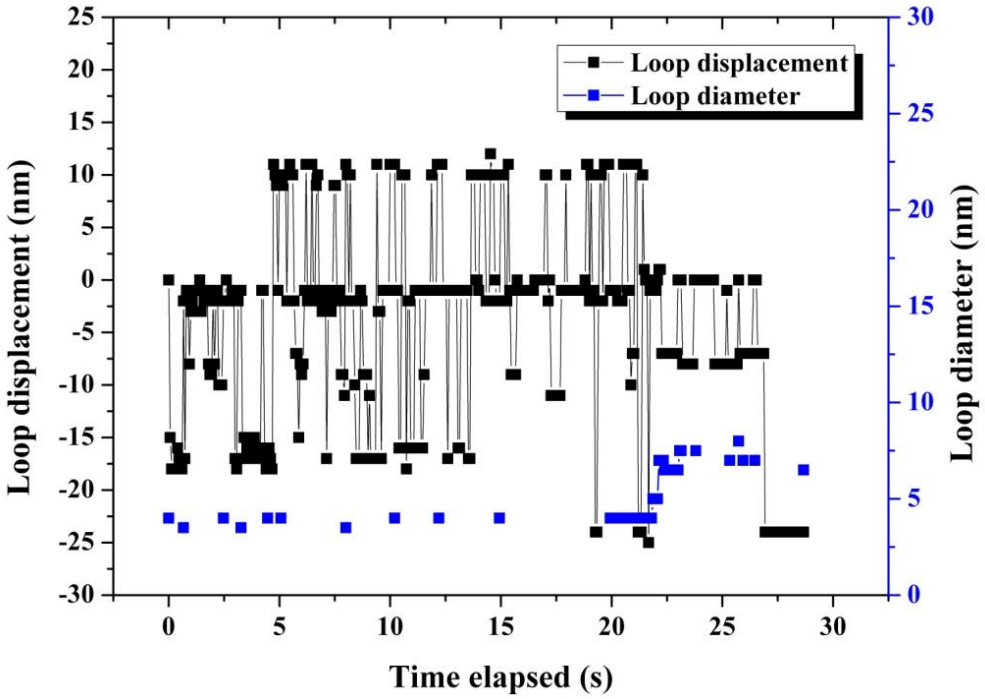
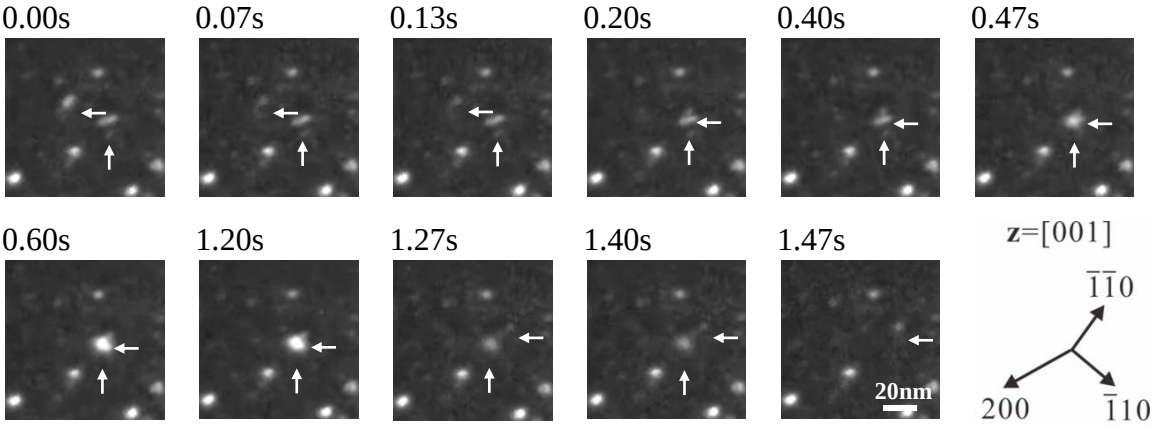


Fig 4.21 The hopping distance of a dislocation loop in UHP-W (800°C) varies as a function of its image size.

4.4.2. Loop-loop elastic interactions and reactions

Loop-loop elastic interactions and reactions make up the basis of loop dynamics once the irradiation dose is beyond the dose limit for cascade overlap (estimated to be > 0.01 dpa in § 4.2). Solely elastic interactions among dislocation loops have been discovered with interesting effects. The Burgers vector of a dislocation loop may change and its habit plane may change by rotation. More commonly observed are cases in which both elastic interactions and loop reactions are involved. For example, one loop may approach neighbouring loops by attractive forces, followed by subsequent absorption or coalescence reactions. Fig 4.22 through Fig 4.31 are case studies of the various scenarios discussed here, taken from both UHP-W and W-alloys during the irradiation.

Fig 4.22 shows the process in which elastic interactions between loops of different sizes led to a Burgers vector change of the smaller loop. Two interacting loops under ion irradiation in W-5Re (500°C, in **z** = [001] orientation) are labelled B (←) and A (↑). Loop A is considerably larger than loop B. The initial Burgers vector of loop B can be deduced from the projection of its 1D motion, in this case parallel to $[\bar{1}10]$. This implies **b** = $\pm$½$[\bar{1}1 \pm 1]$. At 0.20s, loop B was attracted towards A. The two loops remained side-by-side until 1.27s, when the projected direction of motion of loop B changed to $[\bar{1}\bar{1}0]$. This indicates that the Burgers vector of loop B had changed to $\pm$½$[\bar{1}\bar{1} \pm 1]$. Meanwhile, the contrast of loop A evolved from a 'side-view disc' to a 'dot', and it was finally lost to the surface. Note that at this **z** = [001] orientation, all four variants of **b** = ½<111> have equal chances of being lost to the surface. Therefore, it is likely that the contrast change of loop A before its loss resulted from a rotation of its habit plane or a change in its depth position.



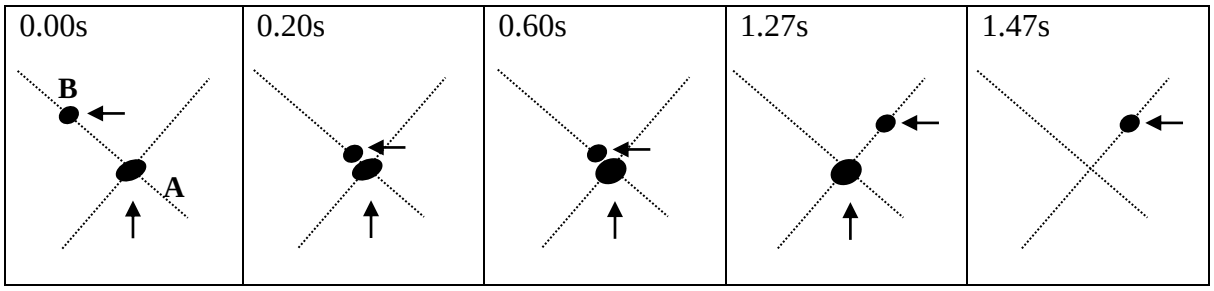
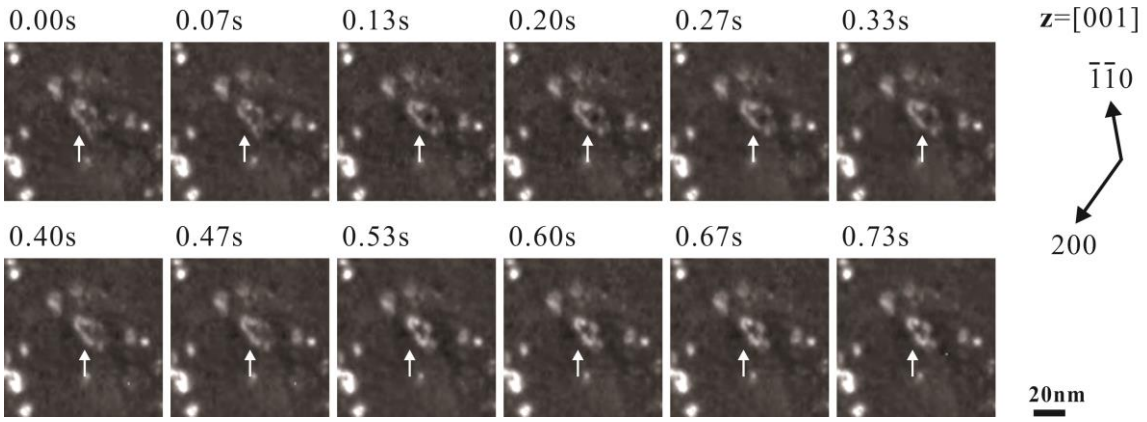


Fig 4.22 The Burgers vector of loop B (←) changes from $\pm$½[$\bar{1}1 \pm 1$] to $\pm$½[$\bar{1}\bar{1} \pm 1$] after interacting with the large loop A (↑) in W-5Re during the irradiation. The sketches illustrate the major changes taken place during the observed interval. (See Appendix, video 3).

Fig 4.23 shows a combined effect of elastic interaction and reactions in UHP-W. During successive frames between 0.13s and 0.53s, the dimension of the loop (labelled as ↑) first expanded from 16 nm to 20 nm, and then shrank to 15 nm. The mechanism in which this occurred is not clear. Possibly the loop first attracted a defect cluster of the nature to achieve expansion, and then subsequently absorbed a defect cluster of the opposite nature, resulting in shrinkage. These clusters were not seen, but similar reactions must have occurred since the size change was substantial.



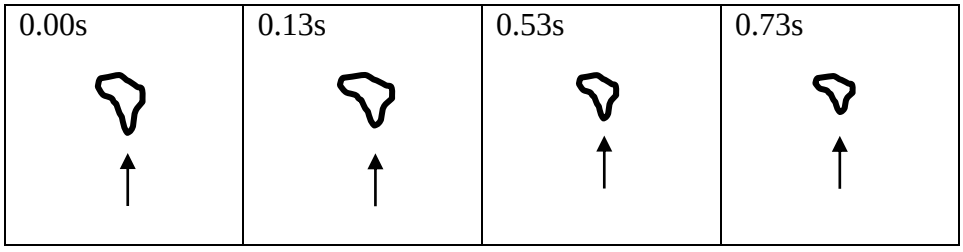


Fig 4.23 Loop shape variation due to elastic interactions and reactions with its neighbourhood in UHP-W, irradiated at 800°C in **z** = [001] orientation. The shape variations at different time intervals are sketched below the frames.

The remaining examples are direct evidence of dislocation reactions being promoted by mutual elastic interactions. The scenarios have been grouped according to the relative image sizes of the reacting loops. In Fig 4.24 and Fig 4.25, where the two reacting loops differed considerably in image size, absorption took place. In Fig 4.26 and Fig 4.27, where the two closely spaced loops in reaction were of comparable size, coalescence took place.

In Fig 4.24 (W-5Re, irradiated at 500°C in **z** = [001] orientation), the larger loop A (↑ 7.9 nm) took a two-step hop (at 0.07s, and 7.93s) to approach loop B (→ 5.3 nm). The hopping direction of A suggests that its Burgers vector is **b** = ±½[1$\bar{1}$1]. The two loops remained close for about a further 9s before merging. Judging from the unchanging contrast of loop A, it is likely that it has maintained its Burgers vector.

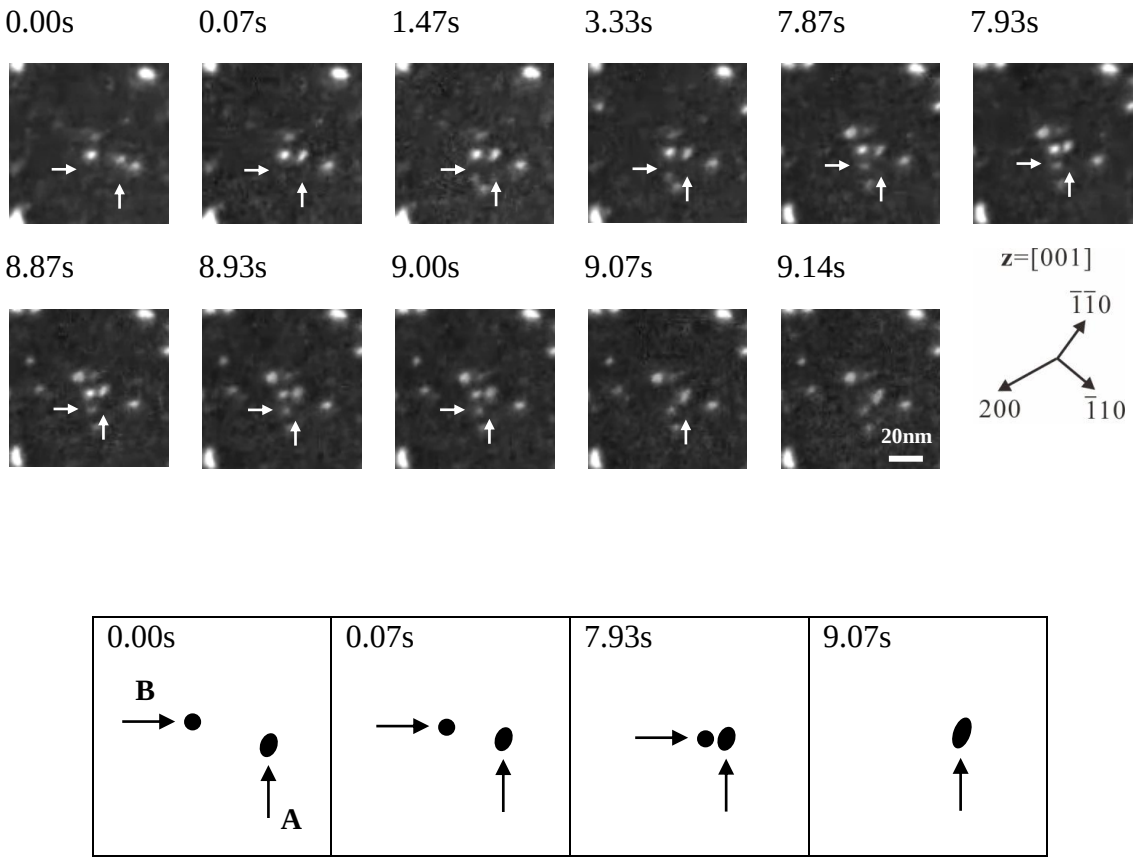
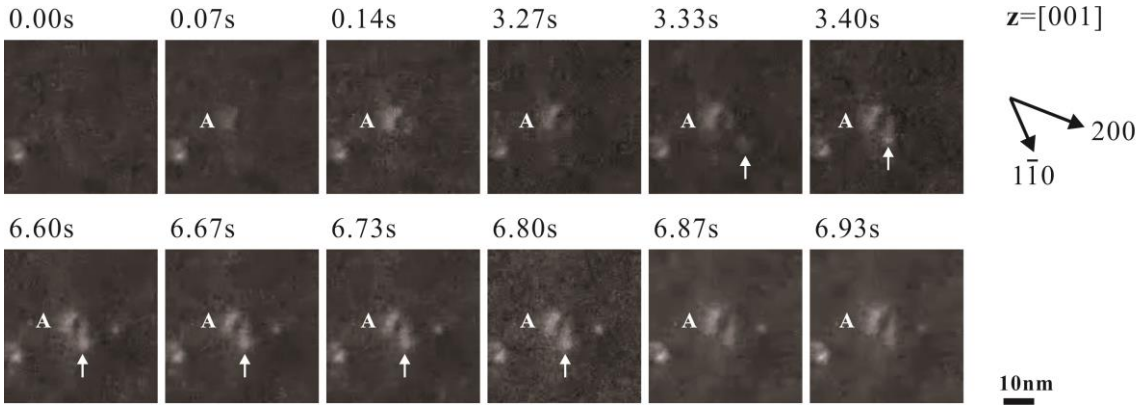
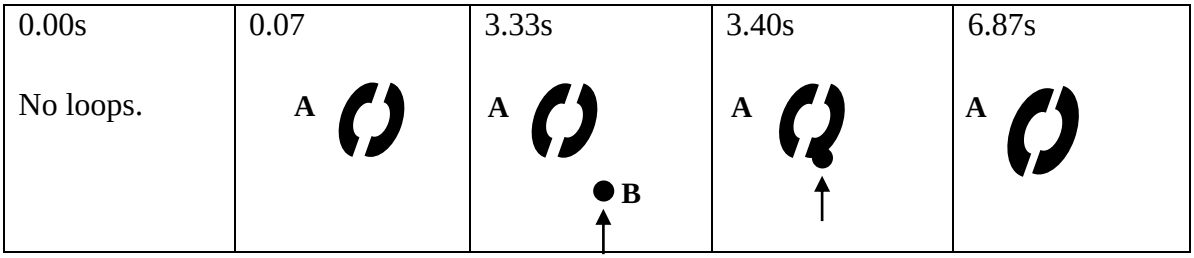


Fig 4.24 Loop absorption in W-5Re, irradiated at 500°C in **z** = [001] orientation. Loop A (↑ 7.9 nm) with **b** = ±½[1$\bar{1}$1] is absorbed by loop B (→ 5.3 nm). The absorption process has also been illustrated with sketches below the frames.

In Fig 4.25 (W-5V, irradiated at 500°C in **z** = [001] orientation), loop A (8.5 nm) shows a double-arc contrast under weak-beam dark-field conditions $\mathbf{g} = 200, 3-4\mathbf{g}$. According to image simulations using the TEMACI software, the feature matches well with $\mathbf{b} = \pm[100]$. At 3.33s, a small loop B labelled with (↑ 3.1 nm) is nucleated and hops in the projected direction of $[\bar{1}10]$ to approach loop A, implying that loop B has a Burgers vector $\mathbf{b} = \pm\frac{1}{2}[\bar{1}1 \pm 1]$. At 6.87s, loop A absorbs loop B and undergoes a notable size growth to 9.6 nm.





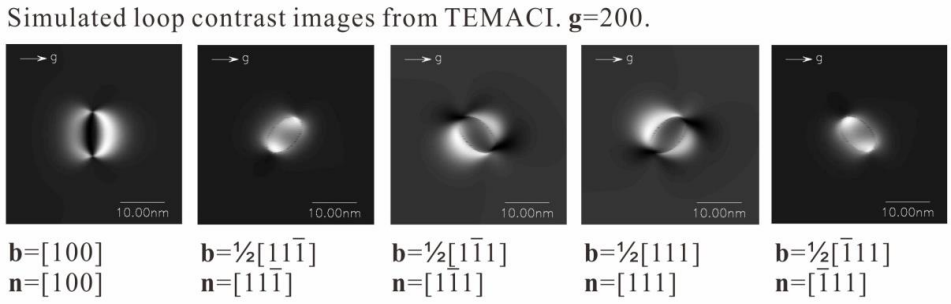


Fig 4.25 Loop absorption observed in W-5V, irradiated at 500°C in **z** = [001] orientation. Loop B (↑ 3.1 nm) with $\mathbf{b} = \pm\frac{1}{2}[\bar{1}1 \pm 1]$ is absorbed by loop A with $\mathbf{b} = \pm[100]$. As a result, loop A increases from 8.5 nm to 9.6 nm in image size. (See Appendix, video 4).

An example of loop coalescence is displayed in Fig 4.26. Frame sequences were extracted from the W-5Re specimen, irradiated at 500°C in **z** = [001] orientation. Loop A (→ 7.4 nm) and loop B (↑ 6.1 nm) of similar size merge into one larger loop (circled, size ~9.0 nm), showing that A and B must be of the same nature. Unfortunately there was no 1D motion shown to derive the Burgers vector of the loops. In the last frame, the large loop was lost, implying that it must be of type **b** = ½<111>, which may easily glide to the surface.

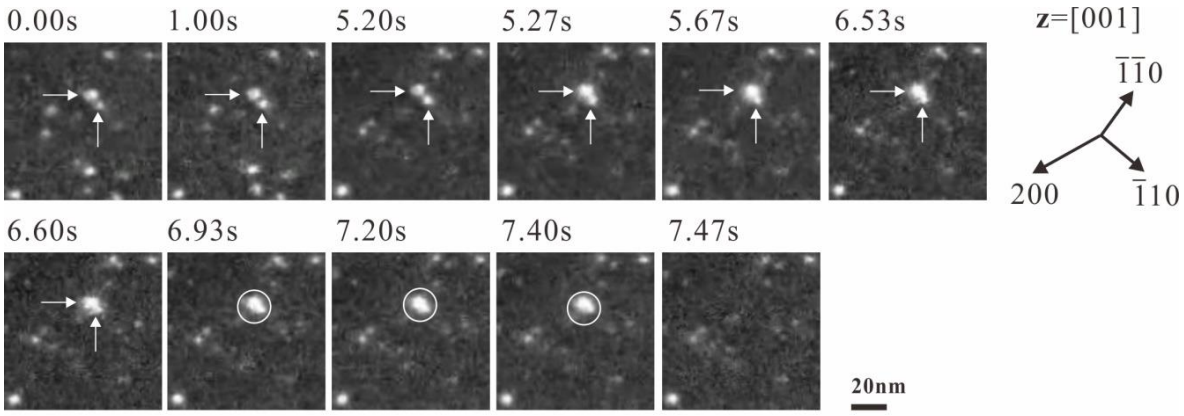


Fig 4.26 Loop coalescence taking place in W-5Re, irradiated at 500°C in **z** = [001] orientation. Loop A (→ 7.4 nm) and loop B (↑ 6.1 nm) of similar size and the same nature merge into one large (○ 9.0 nm) **b** = ½<111> type loop.

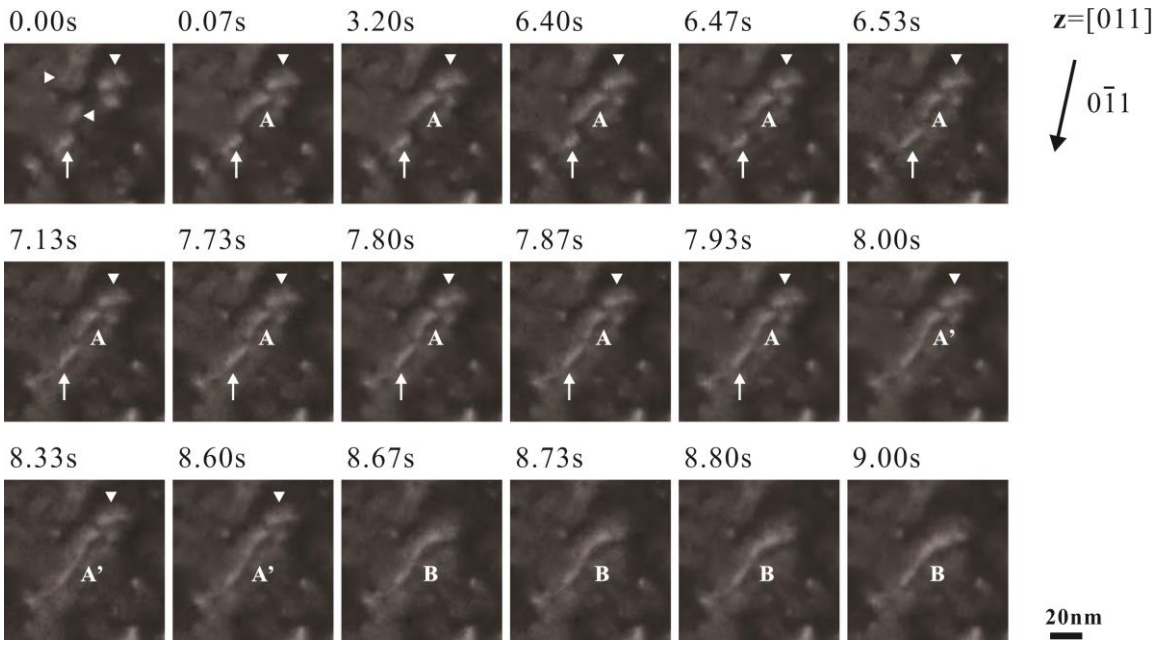
Figs 4.27 - 4.28 illustrate a more complex case of loop-loop interaction followed by coalescence into a string configuration. This example was taken from the W-5V specimen, irradiated at 800°C in **z** = [011] orientation and three major changes have occurred in the frames presented. From 0.00s to 0.07s, loop C (►) moves about 30° to coalesce with loop D (◄), forming loop A. This was the first major change. The second major change took place between 7.73s and 8.00s, when loop A and loop E (↑) gradually join into one single string A'. The third major change occurred when loop F (▼) finally joins this single string A' in forming string B. From 8.60s to 8.67s, loop F (▼) hopped along the $[0\bar{1}1]$ direction,

implying that its Burgers vector was **b** = $\pm$½[$1\bar{1}1$] or $\pm$½[$\bar{1}\bar{1}1$]. This can also be deduced from the **g.b** criterion (§ 2.6.3).

This interaction can be analysed in detail as follows. First, all loops involved in the coalescence process (A to F) must be of the same nature, almost certainly interstitial, due to the increasing length of the string (loop) after each step of loop coalescence. Furthermore, the curly shape of string B has also been investigated with the help of image simulations. Any loop visible in **g** = $0\bar{1}1$ would have **b** = $\pm$½[$1\bar{1}1$] or $\pm$½[$\bar{1}\bar{1}1$]. Simulations have been performed under the imaging conditions of the frames, for a foil thickness of 100 nm. Loops were assumed to be 10 nm in diameter and located at 15 nm beneath the upper foil surface. Four habit planes were considered for each type of Burgers vectors, covering cases when the loops were of pure edge type and contained shear components. The results of the simulations are summarized in Fig 4.28. Based on observations, it has been known that B is made up of string A' and loop F. Comparing the simulated contrast images, string A' fits best with loops of ½[$\bar{1}\bar{1}1$] lying on **(**$\bar{1}\bar{1}1$) planes, suggesting that it is of pure edge type. Meanwhile, loop F matches well with loops of **b** = ½[$\bar{1}\bar{1}1$] lying on **(**$0\bar{1}1$) planes. Moreover, the angular distance between string A' and loop F was fairly close to 35°, which is the angle between ($\bar{1}\bar{1}1$) and ($\bar{1}01$) or ($\bar{1}\bar{1}0$) planes. Therefore, it is highly possible that the curly shape of string B is a result of the coalescence between a pure edge string and a loop with shear components. It is therefore not necessary for all loops to rotate habit planes to their pure edge orientation in order for coalescence to proceed. This could also be a plausible explanation for the geometrical features of dislocation networks seen in W-5Ta and W-5V (Fig 4.18 - 4.19), i.e. sometimes the projected direction of loop strings are not perpendicular to the (110) vectors.

To sum up, loop-loop elastic interactions are closely associated with loop reactions. Elastic interaction may promote reactions by causing a change of Burgers vector or habit

plane, and even force ½<111> loops into cooperative 1D motion. Subsequent to loop elastic interactions, loop absorption and coalescence reactions are involved, giving rise to loop growth and loop string formation which are crucial in the evolution of damage microstructure.



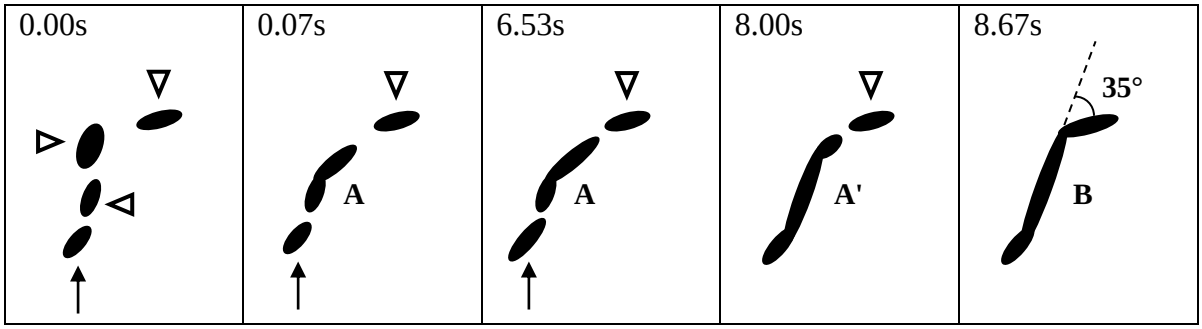


Fig 4.27 Loop string formation in W-5V (800°C, in **z** = [011] orientation) - lateral displacements plus habit plane variation of ½<111> loops. (See Appendix, video 5).

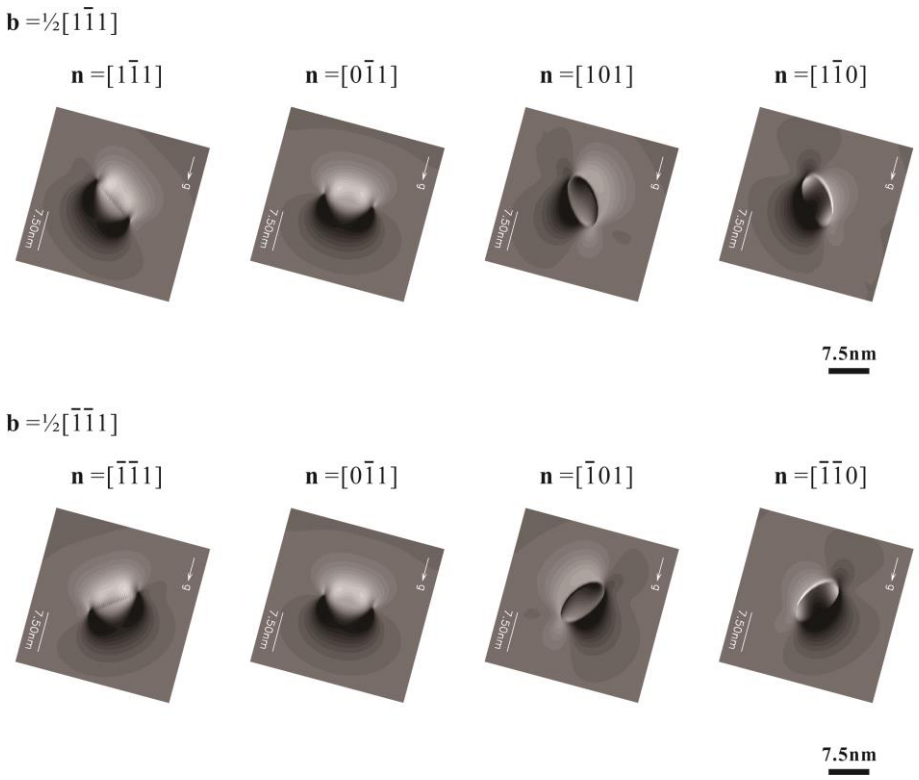


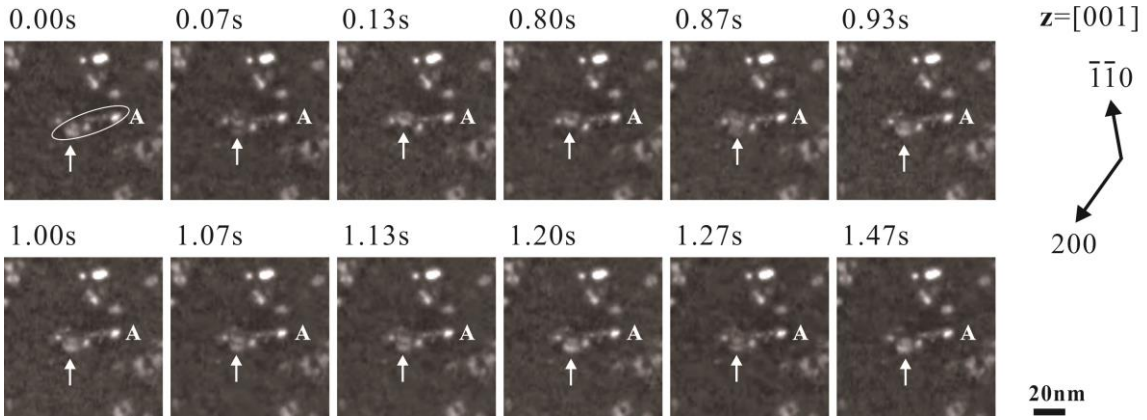
Fig 4.28 TEMACI image simulations of loop with **b** = ±½[1$\bar{1}$1] and ±½[$\bar{1}\bar{1}$1] under weak-beam dark-field **g** = 0$\bar{1}$1, 3.5**g**. **n** stands for habit plane normal. Foil thickness: 100 nm; loop diameter: 10 nm; depth of the loop in the foil: 15 nm.

4.4.3. Loop-string and string-string elastic interactions and reactions

Loop string formation was found either in preferred grain orientations (**z** = [111] and [011]), or in **z** = [001] orientation but restricted to UHP-W under certain irradiation conditions (≥ 600°C; ≥ 0.4 dpa). Nevertheless, when loop strings did form and eventually dominated the microstructure, it became increasingly important to take into account the elastic interactions and reactions between individual loops and loop strings.

The effect of loop-string elastic interaction and reactions has two aspects. First, an individual loop may be attracted to the string by 1D hopping along its projected Burgers vector direction, in order to coalesce with the rest of the loop string components; second, the geometry of loop strings may be altered by translation and rotation, due to interaction with individual loops in the neighbourhood.

Fig 4.29 illustrates the first aspect, taking the UHP-W specimen as an example, irradiated at 800°C in **z** = [001] orientation. Loop B (↑), probably with **b** = $\pm$½[$\bar{1}\bar{1} \pm 1$], hopped in parallel with [$\bar{1}\bar{1}0$] in order to align with the other loop components of pre-existing string A. The hopping motion of loop B iterated in cycles until eventually the attractive force from string A became strong enough to prohibit further displacements of loop B. Subsequently, loop B coalesced with the other loop components of string A.



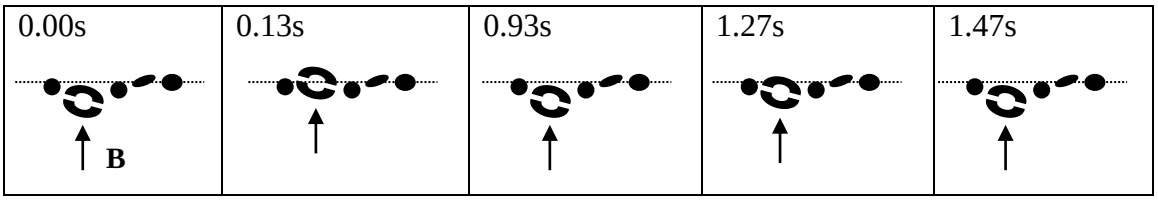


Fig 4.29 Hopping of loop B (↑) with **b** = $\pm$½[$\bar{1}\bar{1} \pm 1$] as a result of attraction from string A in UHP-W, irradiated at 800°C in **z** = [001] orientation. (See Appendix, video 6).

Fig 4.30-4.31 illustrates the second aspect, by following the string geometry variation in W-5V, irradiated at 800°C in **z** = [011] orientation. String segment A labelled with (←) in both Fig 4.30 and 4.31 changed its original geometry with respect to other loops in the string. In Fig 4.30, string segment A made a translational displacement of about 12 nm, so as to align parallel with **g** = $0\bar{1}1$, like the remaining part of the string. It is likely that the string was made up of loops with identical variants of ½<111> and the "straightening-up" behaviour of the labelled string may be a result of the minimization of elastic interaction energy between the string and the surrounding dislocation loops. Fig 4.31 is very similar to Fig 4.30, except that the elastic interaction led to the rotation of segment A, by ~24°. An implication from this rotation is that all the constituent loops in the denoted string have rotated their habit plane by such an amount.

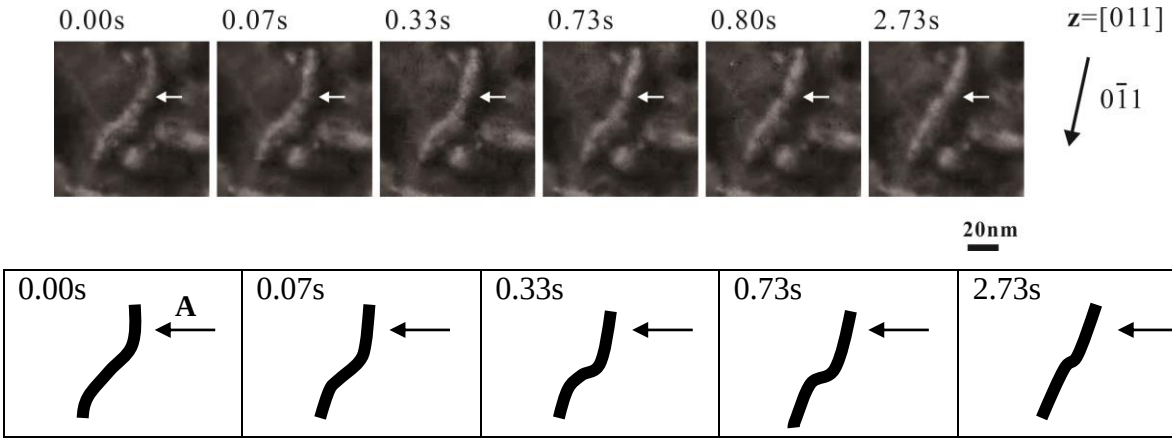


Fig 4.30 String segment A (←) changed its geometry with respect to the elastically interacting environment by translational displacement (~12 nm) in the W-5V specimen, irradiated at 800°C in **z** = [011] orientation.

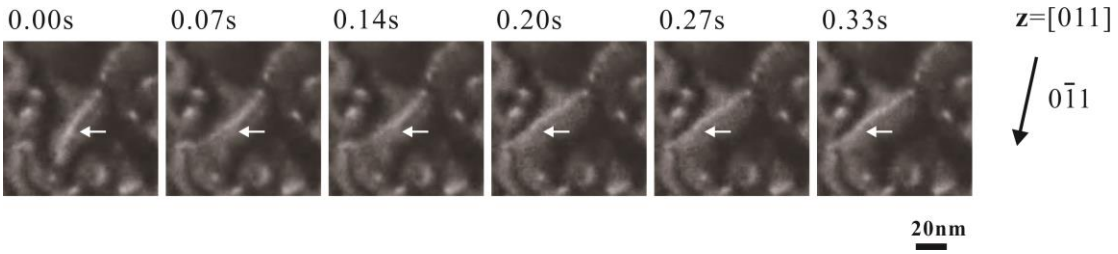


Fig 4.31 String segment A (←) changed its geometry by the cooperative rotation of habit planes of the constituent dislocation loops (~24°). (See Appendix, video 7).

Fig 4.32 illustrates an interesting observation of a string of loops undergoing large angles of rotation during a recording of ~300s. The example was taken from the UHP-W specimen, irradiated at 800°C in the **z** = [001] orientation. The string of loops indicated underwent three major stages of rotation, i.e. 23° at 0.20s, a further 24° at 58.60s and finally 16° at 295.80s. The interpretation of these rotations of specific angles requires caution. It is possible that all constituent loops in the string rotated cooperatively. In this case, according to the direction of **g** = $\bar{1}10$, the loops probably had **b** = ½<111> and were closest to a pure edge orientation at 58.60s (habit plane {111}), while in the remaining periods the loops were probably in a sheared configuration (habit plane {110} or between {110} and {111}). Alternatively, it could also be the case that some of the constituent loops, if not all, made a lateral translation instead of rotating their habit planes, and so the string appeared to have rotated by the observed angles.

Finally, Fig 4.33 shows a scenario of string-string elastic interaction and reaction, which is the most complex level of damage microstructure evolution observed in UHP-W and W-alloys. In this W-5V specimen, irradiated at 800°C in **z** = [011] orientation, three loop strings gradually gathered at one end to form a triple point at 0.20s. At 0.33s, the triple point suddenly vanished. String A was drastically shortened after its detachment from the triple point. Strings B and C remained intersected, however their gross length decreased from 188 nm to 169 nm.

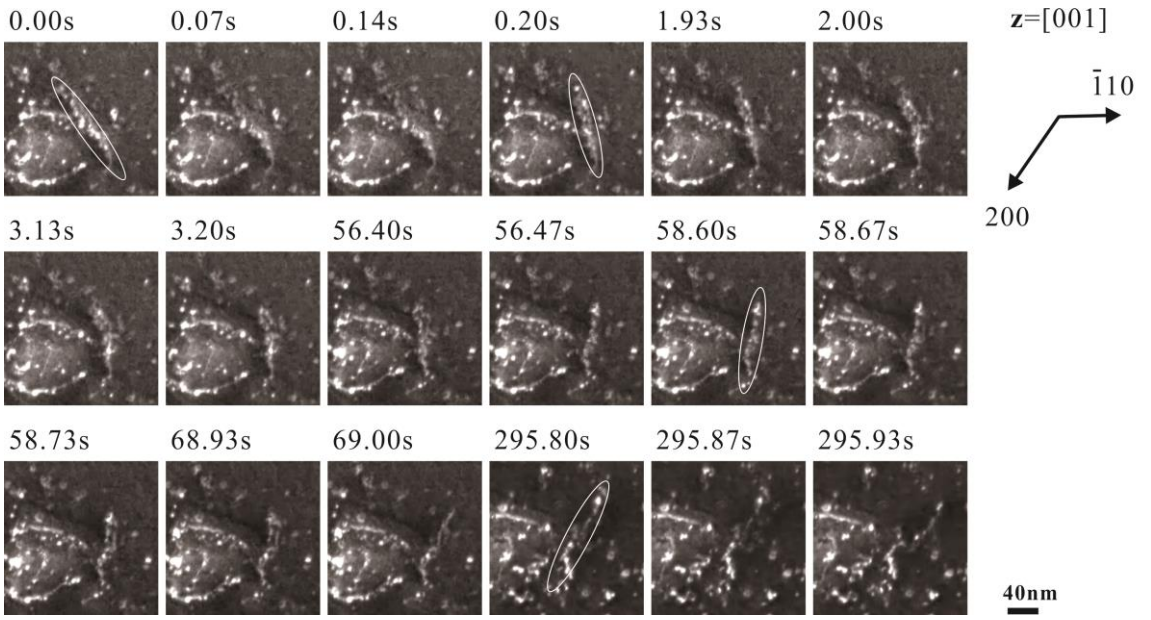


Fig 4.32 The circled string of loops found in the UHP-W specimen, irradiated at 800°C in **z** = [001] orientation underwent three stages of rotation, i.e. 23° at 0.20s, a further 24° at 58.60s and finally 16° at 295.80s. (See Appendix, video 8).

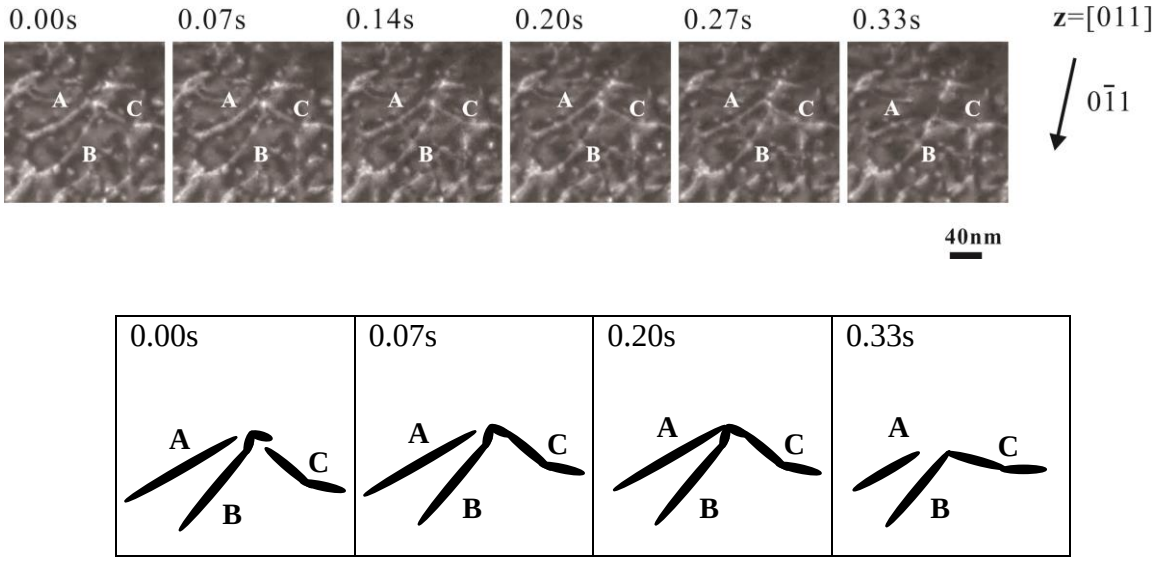


Fig 4.33 Loop string-string interaction and reaction are taking place in W-5V, irradiated at 800°C in **z** = [011] orientation. As a result, the relative geometries of strings A, B and C have changed. (See Appendix, video 9).

4.5. Post-irradiation characterizations

The most detailed characterizations of the induced damage in W/W-alloys were carried out after the irradiation. All areas exposed to the electron beam (Hitachi H-9000NAR, 300 kV) during the ion irradiation were avoided, and at least one dataset was obtained from the **z** = [001] orientation for each combination of irradiation condition/material. Defect types, defect size distributions, number densities, geometries and nature were investigated to reveal the effects of temperature, dose and alloying elements on damage microstructure. The influence of grain orientation (i.e. non **z** = [001] grains) upon microstructure is covered briefly at the end of this section.

4.5.1. Radiation damage microstructures

The results on radiation damage contrast features are described in the following six sub-sections. The first four describe the features of dislocation loops in **z** = [001] grains, in pure tungsten and the three alloy systems; the fifth shows how grain orientation may affect damage morphology (case analyses in irradiated W-5Ta and W-5V); and the closing sub-section demonstrates the presence of spherical voids in UHP-W as a result of ion irradiation. The imaging conditions adopted for dislocation loops were two-beam kinematical-bright field and weak-beam dark-field ($\mathbf{g} = 200, 3-4\mathbf{g}$); whereas the voids were observed in out-of focus conditions to produce phase contrast.

4.5.1.1. (300-800°C / 1.0 dpa) irradiated UHP-W

In this section, the temperature dependence of the post-irradiation damage microstructure in UHP-W is illustrated. With increasing temperature, dislocation loops induced by the ion damage increased in size (Fig 4.34) and decreased in number density (Fig 4.35-4.39). However, the trends only became significant at irradiation temperatures above 500°C. In Fig 4.34, it may be seen that 1-2 nm loops dominate in the temperature range 300-500°C,

whereas at 600°C the dominating size category is 4-5 nm and at 800°C it is 5-6 nm. Additionally, it is worth noting the sharp decrease of the 1-2 nm loop population, dropping from ~27.5% of the total at 300°C to ~1.5% at 800°C.

Comparing the microstructure features displayed in Fig 4.35-4.39, at 300°C and 500°C individual dislocation loops were randomly distributed; at 600°C and 800°C, dislocation loops started to align and form loop strings, the projected directions of which were almost parallel to <110>. The higher the irradiation temperature, the more evident was loop string formation. Burgers vector analysis (§ 2.6.3) indicated that dislocation loops which aligned into strings had **b** = ½<111>.

The damage microstructure of UHP-W was also found to contain loops of type **b** = <100>, co-existing with loops of type **b** = ½<111>. The presence of the two dislocation loop types is illustrated for the 500°C irradiation in Fig 4.37 and the 800°C irradiation in Fig 2.16 and 2.18. The <100> loops can easily be recognized by applying the diffraction contrast invisibility rules (see Table 2.4). § 4.5.2.2 presents in detail the overall fractions of ½<111> loops versus <100> loops in W/W-alloys, as a function of irradiation temperature and alloying elements.

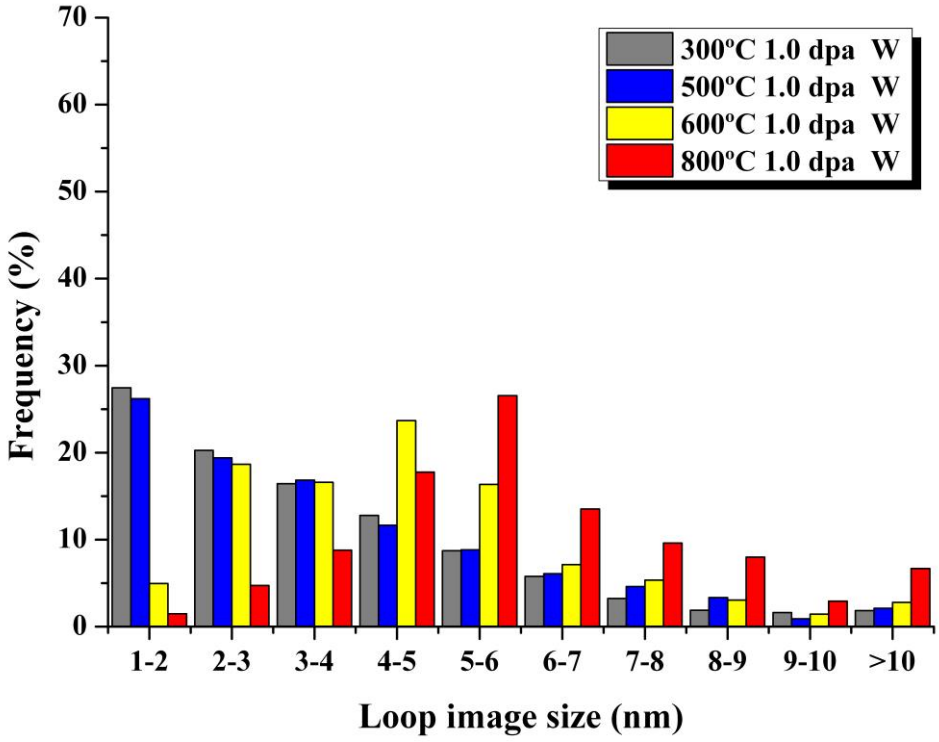


Fig 4.34 Overall loop size distribution in 1.0 dpa irradiated UHP-W, as a function of irradiation temperature in **z** = [001] orientation. Data were obtained from weak-beam dark-field images taken in **g** = {200} and {020}.

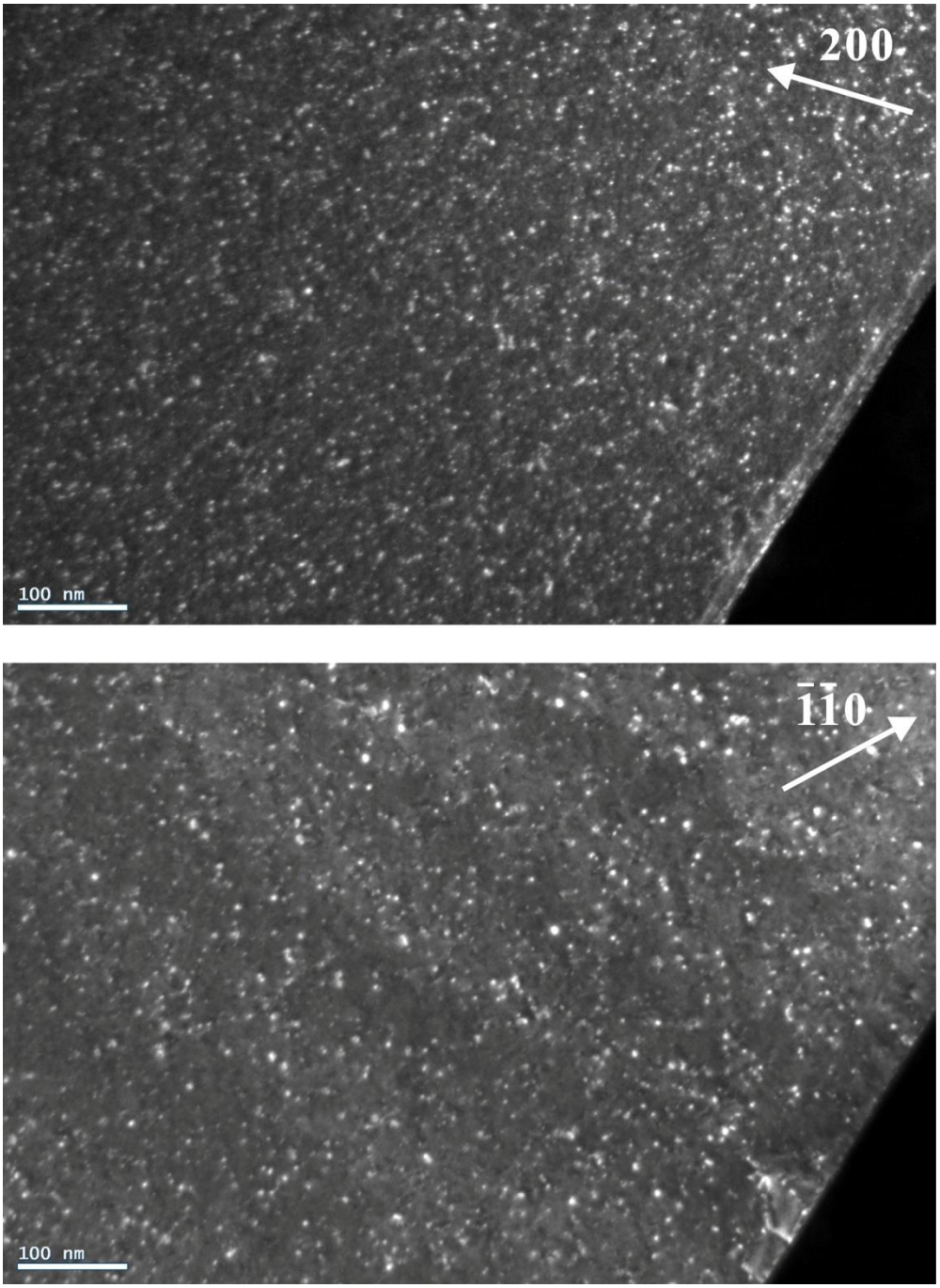


Fig 4.35 1.0 dpa irradiated UHP-W, 300°C in **z** = [001] orientation. Micrographs were taken under weak-beam dark-field conditions: (**g** = 200, ~3**g**); (**g** = 110, ~4**g**).

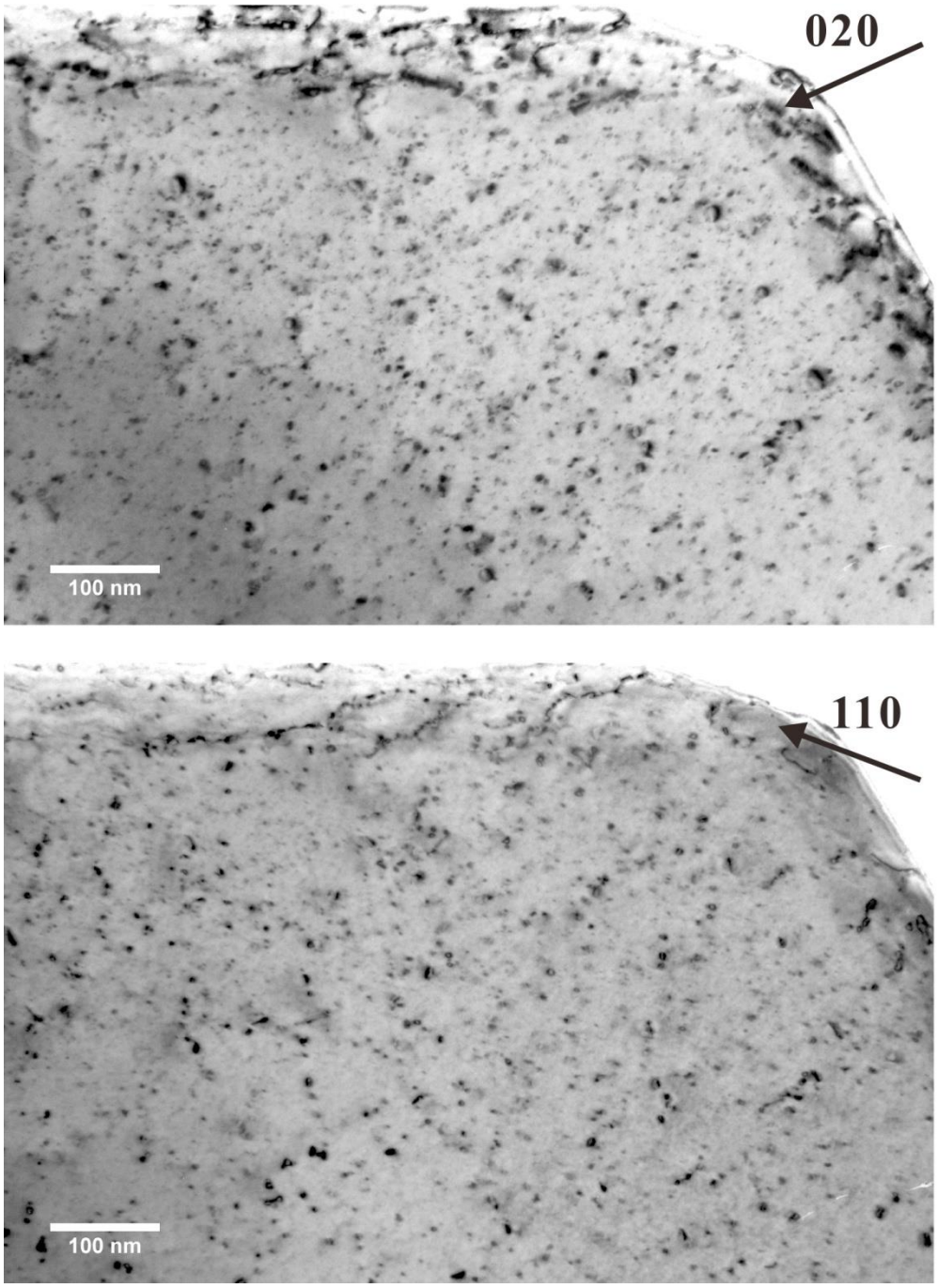


Fig 4.36 1.0 dpa irradiated UHP-W, 500°C in **z** = [001] orientation.

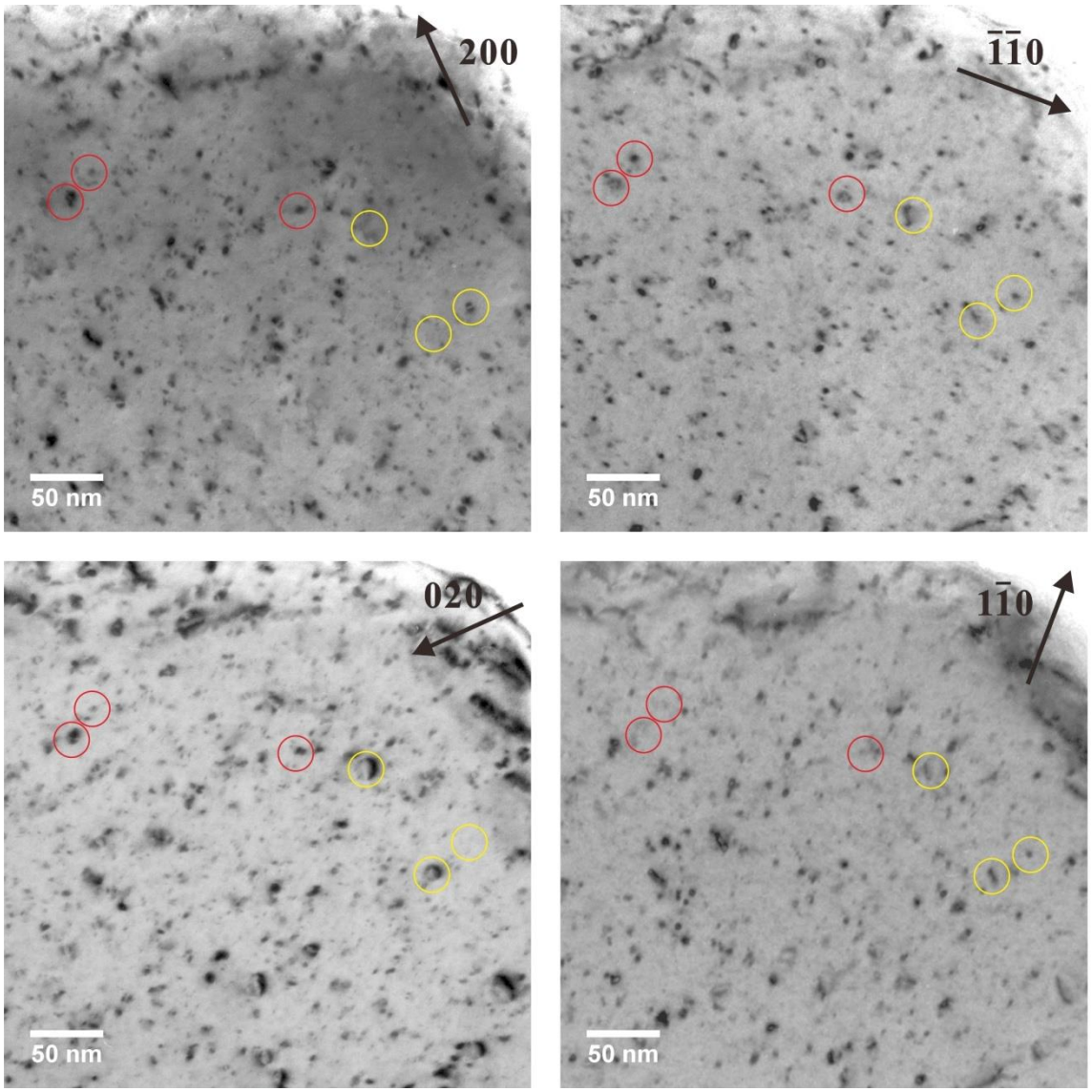


Fig 4.37 Coexistence of ½<111> loops (red circles) and <100> loops (yellow circles) in 1.0 dpa irradiated UHP-W, 500°C in **z** = [001] orientation.

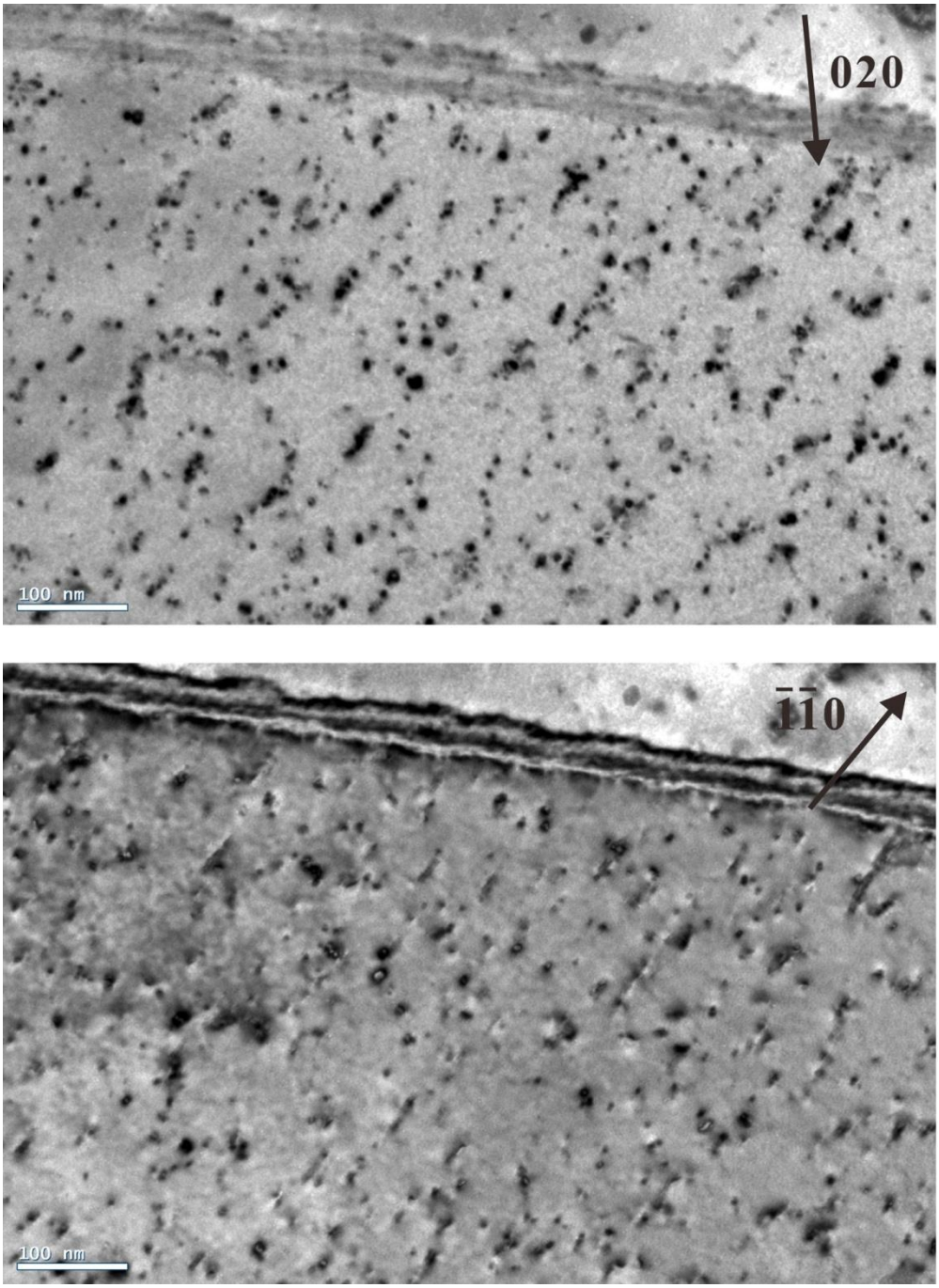


Fig 4.38 1.0 dpa irradiated UHP-W, 600°C in **z** = [001] orientation.

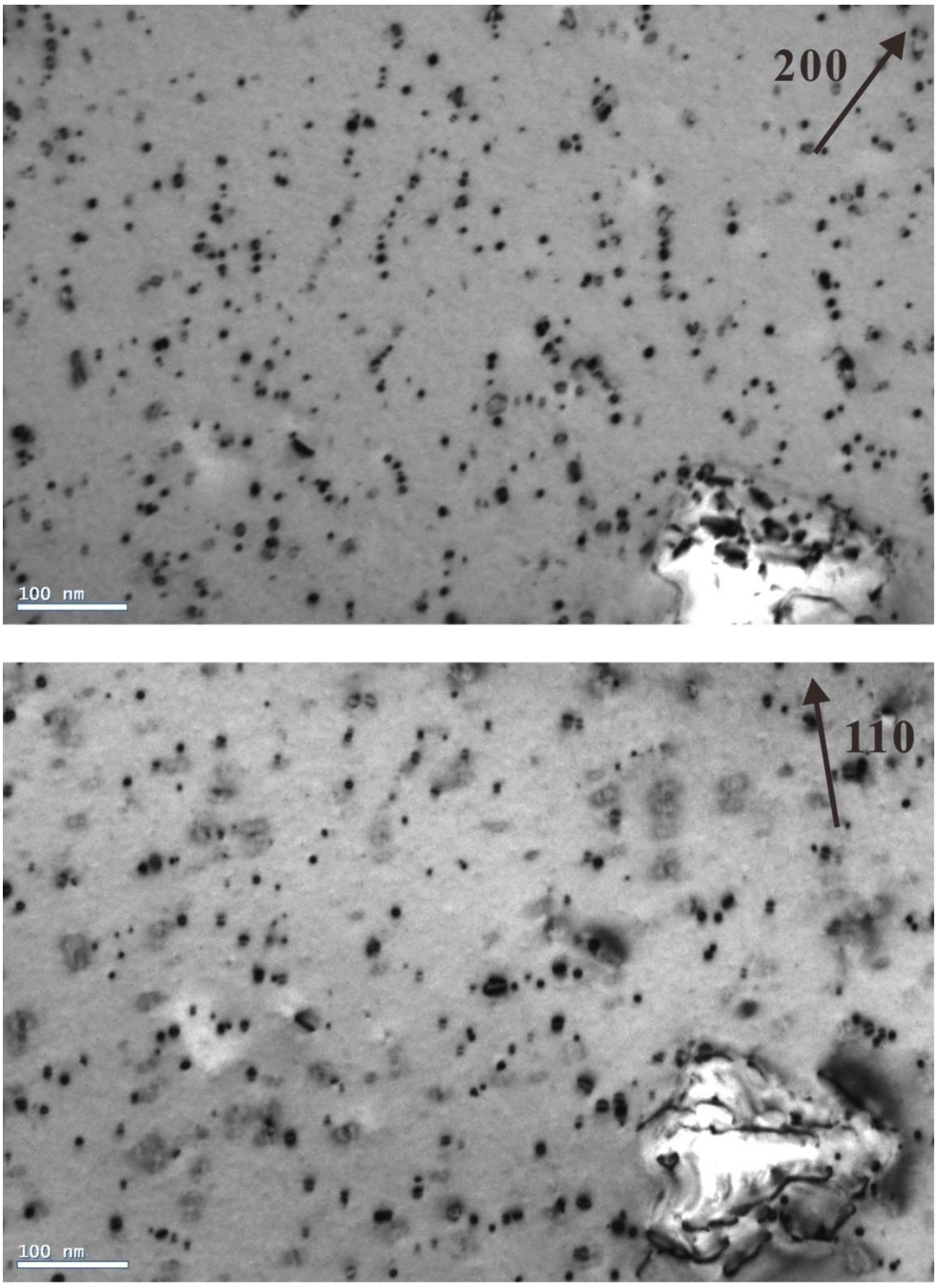


Fig 4.39 1.0 dpa irradiated UHP-W, 800°C in **z** = [001] orientation.

4.5.1.2. (500-800°C / 1.0 dpa) irradiated W-5Re

There was an abrupt change in the damage microstructure of W-5Re irradiated to a dose of 1.0 dpa with increasing irradiation temperature. The change in microstructure can be seen in the loop image size distributions (Fig 4.40) and the micrographs (Fig 4.41-4.44) recorded under equivalent two-beam diffraction conditions. At 500°C and 600°C, the dislocation loop size distributions and the loop number densities appeared quite similar. The dominating loop size category in both cases was 1-2 nm, which consisted of ~35% of the loop population. However, at 800°C the fraction of 1-2 nm loops dropped to ~20% and the dominating loop size category shifted to 4-5 nm, making up ~24% of the loop population. At the same time, the loop number density decreased drastically. At 800°C fewer loops were nucleated but more loop growth occurred.

Unlike the UHP-W specimens at the same dose, no evidence of loops forming strings was present, even at an irradiation temperature of 800°C. However, co-existing ½<111> and <100> loops were again present. Fig 4.42 illustrates this in W-5Re irradiated to a dose of 1.0 dpa at 500°C. Quantitative analyses of the fraction of ½<111> loops versus <100> loops are presented in § 4.5.2.2.

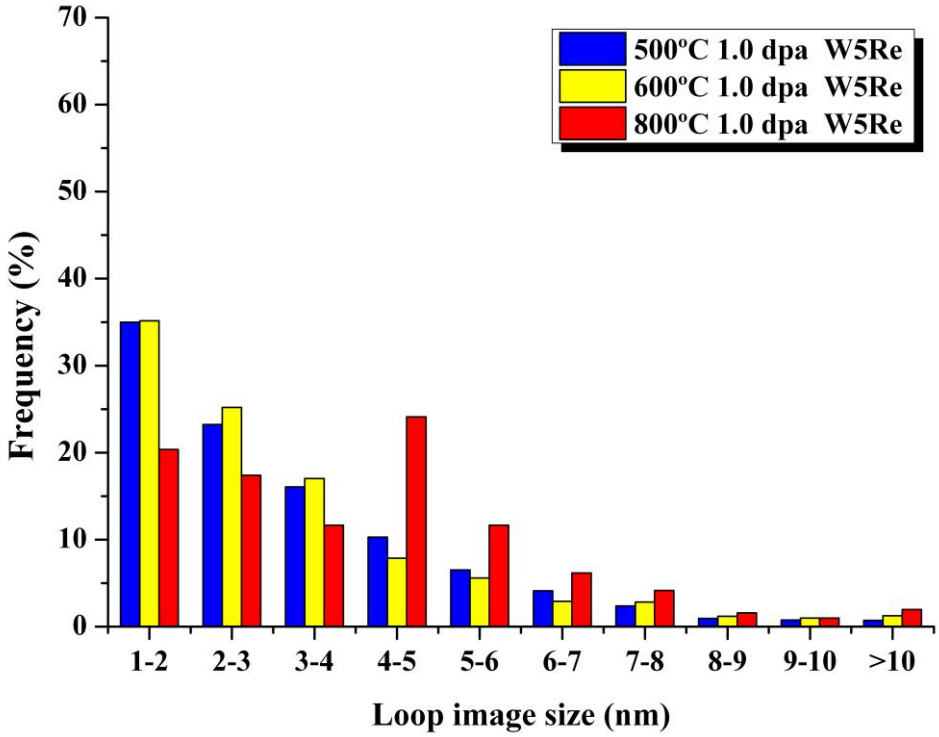


Fig 4.40 Overall loop size distribution in 1.0 dpa irradiated W-5Re, as a function of irradiation temperature in **z** = [001] orientation.

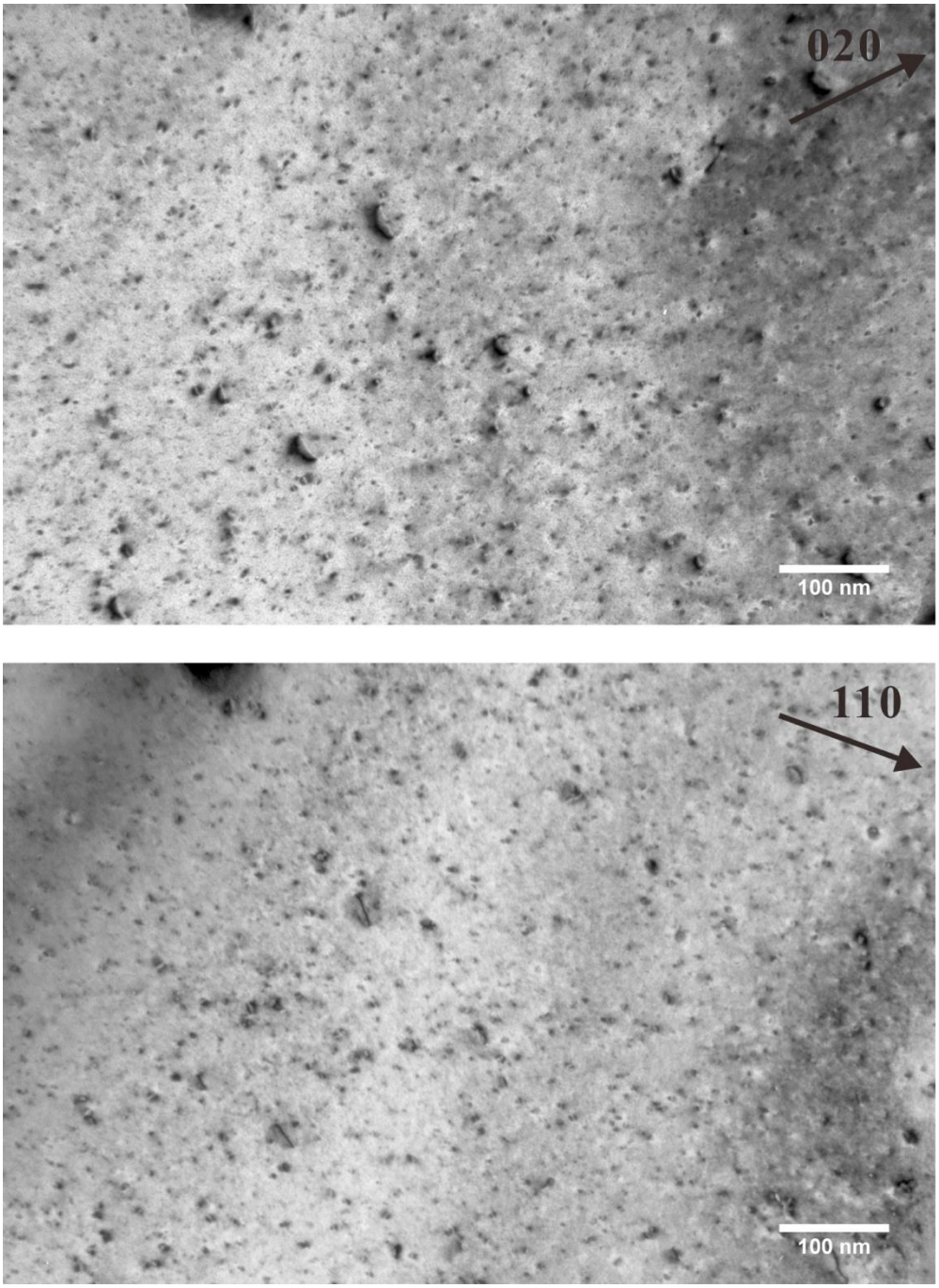


Fig 4.41 1.0 dpa irradiated W-5Re, 500°C in **z** = [001] orientation.

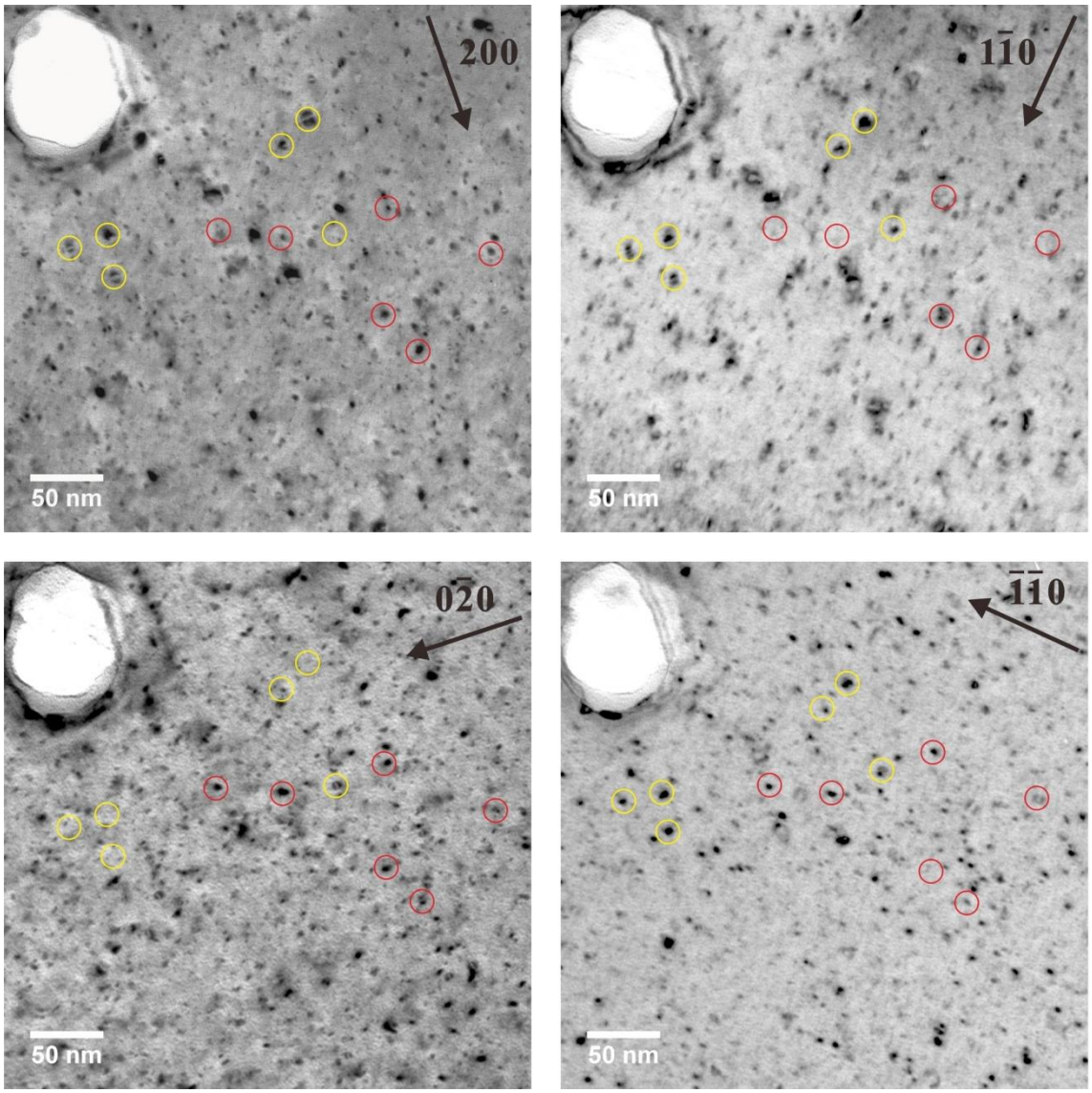


Fig 4.42 Coexistence of ½<111> loops (red circles) and <100> loops (yellow circles) in 1.0 dpa irradiated W-5Re, 500°C in **z** = [001] orientation.

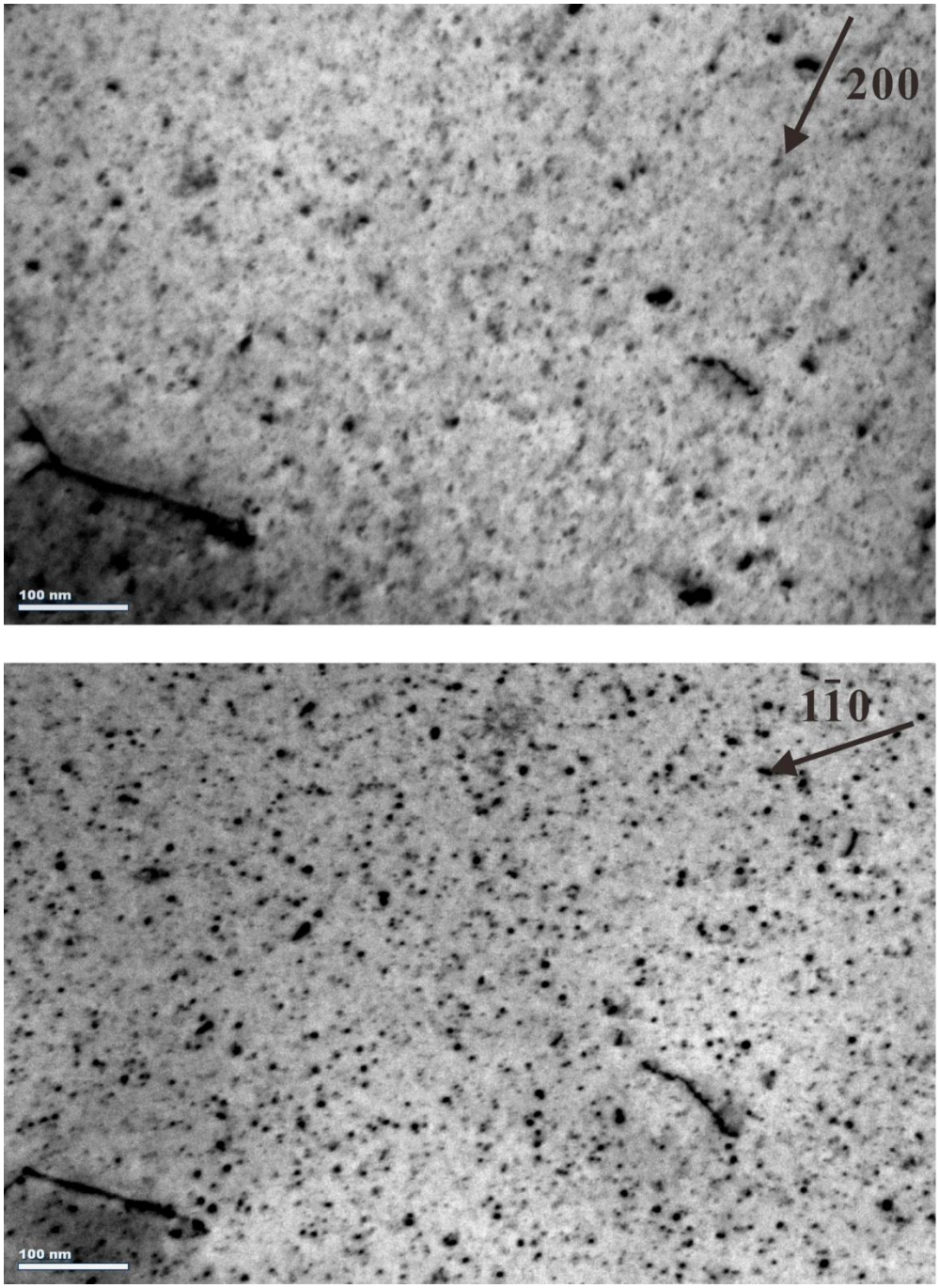


Fig 4.43 1.0 dpa irradiated W-5Re, 600°C in **z** = [001] orientation.

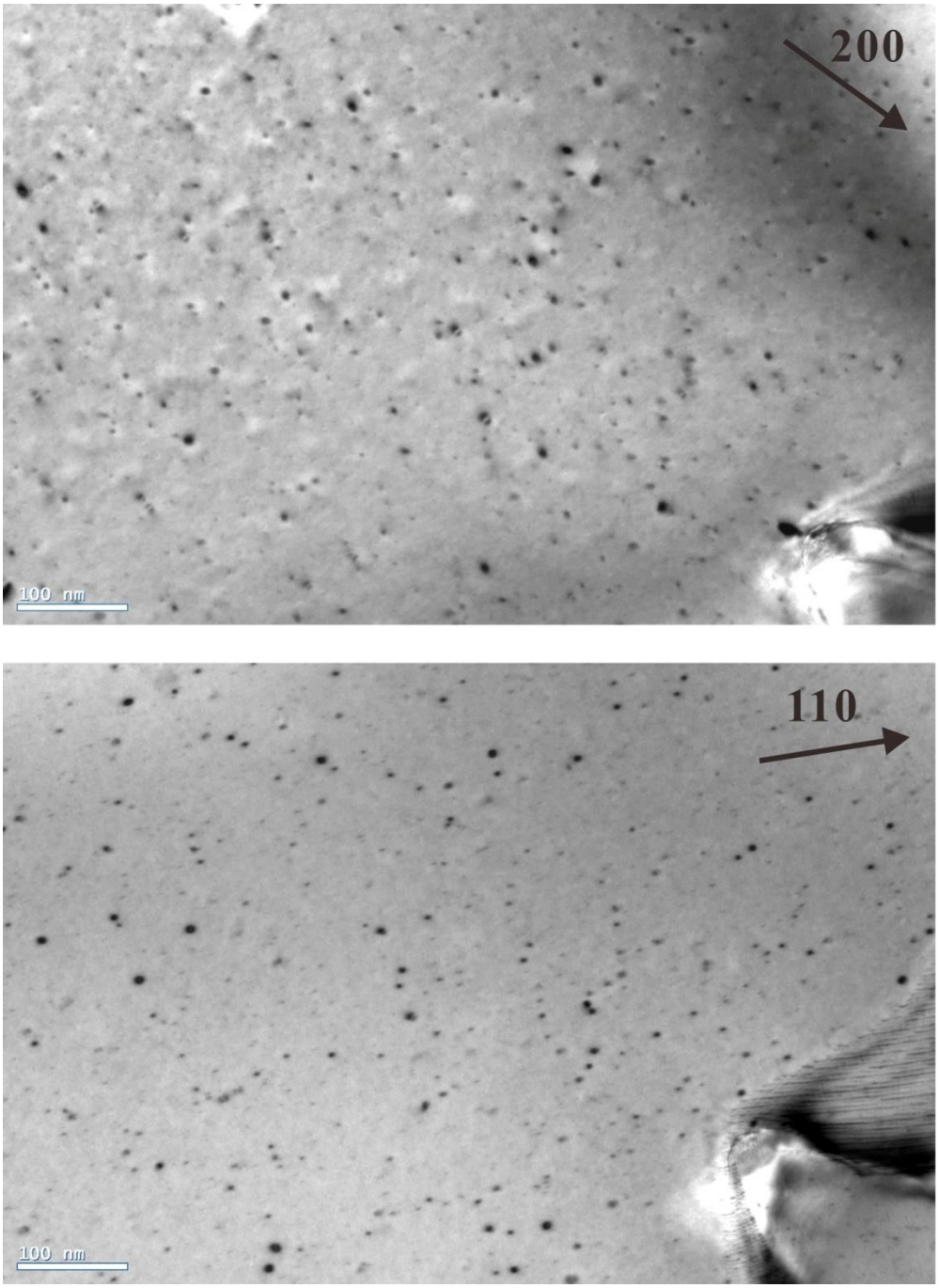


Fig 4.44 1.0 dpa irradiated W-5Re, 800°C in **z** = [001] orientation.

4.5.1.3. (500-800°C / 1.0 dpa) irradiated W-5Ta

The changes in damage microstructures in W-5Ta specimens were minor within the irradiation temperature range of 500-800°C. The loop size distributions of Fig 4.45 show that the dominant loop size category remained at 1-2 nm, although the fraction of the total loops in this size category gradually fell from ~42% to ~30%. There was some indication of a microstructure transition above 600°C similar to that observed in W-5Re, in terms of loop number density decrease and the upward shift of loop size distributions. The fraction of 4-5 nm loops increased from ~6% to ~11% between 600°C and 800°C. Loops ≥ 8 nm were only seen at 800°C. Ta therefore seems to have a larger effect than Re on restricting loop growth under irradiation.

Figs 4.46-4.49 compare the damage microstructures in W-5Ta at different irradiation temperatures. There seems a clear decrease in loop number density from 500°C to 600°C, but no immediately distinguishable difference was found for temperatures beyond. No loop string formation was observed in W-5Ta specimens in the grain orientation selected for post-irradiation analysis, i.e. **z** = [001], regardless of the irradiation temperature.

Two types of dislocation loop geometries, i.e. ½<111> and <100> were again confirmed in all irradiated W-5Ta specimens. The co-existence of ½<111> and <100> loops is explicitly presented for the case of 500°C irradiation in Fig 4.47. Please refer to § 4.5.2.2 for further quantitative details.

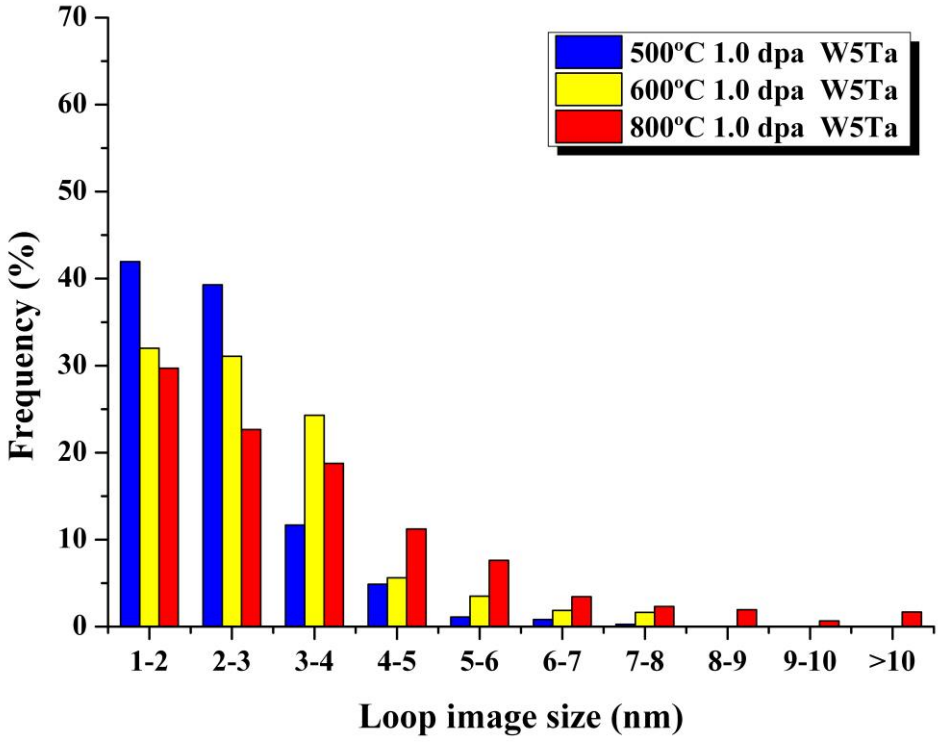


Fig 4.45 Overall loop size distribution in 1.0 dpa irradiated W-5Ta, as a function of irradiation temperature in **z** = [001] orientation.

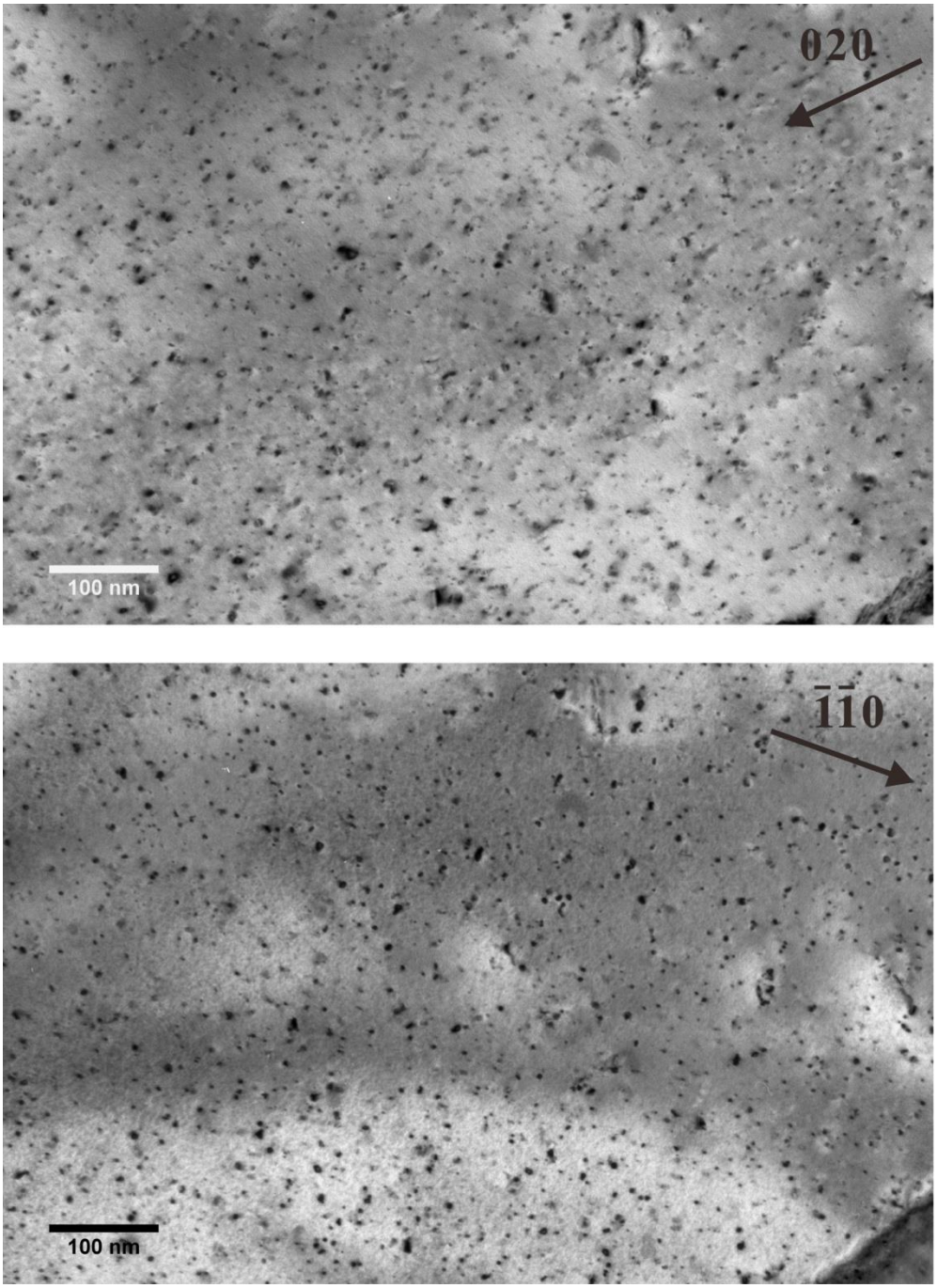


Fig 4.46 1.0 dpa irradiated W-5Ta, 500°C in **z** = [001] orientation.

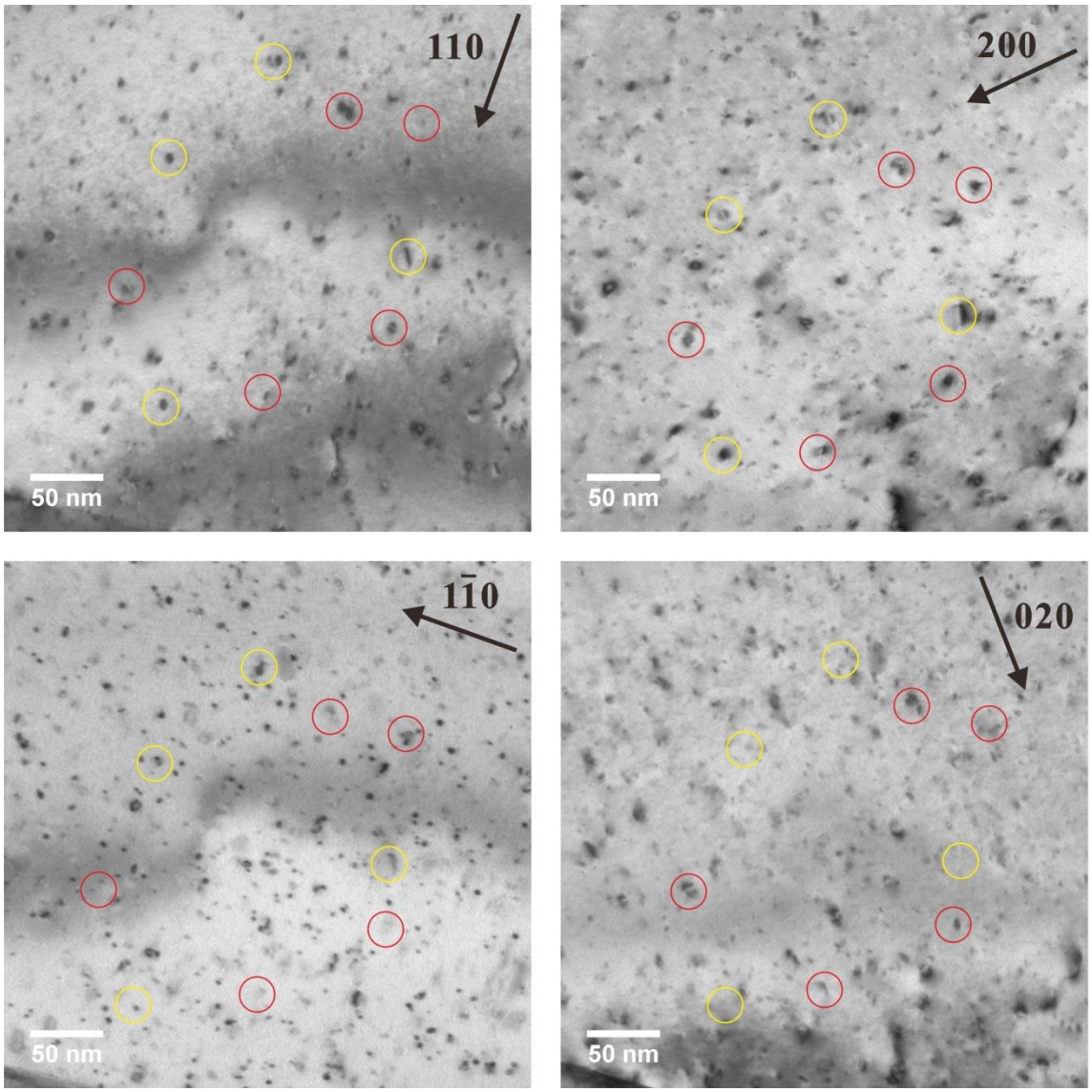


Fig 4.47 Coexistence of ½<111> loops (red circles) and <100> loops (yellow circles) in 1.0 dpa irradiated W-5Ta, 500°C in **z** = [001] orientation.

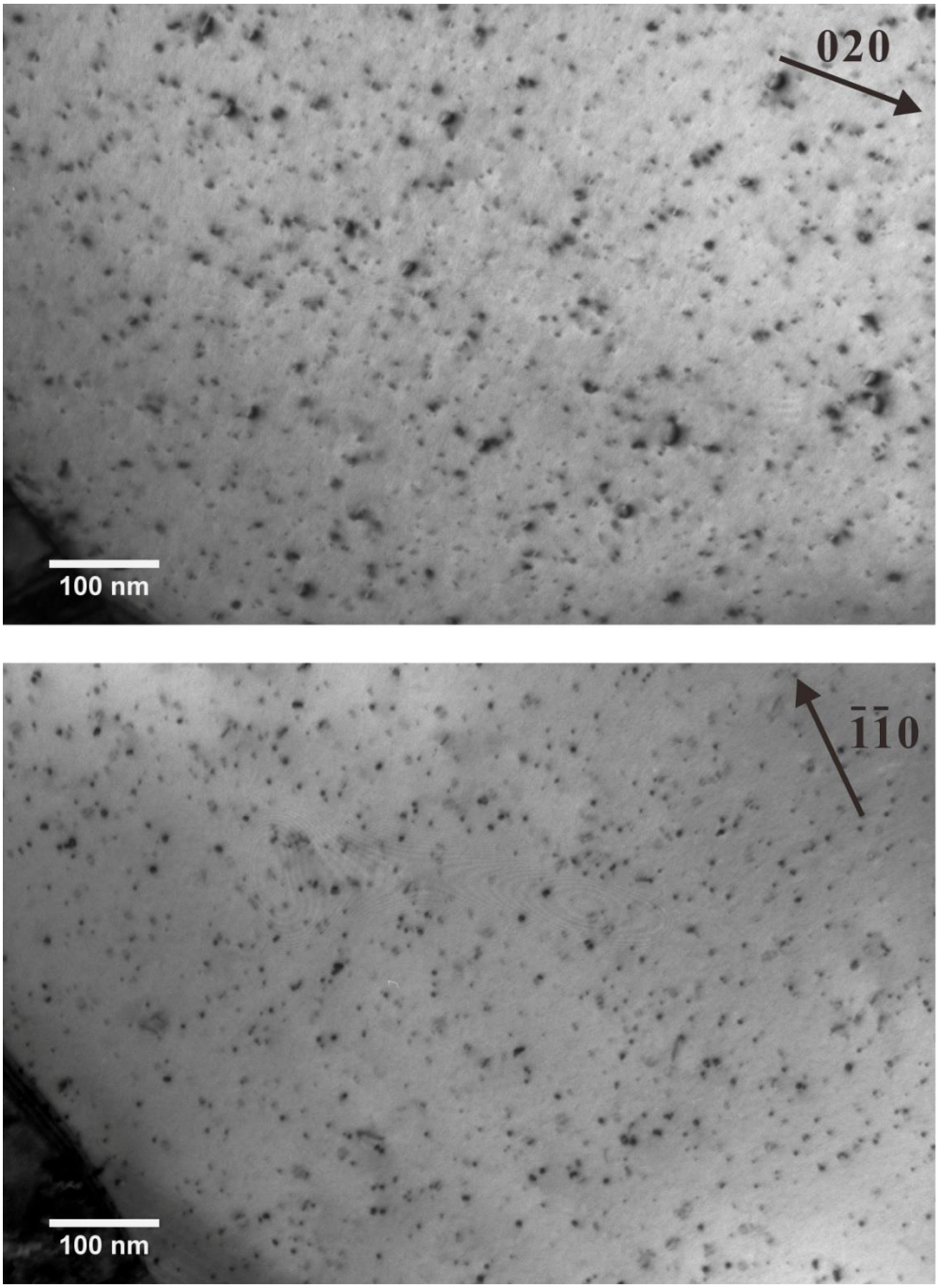


Fig 4.48 1.0 dpa irradiated W-5Ta, 600°C in **z** = [001] orientation.

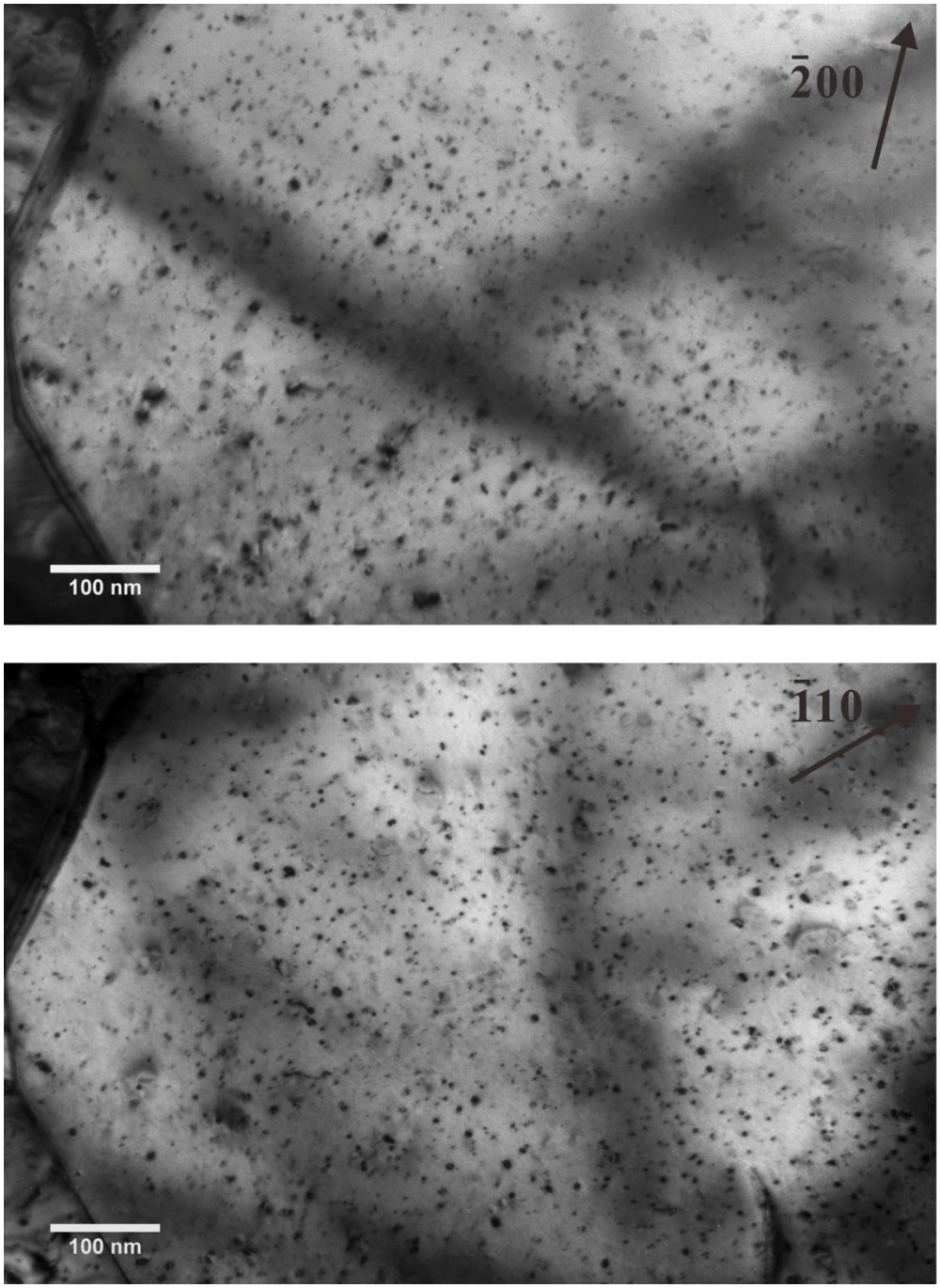


Fig 4.49 1.0 dpa irradiated W-5Ta, 800°C in **z** = [001] orientation.

4.5.1.4. (500-600°C / 1.0 dpa) irradiated W-5V

Datasets of **z** = [001] grains were available only for 500°C and 600°C irradiations in W-5V. The limited thin regions of the W-5V specimen irradiated at 800°C did not contain a **z** = [001] oriented grain. Fig 4.50 displays the overall loop size distributions for the two temperatures analysed. The effect of the irradiation temperature seems small. The dominant size category in both cases was as 1-2 nm, making up about ~65% of the total loop population. The fraction of 2-3 nm loops was somewhat larger (~25%) at 600°C than at 500°C (~19%). The fractions of loops with diameters larger than 4 nm were surprisingly low, merely ~6% at 500°C and ~4% at 600°C. This compares with ~60% for UHP-W, ~23% for W-5Re and ~13% for W-5Ta in 600°C irradiations. The observation suggests that the effectiveness of alloying atoms in restricting loop size increase is most probably V>Ta>Re.

Weak-beam dark-field micrographs of the damage microstructures in W-5V irradiated at 500°C and 600°C are shown in Fig 4.51 and 4.52, respectively. The loop number densities appear to have dropped slightly with increasing temperature. No evidence of massive loop string formation was found.

As in the other materials both ½<111> and <100> loops were present in irradiated W-5V specimens. This is demonstrated for the 500°C irradiation in Fig 4.53. However, in W-5V it seems that at least a few <100> loops had undergone "abnormal" growth and therefore appeared larger on average. Quantitative and statistical analyses of the <100> loop dimensions in irradiated W/W-alloys are included in § 4.5.2.3.

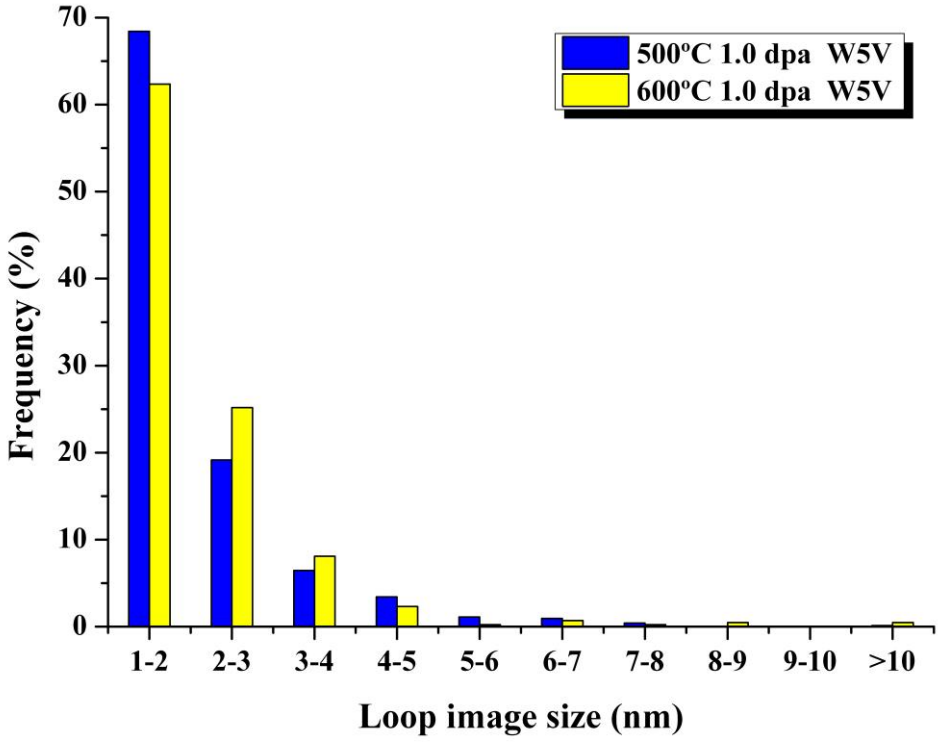


Fig 4.50 Overall loop size distribution in 1.0 dpa irradiated W-5V, as a function of irradiation temperature in **z** = [001] orientation.

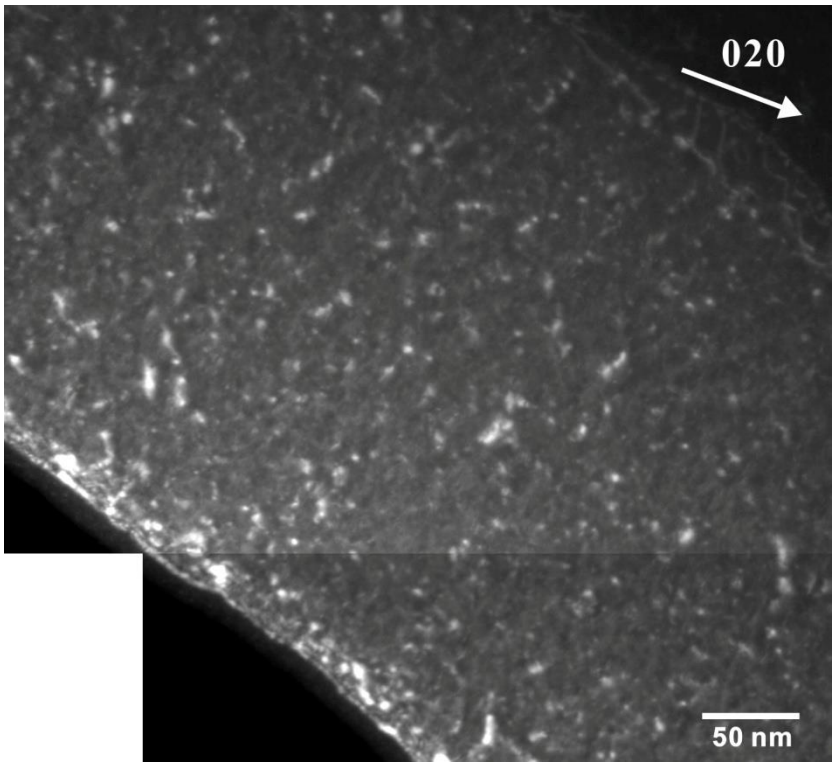


Fig 4.51 1.0 dpa irradiated W-5V, 500°C in **z** = [001] orientation.

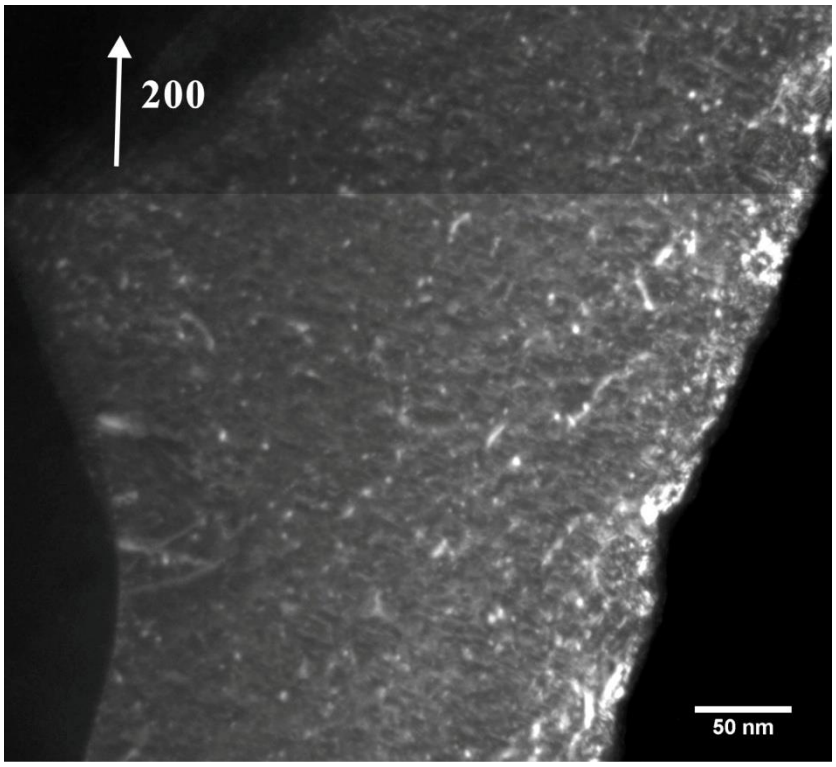


Fig 4.52 1.0 dpa irradiated W-5V, 600°C in **z** = [001] orientation.

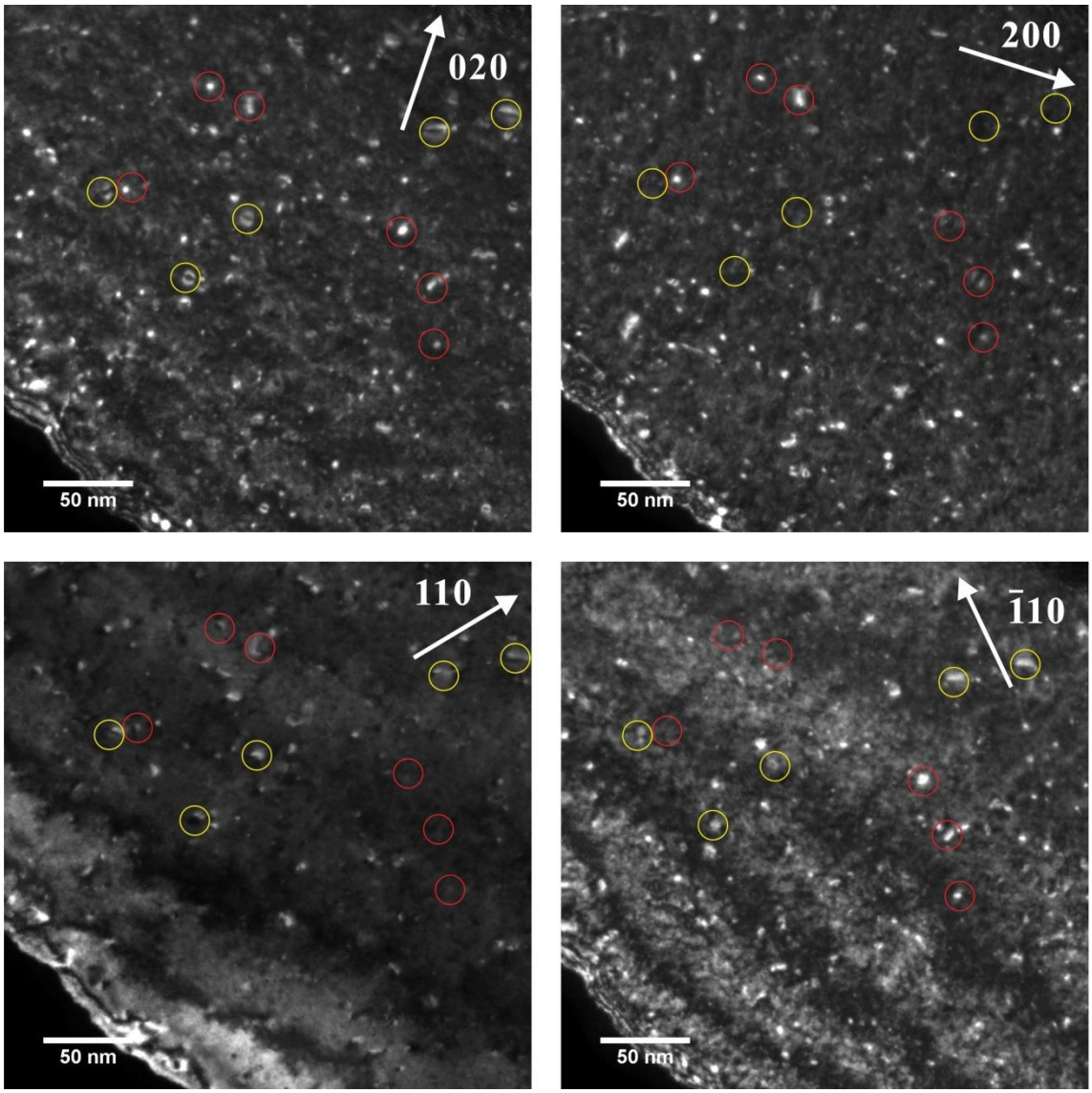


Fig 4.53 Coexistence of ½<111> loops (red circles) and <100> loops (yellow circles) in 1.0 dpa irradiated W-5V, 500°C in **z** = [001] orientation.

4.5.1.5. Damage microstructures in non z = [001] grains

Two examples of grain orientations other than **z** = [001] are shown here: i.e. **z** = [011] (Fig 4.54) and **z** = [111] (Fig 4.55). The specimens selected for illustration were W-5Ta and W-5V, simply because suitable thin, flat grains of these orientations were present in these specimens.

The formation of dislocation loop strings was observed in these non **z** = [001] grains, under all irradiation conditions covered in the scope of the in-situ irradiation experiments. The projected directions of the strings were either parallel or at an angle close to [100]. In the **z** = [011] specimens the strings join to form dislocation networks, which coarsened with an increase in irradiation temperature. In addition to strings and networks, there were also populations of individual loops, embedded in the sea of this complex sub-microstructure. Note that in **z** = [001] specimens, string formation in UHP-W was seen only at temperatures higher than 600°C and not at all in the W-alloys. This implies that certain grain orientations, such as **z** = [011] and [111] facilitate the collective movement or re-alignment of individual dislocation loops, hence forming strings and eventually networks.

A last remark on this topic concerns the effects of alloying elements. Based on Fig 4.54, it seems that a less-dense dislocation network developed in W-5V than in W-5Ta at the **z** = [011] orientation. The underlying mechanism may be associated with the influence of different alloying atoms on the mobility of dislocation loops, to be discussed in detail in Ch 6.

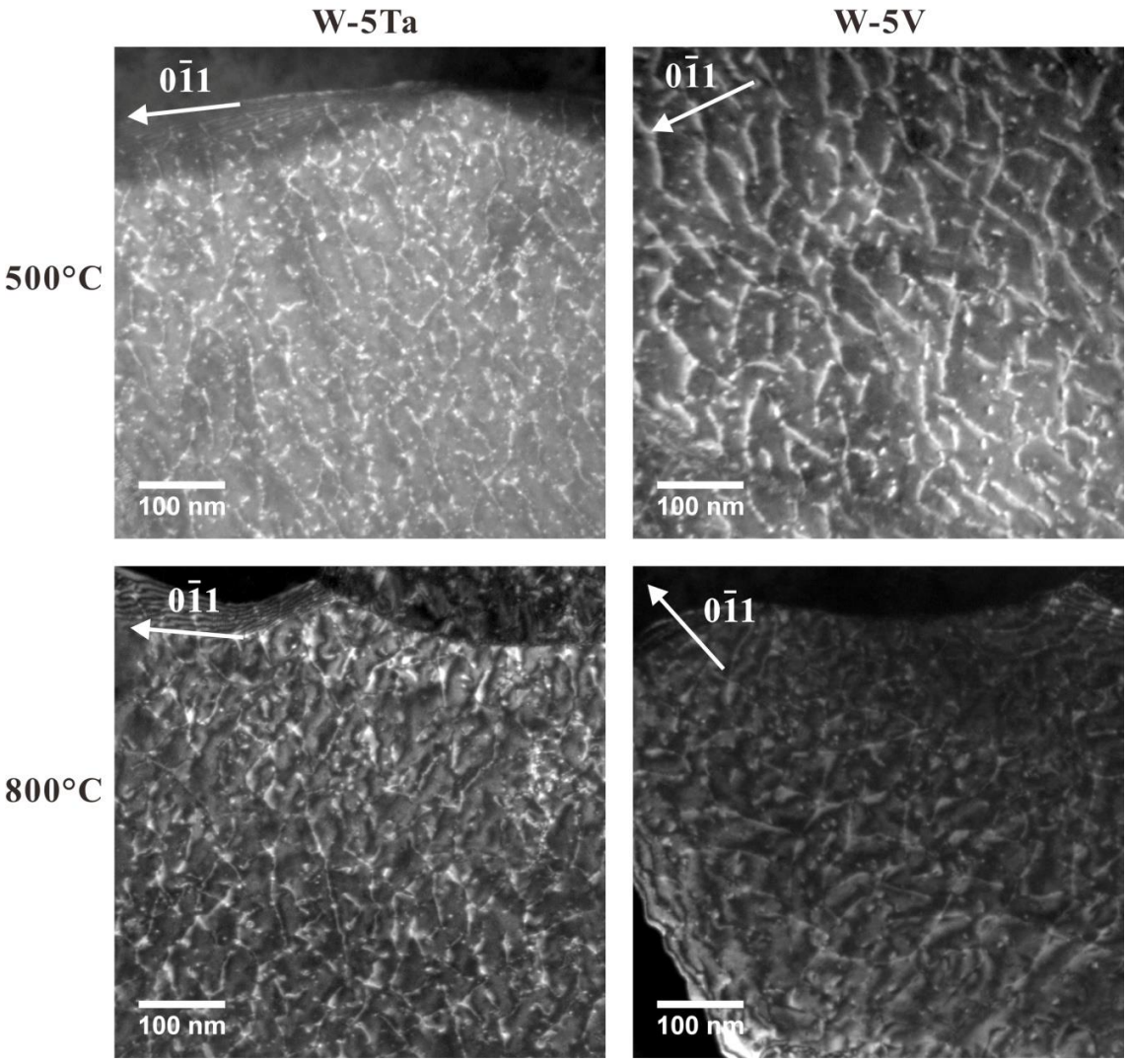


Fig 4.54 Dislocation-network featured damage microstructures in W-5Ta and W-5V, irradiated to 1.0 dpa at 500°C and 800°C in **z** = [011] orientation.

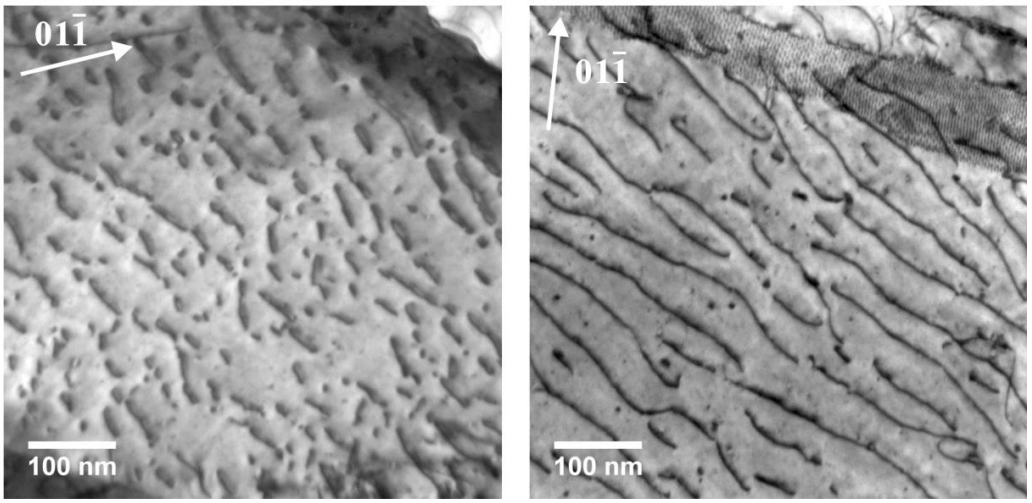


Fig 4.55 1.0 dpa irradiated W-5V, 800°C in **z** = [111] orientation.

4.5.1.6. Spherical voids in UHP-W (600, 800°C)

In UHP-W specimens irradiated at 600°C and 800°C, voids were observed by phase contrast imaging (Fig 4.56). These are seen as white circular dots in the under-focused image and as black circular dots in the over-focused image, suggesting they are spherical in shape. In the UHP-W specimen irradiated at 300°C, no such phase contrast features were found, suggesting that voids (large clusters of vacancies) either did not exist in UHP-W under this irradiation condition or were too small to be resolved in the conventional TEMs. Time did not permit a comprehensive search for voids in the alloy specimens. The absolute measurements of void sizes are not possible if ≤ 2 nm [95]. Nevertheless, attempts were made to compare the void image size in under-focus conditions in Fig 4.57. The areal number densities of voids observed were averaged among four out-of-focus conditions. With an increase in irradiation temperature, the density of voids dropped by ~20% whereas the average size increased somewhat.

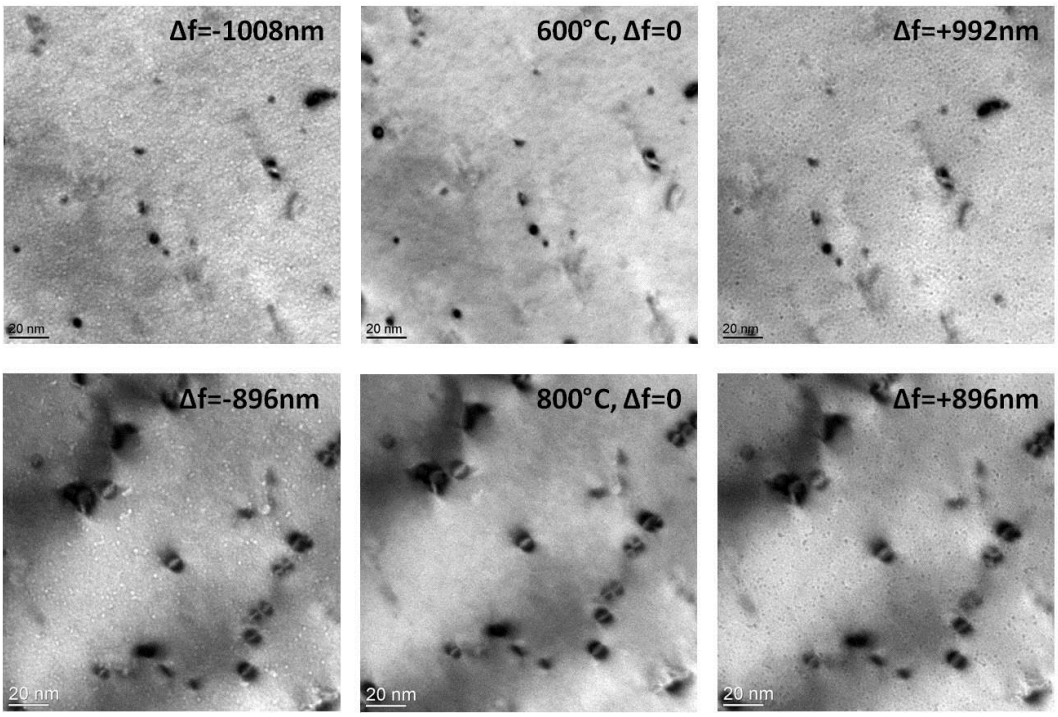


Fig 4.56 Phase contrast images of voids present in the UHP-W specimens, irradiated to 1.0 dpa at 600°C and 800°C, in **z** = [001] orientation. Δf stands for the defocus value.

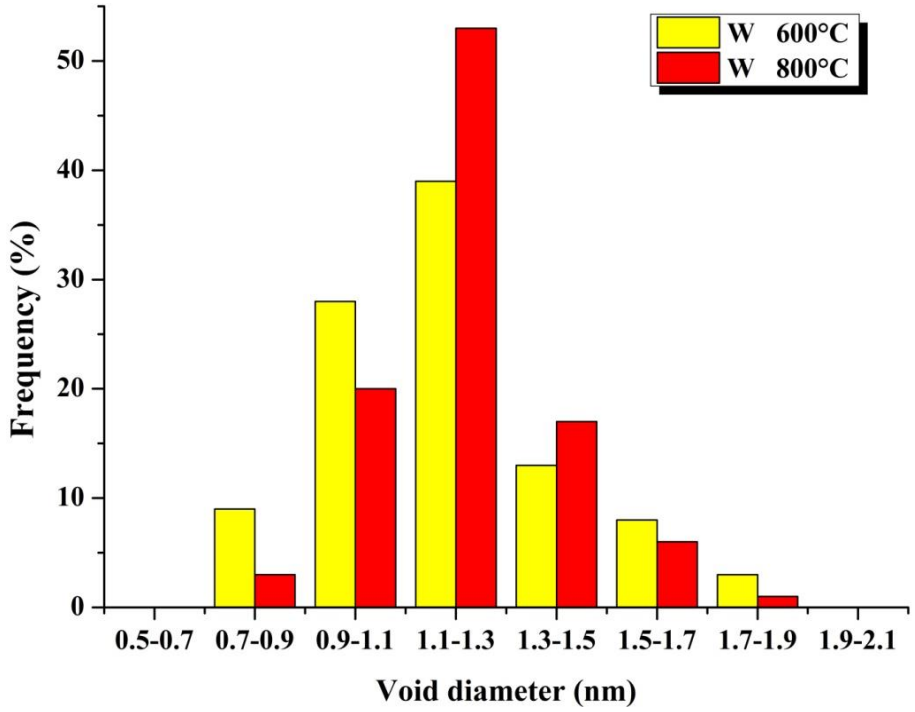


Fig 4.57 Size measurements of voids in 600°C and 800°C irradiated UHP-W, imaged in under-focused condition ($\Delta f \approx -1\mu m$). Void average image size: (1.177±0.023) nm at 600°C; (1.199±0.019) nm at 800°C, error assigned as the standard deviation of the mean. Void number density: $(3.91\pm0.46)\times10^{16}$ m^{-2} at 600°C; $(3.24\pm0.30)\times10^{16}$ m^{-2} at 800°C.

4.5.2 Quantitative characterization and analyses

4.5.2.1. Loop number densities

Dislocation loop areal number densities in all irradiated specimens at a dose of 1.0 dpa were extracted from weak-beam dark-field micrographs taken under $\mathbf{g} = 200, 3-4\mathbf{g}$ diffraction conditions. The density values were then averaged among all symmetrically equivalent $\mathbf{g} = 200$ conditions from the same area of interest. Regions both under and outside the electron beam were studied. Most areas exposed to the electron beam during the irradiation were at the **z** = [001] orientation, exceptions include W-5Ta (800°C, **z** = [113]) and W-5V (800°C, **z** = [011]). All areas outside the electron beam were at the **z** = [001] orientation.

Fig 4.58 summarizes the results. The plot reveals the following trends: 1) with increasing irradiation temperature, the loop number density decreased in all materials; 2) at all temperatures where the alloying effect were studied, the loop number density was highest

in W-5V, followed by W-5Ta and W-5Re and then UHP-W; 3) at 800°C, the differences in number densities between the alloys were substantially smaller than at 500°C; 4) despite some exceptions in non-[001] orientation irradiations, the plot strongly suggests that in the presence of an electron beam, the loop number density was lower.

Note that the damage profile of 150 keV W^+ irradiations is approximately within 30 nm according to the prediction by SRIM, whereas the thicknesses of all the analysed area of interest are no smaller than this value. This implies that the 'areal' number densities would not change with the foil thickness.

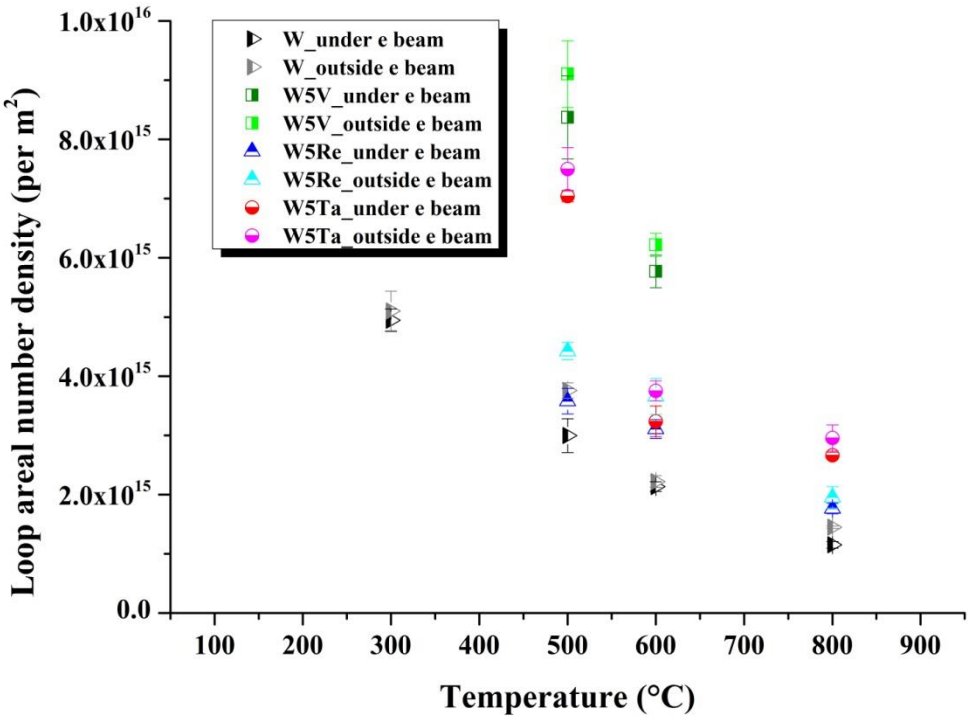


Fig 4.58 Loop areal number densities in all 150 keV W^+ irradiated materials, to a dose of 1.0 dpa. Data from regions both under and outside the electron beam are included.

4.5.2.2. Dislocation loop Burgers vector characterization

Loop analysis from this section onwards refers to areas outside the in-situ electron beam. In § 4.5.1, the damage microstructures in W/W-alloys were shown to be of a mixture of ½<111> and <100> loops. The effects of alloying element and irradiation temperature on the fraction of loops with **b** = ½<111> were analysed.

Fig 4.59 compares the fraction of ½<111> loops among all materials with respect to the irradiation temperature. In UHP-W, with increasing temperature, the fraction of ½<111> loops gradually increased. At 800°C, almost all loops observed had Burgers vectors of type ½<111>, suggesting that <100> loops are probably not a thermally stable configuration for defect clusters at high temperatures. W-5Re exhibited a similar behaviour to that of UHP-W specimens, but the rate of increase of the fraction of ½<111> loops was considerably slower. The fraction of ½<111> loops in W-5Ta did not seem to increase with temperature. At 800°C, there was still an extensive fraction of <100> loops present, i.e. ~35%. For the W-5V specimen, data was only successfully obtained from the 500°C irradiation and the result was similar to that of W-5Re. The fact that a higher fraction of <100> loops was found in the W-alloys as opposed to their UHP-W counter-parts, may suggest the <100> configuration was more stable in the W-alloys at elevated temperatures.

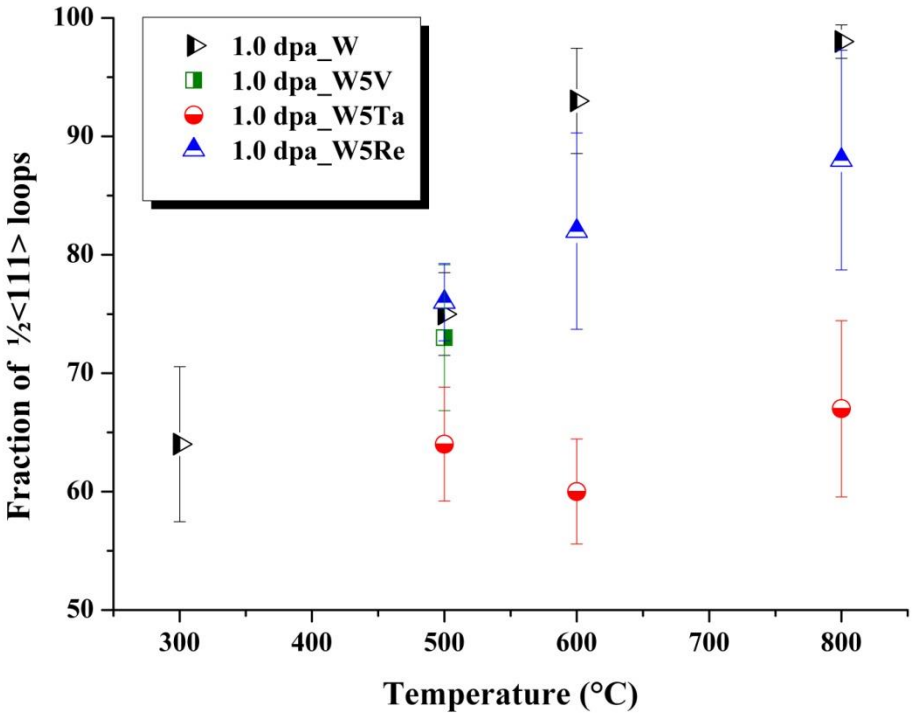


Fig 4.59 The fraction of ½<111> loops in irradiated W/W-alloys as a function of the irradiation temperature, at a dose of 1.0 dpa.

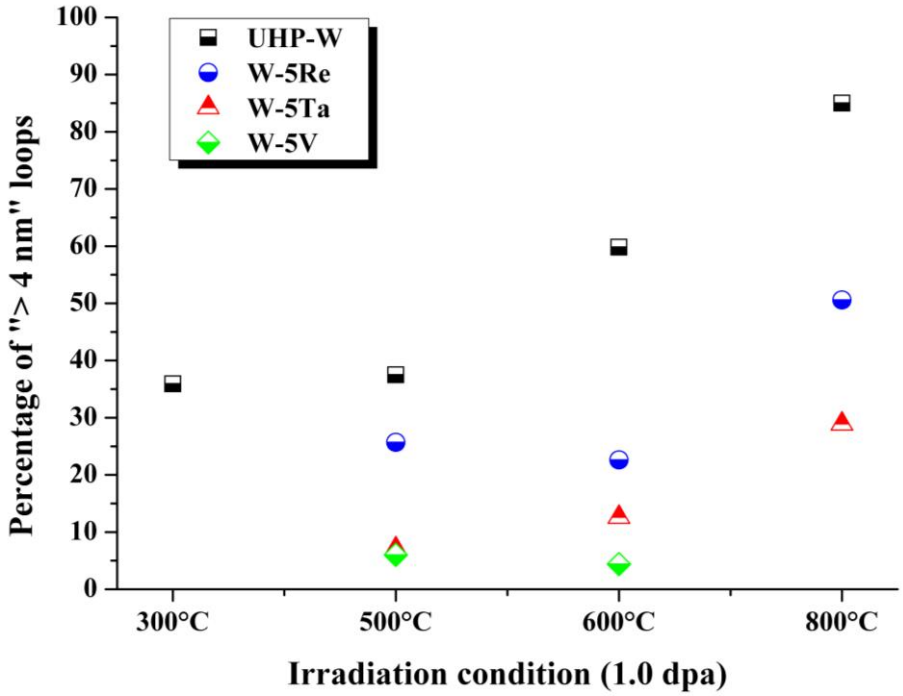


Fig 4.60 The percentage of "> 4 nm" loops as a function of material and irradiation conditions.

4.5.2.3. Dislocation loop nature determination

Methods for determining the interstitial or vacancy nature of dislocation loops were described in § 2.6.3. Results of such analysis are presented here for UHP-W, W-5Ta and W-5Re irradiated temperatures in a range of 500-800°C. Only loops of size > 4 nm could be analysed (see Fig 4.60). This is considered the lower size limit for making judgements on the inside-outside contrast features of loops. The sampling body consisted up to 150 loops.

Loops of both interstitial and vacancy type were identified, and information on their relative numbers is presented below. It should be noted however that loops > 4 nm make up in some cases only a small fraction of the total. These inside-outside experiments say nothing about the nature of loops smaller than 4 nm. It should not be assured that the smaller loops are mostly vacancy in nature (as is the case at very low doses). Indirect evidence in § 4.4.2. indicated that at least some of the small mobile ½<111> loops are of interstitial type.

Fig 4.61 is a plot of the fraction of analysed ½<111> loops which are interstitial in nature, as a function of material composition and irradiation temperature. Several trends can be seen from the figure. The fraction of interstitial ½<111> loops: 1) was around 50% between 500°C and 600°C in UHP-W, but increased to ~65% abruptly at 800°C; 2) was slightly higher in the alloys than in UHP-W between 500°C and 600°C, but UHP-W overtook at 800°C; 3) underwent gradual but subtle increase in W-5Re and W-5Ta throughout the temperature range; 4) was independent of the alloying element (Re, Ta), provided the same amount of addition.

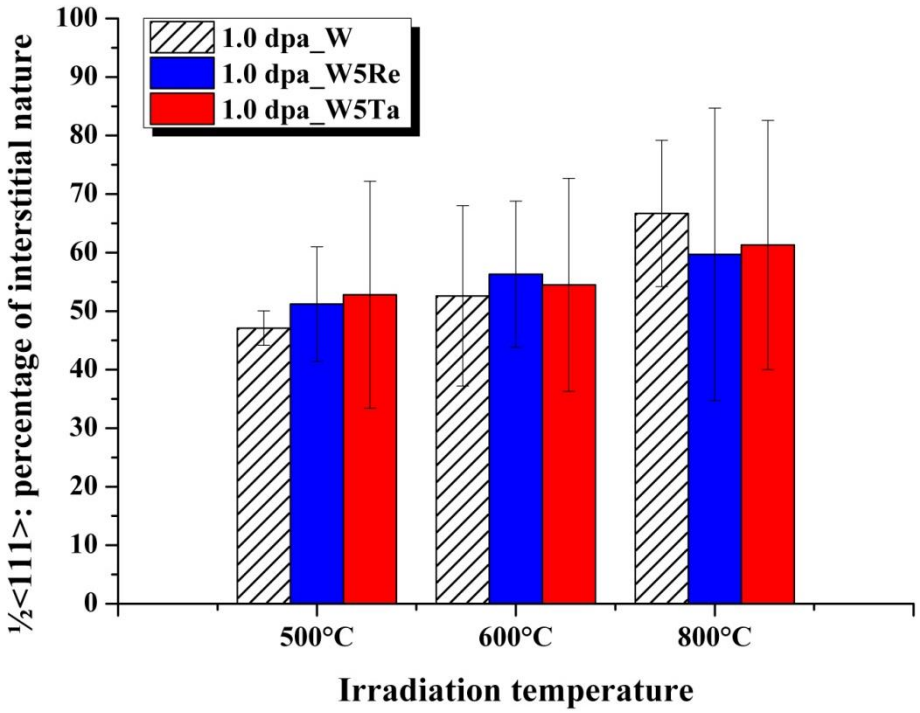


Fig 4.61 The fraction of ½<111> loops of size > 4 nm which are interstitial in nature in irradiated W/W-alloys as a function of the irradiation temperature, at a dose of 1.0 dpa.

Table 4.1 Summary of results on in-situ irradiations of W/W-alloys

Material / Irradiations	Overall microstructure	Loop density	Loop size	Loop geometry ½<111> + <100>	Loop nature (interstitial)
UHP-W, **z** = [001] RT-800°C, 0.01-1.0 dpa	Loop raft/string formation: T ≥ 600°C and dose ≥ 0.4 dpa. Uniform loop distribution for T and doses below. Void-like features found.	T↑, density ↓	T ↑, size ↑ Dose ↑, size ↑	T ↑, ½<111> (%) ↑	T ↑, I-loop (%) ↑
W-5Re, **z** = [001] 500-800°C, 0.01-1.0 dpa	Uniform loop distribution.	T↑, density ↓	T ↑, size ↑	T ↑, ½<111> (%) ↑	T ↑, I-loop (%) ↑
W-5Ta, **z** = [001] 500-800°C, 0.01-1.0 dpa	Uniform loop distribution.	T↑, density ↓	T ↑, size ↑	Not sensitive to T.	T ↑, I-loop (%) ↑
W-5V, **z** = [001] 500-600°C, 0.01-1.0 dpa	Uniform loop distribution.	T↑, density ↓ Strongest effect on loop density (V>Ta>Re)	T ↑, size ↑ Strongest suppression effect (V>Ta>Re,Im).	/	/
Non "**z** = [001]" 500-800°C, 0.01-1.0 dpa	Loop strings form and may evolve further into networks with dose increase.	/	/	/	/

Chapter 5

In-situ Annealing of Radiation Damage in Tungsten

5.1. Introduction

According to the current ITER design, tungsten is expected to maintain its integrity, in particular its thermal and mechanical properties, during tens of months of service while being exposed to fast neutron bombardment at above 1200°C in the plasma-facing region of the divertor. It follows that as well as studying the radiation damage in tungsten, the thermal stability of these defects induced by displacement damage is worthy of study.

This chapter is a continuation of the in-situ irradiation work presented in chapter 4. In-situ annealing for up to 120 min was performed upon completion of the irradiation in the same facility. UHP-W specimens were irradiated at R.T. with 150 keV W^+ ions to a dose of 10^{18} W^+m^{-2} (~1.0 dpa), at a dose rate of ~6.25×10^{14} $W^+m^{-2}s^{-1}$. Thin foils of UHP-W were oriented so that the imaging electron beam (300 kV) was perpendicular to the {001} surface. Then the temperature was ramped up to 300°C, 500°C or 800°C at 25°C/min, and held for 120 min. The imaging conditions adopted were weak-beam dark-field ($\mathbf{g} = 200, 3-4\mathbf{g}$) and kinematical bright-field ($\mathbf{g} = 200$). All videos were recorded at 15 fps. The annealing behaviour of radiation damage in tungsten was characterised by analysing the time and temperature dependence of dislocation loop number density, loop overall size distribution,

and loop geometry as well as loop nature. Several case studies are further included to illustrate the dynamic behaviours responsible for the microstructural evolution observed.

An important note to the annealing experiment is that the requirements for the cleanliness of the sample surface and the vacuum of the microscope column (~10^{-8} Pa) are more stringent than in conventional irradiation experiments. In an unsuccessful annealing session at 800°C for 120 min shown in Fig 5.1, an electron-beam marked region was found. Since the microscope was operating at 300 kV, which is below the displacement threshold ~500 keV in tungsten [110], this feature is considered to be carbon contamination due to beam-cracking of hydrocarbons originating from the column or deposited on the thin foil during electropolishing. The liquid nitrogen cold-trap was topped up every hour to minimize contamination under the electron beam and this turned out to be effective.

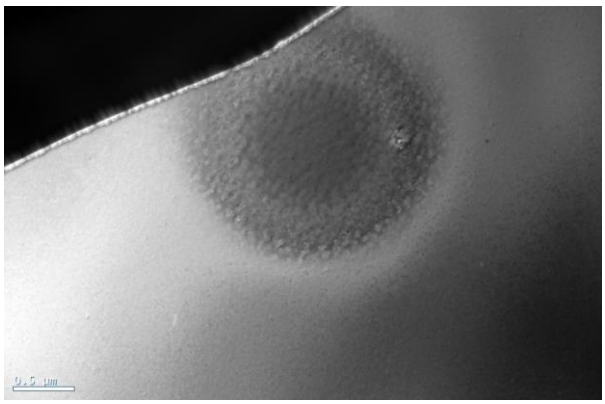


Fig 5.1 300 kV electron-beam induced contamination in tungsten, annealed at 800°C.

5.2. Damage characterization during annealing

The characterization of annealed damage in tungsten focuses on the dislocation loops. The areal loop number density, overall loop size distribution, loop geometry and nature were analysed with respect to the annealing temperature and time. Such quantitative data all refer to areas outside the in-situ electron beam. A systematic search for voids was not performed due to limited time.

5.2.1. Evolution of the microstructure

In this section, the statistical changes in dislocation loops were described, based on micrographs (Figs 5.2-5.4), loop areal number density plots (Fig 5.5) and overall loop size distributions (Fig 5.6 a-c).

The radiation damage evolution took place in two stages, first during the ramp-up stage, and then during the annealing stage. Between the on-set of ramp-up (R.T./1.0 dpa) and reaching the chosen annealing temperature (T, t = 0 min), the damage microstructure underwent the most drastic changes. At an annealing time t = 15 min, the loop number densities tended to stabilize at all three annealing temperatures. Quantitatively, by this time the loop number density had dropped by ~36.2%, ~45.8%, and ~61.8% for T = 300, 500 and 800°C respectively. This is mostly accounted for by loss of loops in the smallest size categories. The overall loop size distributions showed a strong decrease in the number of loops in the 1-2 nm size category at 300°C and 500°C, and in both the 1-2 nm and 2-3 nm categories at 800°C. Between annealing times of 15 min and 120 min, the loss of small loops (< 3 nm) left behind many loop-free regions in the microstructure, and loops of larger size become further apart. Some loop growth was observed. The fraction of loops of size > 4 nm, which is the size requirement for loop nature determination, increased from 23.7% in the irradiated UHP-W sample to 37.5%, 41.4%, 49.7% at T = 300, 500 and 800°C respectively, at t = 120 min when the heat treatment was terminated. The formation of loop strings was also observed at higher annealing temperatures. No loop string formation was observed at 300°C, whilst at 500°C strings of several small loops were common. At 800°C very extensive loop string formation took place, accompanied by a few large irregular-shaped dislocation loops. These loops might be the consequence of loop coalescence within the strings.

5.2.2. Analysis of dislocation loop geometry and nature

Quantitative analyses of loop geometries and nature were carried out in grains with [001] orientation outside the electron beam. It was not possible to make one-to-one correlation of loops imaged under various diffraction conditions due to the high loop number density and so the Burgers vectors of individual loops could not be obtained explicitly. Instead, an estimate of the fractions of loops with Burgers vector of type either ½<111> or <100> was made based on the difference in loop number densities in micrographs recorded under {200} and {110} diffraction conditions. Details of this method have been described in § 3.3.2. The fraction of ½<111> loops in the damage microstructure is plotted as a function of annealing temperature and time in Fig 5.7. It can be inferred that the as-irradiated UHP-W specimen (R.T./1.0 dpa) and the annealed specimens both contain a mixture of ½<111> loops and <100> loops, with ½<111> loops in a majority. After annealing for 120min at 300°C, the fraction of ½<111> loops was little affected. At 500°C, the fraction of ½<111> loops increased from ~62% to ~70% during annealing; and at 800°C the final fraction of ½<111> loops was ~87%. In the specimen annealed at 800°C, the fraction of ½<111> loops increased from ~82 to ~87% between t = 30 min and t = 120 min, suggesting that <100> loops are lost rapidly at this temperature. Owing to limited time on the facility, the post-irradiation annealing experiments had to be terminated at t = 120 min. Hence, it was not possible to determine whether beyond this time limit, the fraction of ½<111> loops reached a plateau.

Loop nature analysis based on the inside-outside contrast method was only performed on larger ½<111> loops in the four post-irradiation annealed specimens, i.e. 300°C/120min, 500°C/120min, 800°C/30min and 800°C/120min. Good statistics on the loop nature were obtained from sampling bodies ranging from 40 to 60 loops. The fraction of ½<111> loops of interstitial nature is plotted against the annealing conditions in Fig 5.8, and the size

distributions of all analysed loops are shown in Fig 5.9. The fraction of loops with **b** = ½<111> which were interstitial increased with annealing temperature. In the specimen annealed at 300°C for 120 min, this fraction was ~35% whereas in specimens annealed for this time at 500°C and 800°C the fractions were ~50% and ~58% respectively. At 800°C, there was a small decrease from ~61% to ~58% in the fraction of interstitial loops in specimens annealed for t = 30 min and t = 120 min. In specimens annealed at 300°C, although only about a third of the ½<111> loops analysed were of interstitial-type, their sizes spread between 5-10 nm, whereas the vacancy-type loops were mostly below 8 nm. In particular, no vacancy loops were found in the size category of 8-10 nm. At an annealing temperature of 500°C, the biggest change compared with 300°C was a substantial increase in loops of size >10 nm, from ~1% to ~7% but the numbers of interstitial- and vacancy-nature loops in this size category appeared about equal. At this annealing temperature vacancy-type loops appeared in the 8-10 nm size category, suggesting that growth of both interstitial and vacancy loops occurs at 500°C. Most of the total increase in the fraction of interstitial loops from 300°C to 500°C was due to increases in the numbers of loops with diameters of 4-5 nm as well as 7-8 nm.

At 800°C the relative numbers of interstitial and vacancy loops seen at different annealing times was investigated. At this annealing temperature the total number of loops in the largest size category (>10 nm) was much higher than in specimens annealed at lower temperatures. However, the fraction of interstitial loops in this size category decreased with annealing time from ~17% at t = 30 min to ~11% from at t = 120 min, while the fraction of vacancy loops only decreased from ~8% to ~6%. Furthermore, the size-nature plots suggest a tendency for the ratio of interstitial: vacancy loops within each size category to approach unity.

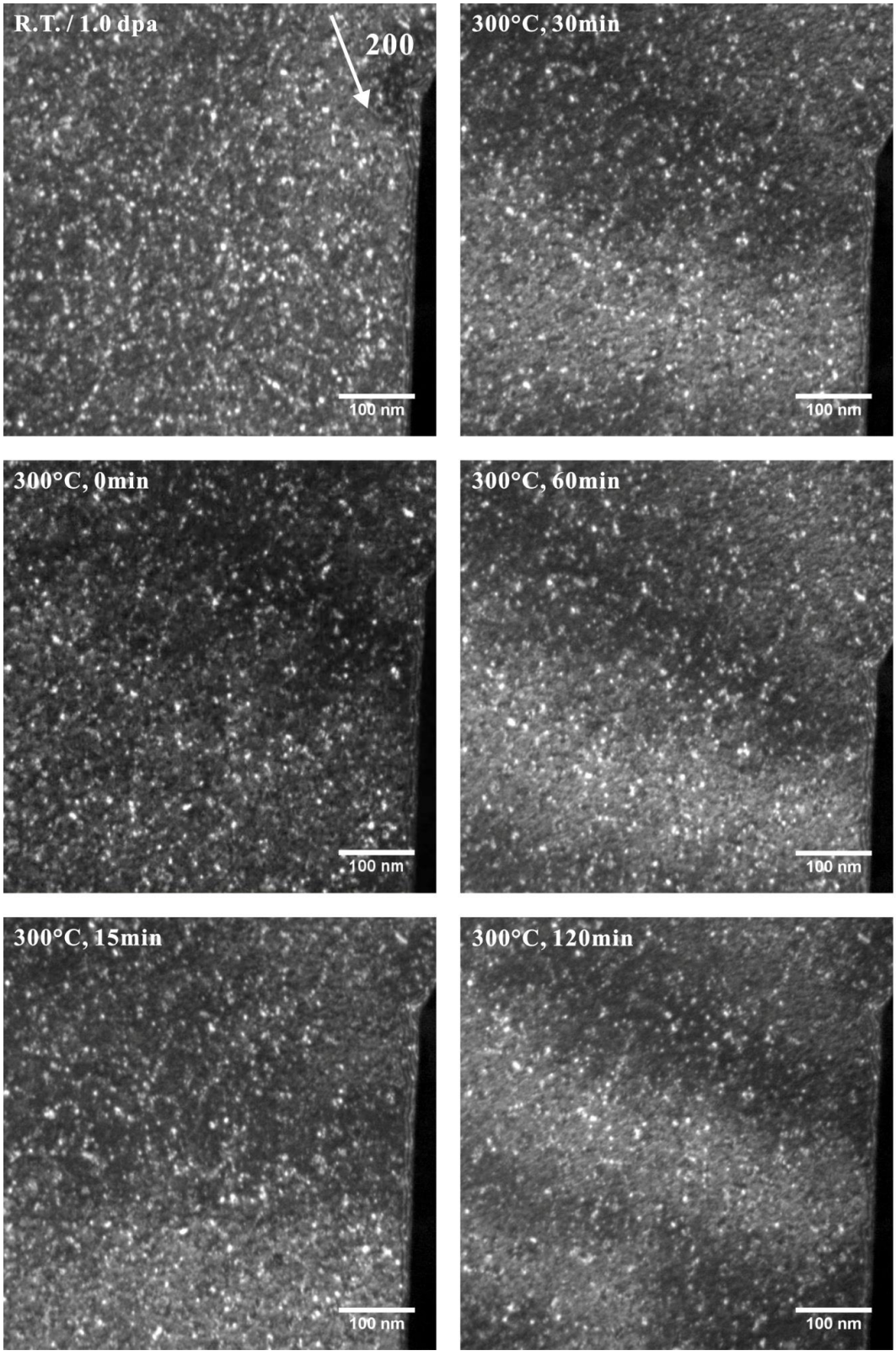


Fig 5.2 Damage evolution (R.T./1.0 dpa) in UHP-W annealed at 300°C for up to 120min.

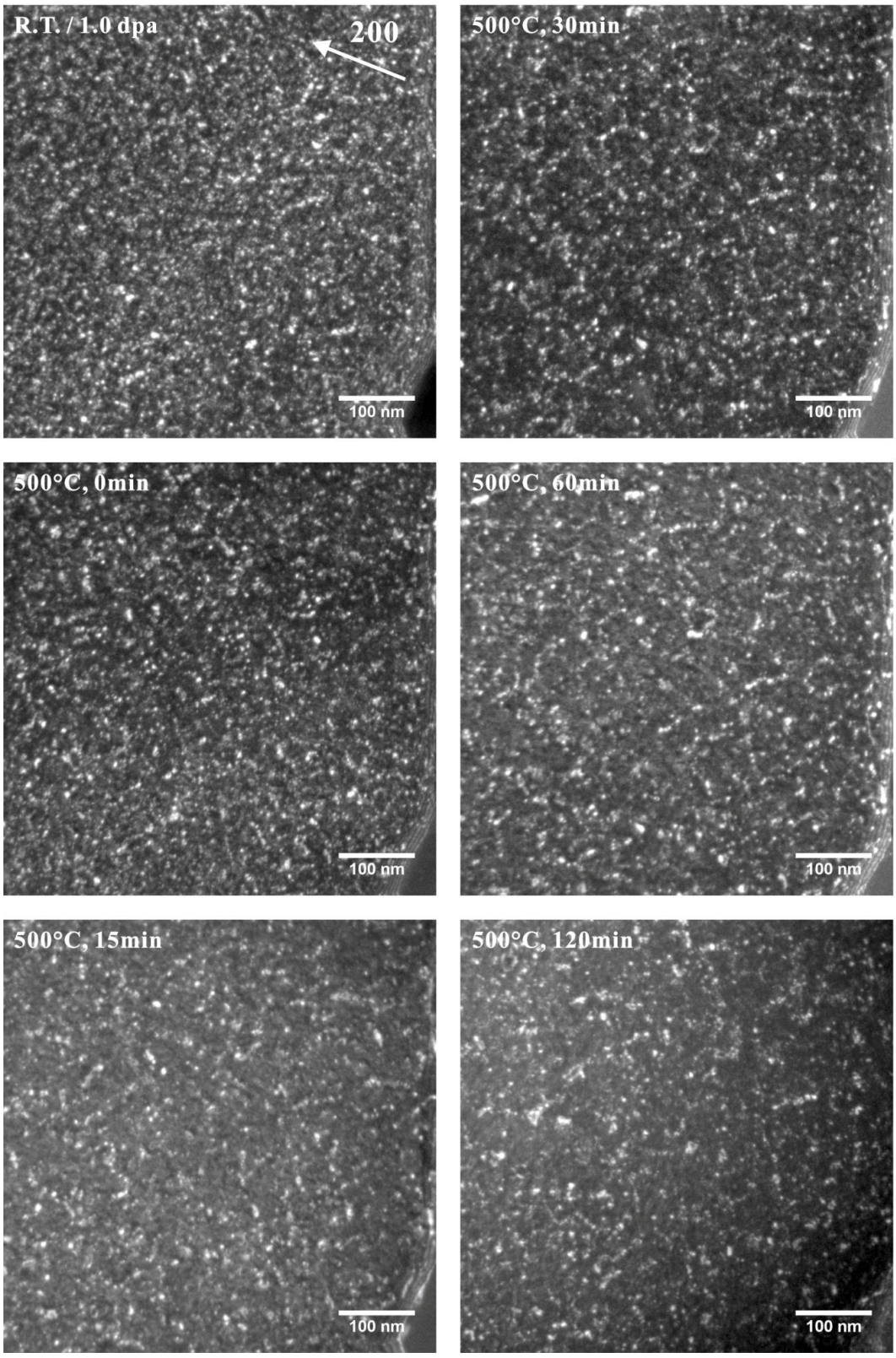


Fig 5.3 Damage evolution (R.T./1.0 dpa) in UHP-W annealed at 500°C for up to 120min.

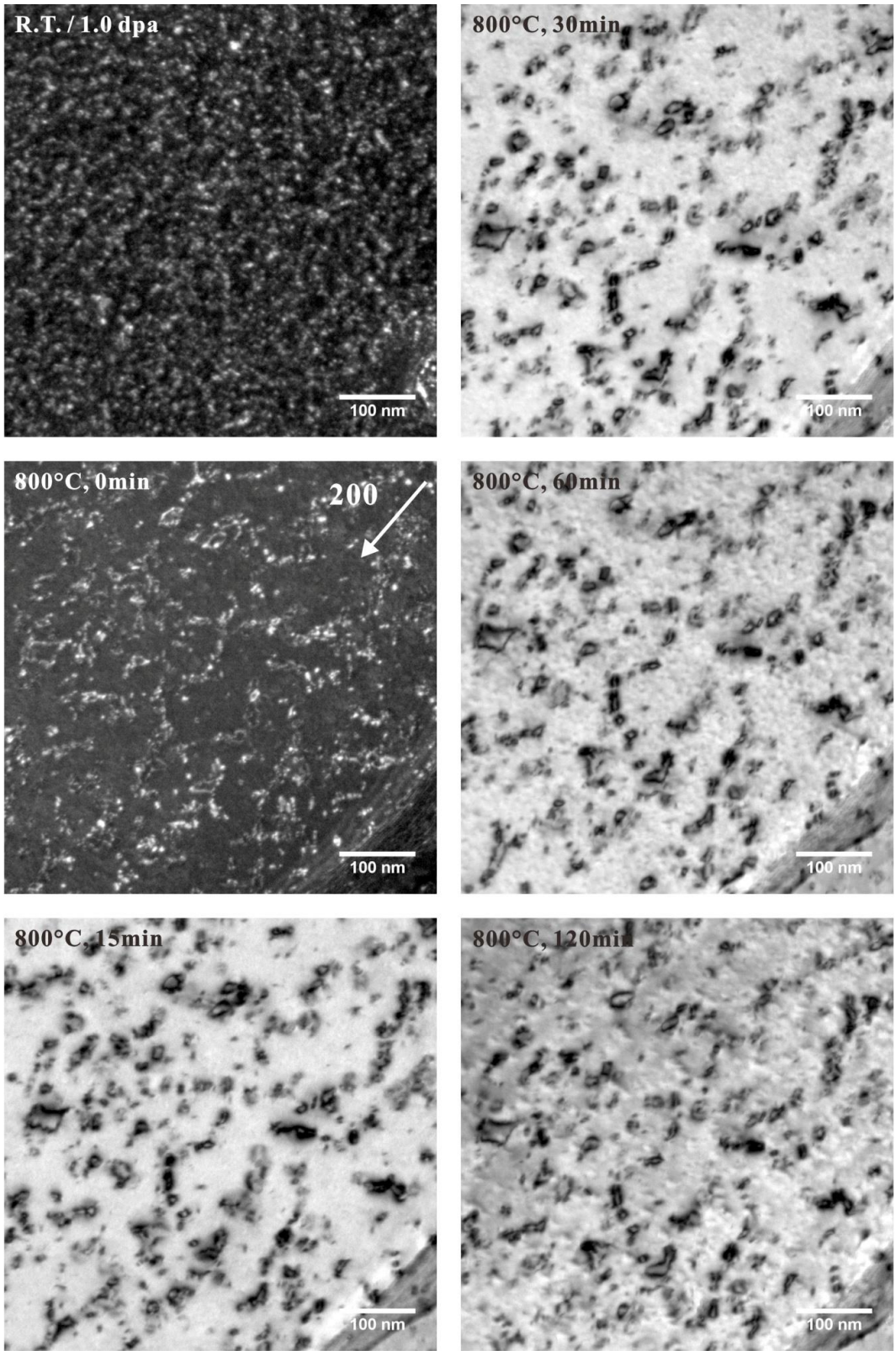


Fig 5.4 Damage evolution (R.T./1.0 dpa) in UHP-W annealed at 800°C for up to 120min.

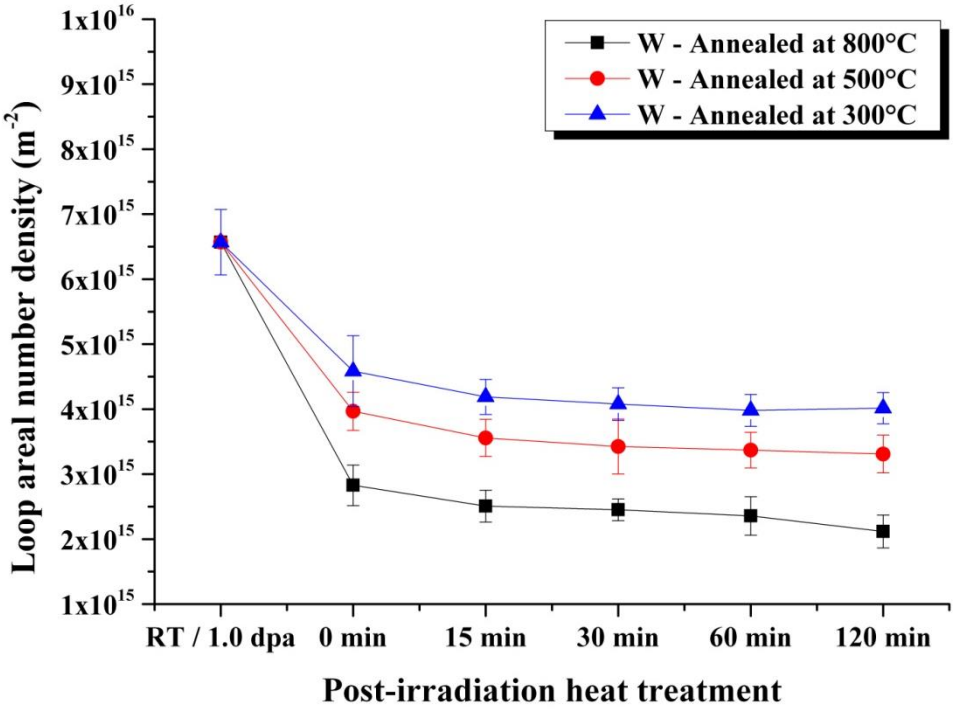


Fig 5.5 Evolution of loop number density in UHP-W (R.T./1.0 dpa) as a function of annealing temperature and time.

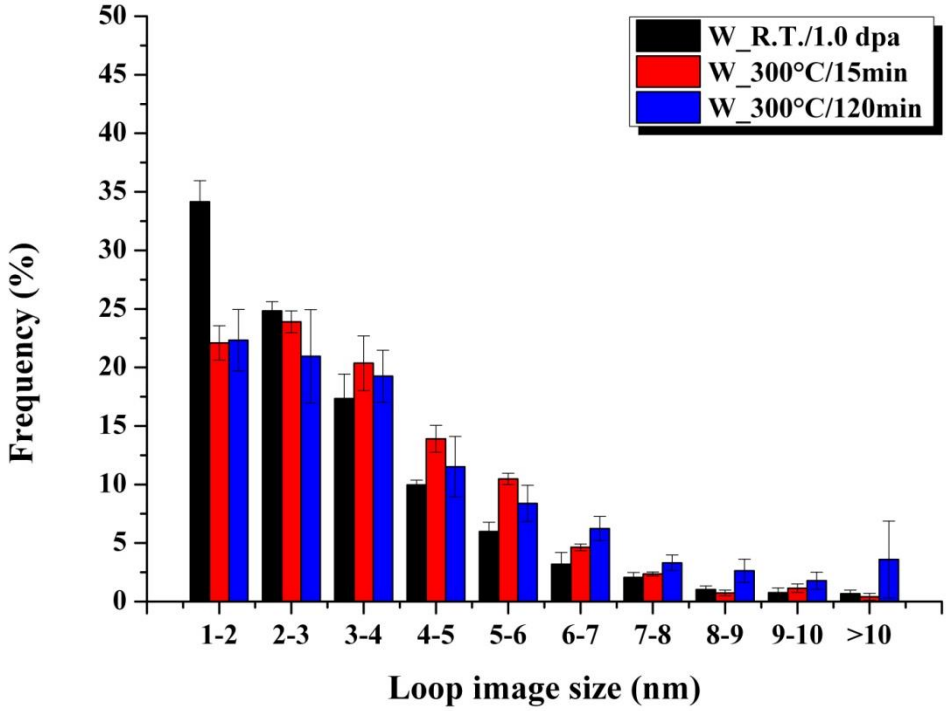


Fig 5.6 a) Loop overall size distribution comparison between irradiated UHP-W (R.T./1.0 dpa) and post-irradiation annealed UHP-W, at 300°C up to 15 min and 120 min.

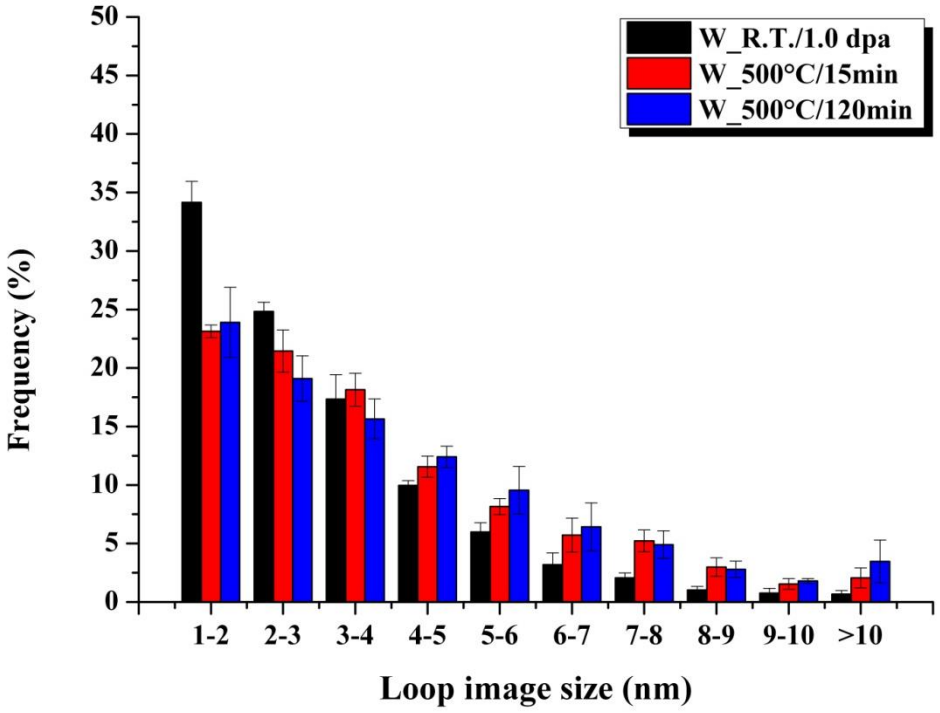


Fig 5.6 b) Loop overall size distribution comparison between irradiated UHP-W (R.T./1.0 dpa) and post-irradiation annealed UHP-W, at 500°C up to 15 min and 120 min.

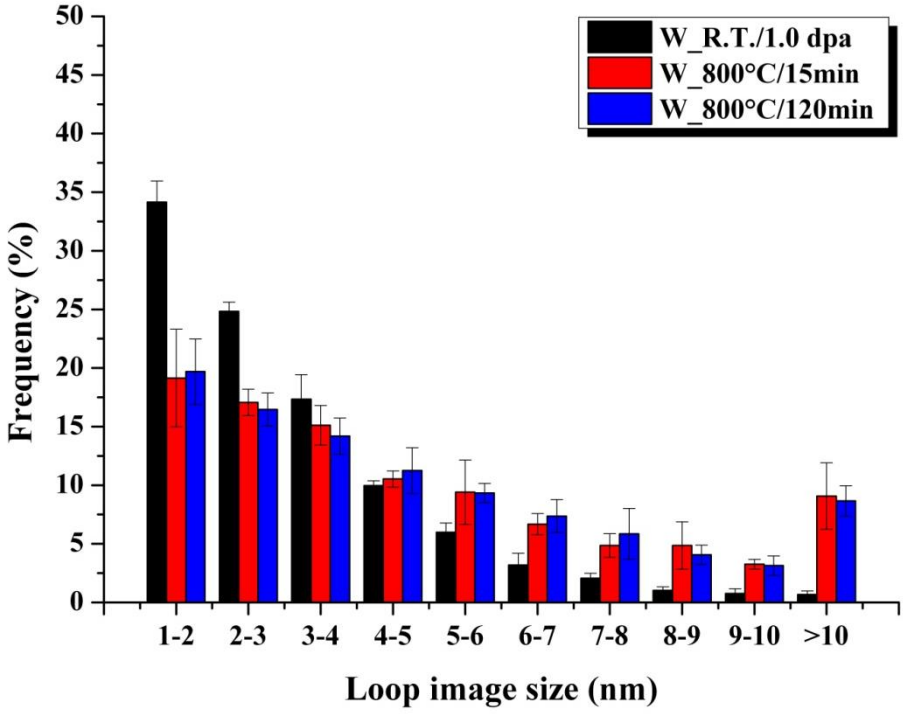


Fig 5.6 c) Loop overall size distribution comparison between irradiated UHP-W (R.T./1.0 dpa) and post-irradiation annealed UHP-W, at 800°C up to 15min and 120min.

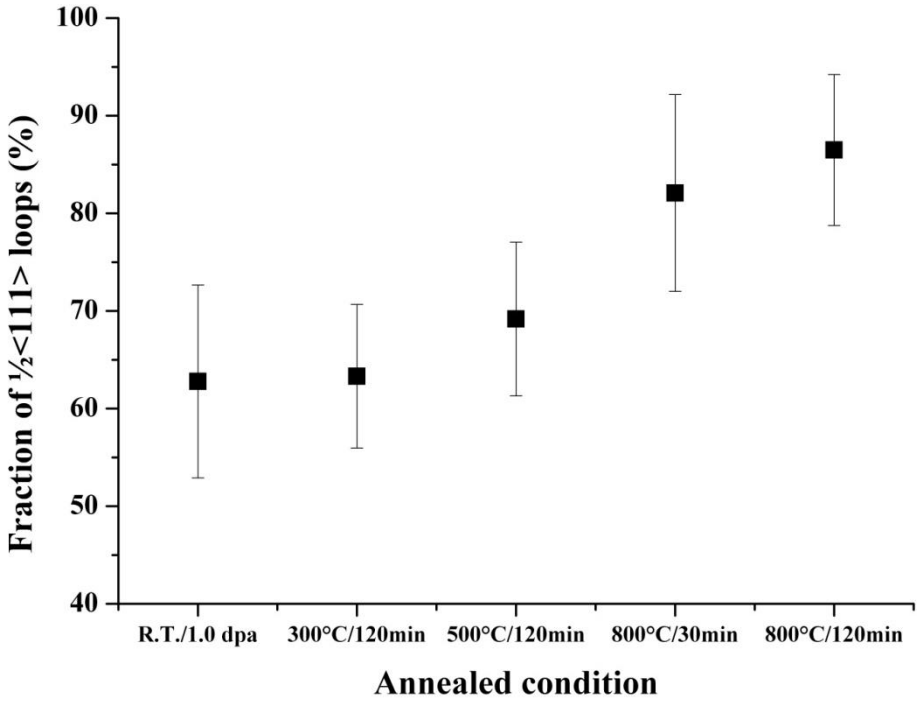


Fig 5.7 The fraction of ½<111> loops in UHP-W (R.T./1.0 dpa) as a function of annealing temperature and time.

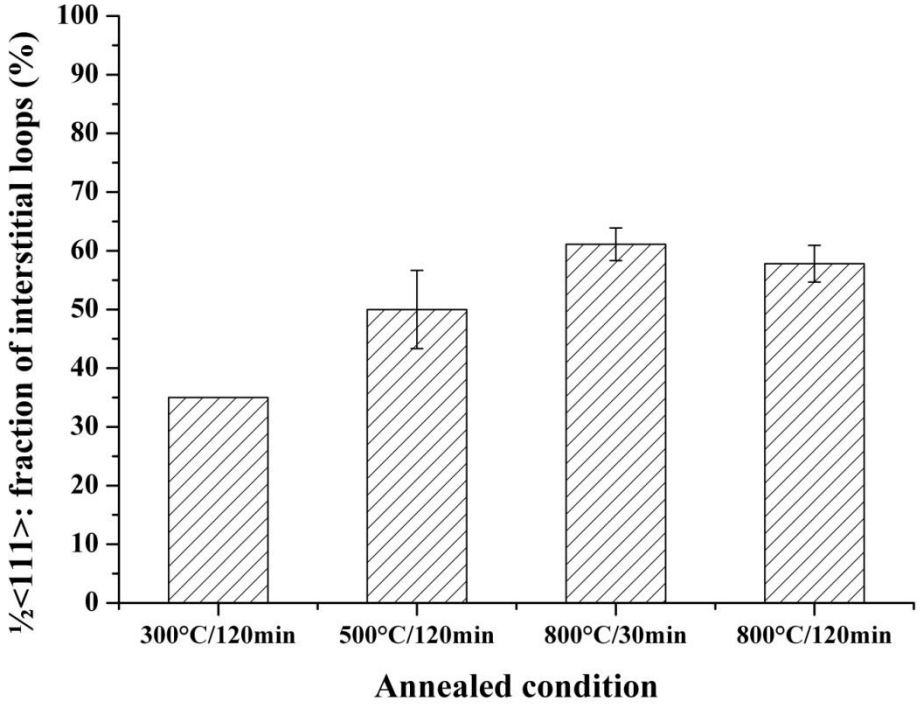


Fig 5.8 The fraction of interstitial loops among loops with **b** = ½<111> in UHP-W (R.T./1.0 dpa) as a function of annealing temperature and time.

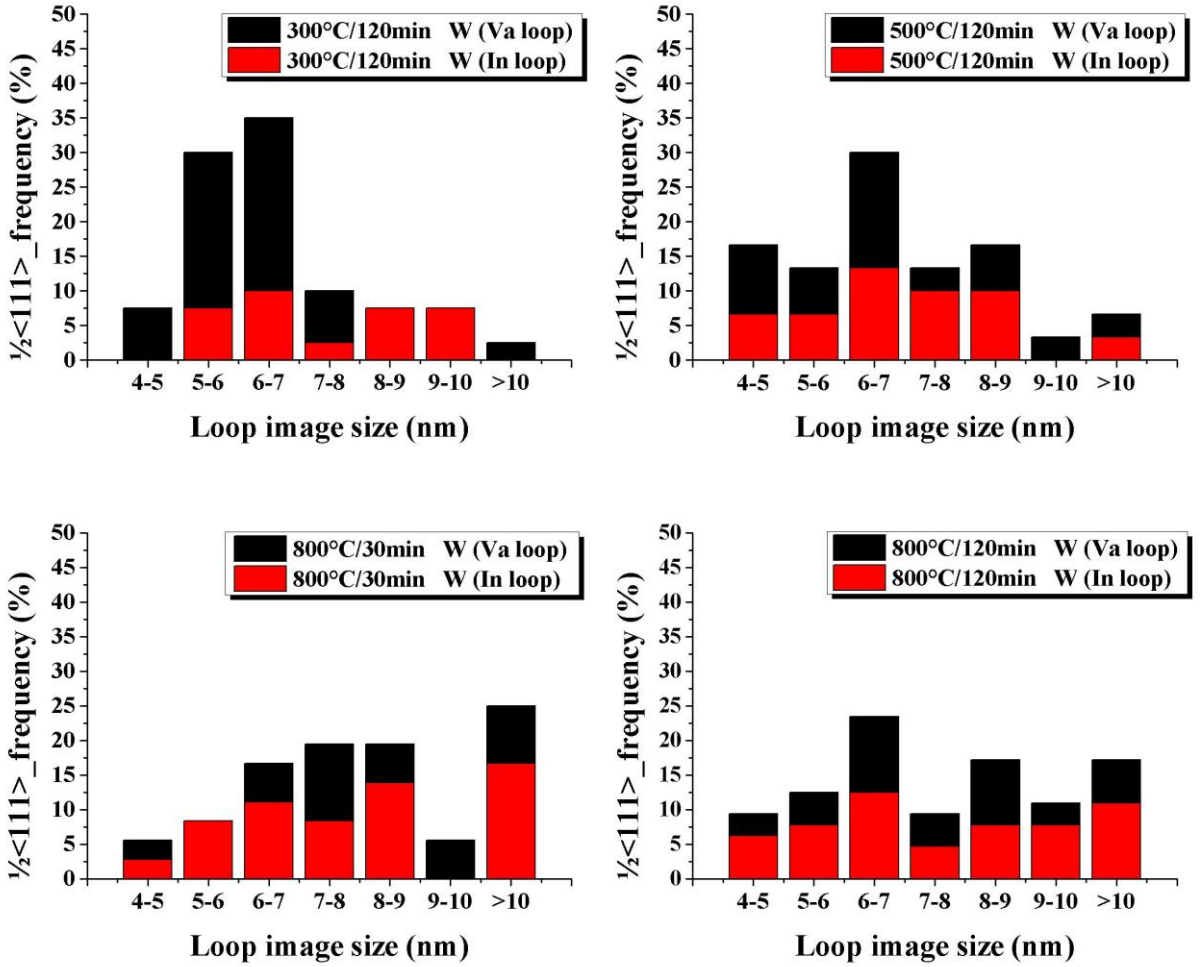


Fig 5.9 The size distributions of interstitial- and vacancy-type ½<111> loops in UHP-W (R.T./1.0 dpa) as a function of annealing temperature and time, normalized against the total sampled ½<111> loop population (typically 40-60 loops).

5.2.3. Case studies of loop dynamic behaviour

Loop dynamic behaviour during the annealing process consisted of a large degree of glide and loss to the surface, the 1-dimentional hopping of loops, the rotation of loop habit planes, and loop-loop interactions and reactions (including absorption and coalescence). Cases of each of the latter three behaviours were studied in detail, with the interpretations validated by image simulations.

5.2.3.1. Loop hopping (one-dimensional movement)

The hopping of loops was found to occur during both irradiation (§ 4.4.1) and post-irradiation annealing. In this section, the influence of annealing temperature on the hopping of loops in UHP-W is explored, quantified as the loop displacement versus time. The irradiation dose (R.T./1.0 dpa) and the diameter of loops analysed (3-4 nm) were kept constant for comparison. Figs 5.10-5.12 show the hopping motion of loops with Burgers vector **b** = $\pm\frac{1}{2}[111]$ or $\pm\frac{1}{2}[11\bar{1}]$ along the projected direction of $\pm[110]$ (refer to § 4.4.1 for the deduction of the loop Burgers vectors) at T = 300, 500 and 800°C respectively, during comparable time of annealing.

The annealing temperature would be expected to affect the mobility of the ½<111> loops, but also to shape their interacting environment by varying the populations of defects (both visible and invisible) which impede loop motion. Fig 5.12 shows that the range of loop displacement has increased by over a factor of 3 from 0-2.5 nm at an annealing temperature of 300°C to 0-8 nm at 500°C and beyond. Additionally, “shoulders” often appear on either side of the displacement peaks, implying that the loops might have dragged and been impeded by obstacles and had to break free from them to continue the hop. One can easily tell the difference in the interacting environment by noting the frequency of these shoulders. For example at 300°C, few shoulders were found; at 500°C, shoulders were frequently seen;

and at 800°C, few appeared. The influence of the environment was possibly weaker at both 300°C (restricted displacement range and small probability of encountering obstacles) and 800°C (greater driving force for hopping and a reduced population of invisible obstacles). The motion of the dislocation loop at 500°C is consistent with hopping through a field of obstacles. Hops of around 8 nm were typically made in 2 or 3 discrete steps. At 800°C, it seems that the maximum loop displacement was comparable, but hops were usually made in single steps.

Hopping was not restricted to individual loops. An example of a pair of loops undergoing collective motion at 800°C is illustrated in Fig 5.13. The projected direction of the hops is parallel to $[1\bar{1}0]$, indicating the Burgers vector of the loop pair is the same, being **b** = $\pm$½$[1\bar{1}1]$ or $\pm$½$[1\bar{1}\bar{1}]$. Gradually the range of displacement reduced substantially to < 5 nm, when the loop pair appeared to be "shivering".

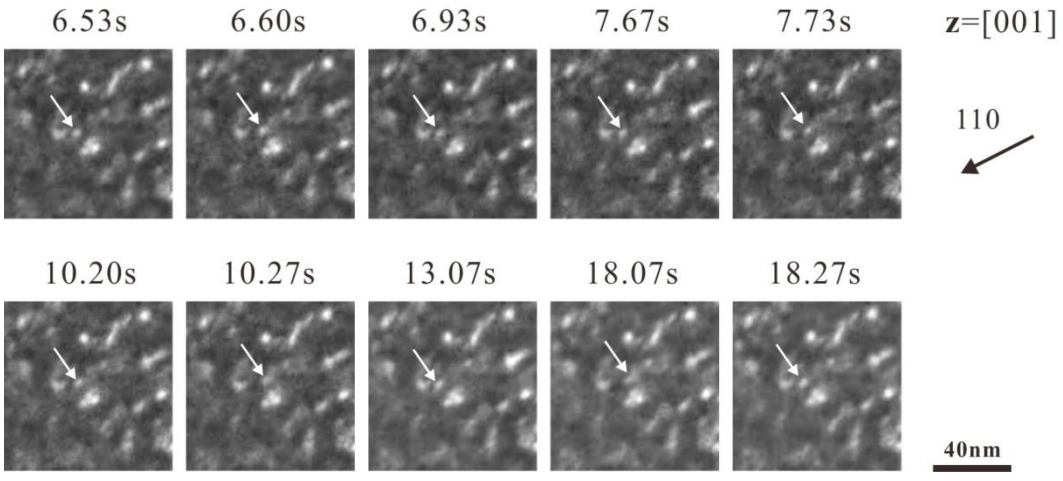


Fig 5.10 Hopping of a dislocation loop along [110] direction in UHP-W (R.T./1.0 dpa), annealed at 500°C.

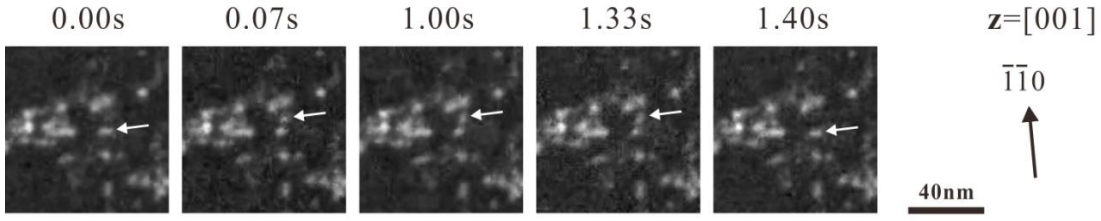


Fig 5.11 Hopping of a dislocation loop along $[\bar{1}\bar{1}0]$ direction in UHP-W (R.T./1.0 dpa), annealed at 800°C.

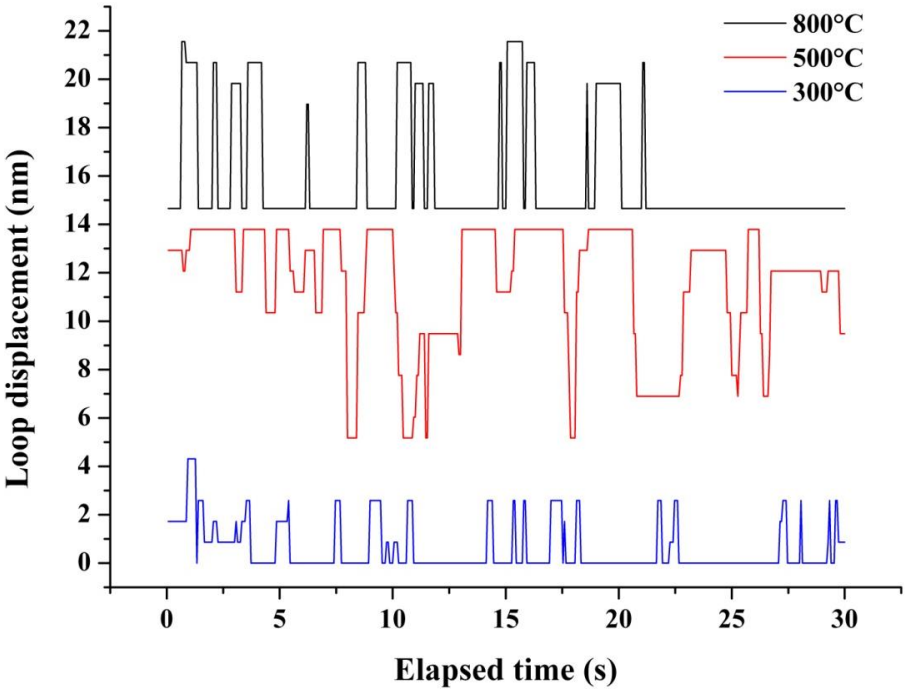


Fig 5.12 Hopping of individual loops has been observed in UHP-W (R.T./1.0 dpa), annealed at a) 300°C, b) 500°C and c) 800°C respectively.

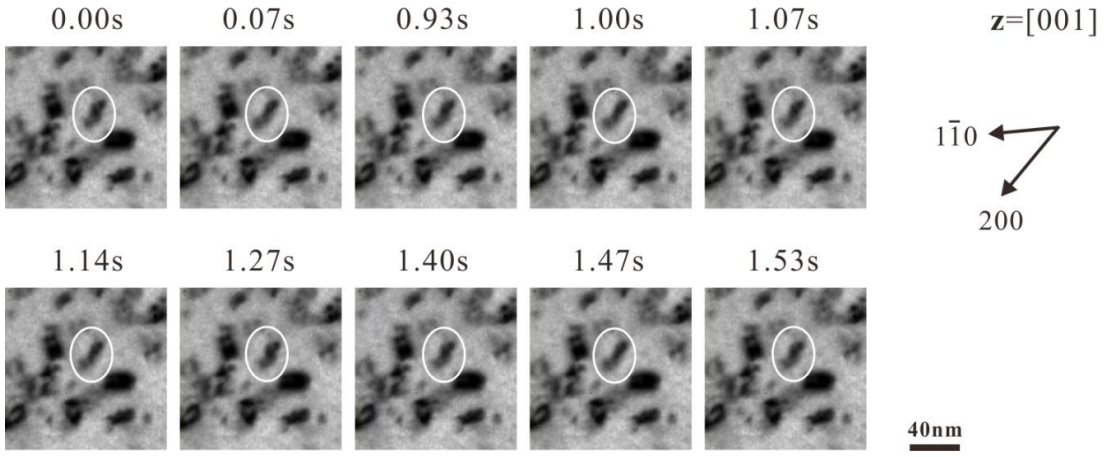


Fig 5.13 Two loops in collective hopping motion, observed in the post-irradiation annealing of UHP-W (R.T./1.0 dpa) at 800°C. (See Appendix, video 10).

5.2.3.2. The rotation of loop habit plane

Dislocation loops often exhibited a change in their habit planes during post-irradiation annealing. An example is shown in Fig 5.14 in the UHP-W specimen (R.T./1.0 dpa) annealed at 500°C .

In Fig 5.14 a), frame sequences were recorded in the **z** = [001] orientation and loop A was set as a reference point. Loop B underwent a transition of contrast features from "double-arc" at 0.00s, to an "elliptical black dot" at 0.20s and back to a "double-arc" at 1.80s. However, the main axis of the "double-arc" contrast has rotated by ~16°. A schematic illustration of this transition is shown in Fig 5.14 b). Based on its contrast shown in **g** = 110, one can infer that the Burgers vector of loop B must be either $\pm$½[111] or $\pm$½[11$\bar{1}$]. Since loop nature determination was not part of the interpretation, loop B was arbitrarily assigned with **b** = ½[111] or ½[11$\bar{1}$] in the image simulations displayed in Fig 5.14 c). If loop B were assigned **b** = ½[111], the image simulations infer that its habit plane **n** would be close to [122] at 0.00s, but would have rotated to the edge-on orientation **n** = [110] at 0.20s, and then to **n** = [111] at 1.80s. Note that the angle between **n** = [122] and [111] was 15.8°, which matched well with the measured value of the angle of rotation of the loop axis. The alternative Burgers vector ½[11$\bar{1}$] also gives agreement with the simulations, with rotations of habit plane from **n** = [12$\bar{2}$] to **n** = [110], and finally **n** = [11$\bar{1}$]. All simulations which appeared to be consistent with the experiment are marked red. The restricted recording rate of the CCD camera made it difficult to keep track of what exactly took place during the intervals of 0.00 - 0.20s and 1.67-1.80s, which resulted in the large rotation of the habit plane in loop B (i.e. 45° and 35.2° respective to the two intervals).

5.2.3.3. Loop interactions and reactions

A more complicated example of loop interaction and reaction is demonstrated here during the annealing of UHP-W (R.T./1.0 dpa) at 800°C. According to Fig 5.15 a), loop A and B appear bound from 0.00s to 0.14s, after which they separate by the rotation of loop A by ~65°. At 0.20s, loop B approached loop A, and was absorbed at 4.07s. The schematic diagrams of the process are shown in Fig 5.15 b). Based on these observations, loops A and B may have occupied comparable depth position in the foil; otherwise the absorption of loop B would have been difficult. The Burgers vector of loop A can be inferred from its contrast with $\mathbf{g} = 1\bar{1}0$, namely $\mathbf{b} = \pm\frac{1}{2}[1\bar{1}1]$ or $\pm\frac{1}{2}[\bar{1}11]$. Image simulations were performed on loop A by assigning the Burgers vector variants to be $\frac{1}{2}[1\bar{1}1]$ or $\frac{1}{2}[\bar{1}11]$, and its diameter to be 10 nm. This is smaller than the observed dimension by a factor of 4 for reasons of computational efficiency, but sufficient to interpret the main objective of habit plane rotation. The results of the image simulations are presented in Fig 5.15 c). If loop A is assigned $\mathbf{b} = \frac{1}{2}[1\bar{1}1]$, the simulations are consistent with a rotation in its habit plane from $\mathbf{n} = [0\bar{1}1]$ to $\mathbf{n} = [101]$. Similarly, if loop A has $\mathbf{b} = \frac{1}{2}[1\bar{1}1]$, the rotation of habit plane probably have been from $\mathbf{n} = [011]$ to $\mathbf{n} = [\bar{1}01]$. The angle of rotation in both cases is calculated as 70°, matching well with the measured value 65°. Owing to its less well-defined contrast shape, the determination of the Burgers vector of the small loop B was difficult even with image simulations. However, judging from its one-dimensional hopping behaviour which allowed it to approach loop A at 0.20s, it may have been a ½<111> loop but the nature of which could not be determined at this point. It follows that the large loop A must be of the same nature as loop B, on account of its growth after absorbing loop B.

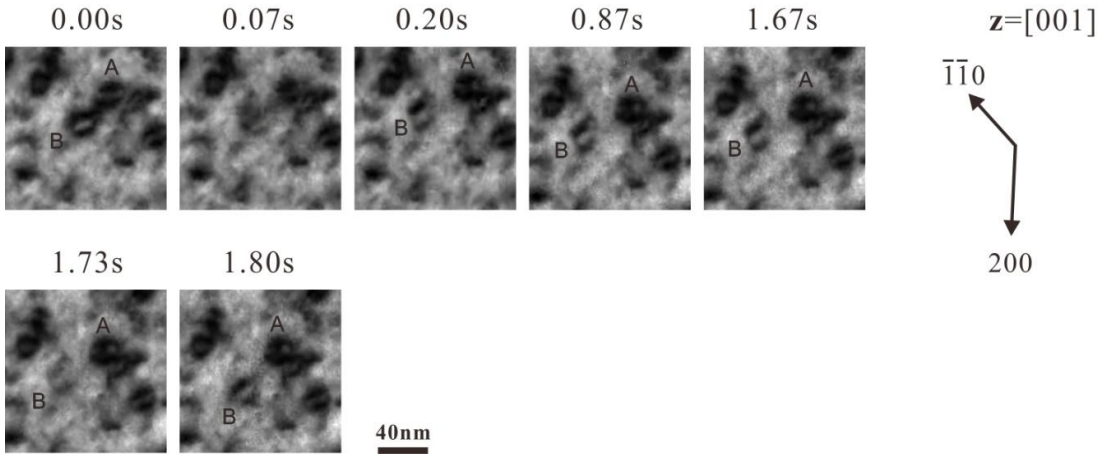


Fig 5.14 a) Change of habit plane in loop B in UHP-W (R.T./1.0dpa) annealed at 500°C. (See Appendix, video 11).

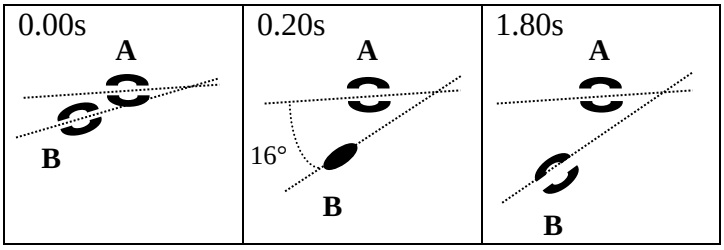


Fig 5.14 b) A schematic diagram of loop B rotating its habit plane.

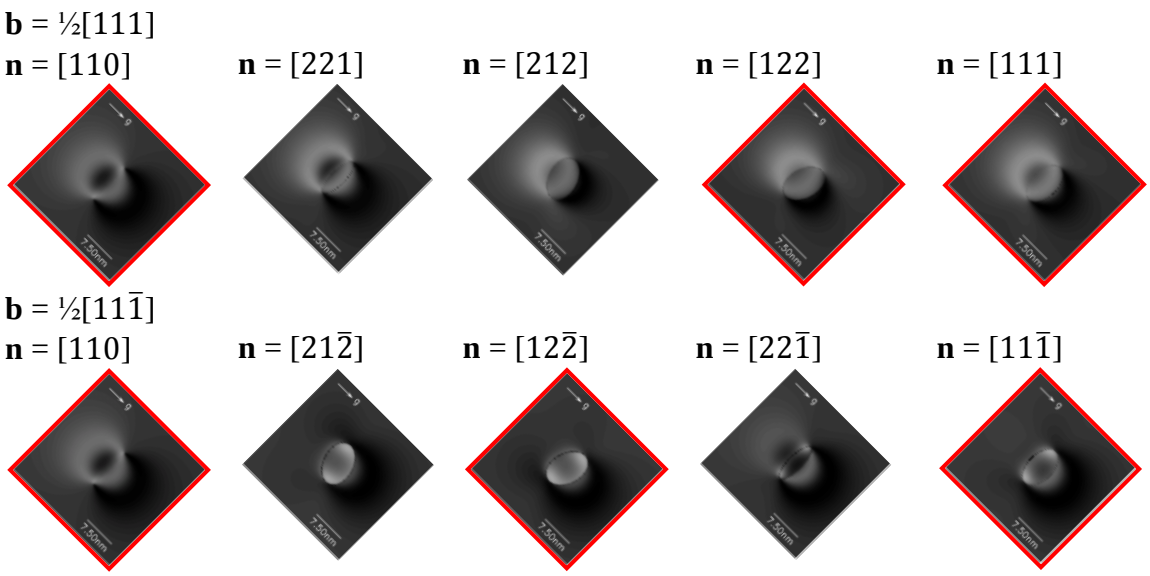


Fig 5.14 c) TEMACI image simulations of a dislocation loop with **b** = ½[111] and ½[11$\bar{1}$] under kinematical-bright field **g** = 110. **n** stands for habit plane normal. Foil thickness: 100 nm; loop diameter: 10 nm; depth of the loop in the foil: 15 nm.

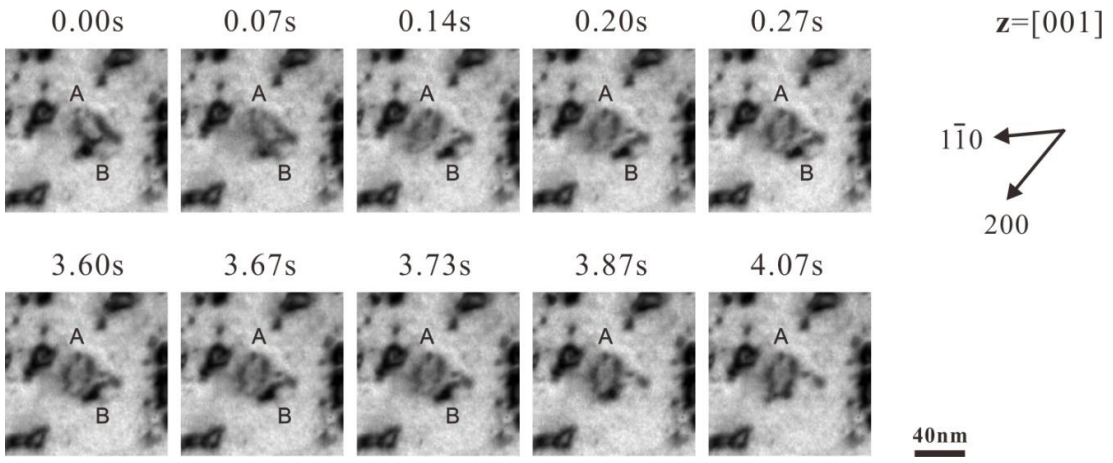


Fig 5.15 a) A bound loop pair A and B become separated by a large angle (~65°) by rotation of loop A. Loop B approaches loop A by attraction and is finally absorbed. (See Appendix, video 12).

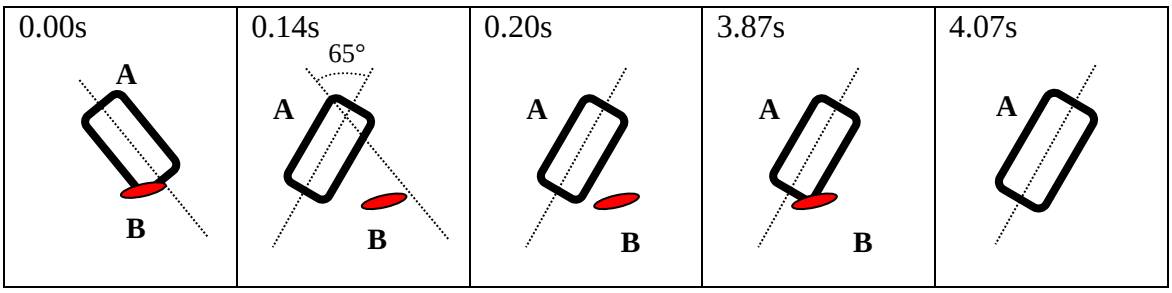


Fig 5.15 b) Schematic diagrams of the transformations encountered by loop A and B.

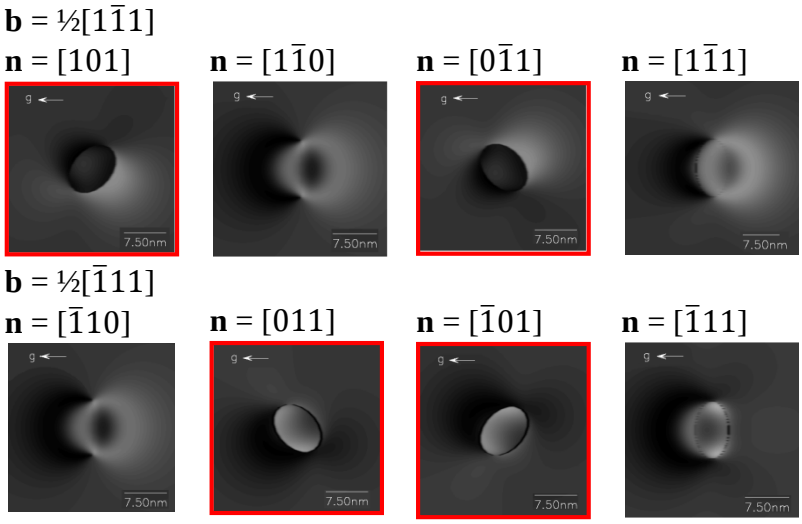


Fig 5.15 c) TEMACI image simulations of a dislocation loop with **b** = ½[$\bar{1}$11] and ½[1$\bar{1}$1] under kinematical-bright field **g** = 1$\bar{1}$0. **n** stands for habit plane normal. Foil thickness: 100 nm; loop diameter: 10 nm; depth of the loop in the foil: 15 nm.

Table 5.1 Summary of results on the in-situ annealing of pre-irradiated tungsten

Experiment condition		Damage microstructure
Irradiation	R.T. / 1.0 dpa	✧ Loop density: ~ 6.6×10^{15} /m^2 ✧ Loop geometry: ½<111> (~63%) + <100>
Annealing	T = 300, 500, 800°C, t = 0-120 min	✧ T constant, t ↑, loop density changes little, loop size ↑ ✧ T ↑, t constant, Loop density ↓, loop size ↑ ½<111> (%) ↑ and I-loop (%) ↑ ✧ T = 800°C, t ↑, ½<111> (%) ↑ and I-loop (%) ↑ Microstructural transformations during post-irradiation annealing are much more sensitive to the annealing temperature than time.

Chapter 6

Discussions

6.1. Introduction

Fast neutron displacement damage in tungsten originates in the production of a spectrum of primary recoil atoms [18]. Each energetic recoil atom then goes on to create a displacement cascade (<1 ps) consisting of hundreds of Frenkel pairs [19], followed by the local melting of the lattice (thermal spike, ~1 ps). Massive atomic rearrangements then lead to local clustering (quenching, ~10 ps). Finally annealing of the displacement cascade (> ns) marks the onset of defect diffusion, agglomeration and annihilation [24]. The mechanisms involved in this early stage of radiation damage in tungsten are discussed in § 6.2, based on a simplified scenario of collision cascades created in thin-foil irradiations by 150 keV self-ions which simulate primary recoils. In this section, the role of irradiation temperature is emphasized and remarks are made on the comparison between tungsten, iron and molybdenum. With an increase in dose, the damage microstructure in tungsten evolves. Explanations of the manner of damage evolution in tungsten are sought in § 6.3 by combining data from (150 keV W^+ ions) thin-foil in-situ irradiation and (2 MeV W^+ ions) bulk implantation. The aspects of loop dynamic behaviour and the roles of temperature, dose, impurities and alloying elements as well as crystallographic orientation are considered. Once the irradiation terminates, the thermal stability of damage arises as a concern. The impact factors affecting the annealing behaviour

of radiation damage in tungsten are discussed in § 6.4. Finally, in § 6.5 remarks are made regarding the differences between thin-foil and bulk ion irradiations.

6.2. Low-dose radiation damage in tungsten (in-situ)

The low dose refers to 0.01 dpa, a damage level at which defects produced within individual cascades would be dealt with. Estimations on the time for a cascade to achieve thermal equilibrium[16] can be comparable to the timescale of experimental observations (20-30s) in this thesis, depending on the irradiation temperature [39]. This time is > 30s between R.T. and 500°C, 9.8s for 600°C and 0.1s for 800°C. Bearing this in mind, it is likely that thermally unfavourable configurations of defect clusters are present in the cascade, since the system might not yet have reached thermal equilibrium.

6.2.1. Defect nucleation mechanism

In low-dose experiments, loops popped-up almost immediately upon irradiation between successive video frames and varied little in size ($T \leq 600$°C). Confirmed by the linearity of the loop density against dose shown in Fig 4.3, the cascades were unlikely to overlap spatially and that loops observed of vacancy type, must have been formed through the collapse process of individual cascades. The fact that the defect yield appeared universally low in all irradiations of such suggested that the probability of cascade collapse was low. Vacancies might have adopted other more stable configurations such as small voids, vacancy sponges, or even platelets, according to formation energies calculated by Gilbert et al. [39]. But it is difficult to confirm within the resolution of conventional TEM.

According to Calder et al. [23], the collision-induced point defects tend to redistribute in such manner that interstitials cluster at the peripheries of cascades, while the core is

[16] The time for the cascade to reach thermal equilibrium is described by the annealing phase, and of course is much larger than the lifetime of the collision and thermal-spike phase.

concentrated with vacancies. Once the cores collapse into vacancy type loops, they must follow certain geometric restrictions, known as the Eyre-Bullough mechanism[17] [96]. The theory states that loops nucleate on the closest-packed {110} planes as a result of the local vacancy super-saturation. Initially, they would appear as faulted ½<110> loops. The stacking fault is then eliminated by a shear process through <100>, forming a perfect loop with **b** = ½<111> or through <110> forming **b** = <100>. In either case, the habit plane of the loop will then rotate to a pure edge orientation, i.e. from {110} to {111} or {100} respectively. Equations 6.1 and 6.2 illustrate how the stacking fault is removed through the two types of shear reactions.

$$\frac{1}{2}[110] + \frac{1}{2}[00\bar{1}] \rightarrow \frac{1}{2}[11\bar{1}] \qquad Eq\ 6.1$$

$$\frac{1}{2}[110] + \frac{1}{2}[\bar{1}10] \rightarrow [010] \qquad Eq\ 6.2$$

The fact that the nucleation process involves the formation of a fault loop may have been an alternative explanation to the observed low defect yield in tungsten. The stacking fault energy in tungsten is about 800 $mJ \cdot m^{-2}$, and thus brings about a large nucleation barrier for the faulted ½<110> cluster nucleus [100].

The morphology of dislocation loops observed in this work agrees well with the Eyre-Bullough mechanism. Although faulted ½<110> loops were not directly observed, the presence of both pure-edge ½<111> loops and ½<111> loops with shear components was confirmed by black-white contrast experiments and image simulations. In addition to the dominant ½<111> loops, evidence of <100> loops was also found, but these loops were gradually eliminated with the increase of temperature. In the only other systematic study of early stage radiation damage in tungsten by Häussermann [68, 69], the observations were

[17] The Eyre-Bullough mechanism was first proposed for interstitial loops, but can account for loops of the other nature.

somewhat different. In tungsten irradiated at R.T. with 20-70 keV Au^+ ions, a small number of faulted ½<110> loops were reported together with a majority of ½<111> loops but not <100> loops. All loops were of vacancy nature.

Two aspects may account for the absence of faulted loops in this work. First, Jäger et al. [70] pointed out that faulted loops have a probable upper size limit of around 1.8 nm at R.T and so might not grow large enough to be resolved in the microscope. Second, the process of unfaulting may be expedited by the increased thermal energy as a consequence of the higher incident ion energy and irradiation temperature. The existence of energetically non-favourable <100> loops in this work may be associated with the non-equilibrium state of the displacement cascade within the timeframe of the low-dose irradiations. When thermal equilibrium is expected to be achieved quickly, e.g. at 800°C, <100> loops were difficult to find (Fig 4.7). Recent simulations of high energy collision cascades of tungsten give support to the loop morphologies found in this work [111]. The simulations adopted the same ion energy (150 keV W^+ ions) and irradiation geometry as experiments in this thesis. Simulated cascades exhibited no break-up into sub-cascades, and typically produced a large quasi-liquid volume favouring the formation of large clusters (10-200 SIA or vacancies). Evidence of both ½<111> and <100> loops were found, the sizes of which were typically ≤ 3 nm. No faulted ½<110> loops were identified.

As noted above, molecular dynamic (MD) simulations of cascades also predict the formation of interstitial loops and small clusters [23, 111]. However, the migration energy of SIAs is over an order of magnitude lower than that of vacancies, i.e. 0.088 - 0.102 eV versus 1.78 eV [20, 44]. Hence, the fate of these highly mobile interstitials in thin-foil irradiations will be mostly lost to the surface. The significant loss of SIAs at surfaces lowers their recombination with the vacancies, leading to more vacancy survival, and may therefore

enhance cascade collapse (examples: Cu_3Au and Ni_3Al [112]). Only a small amount of SIAs will survive and coalesce with similar clusters deeper in the foil, and these may be the loops which appear more gradually later in the irradiation.

6.2.2. The role of irradiation temperature

The irradiation temperature has a strong influence on the defect yield and vacancy loop size distribution in tungsten (Figs 4.5-4.6), which is associated with the mobility of vacancies within cascades. Between liquid He temperature and R.T., the mobility of vacancies is limited (i.e. no long-range migration) and an increase of temperature may extend the lifetimes of thermal spikes by allowing extended time for vacancies to diffuse, cluster and collapse into visible loops [103]. In contrast, the range between R.T. and 800°C would see the activation of long-range migration of vacancies according to the annealing stages of defects in tungsten (Table 1.3). If the migration barrier were overcome, vacancies would be expected to be capable of diffusing out of the cascade core, resulting in decreased core vacancy super-saturation levels, and a reduced driving force for collapse [55]. Freely migrating vacancies may be lost to additional vacancy sinks, including both self-interstitials and interstitial loops (causing annihilation or loop shrinkage) and vacancy clusters such as loops and voids, which may grow. Greater loss of vacancy loops by glide to the free surface would also be expected [113].

The defect yield in 150 keV cascades of tungsten remained low in all experiments ($\leq$ 3%). Its further decrease with increasing temperature is probably due to the reduced driving force for collapse as well as the favoured transition from closed-loops to open-loops or voids among the increasingly mobile vacancy clusters [39]. Such behaviour of vacancies might have also been responsible for the late occurrence (~1s after the start of the irradiation)

of visible loops at 800°C, where additional time was required to achieve the collapse threshold of vacancy super-saturation in a cascade.

A characteristic transition temperature of 500°C was found, consistent with the activation barrier of long-range migration of vacancies in tungsten [55]. Above the temperature not only did the defect yield decrease more quickly, but also the average loop sizes increased. Specifically, an abrupt shift of the dominant loop size category from 1-2 nm to 4-5 nm was found. The total number of vacancies contained in visible loops also decreased (Fig 4.11) which suggests loss of vacancies to sinks other than vacancy loops. Free vacancies may have either annihilated with SIAs or have adopted more stable configurations, such as voids. Between R.T. and 600°C, the loops retained their initial size throughout the course of low-dose irradiations, consistent with the cascade collapse mechanism. At 800°C, loops were seen to grow moderately within ~0.3s of nucleation and then remained constant in size until the end of the irradiation. This suggests that absorption of smaller vacancy clusters in the vicinity of the cascade may have taken place subsequent to the collapse of the core region.

6.2.3. Comparative studies with iron and molybdenum

Cascade phenomena in iron and molybdenum have been extensively studied, taking into account the influences of ion source, ion energy, foil orientation, dose and temperature. Some of these works in literature were summarized in Table 6.1.

In self-ion irradiated iron, studies have found that visible loops do not form until the overlap of cascades occurs, i.e. at doses $\geq 10^{17}$ $Fe^{+}m^{-2}$ [114]. For doses below this, English et al. reported that no visible damage was produced for a range of ion energies (40-240 keV) [115]. Some have attributed this observation to the sub-branching of cascades, which is believed unfavourable for the nucleation of large clusters [18]. However, recent molecular dynamic simulations of 200-500 keV cascades in iron showed that sub-branching of cascades

did not produce well-separated sub-cascades until the recoil energy had significantly decreased (i.e. at the end of the incident atom trajectory) [116]. Hence, an alternative explanation must be sought. Jenkins et al. have looked at the probability of cascade collapse in iron from a "deposited energy density (ion energy/ion mass)" point of view, considering its impact on the vacancy super-saturation in the core of the cascade [100, 117]. 80 keV Fe^+, Kr^+ and W^+ ions were implanted to 5.0×10^{16} ions·m^{-2} at R.T. in **z** = [011] foils. The heavier Kr^+ and W^+ ions created visible vacancy loops, with the defect yield being higher for Fe^+ ions. The measured defect yield for W^+ ions was ~20%. Correction factors such as loop loss to the surface were applied, and the true defect yield increased to nearly 90%. This implied that almost all cascades formed collapsed to loops [117].

The loop types seen in irradiated iron resembled those of tungsten. The nucleation of co-existing ½<111> and <100> loops of vacancy type has been adequately explained by Eyre and Bullough [96]. The temperature dependence of cascade collapse in iron was reported by Yao et al [118]. With an increase in irradiation temperature from R.T. to 300°C, the defect yield dropped. The authors interpreted the trend as a consequence of increased vacancy mobility at 300°C and therefore a slow build up of cascade debris [18] in the damage microstructure, which hindered the collapse process.

The cascade collapse behaviour in molybdenum was also investigated by irradiations with self-ion and (heavy) molecular-ions. In self-ion (60 keV) irradiations between R.T. and 535°C, to a dose of 7.4×10^{15} $Mo^+\cdot m^{-2}$, English et al. reported only vacancy loops with Burgers vector ½<111>. At R.T., most loops were non-edge but with an increase in irradiation temperature, more loops rotated towards pure-edge orientations, which is consistent with the Eyre and Bullough mechanism [96]. Also, the defect yield decreased by

[18] Cascade debris: atomic displacement induced point defects and their clusters.

over 90%, while the average loop size increased from ~2.7 nm to ~4.1 nm. The authors interpreted the observations as a result of enhanced vacancy migration at elevated temperatures and therefore reduced driving force for cascade collapse [119].

Molecular ion irradiations on molybdenum were performed over a range of ion mass (Sb^+, Sb_2^+ and Sb_3^+) and ion energy (60-180 keV) on two foil orientations (**z** = [001], [011]). The increase of "deposited energy density" per displacement cascade seemed to favour not only an increase in the number of visible defects, but also the nucleation of <100> loops, which were not found in the Mo^+ or Sb^+ irradiations. For instance, 60 keV Sb^+ ion irradiation produced no <100> loops but for the 180 keV Sb_3^+ ion irradiations, 1.7% of the total loop population were of <100> type [101, 120].

Table 6.1 Comparison of vacancy clustering in bcc metals at R.T.

Metal	Ion	Orientation	Defect yield (%)	Dose (ions·m^{-2})	Ref
W	60 keV Au^+ 150 keV W^+	various [001]	10 3	$\leq 5.0\times10^{17}$ $\leq 1.25\times10^{16}$	[68] This work
Fe	80-240 keV Fe^+ 80 keV Kr^+ 80 keV W^+	[011]	No visible damage 2 18 ± 5	$\leq 5.0\times10^{16}$	[117] [114]
Mo	60 keV Mo^+	[011]	12 ± 2	7.4×10^{15}	[119]
	60 keV Sb^+ 60 keV Sb_2^+ 60 keV Sb_3^+ 180 keV Sb_3^+		4 ± 1 8 ± 1 12 ± 1.5 28 ± 1	1.0×10^{16}	[101]
	60 keV Sb^+ 60 keV Sb_2^+ 60 keV Sb_3^+ 180 keV Sb_3^+	[001]	- 0.03 2 ± 0.5 7 ± 1	4.0×10^{15}	

6.3. Evolution of radiation damage in tungsten (in-situ; bulk)

The longer-term microstructural evolution during the ion irradiations in tungsten is a comprehensive outcome of the intrinsic dynamic behaviour of dislocation loops, the irradiation parameters (temperature and dose) and the material (composition and crystallography). Plausible interpretations are sought in this section for the variety of trends and observations found in bulk implanted and thin-foil irradiated tungsten and alloys.

6.3.1. The dynamic behaviour of dislocation loops

6.3.1.1. Loop hopping

Prismatic loops, as illustrated in Fig 1.11 may diffuse along their glide cylinders. It is a thermally activated motion and is associated with a characteristic migration barrier. The value of which may suggest the Burgers vector, the nature as well as the interacting environment (concentrations of impurities and small clusters).

In iron, direct observations were reported for ½<111> loops, which appeared to glide back and forth along the (projected) direction of their Burgers vector [108, 118]. A schematic view of which is illustrated in Fig 6.1 [108]. In order for <100> loops to become mobile, an activation energy barrier higher than 2.5 eV must be overcome [121]). Both interstitial and vacancy ½<111> loops may exhibit hopping behaviour [36, 108, 122]. These glissile clusters have been conceived as bundles of crowdions (or voidions) along <111> direction, for interstitial and vacancy loops respectively. If the loops were spatially delocalized in an obstacle-free matrix, the characteristic migration barrier for ½<111> loops is comparable to that of a single SIA (0.34 eV [123]), and the migration of the loop is a result of individual (but correlated) SIA activity [124]. Similar considerations can be made for the hopping of vacancy loops. The migration energy barrier for a monovacancy is around 0.67 eV and vacancy ½<111> loops are about as mobile as a monovacancy [44]. Fig 6.2 illustrates the

considerations above by comparing the diffusion rates of ½<111> loops of the opposite nature as a function of temperature calculated from MD simulations. It is shown that an interstitial ½<111> loop is always more mobile than a vacancy loop of the same size, but their diffusion rates remain on the same order of magnitude [125].

Above is the case for loop hopping in an obstacle-free matrix. In practice, materials would always contain a certain amount of impurity atoms as well as irradiation-induced clusters. For instance, in Arakawa's experiments, there were about 200 ppm of impurities present in the pure iron foils. Along with small clusters, they could effectively trap ½<111> loops during glide motion. As a result, the migration energy barrier for an interstitial ½<111> loop in iron extracted from experiments was found much higher than theoretical values, i.e. 1.3 eV versus 0.34 eV) [108].

Quite a few of the interpretations on loop hopping in iron can be transferred to tungsten. In tungsten, all loops that have exhibited hopping behaviour were identified as **b** = ½<111> (Figs 4.20-4.21). Meanwhile, <100> loops mostly appear as sessile traps for smaller loops or clusters (Fig 4.25), probably also due to a high activation barrier [121]. In the absence of obstacles, the migration barrier of small ½<111> interstitial loops (several nm in diameter) is also comparable to that of a single SIA (~0.1 eV [20]). The high mobility of interstitial loops can be similarly attributed to a crowdion-bundle configuration, where constituent SIAs move in a correlated manner [124]. According to D. Mason, the migration barrier of ½<111> vacancy loops is close to that of an interstitial loop, i.e. 0.1 - 0.2 eV [126], but over an order of magnitude lower than a mono-vacancy, i.e. 1.78 eV [21]. It has been argued that loops in the form of voidion-bundle can partition the amount of displacement over a few atoms, which should be easier than moving one vacancy (effectively one atom) by one lattice spacing unit [126]. Based on theoretical migration energies alone, one cannot tell

the nature of hopping loops observed in tungsten. However, if additional information on the trapping energies (impurities, clusters) were known, the mobility of ½<111> interstitial and vacancy loops may differ and they may therefore be distinguished.

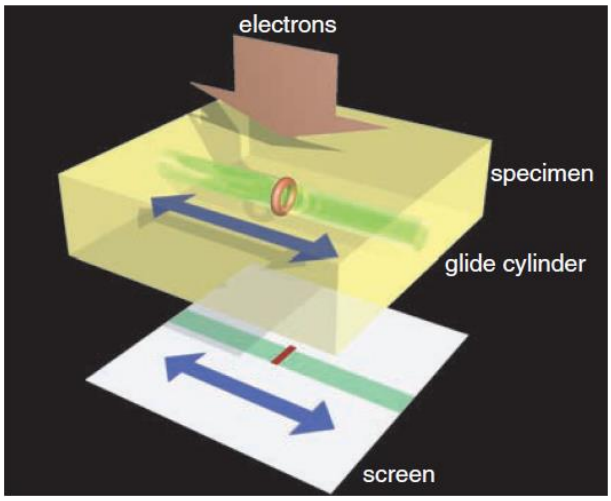


Fig 6.1 Schematic view of a nano-sized interstitial loop (shown as red ring) undergoing 1D-hopping in parallel with its Burgers vector [108].

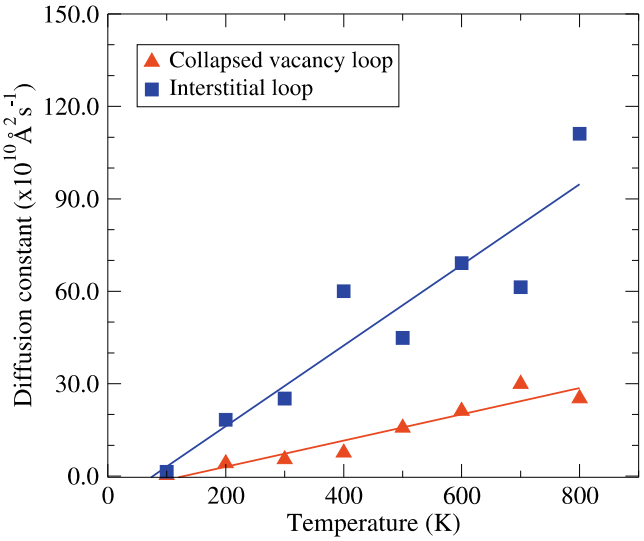


Fig 6.2 Calculated diffusion coefficients as a function of temperature in Fe for 1.9 nm ½<111> (61 vacancies/interstitials) vacancy and interstitial loops [125].

In addition to the geometry and nature of the hopping loops, factors which may affect the lateral range and the fraction of loops which hop were also investigated in tungsten. The first is the temperature. Annealing of pre-irradiated UHP-W specimens at 300°C, 500°C and 800°C respectively showed pronounced differences. Qualitatively, the higher the

temperature, the wider is the range of displacement of the loops, and the higher is the fraction of loops which hop. Unfortunately, the diffusion coefficient of the loops in this work could not be extracted due to the limited recording speed of the CCD (15 fps). In many of the frames obtained, a "ghost" or "shadow" of the hopping loop was found, implying that the loop was hopping at a higher speed than the camera recording rate. However, based on the observation that loops underwent infrequent hops separated by intervals of time, it was quite certain that loops were still retarded by TEM non-resolvable clusters and impurities within the range of temperature studied (R.T. - 800°C). Hence, the migration pattern of hopping loops observed did not follow the Arrhenius rule [127]. The second factor is loop size. In Figs 4.20 - 4.21, it was demonstrated that as a glissile loop grew it decreased in mobility. Arakawa et al. made analogous observations in iron and argued that this an indication of the hopping loop not overcoming the Peierls potential hill at once and as a whole, but by the nucleation and movement of thermal kinks (double kinks) [108]. Obviously for smaller loops, fewer double kinks would be required to form and move, and hence lower migration barrier and higher mobility. Also, the smaller loops would be less affected by the retarding atmosphere, consisting of smaller clusters and impurity atoms. The third factor is the presence of bombarding electrons and ions. Loop hopping has been demonstrated a thermally activated process. In fact, it can also be propelled by the bombardment of high energy electrons and ions. A comparison between Fig 4.21 and Fig 5.12, where the temperature has been held constant at 800°C, suggests that the mobility of loops is enhanced under electron and ion irradiation. Moreover, areas under the electron beam in **z** = [001] grains of irradiated tungsten were consistently lower in loop number density than areas outside the electron beam (Fig 4.58). This suggests that the glide of ½<111> loops to the foil surface is facilitated by the electron beam. Such observations could be explained in terms of the displacement of

impurity atoms subject to irradiation and therefore detrapping of the hopping loop [109], as well as the impacts on the core atoms of the loop which contribute substantially to the fluctuating-random force causing the irradiation-driven diffusion of loops [128].

The influence of the mobility of dislocation loops on the damage microstructural evolution can be profound. Dislocation loops interact through long-range elastic forces, and only when they are sufficiently close can reactions and transformations to complex structures such as loop strings and networks take place.

6.3.1.2. The rotation of loop habit plane

The discussions here refer to dislocation loops with **b** = ½<111>. These loops tend to rotate from their probable nucleation plane {110} towards {111}, a pure edge orientation, in order to reduce their energy by reducing their line length [129]. This may account for the small scale rotations (≤ 35°) observed in this work (e.g. Fig 4.31). However explanations must be sought for the large angle rotations in UHP-W during post-irradiation annealing (up to 45° at 500°C in Fig 5.14, and up to 65° at 800°C in Fig 5.15). Image simulations suggested that the path of habit plane rotation was {110}→{111}→{110}. Each variant of a ½<111> loop has three candidate {110} nucleation planes. In spite of the unfavoured energetics, the extreme case of the loop rotating from its nucleation plane to its crystallographic equivalence might be a consequence of transient thermal fluctuation and short-range inelastic interactions with its neighbourhood. The fact that an immediate small-scale and damped vibration of the loop which had rotated 65° in UHP-W annealed at 800°C supports the argument of interaction. After the large angle rotation, the role of energetics became dominant, i.e. loops would eventually adopt the low-energy pure-edge configuration (as shown in Fig 5.14).

6.3.1.3. Loop-loop interaction: change of loop Burgers vector

An example of a change of Burgers vectors during mutual elastic interaction has been illustrated in Fig 4.22 in irradiated W-5Re. The smaller loop B changed its Burgers vector from $\pm$½[$\bar{1}1 \pm 1$] to $\pm$½[$\bar{1}\bar{1} \pm 1$] after interacting with the adjacent larger loop A. Although Burgers vector change could occur if loop B coalesced with a $\pm$½[$\bar{1}\bar{1} \pm 1$] loop of larger size [130], this possibility can be excluded since no evidence of such can be seen in the frame sequences. Another interpretation originates from a similar observation in iron. It was argued that the change of Burgers vector is a consequence of the nucleation of a shear loop and its propagation through the original loop, with which it shares a common habit plane [131]. Applying this argument to our observation, it follows that loop A acts as the source of shear stress for B. Once the stress level achieves a threshold value by thermal fluctuation, shear will be activated and induce the Burgers vector change, e.g. ½[$\bar{1}11$] would change to ½[$\bar{1}\bar{1}1$] by a [$0\bar{1}0$] shear, but the loop habit plane would remain on ($\bar{1}01$).

6.3.1.4. Loop-loop reactions

The loop reactions observed in this thesis involve the collision of nano-scale dislocation loops with Burgers vector of either ½<111> or <100>. Confirmed by image contrast simulations, the products of such reactions do not always comply with Kirchhoff's law[19] [38]. However, the loop energetics based on isotropic and continuum elastic energy considerations (Gb^2) remain valid. Seven loop reaction prototypes are summarized in Table 6.2, taking into account the various combinations of loop Burgers vectors and their relative sizes. Each reaction prototype is discussed in detail as follows.

---

[19] The Burgers vectors are conserved at dislocation nodes, analogous to Kirchhoff's law of electrical current flow.

Prototype (1) is the mechanism responsible for the development of loop strings and networks witnessed in UHP-W under high temperature/dose irradiation conditions (**z** = [001] grain) or W-Ta/V alloys (non **z** = [001] grains). ½<111> loops of the same variant and nature (predominantly interstitial) align as strings due to elastic interactions and form one single loop through absorption or coalescence, leaving the Burgers vector and nature unchanged [132]. This reaction route retains the geometry of the reactant loops but minimizes the elastic free energy though the reduction of dislocation line length.

Prototype (2) has not been observed directly in this thesis or in the literature. Initially, the model was proposed as a mechanism for the formation of <100> loops in irradiated iron. In proposing this mechanism, Marian et al. [121] considered two loops, i.e. A with **b**= ½[111] lying on (110) and B with **b**= ½[$1\bar{1}\bar{1}$] lying on ($1\bar{1}0$) (illustrated in Fig 6.3). The loops glide on their glide cylinders determined by their Burgers vectors and collide. A [100] junction forms upon the binary loop collision. Since the glide direction of each loop is within the habit plane of the other, glide continues within the other loop after the formation of the [100] junction. In the end, the two interacting ½<111> loops transform into one single <100> loop. Both Marian et al. and Arakawa et al. have emphasized the difficulty of this reaction route by pointing out the stringent requirements: loop A and loop B must be of comparable size and similar shape and the glide process (segment propagation) within each other must be synchronized [121, 133]. As a result, prototype (3) is the more frequently observed event during the collision of two different variants of ½<111> loops. If loop A and loop B have a significant size difference, the product of the reaction adopts the Burgers vector of the larger loop; if loop A and loop B are comparable in size and the synchronization of the glide process were disturbed by thermal fluctuations, the product would retain the Burgers vector of the loop which glided faster.

Prototypes (4) and (5) require loops to be sufficiently adjacent, but such events are unlikely to be captured experimentally owing to the low number density of <100> loops in the damage microstructure of tungsten and their restricted mobility at the temperatures employed in this thesis (due to high activation barriers for glide and climb) [121]. Nevertheless, prototype (4) is theoretically probable, for a reason similar to that of prototype (1). Prototype (5) has been reported in α-Fe, but the reaction pathway is not yet well understood [130].

Both prototypes (6) and (7) are supported by experimental evidence, but the former route is more commonly reported. Marian et al. proposed a reaction pathway for large <100> loops absorbing small neighbouring ½<111> loops [121]. Relative potential energies were calculated and eliminated the possibility of direct rotation from <111> to <100> (energy barrier > 2.5 eV for iron). The <111> self interstitial atoms must evolve through an intermediate <211> configuration which then quickly rotates into a <100> orientation.

To conclude, relative loop size plays a crucial role in the reaction between two nano-scale dislocation loops in tungsten and also other bcc metals. The general rule for this is that the product loop tends to adopt the Burgers vector of the larger loop among the reactants. Also, it can be inferred that the behaviour of loop strings observed may also be explained based the reaction prototypes discussed here, since each segment of a string can be treated as an independent loop.

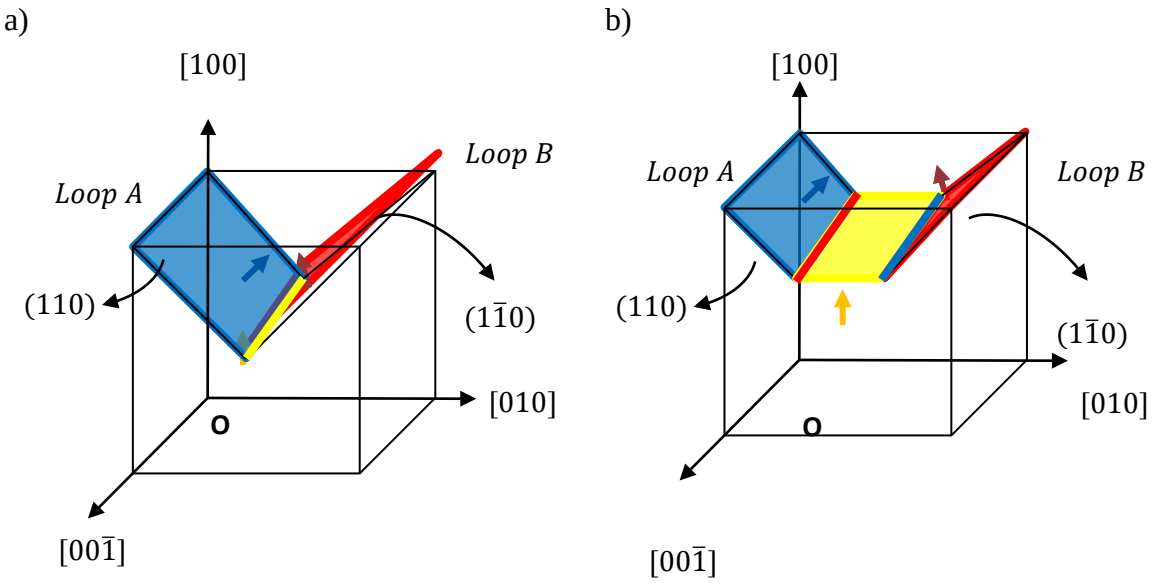


Fig 6.3 Schematic diagram on the formation of a **b** = [100] loop. a) Loop A (blue) with **b**= ½[111] lying on (110) and loop B (red) with **b**= ½[1$\bar{1}\bar{1}$] lying on (1$\bar{1}$0) forms a [100] junction (yellow). b) The [100] junction expands to a **b** = [100] loop (yellow).

Table 6.2 Summary of loop reaction models and experimental observations.

No	Loop A + Loop B → ?	Experiment	Loop size relationship
1	$\frac{1}{2}[\bar{1}\bar{1}1]+\frac{1}{2}[\bar{1}\bar{1}1]\rightarrow\frac{1}{2}[\bar{1}\bar{1}1]$	W-5V (Fig 4.29) α-Fe [134]	A≥B
2	$\frac{1}{2}[111]+\frac{1}{2}[1\bar{1}\bar{1}]\rightarrow[100]$	/	A≈B
3	$\frac{1}{2}[11\bar{1}]+\frac{1}{2}[111]\rightarrow\frac{1}{2}[11\bar{1}]$	α-Fe [130]	A≥B
4	$[100]+[100]\rightarrow[100]$	/	A≥B
5	$[100]+[010]\rightarrow[100]$	α-Fe [130]	A≥B
6	$[100]+\frac{1}{2}[\bar{1}11]\rightarrow[100]$	W-5V (Fig 4.25) W-5Re [135] α-Fe [136]	A>B
7	$[100]+\frac{1}{2}[\bar{1}11]\rightarrow\frac{1}{2}[\bar{1}11]$	α-Fe [130]	A≤B

*A>B: absorption; A≈B: coalescence.

6.3.2. The role of irradiation temperature

Loop size distributions, number densities, the relative fraction of ½<111> and <100> loops and the relative proportions of interstitial and vacancy loops are all affected by the irradiation temperature. In discussing these trends at intermediate or high doses, the increasing interaction between the point defect clusters and dislocation loops must be considered in addition to their enthalpies of formation and energies of migration.

At higher dose levels, the sequence of the stability of defect configuration predicted by Gilbert et al. and Nguyen-Manh et al remain valid [21, 39]. In particular, two aspects are discussed here. One is the loop configuration, ½<111> versus <100>. The other is the stability of vacancy clusters, dislocation loop versus spherical voids.

With an increase in temperature, it has been found that in both bulk and thin-foil irradiated samples of UHP-W the fraction of ½<111> loops increased. This observation is consistent with calculations showing that in elastically isotropic tungsten, the <100> configuration is an unfavourable geometry, with an additional energy of 2.5 eV in comparison with the ½<111> configuration (loop size: 34-37 SIAs). Although unfavourable, <100> loops do appear in the molecular dynamic simulations of cascade collapse events and match with the predicted geometries based on the Eyre-Bullough mechanism [96]. Given appropriate annealing conditions, the <100> loops tend to vanish in the microstructure. The critical temperature for a full ½<111> loop microstructure in tungsten is estimated to be > 800°C (0.29 T_m). Similar observations of co-existing ½<111> and <100> loop microstructures have been reported in molybdenum and iron. In non-magnetic molybdenum, a similar high temperature instability of <100> loops was found. Rau et al. suggested that <100> loops were eliminated almost completely between 700 and 1000°C (0.34 - 0.44 T_m) [137]. The trend shown in iron is the opposite. Iron is magnetic and anisotropic, and

undergoes an allotropic phase transition (α→ γ) at around 912°C. As a consequence, the relative stability of the <100> configuration increases with increasing temperature [138]. Jenkins et al. indicated that in iron the transition to a full <100> loop microstructure occurred around 500°C [134].

The irradiation temperature also affects the form of vacancy clusters. The fact that the relative proportion of vacancy-type ½<111> loops decreases with increasing temperature and voids began to appear above 600°C give indications that spherical voids might be more stable than planar loops for accommodating large quantities of vacancies, in particular at elevated temperatures.

The migration of loops and the interactions among them were mainly responsible for the increase of loop size and fraction of interstitial loops as well as the decrease in loop population with increasing irradiation temperature from R.T. to 800°C. Temperature facilitates the migration of defect clusters. A good example of this is presented in Fig 5.12, which compares loop displacements at different annealing temperatures. The boosted migration ability at higher temperature increases the probabilities of collisions and therefore reactions among clusters and loops, leading to a decrease in loop number density and increase in loop size. Also due to the difference in mobility between vacancy and interstitial loops, as well as between ½<111> and <100> loops of the same nature, the microstructure evolved in preference of the collective movements of interstitial ½<111> loops through elastic interaction, followed by their alignment into strings and coalescence into "finger-shaped" loops.

6.3.3. The role of irradiation dose

At lower irradiation doses, the effect of dose is mostly reflected in an increase in loop number densities. Saturation of radiation damage was observed above a critical dose level, the value

of which decreased with increasing irradiation temperature. With increasing dose, the spatial separation of defect clusters decreased. Thus, they were more likely to be absorbed by the adjacent larger clusters or loops, rather than gaining in size themselves.

Irradiation dose may also promote an increase in loop size, but the mechanism may not be straightforward. On one hand, existing defect clusters may gain in size by attraction and absorption of newly-introduced clusters. On the other, an increase in dose introduces more obstacles on the migration path of defect clusters and restricts the range of their motion. The two competing mechanisms lead to a biased distribution of damage. Loops with **b** = ½<111> and of interstitial nature would tend to be larger compared to their less mobile counterparts. Three observations in UHP-W support this argument: the slight increase with dose in the fraction of ½<111> loops (Fig 3.25 a); the increase with dose in the fraction of interstitial loops with **b** = ½<111> (≥ 4 nm, Fig 3.26); and the upward-shift with dose in the size distributions of interstitial loops with **b** = ½<111> (Fig 3.29 a).

6.3.4. The role of impurity atoms: C/O (interstitial) and Re/Ta/V (substitutional)

Direct observations of loop hopping during in-situ irradiation suggest that impurities in tungsten may lower loop mobility. Further evidence was found in the size-nature plots (e.g. Figs 3.30 - 3.33), in which the frequency of large interstitial loops was substantially lower in less pure W and alloys. According to Muzyk et al. [139], the interaction between alloying atoms and <111> crowdions (½<111> loops can be regarded as a bundle of <111> crowdions) can be quantitatively described with a binding energy calculated from *ab initio* and cluster expansion methods. The sign of the binding energy indicates whether the interaction is attractive (positive) or repulsive (negative), while the absolute value represents the strength of binding. It was found effect of alloying atoms on suppressing the defect mobility appear in the sequence V>Re>Ta, see Fig 6.4. Although the binding energy of a V-

C complex in tungsten has been calculated as up to 1.36 eV [40], the impact of such interstitial impurities in our work may be low due to their low concentration (≤ 30 appm). It can be expected on this basis that the trapping capability of the impurities should follow the sequence V>Re>Ta>C/O. However, the loop number density and size distribution data indicate a sequence V>Ta>Re>C/O. A possible explanation to this discrepancy might lie in the choice of interatomic potentials adopted in the energy calculations, or the overlook of radiation induced effects, such as Ta-Ta/Re-Re clustering. Evidence of Re-Re clustering has been reported for high dose irradiations (37.5 dpa / 300°C), but unfortunately has not yet been systematically studied [77].

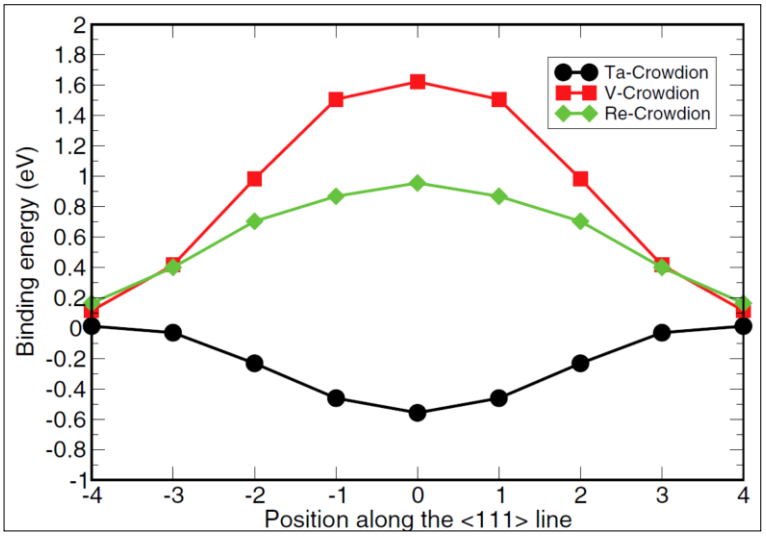


Fig 6.4 Binding energy of a crowdion interacting with Ta, V and Re atoms in W [139].

6.3.5. The role of crystallographic orientation

In "**z** = [001]" grains, loop rafts and strings developed only in pure tungsten, but requiring either high temperature or high dose (e.g. T ≥ 500°C or dose ≥ 1.5 dpa in bulk). However, non "**z** = [001]" grains allowed the formation of loop strings not only in alloys where loop mobility were more restricted, but also at a lower temperature. The increase of dose merely facilitated the evolution of loop strings to more complex networks. The most immediate interpretation for this phenomenon might be the directional dependence of collision cascades in tungsten, so called "channelling effect[20]", found effective when $E_{PKA} \geq 300$ keV [24]. Nevertheless, the scenario requires a strict alignment of the PKA with the channelling direction, which is likely not satisfied in this thesis. Even if the required geometry were satisfied, this should only affect the depth distribution of defects and apparently not their geometry, where ½<111> loops of the same Burgers vectors variants would be required. This is because loops form as a result of the quenching of the melted cascade region, which would have no correlation with the initial PKA direction. One possible explanation of the strong orientation dependence of damage microstructure in tungsten may have been the effect of surface attraction [140]. In "**z** = [001]" grains, the probability of loop loss through glide would be equal for all variants of ½<111>, whereas in "**z** = [011]" grains for instance, loops with $\mathbf{b} = \pm\frac{1}{2}[11\bar{1}]$ and $\pm\frac{1}{2}[\bar{1}1\bar{1}]$ would always be preserved in the foil, and the rest subject to loss to the surface. This impact of the surface attraction therefore leaves the non "**z** = [001]" grains with a limited variety of loop geometry, and the coalescence among which therefore leads to the formation of loop strings/rafts.

[20] Channelling is the displacement of atoms along open directions in a crystal structure.

6.4. Thermal stability of radiation damage in tungsten (in-situ)

The annealing temperatures selected were designated to match with the annealing stages defined in Table 1.3, where most probably 300°C, 500°C and 800°C correspond to stages III, IV and V respectively. The annealing temperature plays a more significant role than annealing time in the transformation of the damage microstructure. At ≥ 500°C, vacancies become mobile and may undergo fast long range migration. Consequently, at 500°C and 800°C in UHP-W a reduction in loop population and growth of remaining loops occurs rapidly in the first 15 min by absorption and recombination of point defects and clusters, as well as by reactions among loops. However, as loops grow their mobility decreases, and little further change occurs with increasing annealing time (demonstrated in Fig 4.21). At 300°C, only SIAs and clusters are sufficiently mobile, and thus a slower reduction of loop population might be expected during the ramp-up process. The time dependence of the loop number density and size distribution at 300°C imply that the migration of visible loops is strongly inhibited, but given enough time loops are able to gain an increase in size probably by the absorption of nearby SIAs and clusters.

Furthermore, it has been demonstrated that with either extended annealing time (at 800°C) or increase in annealing temperature, the fraction of <100> loops decreases, suggesting that <100> loops in tungsten are less thermally stable than ½<111> loops. This is in good agreement with conclusions drawn from in-situ irradiations, as presented in § 6.3.2.

6.5. Effects of surface image forces and the validity of extracting bulk damage properties from 2 MeV W^+ implantations

Free surfaces exert image forces that tend to attract dislocation loops in the damage microstructure. Loop loss to the surface is a thermally activated process and may be observed when the attractive force from the surface can overcome the hindering forces (i.e. lattice

friction, pinning of obstacles, and interactions with neighbouring defects). A favourable geometry is also required, i.e. the glide cylinder of the loop should intersect with the surface.

Direct experimental evaluation of the effects of surface images forces can be based on the analysis of the fractions of each Burgers vector variant, i.e. a systematic smaller fraction or the absence of specific loop geometry may suggest the strength of influence due to loop loss [140]; the measurement of the denuded zone by imaging cross-sections of the damage microstructure or performing electron diffraction tomography. In this section, an estimate of the range of denuded zone in tungsten is obtained, inferred from calculations of the total image force (Ft) on loops in silicon, shown in Fig 6.5 [141].

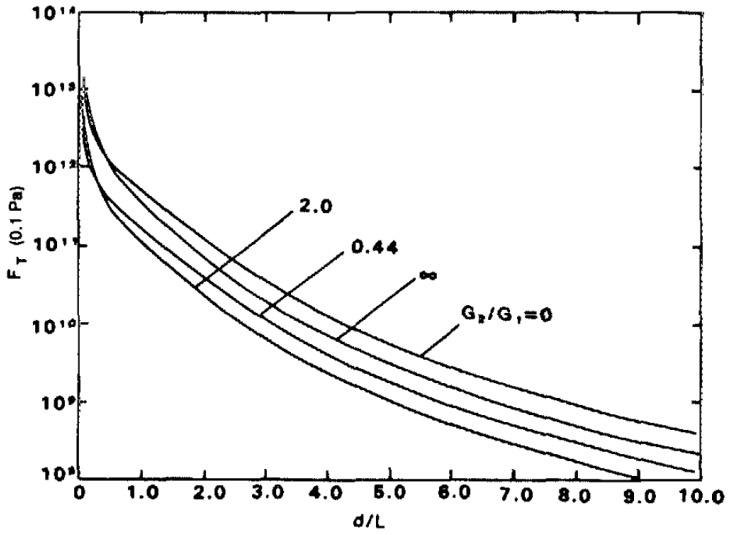


Fig 6.5 The total image force F_t acting on the dislocation loop (square-shaped) plotted as a function of d/L for silicon. τ_f: lattice frictional stress (macroscopic yield stress); d: loop distance from the surface; L: loop size; G_2: shear modulus of the layer above silicon, in this case air; G_1: shear modulus of silicon; $G_2/G_1=0$ [141].

If a loop falls in the denuded zone, it means that the image force F_t acting on which should exceed the lattice frictional stress or the macroscopic yield stress for it to glide to the surface, given by $8L\tau_f/b$ according to the Peach-Koehler formula [38]. The yield stress τ_f for tungsten is around 0.7 GPa [142] between 300°C and 800°C, which covers most temperatures investigated. The length of Burgers vector for a ½<111> prismatic loop is around 2.74 Å

[86], i.e. b = 2.74 Å. Most ½<111> loops in irradiated tungsten are less than 5 nm and L is assigned with 5 nm. Hence, the force opposing the glide motion of a 5 nm ½<111> loop in tungsten is around 1.0×10^{11} Pa. The condition at which the image force F_t exceeds this opposing force $8L\tau_f/b$ is satisfied when $d/L < 1$. In other words, depth region < 5 nm would be subject to strong loop loss to the surface and the total width of the denuded zones is 10 nm (two surfaces per thin foil). A revisit on the calculated damage profile for 2 MeV W^+ irradiations shown in Fig 2.4 indicates that these regions do not exceed 20% of the total displacement damage and that the extraction of bulk damage properties from which may still considered valid. Furthermore, the estimated dimension of the denuded zone is consistent with in-situ observations in Chapters 4 and 5. According to SRIM calculations, the peak damage depth of 150 keV W^+ irradiations corresponds to 10 nm. The majority of loops observed remained stable, including some very large loops exceeding 10 nm, during both isochronal annealing and post-irradiation microscopy sessions.

6.6. Extensive comparison of bulk irradiations with thin-foil ion irradiations in tungsten

The comparison of bulk versus thin-foil irradiations in this thesis is dealt with caution. In addition to the consideration of a free surface, there is difference in ion energy. Four aspects are covered for comparison, including the depth distribution of radiation defects, the number density of dislocation loops, the fraction of ½<111> loops against <100> loops and statistics on their interstitial/vacancy nature. Discussions are brought forward for identical test conditions (irradiation parameters; material composition; crystallography) and aim to separate the influence of free surface and ion energy.

6.6.1. Depth distribution of radiation defects

PKAs and their recoils create Frenkel pairs within displacement cascades, the depth distribution of which vary solely as a function of ion energy. Note that the quantities of SIAs

and vacancies will be kept balanced and their recombination, clustering and diffusion in the lattice are controlled by the energy barriers of migration. In other words, clusters of SIAs and vacancies are expected throughout the range of depth profile, though the position of the peak damage would vary. Once a free surface is present in the vicinity of radiation damages, the balance between SIAs and vacancies alters. SIAs and clusters are more easily drawn to the surface due to stronger strain fields, compared with vacancies [38]. Hence, the top surface appears as a 'depleted-zone', of only vacancies and clusters. SIAs and clusters which remain present are only found in deeper regions of the foil. Scenario of such has been confirmed in thin-foil irradiated Mo, by electron diffraction tomography [120].

6.6.2. Dislocation loop number density

Known from the NRT model, a PKA of higher energy obviously produces a larger number of Frenkel pairs which favours the accumulation of visible radiation defects, here referred to as dislocation loop number density. As a result, the influence of free surface cannot be examined by direct comparison of the loop number density data acquired in this thesis. But a qualitative picture can be depicted in two aspects. On one hand, a free surface breaks the balance of SIAs and vacancies upon creation, therefore reducing the rate of recombination and enhancing the survival of vacancies, i.e. more vacancy clusters form (loop or void). On the other, the substantial loss of SIAs could have clustered to form interstitial loops now become absent, i.e. less interstitial loops are formed. Combined with the observations of the disappearance of loops by glide frequently seen in videos, one may infer that free surfaces effectively reduce the loop number density. In the thin-foil in-situ irradiations, the energy of the electron beam 300 keV is well below the displacement threshold ~500 keV for tungsten. Therefore, direct contributions of loop number density are not considered for the electron beam. However, the synergies of ion beam and electron beam do have an influence on the

trend of loop loss, by means of detrapping loops from impurities and small clusters [109, 110].

6.6.3. The fraction of ½<111> loops against <100> loops

Bulk and thin-foil irradiations are consistent in the morphology of loops. Both ½<111> and <100> have been identified, and ½<111> loops were dominant (> 60%) in the damage microstructure. However, comparing the plot of the fraction of ½<111> loops in UHP-W as a function of irradiation temperature for a dose of 10^{18} $W^{+}m^{-2}$, the trend in the thin-foil experiments seemed more sensitive to temperature (Fig 3.25; Fig 4.59). Loop loss to the surface by glide may have been the reason. Within the temperature investigated ($T \leq 800°C$), loop glide is mostly ascribed to interstitial ½<111> loops, whereas vacancy ½<111> loops are less mobile and <100> loops only become mobile when climb is activated ($T > 0.4T_m$) [143]. As a consequence, the fraction of ½<111> loops probably remained constant at $T \leq 500°C$, if loop loss were corrected in the thin-foil data. But the consistent increase of ½<111> loops at $T > 500°C$ is most likely real, as the annealing stage rises from III to IV [55].

6.6.4. Statistics of loop nature (interstitial/vacancy)

Final remarks on the comparison of bulk and thin-foil irradiation results focus on the statistics of loop nature. Ion energy is expected to affect the population of interstitial and vacancy loops, but not so strongly their relative population, since they were introduced as Frenkel pairs. However, a large difference in the fraction of interstitial loops was found. Take interstitial ½<111> loops in UHP-W for example, bulk implantations indicated a fraction of 70-90%, while only 45-65% for thin-foil irradiations. This suggests that the loss of interstitial ½<111> loops to the free surface in thin-foils was considerably high, and bulk data is more reliable than thin-foil data on the relative statistics of loop nature.

6.7. A brief note on the observation of large vacancy loops in this thesis

Vacancy loops (≥ 6 nm) were present after nearly all irradiations in this thesis, which entailed a temperature range from 300°C up to 800°C among pure tungsten (UHP-grade, CG-grade) and (Re, V, Ta)-alloys. The only exception found was the UHP-W irradiated at 500°C up to 1.5 dpa with 2 MeV W^+ ions. The fraction of large vacancy loops varied with respect to irradiation condition and chemical composition of the material. Generally speaking, the increase of temperature and dose tended to eliminate the population of vacancy loops, and the impact of which were most pronounced in the UHP-tungsten. Take Fig 3.29 a) for example, one can tell the distinctive roles of temperature and dose in UHP-tungsten. With the increasing temperature, the population of small vacancy loops decreased and that of large vacancy loops increased. This suggests that temperature is in favour of the growth of vacancy loops, possibly through coalescence or absorption. With the increase of dose, vacancy loops either retained their dominant size categories or shifted to smaller values, indicating a reduction mechanism controlled by loop shrinkage.

The effect of dose on vacancy loop size and population can be interpreted as a consequence of the strain field at the peripheral of the loop being able to attract SIAs more strongly and that more SIAs would be produced at higher doses. But it is a difficult task to explain the initial presence of large vacancy loops. The same challenge applies to interpreting the effect of temperature.

The classical understanding of vacancy loops nucleation is through cascade collapse processes and this has been confirmed by both in-situ irradiations and molecular dynamic simulations [111, 135]. But the growth of these loops encounters several difficulties. First, it is the restricted mobility of monovacancies. It is well established that they are associated with a large migration barrier (1.78 eV) and do not become mobile until $0.2T_m$ [40, 71, 144]. On

the other hand, the irradiations in this thesis were performed between 300°C and 800°C, which correspond to $0.15T_m$ and $0.3T_m$. Even if analysing the temperatures where vacancies were mobile, i.e. assuming a single activation barrier (migration of monovacancies) being present, the amount of vacancy loop size increase found experimentally is considerably higher than theoretically predicted. D. Mason et al. reported this on low-dose irradiated tungsten [83]. That is to say, the vacancy loops are not expected to grow by absorbing monovacancies at the peripheral sites. Second, at all temperatures the excess of SIAs arriving at the peripheral of vacancy loops would be expected as a result of the strength of strain field. The concentrations of vacancies and SIAs upon production are assumed equal in this case. As a result, vacancy loops will tend to shrink.

Hence, alternative growth mechanisms must be responsible for the vacancy loops in tungsten. Electron irradiations on zirconium suggested that stress relieve may be a cause, although no solid evidence is yet available that it should also apply to self-ion irradiated tungsten. M. Griffiths et al. have reported that where there was an energy gain to the system (e.g. growing oxide), there were nucleation and growth of vacancy loops to relieve an appropriate stress [145, 146]. Similar observations were also found in neutron irradiated molybdenum and its alloy TZM (Mo, 0.5wt.% Ti, 0.1wt% Zr). The net reduction of SIAs (associated with large strain fields) in the material during the irradiation was achieved as a result a sharp rise in vacancy loop density and size, along with the shrinkage of voids where they were nucleated on. This effectively exerted a larger interstitial bias and attracted more SIAs to annihilate [147]. A further explanation of vacancy loop growth was given by Mason et al [83], where the loop-loop and loop-void long-range elastic interactions were responsible for the large scale in size increase. Vacancy size distributions from experiments were reproduced well by the object Kinetic Monte Carlo simulations for all temperatures. Finally,

the fact that larger fractions of large vacancy loops were found in CG-tungsten and its alloys might have been a result of segregation of impurities and alloying elements at vacancy loops, which stabilized the damage configuration [145].

Chapter 7

Conclusions

7.1. Summary of key results

- ✧ 2 MeV (1.9 MeV) W^+ ion implantations were performed on bulk specimens of pure tungsten (UHP, > 99.9999 wt%; CG, > 99.95 wt.%) and tungsten alloys (≤ 5 wt.% Re, Ta, V). Temperature range: 300-750°C. Dose range: 3.3×10^{17} ~ 2.5×10^{19} W^+/m^2.
- ✧ Thin-foil in-situ irradiations with 150 keV W^+ ions were carried out on UHP-W and tungsten alloys (5 wt.% Re, Ta, V). Temperature range: R.T. - 800°C. Dose range: 10^{16} ~ 10^{18} W^+/m^2.
- ✧ In-situ annealing was conducted on UHP-W thin foils, pre-irradiated at R.T. with 150 keV W^+ ions to a dose of 10^{18} W^+/m^2. The duration of annealing was up to 120 min, at temperatures 300, 500 and 800°C.
- ✧ Damage nucleation in UHP-W was studied by in-situ irradiations at low doses (≤ 10^{16} W^+/m^2). Black-white contrast analysis demonstrated the presence of vacancy loops with **b** = ½<111> and <100>, and confirmed that loops were formed by collapse of individual cascades. Evidence of interstitial loops was not found at these doses, probably due to the presence of a free surface in the vicinity of cascades serving as a strong sink for the SIAs. Defect yields were low (~ 3%, R.T.) and decreased further to ~ 0.2% at 800°C. The drop in defect yield was accompanied by an increase in loop average size, from ~ 2 nm to ~ 8 nm. At 500°C, the rate of the changes in defect yield and average

loop size accelerated, suggesting a correspondence with the increasing mobility of single vacancies.

- ✧ The further course of damage evolution (10^{16} ~ 10^{18} W^{+}/m^{2}) in both bulk-irradiated and thin-foil irradiated specimens was strongly influenced by the dynamic behaviour of loops, such as loop hopping and loop interactions/reactions, and by specimen orientation. This led to features such as the formation of loop strings and networks. The mobility of defects was enhanced by an increase in temperature, but was suppressed by dose accumulation and the presence of alloying atoms.
- ✧ Post-irradiation characterization of both bulk-irradiated and thin-foil irradiated specimens demonstrated consistently that the radiation damage microstructure consisted of (> 60%) ½<111> loops and <100> loops, mostly of interstitial type. With an increase in irradiation temperature, ½<111> loops of interstitial nature tended to dominate the damage microstructure. Also, the overall loop size distributions shifted towards larger sizes, along with a substantial decrease of loop number densities. The influence of dose was most pronounced on the loop number density data of the alloys in low temperature irradiations. In the elevated temperature regions (i.e. ≥ 500°C), loop number densities tended to saturate with dose. The presence of alloying elements and impurity atoms favoured a higher number density of loops, and suppressed the growth of these loops in the sequence V > Ta> Re > impurities.
- ✧ In-situ annealing of UHP-W showed that the annealing temperature played the decisive role in altering loop geometries, size distributions and number densities. The evolution of damage microstructure was much less sensitive to annealing time.

7.2. Outlooks on the understanding of radiation damage in tungsten

A revisit on the research goals set in the beginning of this thesis shows that all five key points have been answered comprehensively. The species of radiation defects in tungsten is known. Their dependence on the irradiation temperature, dose, material (composition, grain orientation) and the process of damage evolution are also known. However, these understandings of radiation damage are on the level of 'what's and 'how's. The 'why' part requires further efforts, perhaps through multi-scale modelling. Two experimental observations are listed as follows, important and yet not fully understood.

❖ The formation of <100> loops in tungsten.

This thesis has found direct evidence of <100> loops in tungsten for the first time. Prior to this discovery, they were considered energetically forbidden [138]. Recent MD simulations showed that they may nucleate within displacement cascades, as a rare event [111], which is consistent with the discovery of <100> loops in the low-dose (0.01 dpa) thin-foil experiments. But whether these loops may originate from the loop collisions (reactions) is not confirmed. In addition to their conventionally unexpected occurrence, their relative high fraction at low temperatures is a more difficult puzzle (~25%, 500°C). The fraction of <100> loops decreases with the increase of temperature. What mechanisms control the thermal stability of <100> loops? The increase of ion energy seems to favour the formation of <100> loops. Why?

❖ The orientation dependence of radiation damage microstructure.

The non **z** = [001] orientations were found to facilitate the formation of loop strings and networks in tungsten. In Ch 6, this has been argued from a channelling point of view, and an assumption was made such that the nucleation of loops of different Burgers vector variants

can be biased consequently. MD simulations of high-energy cascades in tungsten are needed, as a function of PKA direction.

In a wider picture of tungsten applications in fusion reactors, this thesis fits into the application of tungsten as a structural component in the divertor and a PFC in the first wall. The immediate step to take forward is the establishment of relationship between the damage microstructure observed in this thesis with mechanical properties data, which may provide useful insights to the ductilization of tungsten. So far this work has only been completed for 300°C bulk implantations [77, 148]. Irradiation hardening occurred in both pure tungsten and alloys, in close correlation with the loop number density. This alone has suggested that the simple alloying route (Re, Ta, V) to ductilizing tungsten has not been successful. Since Re and Ta are also transmutation products of tungsten, the material will become increasingly brittle after irradiation exposure. The second step forward is the identification of the difference between self-ion irradiations and fusion neutron irradiations. Dose rate, energy spectrum of the recoils and defect species all are different. In this thesis, only the interactions between dislocation loops have been investigated. But in order to understand the damage microstructural evolution in a fusion environment, interactions between loops, voids/bubbles, precipitates and transmutation induced impurities (Re, Os, Ta etc) must be studied thoroughly.

For tungsten application as a PFC in the divertor, the temperature range investigated needs to cover 1200°C, its operating temperature in ITER [7]. Experimentally, one may get around the problem of the unavailability of high temperature irradiation facility by performing the irradiations at achievable temperatures, and post-anneal at elevated temperatures (1000-1400°C). Useful input information for dislocation dynamic simulations can thus be obtained, such as defect configuration, population and their migration energy (or

diffusion constant) to predict the evolution of damage microstructure. In addition to high temperature, efforts are required on seeking ways to preserve the integrity of the tiles upon fast accumulation of gaseous products as well as massive transient heat loads.

References

1. Garry McCracken, P.S., *Fusion: The Energy of the Universe*. 2nd ed. 2013: Academic Press, Elsevier. 228.
2. Miller, A.I., *Heavy Water: A Maunfacturer's Guide for the Hydrogen Century.* Candian Nuclear Society Bulletin, 2001. **22**(1).
3. Bloom, E.E., S.J. Zinkle, and F.W. Wiffen, *Materials to deliver the promise of fusion power - progress and challenges.* Journal of Nuclear Materials, 2004. **329-333**(Part 1): p. 12-19.
4. http://www.iter.org/factsfigures.
5. D.Stork, *DEMO*, in *MSc in Fusion Technology Lecture Course*2010, University of York.
6. Barabash, V., et al., *Neutron irradiation effects on plasma facing materials.* Journal of Nuclear Materials, 2000. **283-287**(Part 1): p. 138-146.
7. Hirai, T., et al., *R&D on full tungsten divertor and beryllium wall for JET ITER-like wall project.* Fusion Engineering and Design, 2007. **82**(15-24): p. 1839-1845.
8. http://www.efda.org/fusion/jet-tech/fusion-technology/plasma-facing-components/.
9. Wu, C.H., et al., *EU results on neutron effects on PFC materials.* Fusion Engineering and Design, 1998. **39–40**(0): p. 263-273.
10. S.J. Zinkle, N.M.G., *Operating temperature windows for fusion reactor structural materials.* Fusion Engineering and Design, 2000. **51-52**: p. 55-71.
11. Nave, R. *Hydrogen fusion reactions*. http://hyperphysics.phy-astr.gsu.edu/hbase/nucene/fusion.html.
12. http://en.wikipedia.org/wiki/Melting_points_of_the_elements_(data_page).
13. G.A.Cottrell, R.P., N.P.Taylor, *Transmutation and phase stability of tungsten armor in fusion power plants.* Fusion Science and Technology, 2006. **50**(1): p. 89-98.
14. Gibson, K., *Neutron Interactions in Matter and Neutron Damage*, in *MSc in Fusion Technology Lecture Course*2010, University of York.
15. Marian, J. and T.L. Hoang, *Modeling fast neutron irradiation damage accumulation in tungsten.* Journal of Nuclear Materials, 2012. **429**(1–3): p. 293-297.
16. Carron, N.J., *An Introduction to the Passage of Energetic Particles Through Matter.* . 2007: Taylor & Francis. 384.
17. F. Maury, M.B., P. Vajda, A. Lucasson, P. Lucasson, *Frenkel pair creation and stage I recovery in W crystals irradiated near threshold.* Radiation Effects, 1978. **38**: p. 53-55.
18. Kiritani, M., *Point defect processes in the defect structure development from cascade damage.* Materials Science Forum, 1987. **15-18**: p. 1023-1046.
19. Troev, T., N. Nankov, and T. Yoshiie, *Simulation of displacement cascades in tungsten irradiated by fusion neutrons.* Nuclear Instruments and Methods in Physics Research Section B: Beam Interactions with Materials and Atoms, 2011. **269**(6): p. 566-571.
20. Amino, T., K. Arakawa, and H. Mori, *Activation energy for long-range migration of self-interstitial atoms in tungsten obtained by direct measurement of radiation-induced point-defect clusters.* Philosophical Magazine Letters, 2010. **91**(2): p. 86-96.
21. Nguyen-Manh, D., A.P. Horsfield, and S.L. Dudarev, *Self-interstitial atom defects in bcc transition metals: Group-specific trends.* Physical Review B, 2006. **73**(2): p. 020101.
22. Brinkman, J.A., *Production of Atomic Displacements by High-Energy Particles.* Journal of American Physics, 1956(24): p. 246-267.
23. Calder, A.F., et al., *On the origin of large interstitial clusters in displacement cascades.* Philosophical Magazine, 2010. **90**(7-8): p. 863-884.

24. Was, G.S., *Fundamentals of Radiation Materials Science: Metals and Alloys*. 2007: Springer.
25. G.H. Kinchin, R.S.P., *The Displacement of Atoms in Solids by Radiation.* Reports on Progress in Physics, 1955. **18**(1).
26. Jens Lindhard, A.W., *Stopping power of electron gas and equipartition rule.* Mat. Fys. Medd. Dan. Vid. Selsk., 1964. **34**(4).
27. M. J. Norgett, M.T.R., I. M. Torrens, *A proposed method of calculating displacement dose rates.* Nucl. Eng. Des, 1975. **33**: p. 50-54.
28. *Bohr radius of tungsten*. Available from: http://www.americanelements.com/wtic.html.
29. P.Hirsch, A.H., R.Nicholson, D.W.Pashley, M.J.Whelan, *Electron microscopy of thin crystals*. 2nd Revised ed. 1977, Malabar, Florida: Robert E.Krieger Publishing Co., Inc.
30. Gilbert, M.R. and J.-C. Sublet, *Neutron-induced transmutation effects in W and W-alloys in a fusion environment.* Nuclear Fusion, 2011. **51**(4): p. 043005.
31. Stoller, R.E., *Primary Radiation Damage Formation*, in *Comprehensive Nuclear Materials*, R.J.M. Konings, Editor. 2012, Elsevier Ltd: Amsterdam. p. 293-332.
32. Nordlund, K., *Modified NRT equations for damage and mixing developed by the OECD NEA primary damage group*

in *Summary Report of the Technical Meeting on Primary Radiation Damage: from nuclear reaction to point defects* 2012, IAEA Nuclear Data Section: Vienna, Austria.

33. www.nueng.ca/harms/harms-candu3-physics.pdf.
34. Pampin, R., *Tungsten transmutation and resonance self-shielding in PPCS models for the study of sigma-phase formation*, in *UKAEA FUS 525*2005: Oxford, Culham.
35. A. S. Kovalev, A.D.K., A. M. Kosevich, A. I. Landau, *Theoretical Description of the Crowdion.* Phys. Stat. Sol. (b), 1993. **177**(117).
36. Matsukawa, Y. and S.J. Zinkle, *One-Dimensional Fast Migration of Vacancy Clusters in Metals.* Science, 2007. **318**(5852): p. 959-962.
37. Wirth, B.D., *How Does Radiation Damage Materials?* Science, 2007. **318**(5852): p. 923-924.
38. John Price Hirth, J.L., *Theory of dislocations*. 2nd ed. 1982, Malabar, Florida: Krieger publishing company. p.25-26.
39. Gilbert, M.R. and et al., *Structure and metastability of mesoscopic vacancy and interstitial loop defects in iron and tungsten.* Journal of Physics: Condensed Matter, 2008. **20**(34): p. 345214.
40. Dudarev, S.L., *Density Functional Theory Models for Radiation Damage*.* Annual Review of Materials Research, 2013. **43**(1): p. 35-61.
41. http://www.doitpoms.ac.uk/tlplib/solid-solutions/precipitates.php.
42. T.Tanno, A.H., J-C.He, M.Fujiwara, S.Nogami, *Effects of transmutation elements on neutron irradiation hardening of tungsten.* Materials transactions, 2007. **48**(9): p. 2399-2402.
43. Seidman, D.N., *Defects in metal crystals. Final report, May 1, 1981-June 30, 1983*, 1983. p. Medium: X; Size: Pages: 152.
44. Derlet, P.M., D. Nguyen-Manh, and S.L. Dudarev, *Multiscale modeling of crowdion and vacancy defects in body-centered-cubic transition metals.* Physical Review B, 2007. **76**(5): p. 054107.
45. J.E. Osher, J.C.D., *Ion source and accelerator development for the LLL 14-MeV neutron source facility.* Proceedings of the 1976 Proton Linear Accelerator Conference, 1976. **F01**: p. 316-320.
46. IAEA-TECDOC-1153, *Use of Accelerator Based Neutron Sources*, 2000: Austria.
47. http://www.lbl.gov/tt/techs/lbnl1764.html.

48. A. Araujo, C.P., M.A.F. Veloso, A.L. Costa, H.M. Dalle, *Flux and Dose Rate Evaluation of Iter System Using MCNP5.* Brazilian Journal of Physics, 2000. **40**(1): p. 58-62.
49. http://geoinfo.nmt.edu/resources/uranium/basics.html.
50. D.R.Olander, *Fundamental aspects of nuclear reactor fuel elements*, 1976, Technical Information Center, Energy Research and Development Administration, p.402, 430, 438-439, 447.
51. Shimada, M., *Recent result of PMI activity in STAR facility, INL (Recent results from the collaborative research of deuterium behavior in neutron-irradiated and ion-damaged tungsten)*, in *PFC meeting, Oak Ridge National Laboratory (Session II: Joint PFC/MASCO Special Topics Session on Tungsten)*2011.
52. Jannus-Saclay. *Dual/triple beam facilities*. 2008; Available from: http://jannus.in2p3.fr/spip.php?rubrique13.
53. Shimada, M., *Recent result of PMI activity in STAR facility, INL: Recent results from the collaborative research of deuterium behavior in neutron-irradiated and ion-damaged tungsten*, in *Joint PFC/MASCO Special Topics Session on Tungsten*2011, Oak Ridge National Laboratory.
54. Bowkett, K.M. and B. Ralph, *The Annealing of Radiation Damage in Tungsten Investigated by Field-Ion Microscopy.* Proceedings of the Royal Society of London. Series A, Mathematical and Physical Sciences, 1969. **312**(1508): p. 51-63.
55. Bykov, V.N., et al., *Nature and thermal stability of radiation defects in single-crystal tungsten.* Atomic Energy, 1972. **33**(4): p. 930-935.
56. Attardo, M. and J.M. Galligan, *A Field Ion Microscope Study of Neutron Irradiated Tungsten.* Physica Status Solidi (b), 1966. **16**(2): p. 449-457.
57. Jeannotte, D. and J.M. Galligan, *A study of radiation damage in tungsten—I.* Acta Metallurgica, 1970. **18**(1): p. 71-79.
58. Keys, L.K. and J. Moteff, *Neutron irradiation and defect recovery of tungsten.* Journal of Nuclear Materials, 1970. **34**(3): p. 260-280.
59. Keys, L.K., J.P. Smith, and J. Moteff, *High-Temperature Recovery of Tungsten after Neutron Irradiation.* Physical Review, 1968. **176**(3): p. 851.
60. Bueren, H.v., Z. Metallkunde, 1955. **46**(272).
61. L.K.Keys, J.M., *Neutron irradiation and defect recovery of tungsten.* Journal of Nuclear Materials, 1970. **34**: p. 260-280.
62. Keys, L.K., J.P. Smith, and J. Moteff, *Recovery of damage in neutron irradiated W/25 wt% Re.* Journal of Nuclear Materials, 1969. **33**(3): p. 337-339.
63. Brimhall, J.L., B. Mastel, and T.K. Bierlein, *Thermal stability of radiation produced defects in molybdenum.* Acta Metallurgica, 1968. **16**(6): p. 781-788.
64. Tanno, T., et al., *Effects of transmutation elements on the microstructural evolution and electrical resistivity of neutron-irradiated tungsten.* Journal of Nuclear Materials, 2009. **386-388**: p. 218-221.
65. Takashi Tanno, M.F., Shuhei Nogami, Akira Hasegawa, *Microstructure development in neutron irradiated tungsten alloys.* Materials transactions, 2011. **52**(7): p. 1447-1451.
66. He, J.C., A. Hasegawa, and K. Abe, *Effects of transmutation elements on the defect structure development of W irradiated by protons and neutrons.* Journal of Nuclear Materials, 2008. **377**(2): p. 348-351.
67. Thompson, M.W., *The damage and recovery of neutron irradiated tungsten.* Philosophical Magazine, 1960. **5**(51): p. 278-296.
68. F.Häussermann, V., *Analysis of dislocation loops in tungsten produced by 60keV ion irradiation.* Philosophical Magazine, 1972. **25**: p. 561-581.

69. F.Häussermann, V., *A study of the radiation damage produced by energetic gold ions in molybdenum and tungsten.* Philosophical Magazine, 1972. **25**: p. 583-598.
70. Jäger, W. and M. Wilkens, *Formation of vacancy-type dislocation loops in tungsten bombarded by 60 keV Au ions.* physica status solidi (a), 1975. **32**(1): p. 89-100.
71. Bobkov, A.F., et al., *Field ion microscopy of radiation defects in tungsten irradiated with 50-keV W+ ions.* Atomic Energy, 1980. **48**(5): p. 331-333.
72. A. L. Suvorov, A.G.Z., A. F. Bobkov, S. V. Zaitsev, V. P. Babaev, M. I. Guseva, S. N. Korshunov, I. N. Nikolaeva, A. A. Zaluzhnyi, *Effect of Various Components of Slightly Diluted Tungsten-Based Alloys on the Formation of Defects in Atomic Displacement Cascade Regions: Field-Ion Microscopic Analysis.* Technical Physics, 2003. **48**(1).
73. R.M.Scanlan, D.L.S., D.N.Seidman, *An in situ field ion microscope study of irradiated tungsten.* Philosophical Magazine, 1971. **23**: p. 1439-1478.
74. Plansee-Group. *High performance materials: Tungsten*. 2012; Available from: http://www.plansee.com/en/Materials-Tungsten-403.htm.
75. Rieth, M., et al., *Recent progress in research on tungsten materials for nuclear fusion applications in Europe.* Journal of Nuclear Materials, 2013. **432**(1–3): p. 482-500.
76. Reiser, J., et al., *Tungsten foil laminate for structural divertor applications – Analyses and characterisation of tungsten foil.* Journal of Nuclear Materials, 2012. **424**(1–3): p. 197-203.
77. Armstrong, D.E.J., et al., *Hardening of self ion implanted tungsten and tungsten 5-wt% rhenium.* Journal of Nuclear Materials, 2013. **432**(1–3): p. 428-436.
78. Hardie, C., *Dose rate effects in FeCr*, 2011, MFFP January Meeting: Oxford.
79. Hattar, K., *Temperature monitoring and dose measurement of the ion beam at Sandia*, 2013, Sandia National Laboratories.
80. Kirk, M.A., et al., *In situ transmission electron microscopy and ion irradiation of ferritic materials.* Microscopy Research and Technique, 2009. **72**(3): p. 182-186.
81. Marquis A., J.K., *Uncertainty of temperature measurement on the IVEM-tandem facility*, 2013, Argonne National Laboratory.
82. *SRIM 2008.03*, http://www.srim.org/SRIM/SRIM2008.htm.
83. D. R. Mason, X.Y., M. A. Kirk, S. L. Dudarev, *Elastic trapping of dislocation loops in cascades in ion-irradiated tungsten foils*, 2014, arXiv:1402.0689.
84. R. V. Jan, A.S., Phy. Stat. Sol., 1963. **3**(465).
85. International, A., *Standard Practice for Neutron Radiation Damage Simulation by Charged-Particle Irradiation*, Approved by 2003.
86. Davey, W.P., *The Lattice Parameter and Density of Pure Tungsten.* Physical Review, 1925. **26**(6): p. 736-738.
87. Plansee-Group. *Spark erosion techniques*. Available from: http://www.plansee.com/en/Products-Forming-and-machining-tools-Erosion-electrodes-76.htm.
88. A. B. Sivaka, V.A.R., V. M. Chernova, *Diffusion of Self Point Defects in Body Centered Cubic Iron Crystal Containing Dislocations.* Crystallography Reports, 2010. **55**(1): p. 97–108.
89. Oxford-Instruments. *Electrolytic Polishing and Etching*. Sample preparation for EBSD; Available from: http://www.ebsd.com/index.php/sample-preparation/sample-preparation-for-ebsd/electrolytic-polishing-and-etching.
90. Plansee-Group. *High performance materials: Tantalum*. 2012; Available from: http://www.plansee.com/en/Materials-Tantalum-404.htm.
91. Piotrowski, O., C. Madore, and D. Landolt, *Electropolishing of tantalum in sulfuric acid–methanol electrolytes.* Electrochimica Acta, 1999. **44**(19): p. 3389-3399.

92. Nakahara, S.C., A. G., *Simple method for determining the absolute sense of image rotation in a transmission electron microscope.* Ultramicroscopy, 1992. **45**(3-4): p. 365-370.
93. R.F.Egerton, *Electron Energy Loss Spectroscopy in the Electron Microscope*. 2nd ed. 1996, New York & London: Plenum Press.
94. D.B.Williams, C.B.C., *Transmission electron microscopy: A text book for materials science (I-IV)*. 1996: Springer-Verlag.
95. M.L.Jenkins, M.A.K., *Characterization of Radiation Damage by Transmission Electron Microscopy*. Microscopy in Materials Science, ed. M.J.G. B.Cantor. 2001: Institute of Physics Publishing, Bristol and Philadelphia.
96. Eyre, B.L. and R. Bullough, *On the formation of interstitial loops in b.c.c. metals.* Philosophical Magazine, 1965. **12**(115): p. 31-39.
97. Cambridge, U.o. *DoITPoMS*. Available from: http://www.doitpoms.ac.uk/tlplib/stereographic/wulff_plot_poles.php.
98. Groves, G.W.a.K., A., *INTERSTITIAL DISLOCATION LOOPS IN MAGNESIUM OXIDE.* Philosophical Magazine, 1961. **6**(72): p. 1527-&.
99. D.M.Maher, B.L.E., *Neutron irradiation damage in Molybdenum Part.I Characterization of small perfect dislocation loops by transmission electron microscopy.* PHIL MAG, 1971. **23**: p. 409-437.
100. C.A.English, M.L.J., *Insight into cascade processes arising from studies of cascade collapse.* Materials Science Forum, 1987. **15-18**: p. 1003-1022.
101. English, C.A. and M.L. Jenkins, *Molecular ion irradiations of molybdenum.* Philosophical Magazine, 2010. **90**(7-8): p. 821-843.
102. T.W. Ridler, S.C., *Picture thresholding using an iterative selection method.* IEEE Trans. System, Man and Cybernetics, , 1978. **SMC-8**: p. 630-632.
103. Jenkins, M.L., M.A. Kirk, and W.J. Phythian, *Experimental studies of cascade phenomena in metals.* Journal of Nuclear Materials, 1993. **205**(0): p. 16-30.
104. Eyre, B.L. and et al., *Electron microscope image contrast from small dislocation loops. I. Theoretical predictions for edge dislocation loops in a BCC crystal.* Journal of Physics F: Metal Physics, 1977. **7**(8): p. 1359.
105. Eyre, B.L. and et al., *Electron microscope image contrast from small dislocation loops. II. Application of theoretical predictions to defect analysis in irradiated metals.* Journal of Physics F: Metal Physics, 1977. **7**(8): p. 1371.
106. Zhou, Z., *Electron Microscopy and Elastic Diffuse Scattering of Nanostructures*, in *Materials*2005, University of Oxford.
107. W.J.Phythian, B.L.E., D.J.Bacon, *Irradiation damage in vanadium alloys using heavy ion and proton accelerators.* Journal of Nuclear Materials, 1988. **155-157**: p. 1274-1279.
108. K.Arakawa, K.O., M.Isshiki, K.Mimura, M.Uchikoshi, H.Mori, *Observation of the One-Dimensional Diffusion of Nanometer-Sized Dislocation Loops.* Science, 2007. **318**: p. 956-959.
109. Satoh, Y., H. Matsui, and T. Hamaoka, *Effects of impurities on one-dimensional migration of interstitial clusters in iron under electron irradiation.* Physical Review B, 2008. **77**(9): p. 094135.
110. Corbett, J.W., ed. *Solid State Physics, Advances in Research and Applications, supplement 7*. Electron radiation damage in semiconductors and metals. 1966, Academic Press.
111. A.E. Sand, S.L.D., K. Nordlund, *High energy collision cascades in tungsten: dislocation loops structure and clustering scaling laws.* Condensed Matter, 2013. **eprint arXiv:1306.3824**.
112. Müller, S., et al., *The influence of the surface on the production and development of displacement cascades in Ni3Al and Cu3Au.* Philosophical Magazine A, 1997. **75**(6): p. 1625-1640.

113. Mason, D., *Microstructural evolution in irradiated thin-film tungsten - towards understanding the experimental results*, 2013.
114. Kirk, M.A., et al., *The collapse of defect cascades to dislocation loops.* Journal of Nuclear Materials, 1987. **149**(1): p. 21-28.
115. C.A. English, B.L.E., M.L. Jenkins, *Heavy-ion damage in alpha-Fe.* Nature, 1976. **263**.
116. E. Zarkadoula, S.L.D., D.M. Duffy, M.A. Seaton, I.T. Todorov, K. Nordlund, M.T. Dove, K. Trachenko, *The nature of high-energy radiation damage in iron.* Journal of Physics: Condensed Matter, 2013. **25**
117. M.L. Jenkins, C.A.E., B.L. Eyre *Heavy-ion irradiation of iron.* Philosophical Magazine, 1978. **38**(1): p. 97-114.
118. Yao, Z., et al., *Heavy-ion irradiations of Fe and Fe–Cr model alloys Part 1: Damage evolution in thin-foils at lower doses.* Philosophical Magazine, 2008. **88**(21): p. 2851-2880.
119. English, C.A., et al., *The influence of material purity and irradiation temperature on self-ion damage in molybdenum.* Philosophical Magazine, 1977. **35**(3): p. 533-548.
120. Li, M., et al., *Study of defect evolution by TEM with in situ ion irradiation and coordinated modeling.* Philosophical Magazine, 2012: p. 1-31.
121. Marian, J., B.D. Wirth, and J.M. Perlado, *Mechanism of Formation and Growth of ⟨100⟩ Interstitial Loops in Ferritic Materials.* Physical Review Letters, 2002. **88**(25): p. 255507.
122. Osetsky, Y.N., D.J. Bacon, and A. Serra, *Thermally activated glide of small dislocation loops in metals.* Philosophical Magazine Letters, 1999. **79**(5): p. 273-282.
123. Fu, C.-C., F. Willaime, and P. Ordejón, *Stability and Mobility of Mono- and Di-Interstitials in α-Fe.* Physical Review Letters, 2004. **92**(17): p. 175503.
124. Derlet, P.M., M.R. Gilbert, and S.L. Dudarev, *Simulating dislocation loop internal dynamics and collective diffusion using stochastic differential equations.* Physical Review B, 2011. **84**(13): p. 134109.
125. Gilbert, M.R., et al., *Vacancy defects in Fe: Comparison between simulation and experiment.* Journal of Nuclear Materials, 2009. **386-388**: p. 36-40.
126. Mason, D., *Microstructural evolution in irradiated thin-film tungsten - towards understanding the experimental results*, 2013, CCFE: Culham. p. 1-6.
127. Dudarev, S.L., *The non-Arrhenius migration of interstitial defects in bcc transition metals.* Comptes Rendus Physique, 2008. **9**(3–4): p. 409-417.
128. Dudarev, S.L., P.M. Derlet, and C.H. Woo, *Driven mobility of self-interstitial defects under electron irradiation.* Nuclear Instruments and Methods in Physics Research Section B: Beam Interactions with Materials and Atoms, 2007. **256**(1): p. 253-259.
129. Fikar, J. and R. Schäublin, *Atomistic simulations of nanometric dislocation loops in bcc tungsten.* Nuclear Instruments and Methods in Physics Research Section B: Beam Interactions with Materials and Atoms, 2009. **267**(18): p. 3218-3222.
130. Arakawa, K., T. Amino, and H. Mori, *Direct observation of the coalescence process between nanoscale dislocation loops with different Burgers vectors.* Acta Materialia, 2011. **59**(1): p. 141-145.
131. Arakawa, K., et al., *Changes in the Burgers Vector of Perfect Dislocation Loops without Contact with the External Dislocations.* Physical Review Letters, 2006. **96**(12): p. 125506.
132. Wen, M., N.M. Ghoniem *, and B.N. Singh, *Dislocation decoration and raft formation in irradiated materials.* Philosophical Magazine, 2005. **85**(22): p. 2561-2580.
133. Arakawa, K. and H. Mori, *Energetics of formation process of a prismatic dislocation loop via the collision between two 1/2 loops in α-iron.* Journal of Physics: Conference Series, 2009. **165**(1): p. 012005.

134. Jenkins, M.L., et al., *Dynamic observations of heavy-ion damage in Fe and Fe-Cr alloys.* Journal of Nuclear Materials, 2009. **389**(2): p. 197-202.
135. Yi, X., et al., *In situ study of self-ion irradiation damage in W and W–5Re at 500 °C.* Philosophical Magazine, 2012. **93**(14): p. 1715-1738.
136. Yao, Z., et al., *The temperature dependence of heavy-ion damage in iron: A microstructural transition at elevated temperatures.* Philosophical Magazine, 2010.
137. Rau, R.C., F.S. D'aragona, and R.L. Ladd, *Neutron damage in molybdenum irradiated at high temperatures.* Philosophical Magazine, 1970. **21**(171): p. 441 - 452.
138. Dudarev, S.L., R. Bullough, and P.M. Derlet, *Effect of the α-γ Phase Transition on the Stability of Dislocation Loops in bcc Iron.* Physical Review Letters, 2008. **100**(13): p. 135503.
139. Muzyk, M., et al., *Phase stability, point defects, and elastic properties of W-V and W-Ta alloys.* Physical Review B, 2011. **84**(10): p. 104115.
140. Jäger, W., M. Rühle, and M. Wilkens, *Elastic interaction of a dislocation loop with a traction-free surface.* physica status solidi (a), 1975. **31**(2): p. 525-533.
141. Narayan, J. and K. Jagannadham, *Effect of free surface and interface on thermal annealing of dislocation loops in silicon.* Journal of Applied Physics, 1987. **62**(5): p. 1694-1697.
142. F. F. Schmidt, H.R.O., *The engineering properties of tungsten and tungsten alloys*, D.m.i. center, Editor 1963: Columbus, Ohio.
143. Blanchard, J., *Fracture and Creep in the All-Tungsten ARIES Divertor*, in *Japan/US Workshop on Power Plant Studies and Advanced Technologies* 2013.
144. Dudarev, S.L., *Formation and evolution of defect microstructure in tungsten*, in *Oxford MFFP Tungsten Workshop*2013: Oxford.
145. Griffiths, M., M.H. Loretto, and R.E. Smallman, *Electron damage in zirconium: I. defect structure and loop character.* Journal of Nuclear Materials, 1983. **115**(2–3): p. 313-322.
146. Griffiths, M., M.H. Loretto, and R.E. Smallman, *Electron damage in zirconium: II. Nucleation and growth of c-component loops.* Journal of Nuclear Materials, 1983. **115**(2–3): p. 323-330.
147. Evans, J.H., *Radiation-induced shrinkage of voids in molybdenum and TZM.* Nature, 1979. **278**: p. 728-729.
148. D. E. J. Armstrong, A.J.W., S. G. Roberts, *Mechanical properties of ion-implanted tungsten–5wt% tantalum.* Physica Scripta, 2011. **T145**(014076).

Appendix

List of videos (presented in real time)

1. (Fig 4.2) Damage development in UHP-W, irradiated up to 0.01 dpa (1.25×10^{18} W^+/m^2) at 800°C with 150 keV W^+ ions. Grain orientation: [001].

2. (Fig 4.20) Loop hopping in UHP-W, during the irradiation of 150 keV W^+ ions at 800°C. Grain orientation: [001].

3. (Fig 4.22) The Burgers vector of a small ½<111> loop changes after the elastic interaction with a neighbouring ½<111> loop of larger size. W-5Re, irradiated at 500°C with 150 keV W^+ ions in [001] orientation.

4. (Fig 4.25) The absorption of a small ½<111> loop by a large <100> loop in W-5V, irradiated at 500°C with 150 keV W^+ ions in [001] orientation.

5. (Fig 4.27) Loop string formation in W-5V as a result of the 1D displacement of loops and a variation of their habit planes. Irradiation condition: 800°C, **z** = [001] direction.

6. (Fig 4.29) Loop-string interaction in UHP-W, irradiated at 800°C with 150 keV W^+ ions in [001] orientation.

7. (Fig 4.30) Loop string segment changes its geometry with respect to the elastically interacting environment by translational displacement in W-5V, irradiated at 800°C with 150 keV W^+ ions in [011] orientation.

8. (Fig 4.32) A string of loops in UHP-W undergoes three stages of collective rotation, irradiated at 800°C with 150 keV W^+ ions in [001] orientation.

9. (Fig 4.33) String-string interaction and reaction in W-5V, irradiated at 800°C with 150 keV W^+ ions in [011] orientation.

10. (Fig 5.13) Two loops in collective hopping motion, observed in the in-situ annealing of UHP-W (R.T. / 1.0 dpa) at 800°C.

11. (Fig 5.14) The change of habit plane of ½<111> loop in UHP-W (R.T. / 1.0 dpa), in-situ annealed at 500°C.

12. (Fig 5.15) The transformation of a bound loop pair in UHP-W (R.T. / 1.0 dpa) annealed at 800°C, involving large angle rotation of loop habit plane and loop absorption.